Numerical investigation of the effects of coupled radiative heat transfer on free turbulent jets of water vapor

Jan Mateu Armengol

To cite this version:

Jan Mateu Armengol. Numerical investigation of the effects of coupled radiative heat transfer on free turbulent jets of water vapor. Thermics [physics.class-ph]. Université Paris Saclay (COmUE); Universidade estadual de Campinas (Brésil), 2019. English. NNT : 2019SACLC052 . tel-02275920

HAL Id: tel-02275920
https://theses.hal.science/tel-02275920

Submitted on 2 Sep 2019

NNT : 2019SACLC052

Étude numérique des effets du couplage du rayonnement thermique aux jets turbulents libres de vapeur d'eau

Thèse de doctorat de l'Université Paris-Saclay et Unicamp
préparée à CentraleSupélec

Ecole doctorale n°579 Sciences mécaniques et énergétiques, matériaux et géosciences (SMEMAG)
Spécialité de doctorat : Thermique

Thèse présentée et soutenue à Gif-sur-Yvette, le 13/06/2019, par

JAN MATEU ARMENGOL

Composition du Jury :

Patrick Le Quéré Directeur de Recherche, CNRS (LIMSI)	Président
Christophe Bailly Professeur, École Centrale de Lyon (LMFA)	Rapporteur
Pedro Coelho Professeur, Universidade de Lisboa (IDMEC)	Rapporteur
Carlos David Pérez Segarra Professeur, Universitat Politècnica de Catalunya (CTTC)	Examinateur
Ronan Vicquelin Maître de conférences, Centralesupélec (EM2C)	Co-encadrant
Rogério Gonçalves Dos Santos Professeur, Universidade de Campinas (FEM)	Directeur de thèse
Olivier Gicquel Professeur, Centralesupélec (EM2C)	Directeur de thèse

Thèse de doctorat

Acknowledgments

In the first place, I would like to thank my thesis directors, Prof. Rogério Gonçalves dos Santos and Prof. Olivier Gicquel. This thesis would not have been possible without their ideas and support.

I am very grateful to my co-supervisor Prof. Ronan Vicquelin for his guidance, encouragement and his numerous enlightening remarks.

Many thanks to Prof. Axel Coussement for providing the YWCx code besides many valuable inputs during the development of this thesis, and for welcoming me several times in the BURN lab in Brussels.

My sincere gratitude to Prof. Jesús Xamán for his guidance in the development of the RANS code during the summer stage I spent in México, as well as all his encouragement throughout this work.

I also acknowledge Prof. Flávio de Campos Bannwart for his collaboration in this work and the valuable knowledge that he carefully has taught me.

I would like to thank Prof. Philippe Rivière for providing line-by-line results for validation of the ck model in the present configurations.

Afraid of forgetting someone important, I express a big thank to all the colleagues from Unicamp and EM2C lab that have shared this experience with me, helped me in the difficult times and brought me the certainly needed humanism to deal with such a theoretical work.

I wish to thank CAPES (Brazilian Federal Agency for Support and Evaluation of Graduate Education within the Ministry of Education of Brazil) and Centrale Recherche S.A. for the financial support. This work was performed using HPC resources from the "Mésocentre" computing center, and from CINES under the allocation 2018-A0042B10159 made by GENCI.

To my mother, my father, my brother, and all friends and family from Barcelona: thank you.

Abstract

Radiation plays an important role in a broad range of thermal engineering applications comprising turbulent flows. The growing need for accurate and reliable numerical simulations to support the design stages of such applications is the main motivation of this thesis.

Of special interest in this work are the free-shear flows and the fundamental understanding of how radiation can modify their fluid dynamics and heat transport as well as how their turbulence fluctuations can alter radiative transfer. The goal of this thesis is to provide high-fidelity data of turbulent free jets coupled with thermal radiation in order to develop and validate free-shear turbulent models accounting for coupling interactions. To this end, turbulent free jets are described by direct numerical simulations (DNS) coupled to a reciprocal Monte-Carlo method to solve the radiative transfer equation. The spectral dependency of the radiative properties is accounted for with an accurate Correlated-k method. The numerical study is carried out with state-of-the-art fidelity to be as representative as possible of an actual jet in a participating medium. The simulation is optimized in terms of processing time taking advantage of an acceleration method called Acoustic Speed Reduction and by injecting artificial turbulence to enhance inlet boundaries.

Two direct simulations of heated jets coupled with thermal radiation are carried out. On the one hand, a heated jet with moderate radiation is simulated. The analysis of its high-fidelity coupled DNS data has allowed to derive a new scaling law for the decay of the temperature profile. This scaling accounts for the effects of modified density due to moderate radiation. Moreover, it allows for distinguishing whether thermal radiation modifies the nature of heat transfer mechanisms in the jet developed region or not. On the other hand, a strongly heated free jet is computed in order to quantify the effects of radiation on mean temperature and velocity fields as well as on second order moments. In the strongly heated jet, radiation has a significant contribution in the mean enthalpy balance on both the developing and the developed zones. Then, mean temperature fields are strongly affected by radiation in the strongly heated jet. Further analysis of temperature fluctuations through the enthalpy fluctuations balance has shown that the correlation between enthalpy fluctuations and radiative power fluctuations significantly contributes to the dissipation of the enthalpy variance. When radiation is taken into account, the molecular dissipative term nearly decreases by a factor of two. This is because production decreases with radiation since temperature gradients are smoother, but also because enthalpy variance is dissipated by radiation.

Besides the coupled DNS data, a RANS solver for variable-density flows coupled with thermal radiation has been implemented during the course of this thesis. The goal is to directly quantify the accuracy of the existing turbulent models, and to identify key parameters for further modeling of coupling interactions.

Résumé

Le rayonnement thermique joue un rôle important dans un large éventail d'applications de génie comprenant des écoulements turbulents. La motivation principale de cette thèse est le besoin croissant de précision et fiabilité dans les simulations numériques appliqué à ce domaine. Cette thèse s'intéresse tout particulièrement à la compréhension physique de l'impact du rayonnement sur la dynamique des fluides et le transfert thermique, ainsi que de l'influence des fluctuations turbulentes sur le transfert radiatif dans les écoulements à couche de cisaillement. L'objectif de cette thèse est de fournir des données haute-fidélités de jets libres turbulents couplés au rayonnement thermique afin de développer et de valider des modèles turbulents d'écoulements à couche de cisaillement prenant en compte les interactions de couplage. À cette fin, les jets libres turbulents sont décrits par des simulations numériques directes (DNS) couplées à une méthode de Monte-Carlo réciproque pour résoudre l'équation de transfert radiatif. La dépendance spectrale des propriétés radiatives est prise en compte avec la méthode *Correlated-k*. L'étude numérique est réalisée avec la plus grande fidélité pour être aussi représentative que possible d'un jet réel dans un milieu participatif. La simulation est optimisée en termes de temps de calcul en tirant parti d'une méthode d'accélération (*Acoustic Speed Reduction*) et en injectant de la turbulence artificielle pour améliorer les conditions d'entrée.

Deux simulations directes de jets chauffés couplés au rayonnement sont réalisées. D'une part, un jet chauffé avec un rayonnement modéré a été simulé et l'analyse de ses données DNS couplées a permis de dériver une nouvelle loi d'échelle pour la décroissance du profil de température. Cette mise à l'échelle rend compte des effets de la densité modifiée due à un rayonnement modéré. De plus, cela permet de distinguer si le rayonnement modifie ou non la nature des mécanismes de transfert thermique dans la région développée du jet. D'autre part, un jet libre fortement chauffé a été calculé afin de quantifier les effets du rayonnement sur les champs de température et de vitesse moyens ainsi que sur les moments de second ordre. Dans le jet fortement chauffé, le rayonnement joue un rôle important dans le bilan d'enthalpie moyen dans les régions initiale et développées du jet. Ensuite, les champs de température moyenne sont fortement affectés par le rayonnement dans le jet fortement chauffé. Une analyse des fluctuations de température dans le bilan des fluctuations d'enthalpie a montré que la corrélation entre les fluctuations d'enthalpie et les fluctuations de puissance radiative contribuent de manière significative à la dissipation de la variance de l'enthalpie. Lorsque le rayonnement est pris en compte, le terme de dissipation moléculaire diminue presque d'un facteur deux. En effet, la production diminue avec les radiations car les gradients de température sont plus faibles, mais aussi parce que la variance de l'enthalpie est dissipée par le rayonnement. Outre les données DNS couplées, un solver RANS pour les écoulements à densité variable couplé au rayonnement a été développé au cours de cette thèse. L'objectif était de quantifier directement la précision des modèles turbulents existants et d'identifier les paramètres clés pour une modélisation plus poussée des interactions de couplage.

Resumo

A radiação desempenha um papel importante em uma ampla gama de aplicações de engenharia térmica inclusive em escoamentos turbulentos. A crescente necessidade de precisão e confiabilidade nas simulações numéricas para apoiar as etapas de design nesse contexto é a principal motivação da presente tese. De especial interesse neste trabalho são os escoamentos livres e o entendimento fundamental de como a radiação pode modificar a dinâmica e o transporte de calor, assim como as flutuações turbulentas destes podem alterar a transferência de calor por radiação nesse tipo de escoamentos. Com o fim de desenvolver e validar modelos para as interações radiação-turbulência, o objetivo da presente tese é fornecer dados de alta fidelidade de jatos turbulentos livres acoplados à radiação térmica. Assim, os jatos livres turbulentos são descritos por simulações numéricas diretas (DNS) acopladas a um método de Monte Carlo recíproco para resolver a equação de transferência radioativa. A dependência espectral das propriedades radioativas é modelada com o método *Correlated-k*. O estudo numérico é realizado com essas ferramentas numéricas para ser o mais representativo possível de um jato real em um meio participante. A simulação é otimizada em termos de tempo de processamento aproveitando um método de aceleração chamado *Acustic Speed Reduction* e injetando turbulência artificial para melhorar as fronteiras de entrada do escoamento.

Duas simulações diretas de jatos aquecidos acoplados a radiação térmica são realizadas. Por um lado, um jato aquecido com radiação moderada é simulado. A análise de seus dados DNS acoplados de alta fidelidade permitiu derivar uma nova lei de escala para o decaimento do perfil de temperatura. Essa lei de escala compensa os efeitos na densidade devidos à radiação moderada. Além disso, permite distinguir se a radiação térmica modifica ou não a natureza dos mecanismos de transferência de calor na região desenvolvida do jato. Por outro lado, um jato livre fortemente aquecido é resolvido para quantificar os efeitos da radiação nos campos médios de temperatura e velocidade, bem como nos momentos de segunda ordem.

No jato fortemente aquecido, a radiação tem uma contribuição significativa no balanço de entalpia. EntÃ£o, os campos de temperatura média são fortemente afetados pela radiação no jato fortemente aquecido. Uma análise mais aprofundada das flutuações de temperatura através do balanço de flutuações de entalpia mostrou que a correlação entre flutuações de entalpia e flutuações de potência radiativa contribui significativamente para a dissipação da variança de entalpia. Quando a radiação é levada em conta, o termo dissipativo molecular quase diminui por um fator de dois. Isso ocorre porque a produção diminui com a radiação, já que os gradientes de temperatura são mais suaves, mas também porque a variança de entalpia é dissipada pela radiação.

Além dos dados do DNS acoplado, um *solver* RANS para escoamentos de densidade variável acoplado à radiação térmica foi implementado durante o curso desta tese. O objetivo é quantificar diretamente a precisão dos modelos turbulentos existentes e identificar os principais parâmetros para modelagem das interações no acoplamento.

Contents

Introduction

Global context of this thesis

World electricity generation has been notoriously growing during the past decades and is projected to increase by a factor of 1.7 by 2040 according to the International Energy Agency (IEA (2018)) as shown in Fig. 1. Embedded in this growth there is the economic development of emerging markets such as Asia and Africa. Furthermore, there are the challenges related to fighting climate change and adapting to its effects.

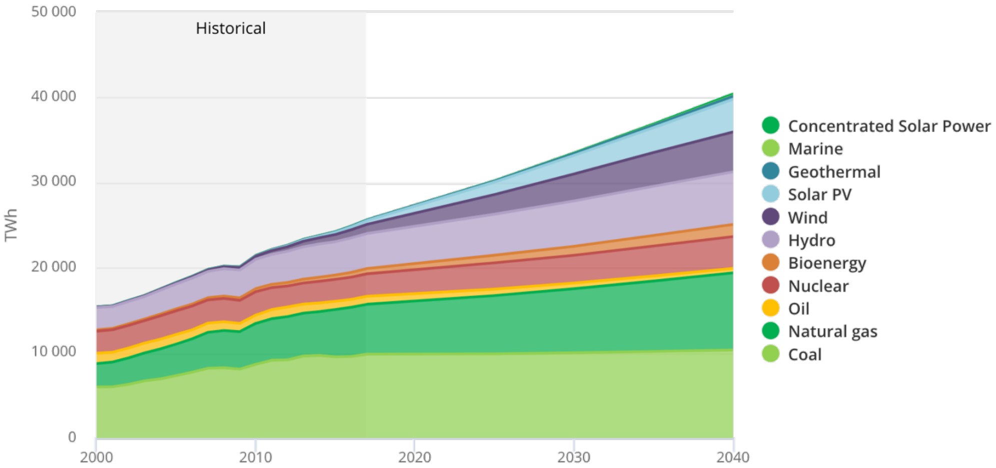

Figure 1: *World electricity generation by technology in the new Policies Scenario which incorporates existing energy policies as well as an assessment of the results likely to stem from the implementation of announced policy intentions. Extracted from IEA (2018)*

On November 28, 2018, the European Commission presented its strategic long-term vision for a climate-neutral future by 2050 (EC (2018)) in line with the Paris Agreement objective to keep the global temperature increase to well below 2^oC and pursue efforts to keep it to 1.5^oC (UNFCCC (2019)). As illustrated in Fig. 2, the strategy includes the long-term objective of cutting greenhouse gas (GHG) emissions in EU territory by 80-95% below 1990 levels by 2050 as part of efforts by developed countries to reduce their emissions.

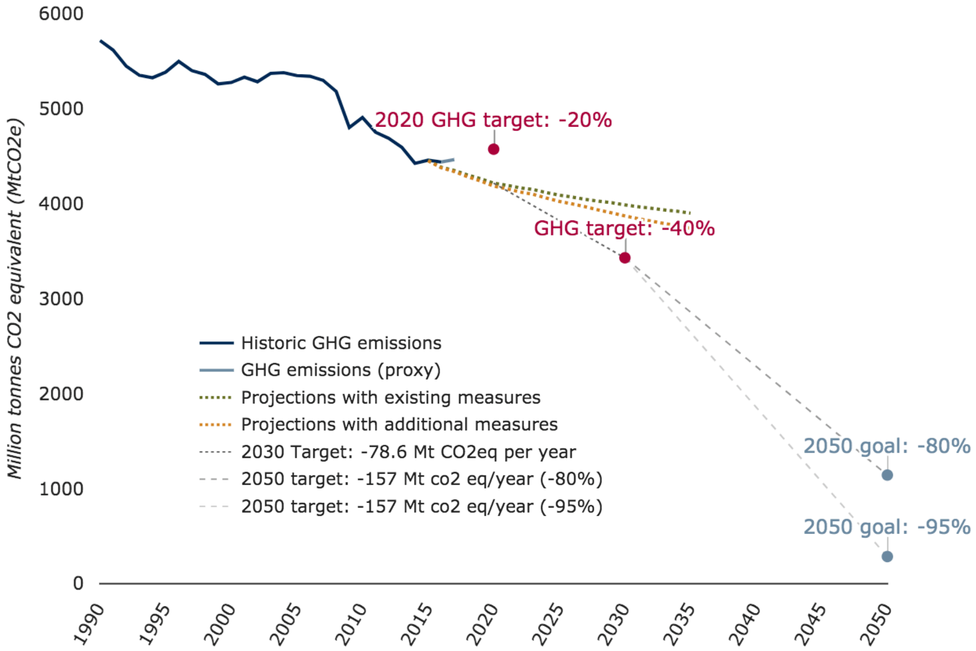

Figure 2: *Greenhouse gas emission trends, projections and targets in the EU. Extracted from EEA 2015.*

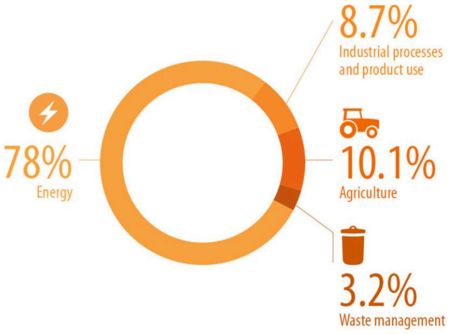

Figure 3: *Greenhouse gas emissions by sector in the EU in 2015 excluding land use, land-use change and forestry. Data form EEA 2015, extracted from EP (2018)*

Data from the European Environment Agency (EEA (2015)) points out that the largest source of greenhouse gas emissions from human activities in the EU comes from energy generation - not restricted to electricity generation - as presented in Fig. 3 extracted from EP (2018). Given the growth perspectives on energy demand, and the imperative target of reducing emissions, the necessity to **optimize the existing energy generation systems**, as well as to introduce cleaner ones seems a general agreement since energy generation is responsible for 78% of emissions.

As reported in IEA (2017), electricity generation represents more than 20% of the world final energy consumption. Focusing on the technologies responsible for such electricity generation, the main prime mover in all power stations in 2012 is the steam turbine (60%) followed by the gas turbine (20%) as shown in Fig. 4, in which their estimated increased role in electricity generation by 2040 is also indicated.

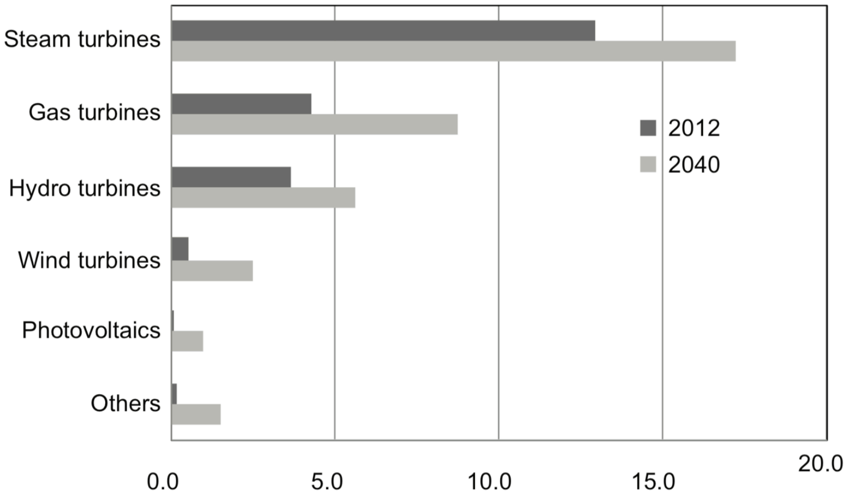

Figure 4: *World electricity generation by prime movers in 2012 and 2040 (trillion kWh). Extracted from Tanuma (2017)*

The efficiency optimization of steam and gas turbines is valuable given their important role in the electricity generation. In the following subsections a short description is provided regarding the optimization of these systems with the sole purpose of highlighting their common features and their link with the present thesis.

Steam turbine

The ultra-supercritical (USC) steam turbines reach net power generation efficiency over 45% by increasing steam temperature and pressure at the turbine inlet up to 600 ^{o}C and 300 bar, respectively. In contrast, sub-critical steam power plants do not exceed 40% of efficiency. There are the advanced-USC steam power plants characterized for temperatures and pressures up to 700 ^{o}C and 350 bar (Tanuma (2017)), respectively, currently under development. To assist the design and optimization of these modern steam turbines, experimental analysis and **numerical simulations** are crucial complementary tools.
Computational fluid dynamics allow for an understanding of the aerodynamics inside a turbine as shown in Fig. 5(a), from which detailed outputs such as the entropy generation field, presented in Fig. 5(b), can be obtained identifying the local lost in performance (Jang et al. (2015)). Some efforts have been done to numerically assess the performance of steam turbines including the works of

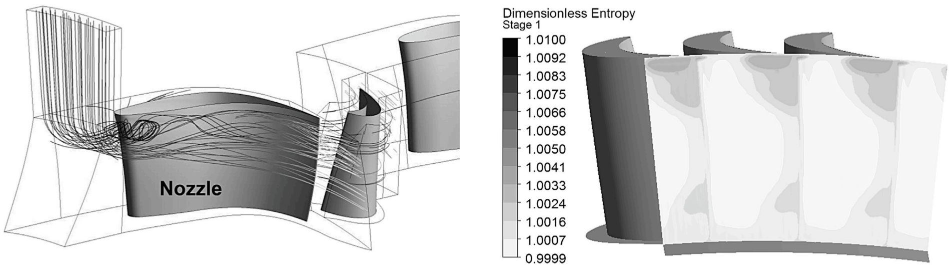

(a) (b)

Figure 5: *(a) Flow mixing at nozzle inlet due to overload valve flow supply (streamlines). (b) Entropy contours at the trailing edge plane of the first stage rotor. Extracted from Jang, Kang, Lee, Kim and Park (2015)*

Wróblewski et al. (2009); Wang et al. (2016); Abadi et al. (2017). However, the modeling of complex systems involving multiple phenomena is still a challenging problem for engineering and computational science. Despite the fact that radiation can be the dominant mode of heat transfer, radiation is often neglected because of the increase in complexity and in time processing. Therefore, the availability of numerical tools capable of generating high-fidelity data appears as a crucial challenge to guide the design of modern steam turbines.

Gas turbine

Similarly to the steam turbine, the efficiency in a gas turbine is also improved by increasing the temperature and pressure at which the turbine operates. Inlet temperatures between 1200^oC and 1600^oC and pressure over 30 bar can be found in gas turbines for power generation reaching efficiencies from 35 up to 40 %.

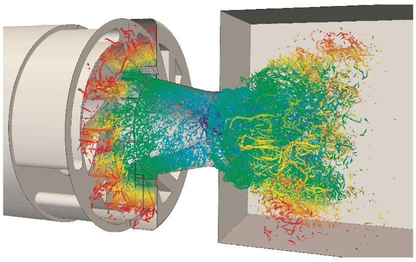

Figure 6: *Flow turbulent structures of an aeronautical gas turbine. Extracted from Moureau, Domingo, and Vervish (2011)*

Great efforts have been undertaken in the numerical simulation of gas turbines. For example, in the work of Moureau et al. (2011) an aeronautical burner is fully simulated with a mesh of 2.6 billion cells; results from this study are illustrated in Fig. 6. However, significant research is still needed in order to increase fuel flexibility, to control emissions, to extend the components lifetime and to boost gas turbine efficiency. Due to the high operation temperature and pressure, turbulent combustion inside gas turbines may be strongly coupled with radiation. And, just as in steam turbines, radiation is often neglected in numerical simulations or approximated by "gray" models or "optically thin" assumption. Few recent numerical studies of gas turbines Koren et al. (2018); Ren et al. (2018); Rodrigues et al. (2019) account for radiative heat transfer. Consequently, the study of accurate numerical tools capable of guiding the design stages of this kind of systems seems convenient in accordance with the global context.

Specific context of this thesis

As pointed out in the previous section, radiation can modify the heat transport and the fluid dynamics inside steam and gas turbines, while turbulence fluctuations can significantly alter the radiative heat transfer. Those interactions are commonly called turbulent-radiation interactions (TRI) which, in a broad sense, stand for the effects that turbulence causes on radiation and vice-versa. Detailed reviews of TRI can be found in the works of Coelho (2007), and Modest and Haworth (2016).

Turbulence effects on radiation arise from fluctuations of temperature and species concentration. When computing the radiative solution from averaged quantities in a turbulent participating media, results may significantly differ from the radiative solution obtained using instantaneous values. In most industrial applications turbulence is modeled through average or filter operations. Those operations give rise to two unclosed terms in the radiative transfer equation (RTE), the correlation between incident radiation and the absorption coefficient, and the correlation between blackbody intensity and the absorption coefficient, usually called Absorption TRI and Emission TRI, respectively. Early experimental studies by Faeth et al. (1987) report that ignoring those correlations can lead to significant errors on mean radiative properties predictions. On the combustion framework many authors have demonstrated the importance of TRI. Coelho (2004) and Li and Modest (2003) show that the enhancement of the radiative heat loss due to turbulent fluctuations in a diffusion flame can be of the order of 50 %. Significant TRI effects were reported in a premixed flame by Wu et al. (2005); Wu et al. (2007) using coupled DNS simulations together with the gray gas assumption. In the nonreactive framework, TRI effects are minor although they increase along with turbulent fluctuations. The analyzed nonreactive systems, through uncoupled simulations, include the homogeneous isotropic turbulence (Kritzstein and Soufiani (1993), da Silva et al. (2009), Roger et al. (2009); and Roger et al. (2010)), a temporally evolving jet analyzed in the work of Roger et al. (2011) and the channel flow presented by

Gupta et al. (2009).

Regarding the effects that radiation causes in turbulence, dynamic coupling between radiation and turbulence is needed rather than a priori analysis. Investigations with coupled radiation allow for a fundamental understanding of how radiation and TRI modify the turbulent structures. Early coupled simulations using Reynolds average Navier-Stokes (RANS) together with a TRI modeling include the works of Song and Viskanta (1987) who assumed the optically thin fluctuation approximation (Kabashnikov and Kmit (1979)) to model TRI in a combustion chamber; and the computation of a sooty turbulent ethylene-air diffusion jet flame by Tessé et al. (2004) whose only assumption for the TRI modeling was that different eddies have uncorrelated properties. Tessé et al. (2004) found that radiative source terms in the energy balance tend to dissipate temperature fluctuations.

As an approach towards precise modeling, radiation effects on turbulence have been studied in the Large Eddy Simulations (LES) context, some coupled studies in the combustion frame (Poitou et al. (2012); dos Santos et al. (2008); Berger et al. (2016)) show that radiation homogenizes the spectral distribution of energy and changes the flame brush structure. Ghosh et al. (2011) studied the radiation effects on a supersonic channel flow using coupled LES. Using the Correlated-k (ck) method to account for the spectral dependence of the radiative properties, they observed that effects of radiation counteract the effects of compressibility. Additionally, in the same work, they also invoked the gray gas assumption in order to artificially account for larger values of optical thickness. Through this assumption, they concluded that radiation affects the turbulence structures in supersonic boundary layers at high optical thickness. Further, a more recent LES study of Ghosh and Friedrich (2015) discussed the radiation effects on a turbulent mixing layer for the reactive and the nonreactive cases.

Direct numerical simulations (DNS) of turbulent flow coupled with radiative heat transfer provide useful data to develop and validate TRI models since all correlations are directly solved. Those models are eventually applied to more complex systems. A variety of coupled DNS works together with the gray gas assumption have been performed on different systems: statistically one-dimensional premixed (Wu et al. (2005); Wu et al. (2007)) and nonpremixed (Deshmukh et al. (2008); Deshmukh and Haworth (2009)) flames, turbulent natural convection between parallel heated plates (Sakurai et al. (2017)) and nonreactive channel flow (Silvestri et al. (2018)). Despite a fictitious gray gas gives trends on how turbulence structures behave on the presence of radiation, it is a poor approximation for radiative properties of a molecular gas in the majority of applications (Edwards (1976)). Up to now, the only works that consider coupled DNS while accounting for the spectral absorption coefficient are performed in channel flows. These works are the studies of Zhang et al. (2013) and Vicquelin et al. (2014). These studies analyzed a nonreactive turbulent channel flow coupled with a reciprocal Monte Carlo method to account for the radiative heat transfer. All these works used the ck method to consider the spectral radiative properties. They observed that radiation decreases temperature fluctuations and turbulent heat transfer, which strongly modifies the structure of the boundary layer. Furthermore, they reported that radiation decreases the thermal production due to opposing behaviors of gas-wall and gas-gas radiative contributions.

The present thesis analyzes the radiation effects on the turbulent structures of a heated plane jet, which is a canonical system of free shear flows. As far as we know, the present set of simulations are the first DNS of a free shear flow to be fully coupled with a spectral radiative heat transfer solver.

The contribution of this thesis

In the context described above, efficient and accurate tools need to be developed in order to satisfactorily predict radiation effects on turbulent flows. In this sense, the goal of the present thesis is to provide high-fidelity data of heated free jets coupled with thermal radiation in order to:

- (i) quantify not only radiation effects on free jets, but also on the behavior of turbulent flows in general,
- (ii) have a reference database for the development of free-shear turbulent models accounting for coupling interactions.

In order to attain these goals, the course of this thesis has lead to the following contributions:

- An optimized parallel coupling between a radiative Monte-Carlo solver and a compressible fluid flow DNS solver has been implemented. A significant amount of processing time for these high-fidelity coupled simulations has been saved due to an implementation of an acceleration method called Acoustic Speed Reduction.
- An implementation from scratch of a RANS solver able to handle variable-density flows and its further coupling with the radiative solver have been carried out. This implementation together with the high-fidelity DNS data allows for a direct quantification of the accuracy of the existing turbulent models as well as an identification of key parameters for further modeling of coupling interactions.
- Based on the generated DNS data, a new scaling law for the decay of the temperature profile in the jet centerline is derived. This scaling accounts for the effects of modified density due to moderate radiation. Moreover, it allows for distinguishing whether thermal radiation modifies the nature of heat transfer mechanisms in the jet developed region or not.
- Effects of radiation on mean temperature and velocity fields are quantified in a strongly heated free jet. Moreover, the effects of radiation in second order moments are also quantified through the enthalpy variance and turbulent kinetic energy balances.

Publications related to this thesis

International Journals

- *J.M. Armengol, R. Vicquelin, A. Coussement , R.G. Santos, O. Gicquel.* Physical study of radiation effects on the flow-field of a plane turbulent jet using Direct Numerical Simulations, - under preparation - International Journal of Heat and Mass Transfer, 2019
- *J.M. Armengol, R. Vicquelin, A. Coussement , R.G. Santos, O. Gicquel.* Scaling of heated plane jets with moderate radiative heat transfer in coupled DNS, -under revision- International Journal of Heat and Mass Transfer, 2019
- *J.M. Armengol, F.C. Bannwart, J. Xamán , R.G. Santos.* Effects of variable air properties on transient natural convection for large temperature differences. International Journal of Thermal Sciences, 2017

Conference proceedings

- *J.M. Armengol, R. Vicquelin, A. Coussement , R.G. Santos, O. Gicquel.* Turbulence-Radiation Interactions in a Spatially Developing Heated Jet. 24th ABCM International Congress of Mechanical Engineering, 2017
- *C. Uriel, CS Salinas, J.M. Armengol, R. Beicker, R.G. Santos.* Numerical investigation of heat transfer by natural convection and radiation in a cavity with participating media. 16th Brazilian Congress of Thermal Sciences and Engineering (ENCIT), 2016
- *J.M. Armengol, R.G. Santos.* Transient Natural Convection in Square Cavity. International Combustion Institute Summer School, São Paulo, Brazil 2015

Structure of the manuscript

Part I The theoretical background for coupling convective heat transfer and radiative energy transfer in turbulent flows is provided. Also, the different employed numerical codes are presented and discussed.

  - **Chapter 1**. The Navier-Stokes equations are presented and their numerical resolution is discussed. The YWCx code for direct numerical simulations (DNS) is presented. Moreover, the implementation and verification of the acoustic speed reduction method used to reduce the required computational cost in DNS is detailed.
  - **Chapter 2**. The Reynolds Averaged Navier-Stokes (RANS) equations for variable-density flows are introduced. Additionally, the implementation of the RANS solver ConDiRa using the Finite Volume Method and high order schemes is carefully discussed.
  - **Chapter 3**. The Radiative Transfer Equation (RTE) in participat-

ing media is introduced. The use of the Monte-Carlo method and the Correlated-k method in the Rainer code is described. Finally, the strategies for coupling Rainer with both the DNS and the RANS solvers are discussed.

Part II The grounds for high-fidelity coupled simulations are prepared. To this end, the heated jet is dimensioned in order to observe the phenomena of interest for this study, while the accuracy and the suitableness of the uncoupled numerical tools are discussed.

- **Chapter 4**. The parameters defining a turbulent plane jet are introduced, and the importance of radiative heat transfer as a function of these parameters is discussed. Then, the jet dimensioning is carried out through a parametric study using coupled RANS simulations.
- **Chapter 5**. DNS of the uncoupled isothermal and uncoupled heated turbulent jets are analyzed and compared with previous results to discuss the adequacy of the numerical setup.
- **Chapter 6**. Through standalone Monte-Carlo computations of heated plane jets, the criteria for the statistical convergence of Rainier is discussed. Also, the employed Correlated-k model for detailing the gas radiative properties is verified by comparison with line-by-line results.

Part III Results for heated free jets coupled with thermal radiation are presented using both DNS and RANS approaches.

- **Chapter 7**. DNS results of a heated jet with moderate radiative heat transfer are presented. This Chapter shows how thermal radiation can modify mean temperature profiles even when thermal radiation becomes locally negligible in the developed region. A new scaling law for the decay of the temperature profile is derived which allows for distinguishing whether thermal radiation modifies the nature of heat transfer mechanisms in the jet developed region or not while removing the indirect effects of modified density.
- **Chapter 8**. The effects of thermal radiation in a strongly heated jet are illustrated through high-fidelity coupled simulations. Besides the effects of radiation on mean temperature and velocity fields, the enthalpy variance and turbulent kinetic energy balances are computed to assess the effects of radiation in second order moments.
- **Chapter 9**. A set of comparisons between the RANS results using the ConDiRa code and the DNS data presented in Chapters 5, 7 and 8 is provided. Taking advantage of the low processing time of the coupled RANS, the scaling derived in Chapter 7 is checked for a series of coupled and uncoupled simulations.

Part I

Fundamentals and Numerical Tools

Chapter 1

Numerical approaches for the Fluid Flow solution

The set of governing equations that describes the fluid flow is introduced and the three main numerical approaches to solve it are discussed. The main features of the YWCx code used for the direct simulation are summarized. Special focus is put on the generation of artificial turbulence which is used to enhance inlet boundaries, as well as the acoustic speed reduction method used to reduce the required computational cost in direct numerical simulations.

Contents

1.1 Governing equations for the fluid flow

Turbulence is a three-dimensional phenomenon in its nature, it is time-dependent and exhibits a random behavior. The governing equations here used to describe the turbulent flow are the Navier-Stokes equations for a compressible fluid in which gravitational effects are not considered. These are the continuity equation, the momentum and energy transport equations, respectively:

$$\frac{\partial \rho}{\partial t} + \frac{\partial \left(\rho u_i\right)}{\partial x_i} = 0, \tag{1.1}$$

$$\frac{\partial \rho u_j}{\partial t}+\frac{\partial\left(\rho u_i u_j\right)}{\partial x_i}=-\frac{\partial p}{\partial x_j}+\frac{\partial \tau_{ij}}{\partial x_i}, \tag{1.2}$$

$$\frac{\partial \rho e_t}{\partial t}+\frac{\partial\left(\rho e_t u_i\right)}{\partial x_i}=-\frac{\partial (p u_j)}{\partial x_j}+\frac{\partial (\tau_{ij} u_i)}{\partial x_j}-\frac{\partial q_i}{\partial x_i}+P_{rad}, \tag{1.3}$$

where ρ, t, u_j, p, τ_{ij}, e_t and q_i denote density, time, instantaneous velocity, pressure, stress tensor, total energy and conductive flux vector, respectively. P_{rad} is the radiative power further discussed in Chapter 3. Assuming Newtonian fluid, the stress tensor $\tau_{i,j}$ is defined as

$$\tau_{ij}=\mu\left(\left(\frac{\partial u_i}{\partial x_j}+\frac{\partial u_j}{\partial x_i}\right)-\frac{2}{3}\delta_{ij}\frac{\partial u_k}{\partial x_k}\right), \tag{1.4}$$

where μ is the dynamic viscosity and δ_{ij} is the Kronecker delta operator. The conductive flux vector q_i writes

$$q_i=-\lambda\frac{\partial T}{\partial x_i}, \tag{1.5}$$

where λ and T denote thermal conductivity and temperature, respectively. The energy transport is defined based on the total energy e_t, which accounts for the sum of internal and kinetic energies: $e_t=\frac{1}{2}u_i u_i+e$, where e is the internal energy. The enthalpy is denoted by $h=e+rT$ where $r=R/W$, R is the universal gas constant and W stands for the molar weight of the mixture. To close the system, the ideal gas equation is here used to compute pressure as $p=\rho r T$.

1.2 Numerical approaches to solve the Navier-Stokes equations

The main difficulty on numerically solving the system of governing Eqs. (1.1 to 1.3) is the wide range of length and times scales that turbulent flows present. Figure 1.1 shows the typical energy spectrum function $E(\kappa)$ of a high Reynolds number flow as a function of the wavenumber κ, where $\kappa=2\pi/l$ is the wavenumber that corresponds to the turbulent motion with lengthscale l.
The size of the largest turbulent motions κ_0 is of the order of the characteristic width of the flow, and as shown in the energy spectrum of Fig. 1.1, these turbulent motions contain most of the kinetic energy. Such large structures are strongly dependent on the problem conditions; thus, they can be highly anisotropic. Through the production mechanism, the largest motions

are responsible to generate the kinetic energy that maintains the turbulence. Richardson (1922) introduced the energy cascade concept for which the kinetic energy of the large eddies is gradually transferred to smaller and smaller eddies. As developed in the work of Kolmogorov (1941), there is a point κ_{EI} during this process of transfer at which the directional information of the larger scales is lost, eddies are then statistically isotropic and present a universal behavior. The energy is further transferred by inviscid processes to smaller eddies until a point κ_{DI} in which viscous effects become significant. The point κ_{DI} divides the universal equilibrium range into:

- The inertial subrange ($\kappa_{EI} < \kappa < \kappa_{DI}$) in which the spectrum only depends on the dissipation rate ϵ and it has the universal form of $E(\kappa) = C\epsilon^{2/3}\kappa^{-5/3}$, where C is a universal constant.
- The dissipation subrange in which energy is dissipated by the work of viscosity down to the smallest length scales $\kappa_\eta = 2\pi/\eta$ associated to the so-called Kolmogorov lengthscale η.

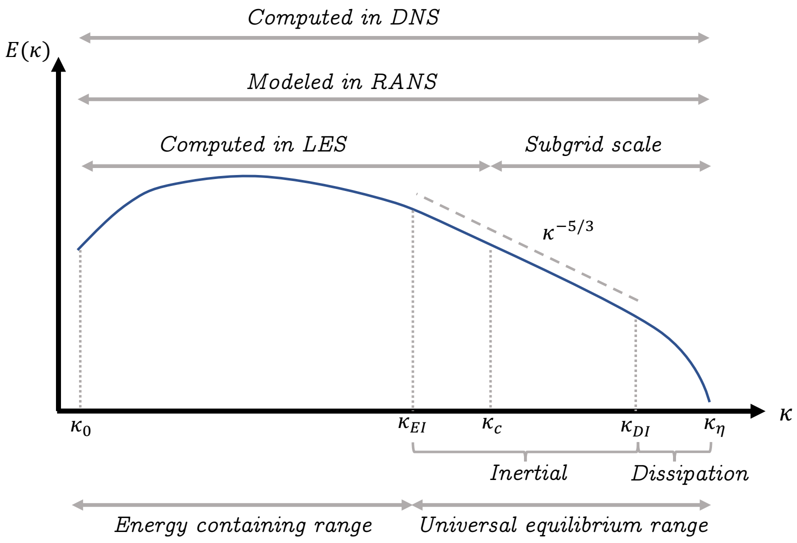

Figure 1.1: *Energy spectrum function $E(\kappa)$ of a high Reynolds number flow as a function of the wavenumber κ.*

In this work, two different approaches which are the Direct Numerical Simulations (DNS) and Reynolds Average Navier-Stokes (RANS) are used to solve the turbulent flow problem. With Large Eddy Simulations (LES), these numerical approaches are among the most common techniques to handle this kind of flows; the use of a specific approach depends on the goals of the simulations, and it ends up usually being a trade-off between accuracy and computational cost.

In DNS, three-dimensional and unsteady computations are performed to explicitly determined all scales of motion without any modeling, as shown in Fig. 1.1. Time and spatial refinements strongly depend on the Reynolds number in

DNS. Therefore, in order to consider affordable simulations in terms of computational cost, the Reynolds number is usually kept low-to-moderate. DNS is here used within the thesis objectives of generating a high-fidelity database to quantify TRI and to set the modeling bases for heated free jets coupled with thermal radiation. This approach is used in the current study taking advantage of the in-house code YWCx which is described in the following section.

In contrast with DNS, the RANS models constitutes cheaper simulations in terms of computational time by solving the governing equations system averaged in time. A set of RANS models has been implemented from scratch in this work, a detailed description is further provided in Chapter 2 and numerical results are presented in Chapter 9. The principal motivation of such implementation is to compare accuracy between RANS models and DNS high-fidelity data in the context of coupled simulations.

Finally, the LES approach solves the governing equations system after a filter is applied. The filtered system is representative of the larger turbulent scales; thus, the effects of smaller and isotropic motions are modeled by the so called subgrid-scale models. As shown in Fig. 1.1, the cut-off wavenumber κ_c that forms the filtered system should be greater than the κ_{EI} which corresponds to the wavenumber of the smallest energy-containing motions. A Smagorinsky model for the subgrid-scale effects has been implemented in the frame of the YWCx code. This implementation opens the way to further coupled simulations of high Reynolds number jets in larger domain extensions. The implementation is detailed in Appendix B.

1.3 Direct Numerical Simulations using the YWCx

YWCx is an oriented objected version of the YWC code. Both versions are in-house codes developed at EM2C laboratory (Coussement (2012),Caudal (2013)) in collaboration with the Aero-Thermo-Mechanic Department of the *Université Libre de Bruxelles*. A detailed description of the general numerical tools used in YWCx and YWC is beyond the scope of this section, instead the main characteristics of these tools are just highlighted. However, a special focus is put on the artificial turbulence generation, and the Acoustic Speed Reduction (ASR) method which have been implemented in YWCx during the development of this thesis.

1.3.1 General numerical tools of YWCx code

In YWCx, just as in YWC, the compressible Navier-Stokes equations are numerically solved on a structured mesh using high-order centered finite-difference scheme for the spatial derivatives, and an explicit 4^{th}-order Runge-Kutta method for the time integration. Such methods follow the work of Kennedy and Carpenter (1994). In addition, high-order implicit filters, proposed in the work of Gaitonde and Visbal (1999), are used for stability purposes. The code is parallelized through domain decomposition using the *Message Passing Interface* (MPI) Standard Library. Details of the YWC implementation are specified in the work of Coussement (2012). Additionally, a useful overview of YWC can be found in Appendix A of the work of Caudal (2013).

1.3.2 Artificial turbulence

A common practice in high-fidelity simulations is to combined mean inlet velocity profiles with synthetic turbulence in order to generate more realistic fluctuating inlet velocity profiles. In the present work, the Passot and Pouquet (1987) model is used to create the artificial turbulence.
This technique promotes turbulent instabilities and reduces the computational domain needed for the turbulence structures to develop. Following the implementation of Caudal (2013), the Passot Pouquet model defines the turbulent kinetic energy spectrum $E(\kappa)$ as

$$E(\kappa) = A\left(\frac{\kappa}{\kappa_0}\right)^4 exp\left[-2\left(\frac{\kappa}{\kappa_0}\right)^2\right], \tag{1.6}$$

where κ is the wavenumber, κ_0 is the wavenumber associated with the largest turbulent scales, A is an independent variable of κ defined by $A = \frac{16n}{3}\frac{u'^2}{\kappa_0}\sqrt{2/\pi}$, u' stands for the characteristic *turbulent velocity* and n is the number of dimensions. Defining the auto-correlation integral scale L_c as

$$L_c = \frac{2\beta n}{3\kappa_0}\sqrt{2/\pi} \quad \text{with} \quad \beta = \begin{cases} 2 & \text{if } n = 2 \\ \pi/2 & \text{if } n = 3 \end{cases}, \tag{1.7}$$

the turbulent kinetic energy spectrum is defined by fixing the auto-correlation integral scale L_c and the *turbulent velocity* u'. As an example, three-dimensional homogeneous and isotropic turbulence (HIT) is generated using the Passot Pouquet model; the resultant velocity fields are shown in Fig. 1.2.

1.3.3 Acoustic Speed Reduction Method

The YWCx solves the compressible Navier-Stokes equations through a fully-explicit formulation. Such formulation has a strong benefit for high-performance computing since no implicit linear system needs to be solved.
When using an explicit formulation, the time step dt is limited by the Courant-Friedrichs-Lewy (CFL) condition expressed for the Courant number $\mathcal{C}$

$$dt < \mathcal{C}^{crit}\text{min}\left(\frac{\Delta x_i}{|u_i + c|}, \frac{\Delta x_i}{|u_i - c|}\right), \tag{1.8}$$

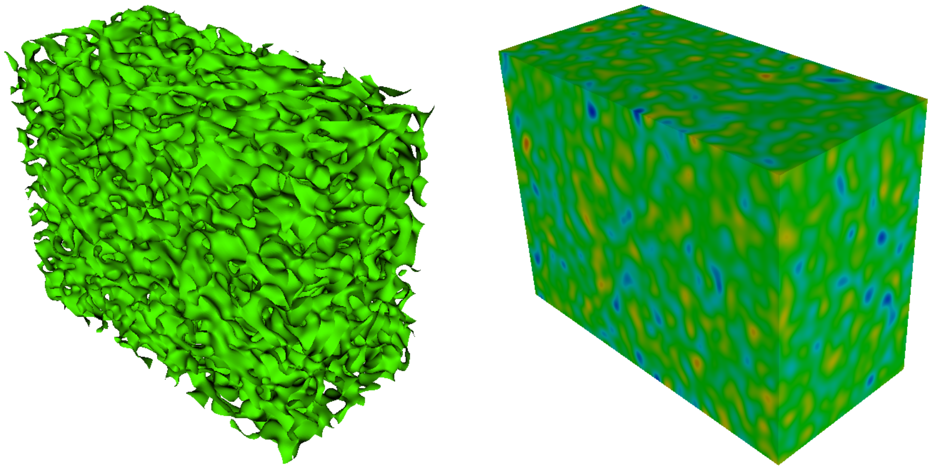

(a) (b)

Figure 1.2: *Three-dimensional HIT generated using the Passot Pouquet model. (a) Isosurface of null x-component velocity, and (b) y-component velocity contours.*

and by the Fourier number (Fo) condition

$$dt < \mathrm{Fo}^{crit}\min\left(\frac{\Delta x_i^2}{\mu/\rho}\right), \tag{1.9}$$

where Δx_i is the characteristic cell size on each i direction, $\mathcal{C}^{crit}$ and Fo^{crit} are the critical stability values for the retained numerical schemes, u is the convective velocity, and c is the speed of sound. Compressible effects are negligible for low Mach number cases; thus, the resolution of the acoustic field is unnecessary. For such cases, explicit numerical formulations have a notorious tendency to be poorly efficient in terms of computational cost because of the difference between convective and sound velocities.

In this context, the so called pseudo-compressibility or artificial compressibility methods try to reduce the gap between convective and sound velocities with artificial manipulation of the governing equations. Choi and Merkle (1993) classified the artificial compressibility methods in:

Pre-conditioning methods in which the time derivatives in the governing equations are multiplied by a matrix that scales the eigenvalues of the system to the same order of magnitude. Among the studies that discuss this family of methods, there are the works of Choi and Merkle (1993); Darmofal and Schmid (1996); Van Leer et al. (1991); Liu and Liu (1993); Turkel (1987).

Perturbation methods in which specific terms in the governing equations are manipulated in order to replace physical acoustic waves by pseudo-acoustic modes. The works of O'Rourke and Bracco (1979); Ramshaw et al. (1985); Wang and Trouvé (2004); Salinas-Vázquez et al. (2013) address this kind of methods.

A perturbation method called Acoustic Speed Reduction (ASR) presented by Wang and Trouvé (2004) has been implemented in the YWCx code during the development of this thesis. The method enlarges the allowed time step by artificially reducing the sound velocity and increasing the Mach number while keeping compressible effects negligible. Consequently, the computational resources needed to achieve statistical convergence are strongly reduced. A detailed discussion of this method can be found in the work of Wang and Trouvé (2004). In a more recent study, Salinas-Vázquez et al. (2013) modified the ASR assuming a value of the heat capacity ratio (γ) close to unity in order to reduce complexity in the numerical treatment. In this work the ASR formulation of Wang and Trouvé (2004) is retained.

In practice, the ASR method modifies Eq. (1.3) by adding two new terms (S_{conv} and S_{diff}):

$$\frac{\partial \rho e_t}{\partial t} + \frac{\partial \left(\rho e_t u_i\right)}{\partial x_i} = -\frac{\partial (p u_j)}{\partial x_j} + \frac{\partial (\tau_{ij} u_i)}{\partial x_j} - \frac{\partial q_i}{\partial x_i} + P_{rad} + S_{\text{conv}} + S_{\text{diff}}, \quad (1.10)$$

where S_{conv} is defined by

$$S_{\text{conv}} = \left(1 - \frac{1}{\alpha^2}\right) \frac{\gamma p}{\gamma - 1} \frac{\partial u_j}{\partial x_j}, \quad (1.11)$$

and S_{diff} is

$$S_{\text{diff}} = -\left(1 - \frac{1}{\alpha^2}\right) \left[\tau_{i,j} \frac{\partial u_i}{\partial x_j} - \frac{\partial q_j}{\partial x_j} + P_{rad}\right]. \quad (1.12)$$

The ASR method reduces the speed of sound by an adjustable factor α accelerating the convergence of the solution by this same factor. Two main criteria can be use to choose the value of this parameter α:

1. The reduced sound velocity $c' = c/\alpha$ should keep the Mach number low to maintain negligible compressible effects.
2. There is no point in increasing α if the time step is already limited by the Fo condition described above. Thus, the time step determined by the CFL condition should be of the same order or smaller than the one determined by the Fo condition.

1.3.3.1 Modified Boundary Conditions

Partially non-reflecting characteristic boundary conditions (Poinsot and Lele (1992)) are considered in YWCx. Boundary conditions for the modified ASR system of equations are derived in Appendix C based on a characteristic analysis. From this derivation, the time derivatives of the primitive variables are computed at the boundary following the expressions:

$$\frac{\partial p}{\partial t} = -\frac{1}{2}\left(\mathcal{L}_3 + \mathcal{L}_1\right), \tag{1.13}$$

$$\frac{\partial \rho}{\partial t} = \frac{1}{c'^2}\left(\mathcal{L}_2 - \frac{1}{2}(\mathcal{L}_3 + \mathcal{L}_1)\right), \tag{1.14}$$

$$\frac{\partial u}{\partial t} = -\frac{1}{2\rho c'}\left(\mathcal{L}_3 - \mathcal{L}_1\right). \tag{1.15}$$

where the artificial sound velocity c' is defined as $c' = c/\alpha$ and the speed of sound is $c = \sqrt{\gamma p/\rho}$. On the one hand, the wave amplitudes $\mathcal{L}_i$ are computed from inner nodes in the case of outgoing waves (waves leaving the domain) using the equations

$$\mathcal{L}_1 = (u - c')\left(\frac{\partial p}{\partial x} - \rho c' \frac{\partial u}{\partial x}\right) \tag{1.16}$$

$$\mathcal{L}_2 = u\left(\frac{\partial p}{\partial x} - c'^2 \frac{\partial \rho}{\partial x}\right) \tag{1.17}$$

$$\mathcal{L}_3 = (u + c')\left(\frac{\partial p}{\partial x} + \rho c' \frac{\partial u}{\partial x}\right). \tag{1.18}$$

where u and x correspond to the velocity and coordinate normals to the boundary, respectively. On the other hand, the wave amplitudes associated with incoming waves tend to zero (but no necessarily equal to zero) in partially non-reflecting boundary conditions. The control of incoming waves amplitudes is done following the work of Coussement et al. (2012).

1.3.3.2 Test case for the ASR formulation

The implementation of the ASR method in YWCx is here tested by reproducing two test cases. The first test corresponds to a two-dimensional vortex which is convected downstream, while the second consists in the evolution of a circular pressure wave.

Test case: vortex convection

A two-dimensional vortex convected along the x-direction for $\alpha = 5$ and $\alpha = 10$ is computed; additionally, the case of $\alpha = 1$ is also computed as a reference. The vortex is defined by the following initial fields of pressure and velocity:

$$p(x,y) = p_0 exp\left(-\frac{\gamma}{2}\left(\frac{\tau}{cR_c}\right)^2 exp\left(-\frac{x^2+y^2}{2R_c^2}\right)\right) \tag{1.19}$$

$$u(x,y) = u_{conv} + \frac{\tau}{R_c^2} y\ exp\left(-\frac{x^2+y^2}{2R_c^2}\right) \tag{1.20}$$

$$v(x,y) = -\frac{\tau}{R_c^2} x\ exp\left(-\frac{x^2+y^2}{2R_c^2}\right) \tag{1.21}$$

where γ is the heat capacity ratio, τ corresponds to the vortex intensity and is here set to $\tau = 1$, R_c stands for the vortex radius here $R_c = 2 \cdot 10^{-2}$m , u_{conv} is the convection velocity set to $u_{conv} = 5$m/s and the reference pressure p_0 is here $p_0 = 1$ atm. The initial temperature field is set to 300K. An inlet condition, defined by $u = 5$ m/s and $v = 0$ m/s, is set at the West boundary, while a constant pressure outlet is set at the East boundary. South and North boundaries are set to be periodic. The considered grid has 321 × 161 nodes along the x and y direction with a constant mesh spacing equal to 10^{-3} m. In Figure 1.3, isolines corresponding to the initial fields of pressure, streamwise velocity u, and cross-section velocity v defining the vortex are shown in Figs. 1.3(a), 1.3(b), and 1.3(c), respectively.

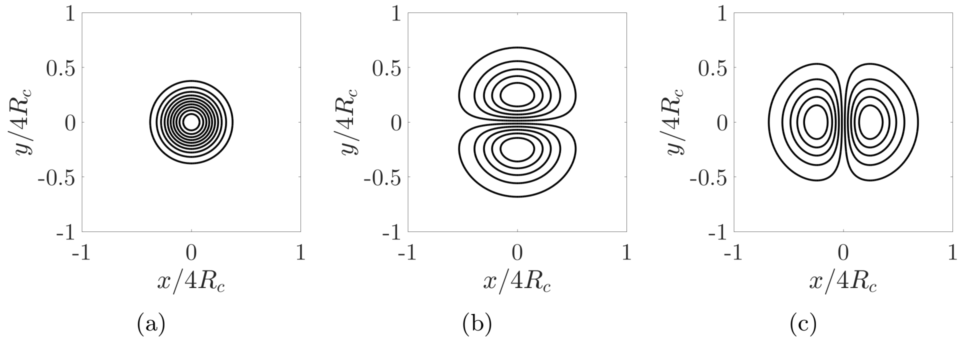

(a) (b) (c)

Figure 1.3: *Isolines corresponding to the initial solution of (a) pressure, (b) streamwise velocity u, and (c) cross-section velocity v.*

In order to test the accuracy of the ASR implementation, the solution for the pressure and velocity fields are shown in Fig. 1.4 after a simulation corresponding to $1.1 \cdot 10^{-2}$s of physical time for $\alpha = 1$, $\alpha = 5$, and $\alpha = 10$.

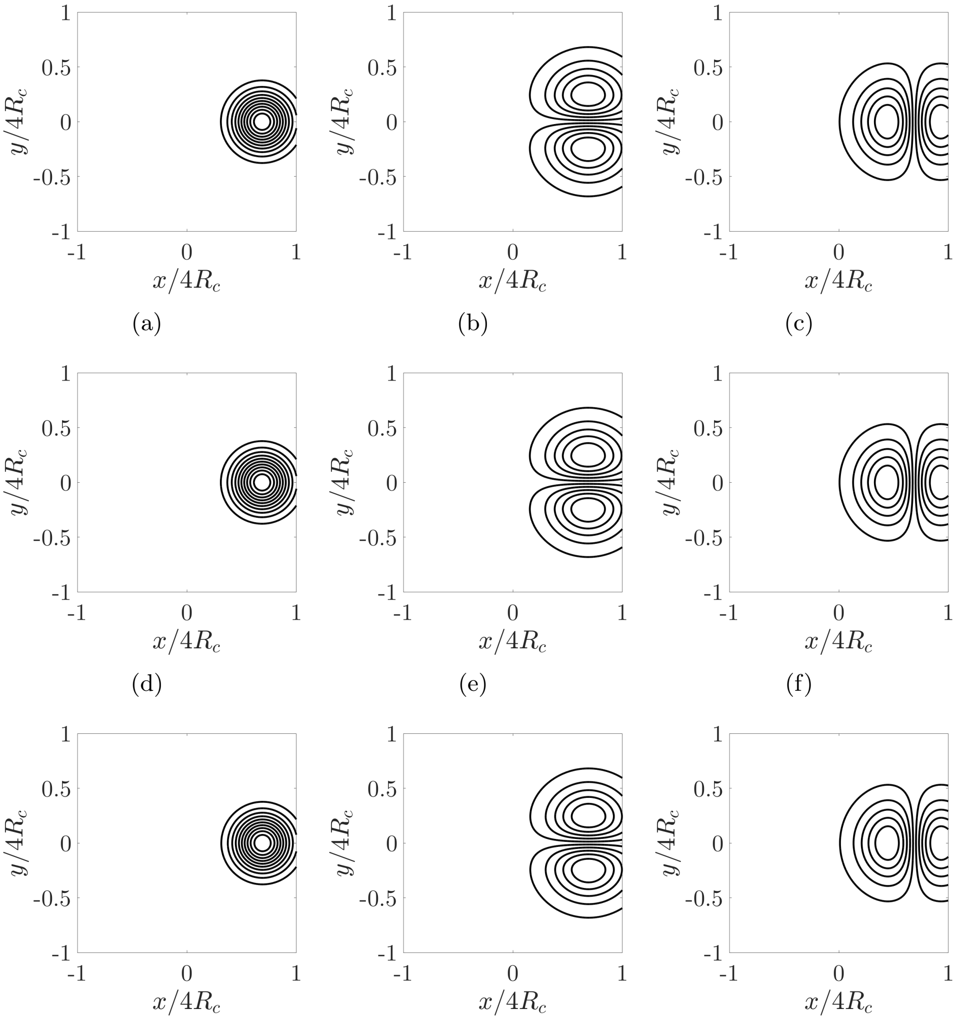

(a) (b) (c)

(d) (e) (f)

(g) (h) (i)

Figure 1.4: *Solutions after simulating* $1.1 \cdot 10^{-2}s$ *of physical time for* $\alpha = 1$ *((a), (b), and (c));* $\alpha = 5$ *((d), (e), and (f)); and* $\alpha = 10$ *((g), (h), and (i)). These solutions are represented by isolines of pressure ((a), (d), and (g)); streamwise velocity* u *((b), (e), and (h)); and cross-section velocity* v *((c), (f), and (i)).*

When compared to the reference solution computed setting $\alpha = 1$, the vortex solutions using both $\alpha = 5$ and $\alpha = 10$ are in very good agreement with the reference solution as shown in Fig. 1.4. The computations corresponding to $\alpha = 5$ and $\alpha = 10$ are respectively of the order of 5 and 10 times cheaper than the reference case; thus, the ASR formulation appears as a useful tool to compute low Mach numbers flows in a compressible formulation.

Test case: the two-dimensional pressure wave

A computation of the two-dimensional test case presented in the work of Lodato et al. (2008) for different values of the accelerator parameter α is here performed. It consists in an initial pressure wave described by the function

$$p(x,y) = p_0 \left(1 + \delta \; exp\left(-\frac{x^2+y^2}{2R_p^2}\right)\right), \tag{1.22}$$

where $p_0 = 101325$ Pa is the undisturbed pressure, δ determines the pressure wave amplitude (here set to $\delta = 10^{-4}$), and R_p is the radius of the wave (here $R_p = 20 \cdot 10^{-3}$ m). The contour of the initial pressure wave is shown in Fig. 1.5(a) in which $\Delta p = p - p_0$ and Δp_{ref} stands for a reference pressure variation, here the maximum variation is taken as $\Delta p_{ref} = \delta p_0 = 10.1325$ Pa. Likewise, the initial density distribution is presented in Fig. 1.5(b) in which $\Delta \rho = \rho - \rho_0$, $\Delta \rho_{ref}$ is the maximum initial ρ variation, and ρ_0 is the undisturbed density computed as $\rho_0 = p_0/(rT_0)$. Temperature is initially set to a constant value of $T_0 = 300$ K, and null velocities are imposed at the initial time $u_0 = 0$.
A uniform mesh of 161×161 nodes with a grid spacing of 10^{-3} m is used. Following §1.3.3.1, all boundary conditions are set to partially non-reflecting outflows.

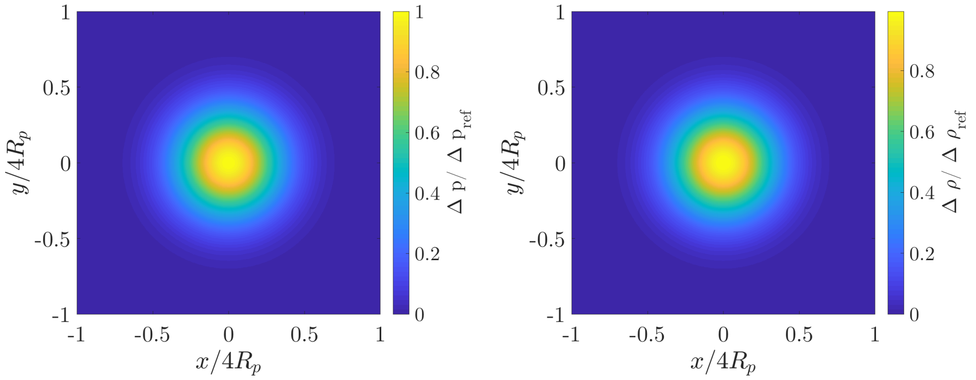

(a) (b)

Figure 1.5: *Pressure wave evolution for (a) $\alpha = 1$, and (b) $\alpha = 10$.*

First, the evolution in time of the pressure wave at $y = 0$ is compared for $\alpha = 1$, $\alpha = 5$ and $\alpha = 10$ in Figs. 1.6(a), 1.6(b), and 1.6(c), respectively. These three Figs. show that ASR method keeps the trends and magnitude of the pressure wave independent of the α value. However, the pressure wave reduces its velocity propagation by a factor α, the corresponding physical time of each profile depending on the α value is detailed in Table 1.1. Note, that the physical time for each sample is proportional to α. Then, for the same number of iterations, the case $\alpha = 10$ advances the solution 10 times further in physical time than the reference case of $\alpha = 1$.

Table 1.1: *Physical time (in seconds) associated to the number of iterations as a function of α in the pressure wave test case.*

Case	0 ite.	50 ite.	100 ite.	150 ite.	200 ite.
$\alpha = 1$	0.0	$6.0 \cdot 10^{-5}$	$1.2 \cdot 10^{-4}$	$1.8 \cdot 10^{-4}$	$2.4 \cdot 10^{-4}$
$\alpha = 5$	0.0	$3.0 \cdot 10^{-4}$	$6.0 \cdot 10^{-4}$	$9.0 \cdot 10^{-4}$	$1.2 \cdot 10^{-3}$
$\alpha = 10$	0.0	$6.0 \cdot 10^{-4}$	$1.2 \cdot 10^{-3}$	$1.8 \cdot 10^{-3}$	$2.4 \cdot 10^{-3}$

Figs. 1.6(d), 1.6(e), and 1.6(f) show respectively the velocity time evolution at $y = 0$ for the $\alpha = 1$, $\alpha = 5$ and $\alpha = 10$ cases. In these Figs., Δu_{ref} corresponds to the maximum velocity variation of the $\alpha = 1$ case, which is $\Delta u_{ref} = 1.21 \cdot 10^{-2}$ m/s. Velocity trends induced by the pressure wave are the same for all studied values of α. However, an increase in the velocity magnitude is observed. Such increase is proportional to α.

The evolution in time of the density variation induced by the pressure wave at $y = 0$ is shown in Figs. 1.6(g), 1.6(h), and 1.6(i) for the $\alpha = 1$, $\alpha = 5$ and $\alpha = 10$ cases, respectively. Density trends and magnitude are wrongly predicted when using the ASR method. These results indicate that density variations induced by a pressure wave are over-predicted by an α^2 factor.

Finally, Figs. 1.6(j), 1.6(k), and 1.6(l) present the temperature variation $\Delta T = T - T_0$ evolution in time at $y = 0$ for the $\alpha = 1$, $\alpha = 5$ and $\alpha = 10$ cases, respectively. Likewise, ΔT_{ref} corresponds to the maximum temperature variation for the $\alpha = 1$ case, which corresponds to $\Delta T_{ref} = 8.05 \cdot 10^{-3}$ K. As observed in Fig. 1.6(k), the maximum temperature variation is of the order of 80 times ΔT_{ref}, while in Fig. 1.6(l) this variations is more than 300 times grater than for the case $\alpha = 1$.

Results of the pressure wave test case can be summarized in the following:

- Results of the wave propagation velocity scales perfectly with the α factor. As expected, the modified wave propagation velocity is $c' = c/\alpha$.
- When using the ASR method the pressure wave trends and magnitude are preserved.
- Results when using the ASR method preserve trends of induced velocity, while its magnitude increases proportionally to α.
- Density and temperature variations induced by pressure waves are over-predicted by the ASR method. Setting $\alpha = 10$, an artificial variation of almost 3 K is observed for a wave with $\Delta p = 10.1325$ Pa. Thus, ASR is solely applicable in low Mach numbers flows in which pressure waves are small enough to induce negligible changes in velocity, temperature and density.

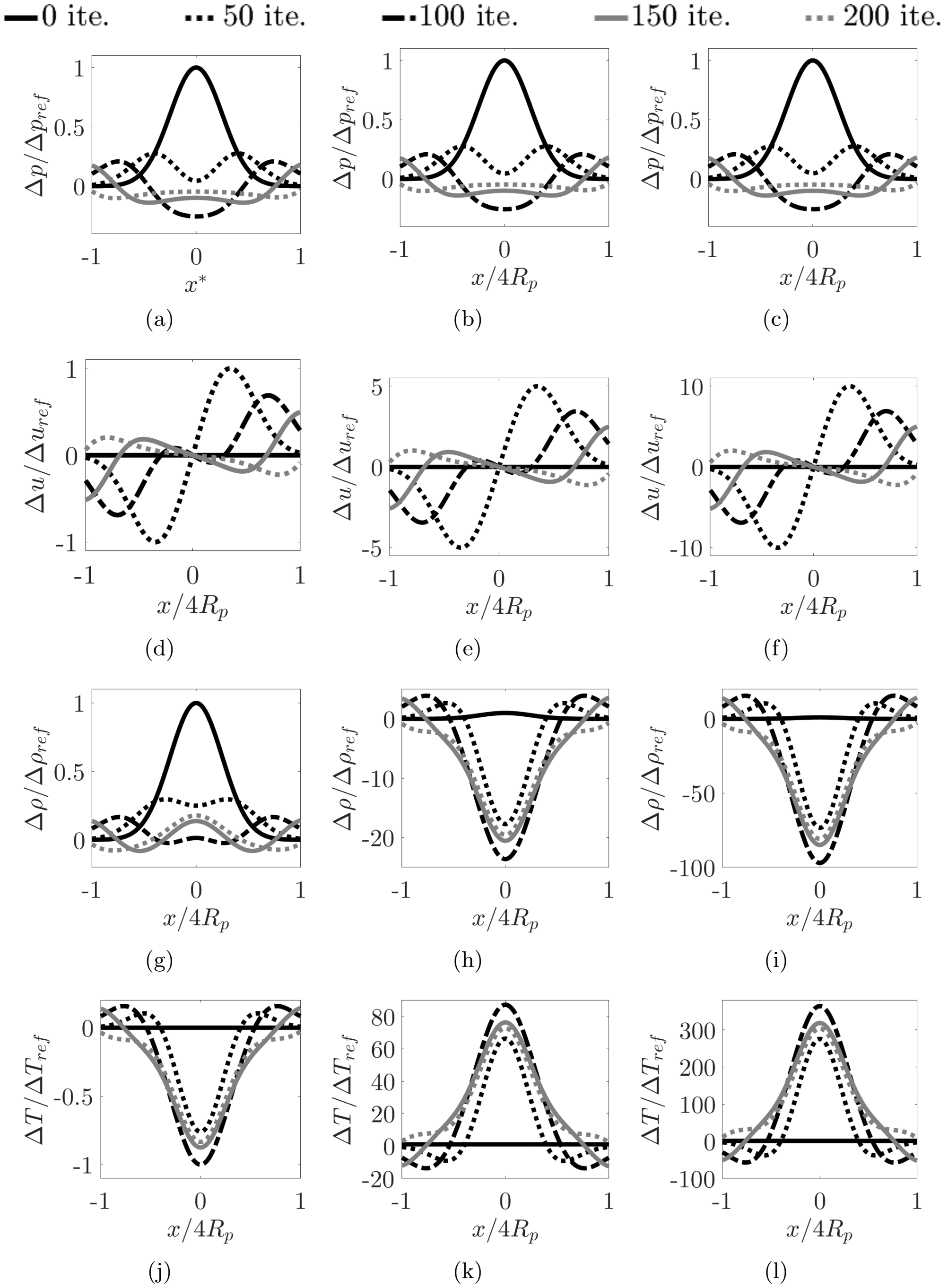

Figure 1.6: *Pressure wave time evolution for (a) $\alpha = 1$, (b) $\alpha = 5$, and (c) $\alpha = 10$. Variation of velocity as a function of time for (d) $\alpha = 1$, (e) $\alpha = 5$, and (f) $\alpha = 10$. Density variation as a function of time for (g) $\alpha = 1$, (h) $\alpha = 5$, and (i) $\alpha = 10$. Temperature variation as a function of time for (j) $\alpha = 1$, (k) $\alpha = 5$, and (l) $\alpha = 10$.*

1.4 Conclusions

This Chapter has introduced the governing equations that describes the fluid flow problem. Moreover, the main numerical approaches to solve these equations have been discussed. The numerical code YWCx used to solve the set of governing equations in a DNS approach has been introduced.
Two features developed in the YWCx framework during the course of this thesis have been detailed: the generation of artificial turbulence in order to enhance inlet boundaries; and the acoustic speed reduction method used to reduce the required computational cost in direct numerical simulations. To test the implementation of the ASR method, two test cases are perfomed. These are a two-dimensional vortex convection and a two-dimensional pressure wave. The ASR formulation appears as a useful tool to reduce the required processing time in compressible formulations. However, ASR is solely applicable in low Mach numbers flows in which pressure waves are small enough to induce negligible changes in velocity, temperature and density.

Chapter 2

Modeling of turbulence using Reynolds Average Navier-Stokes

In this Chapter, theoretical background for an implementation of the variable-density $k-\epsilon$ *and* $k-\omega$ *turbulent viscosity models are given. First, the Reynolds Averaged Navier-Stokes (RANS) and its unclosed terms are discussed. Then, the ConDiRa (CONvection, DIfusion and RAdiation) RANS code, developed in this thesis, is introduced. Next, the numerical discretization of the governing equations following the Finite Volume Method and high order schemes is detailed. Finally, the numerical code is verified by comparison with some benchmark problems.*

Contents

2.1 Averaging the governing equations

In the majority of engineering applications, we are mostly interested in the mean characteristics of the flow rather than instantaneous values. In this context, Reynolds Averaged Navier Stokes (RANS) models save a notorious computational cost since they directly solve a system of equation for the time averaged quantities. The time average of a fluctuating quantity $f(t)$ is defined as

$$\langle f\rangle = \frac{1}{T}\int_T f(t)dt, \tag{2.1}$$

where T is the time-averaged period which should be much larger than the characteristic time of the fluctuations. Fluctuations of $f(t)$ are defined by

$$f' = f - \langle f\rangle. \tag{2.2}$$

For variable density flows, it is useful to avoid extra unknowns related to density correlations by means of the Favre average. The time Favre average of a fluctuation quantity $f(t)$ is a mass-weighted time average in the form

$$\{f\} = \frac{\langle \rho f\rangle}{\langle \rho\rangle}. \tag{2.3}$$

Likewise, Favre fluctuations are defined as

$$f'' = f - \{f\}. \tag{2.4}$$

Then, mass, momentum and energy balance equations for mean Favre quantities are respectively

$$\frac{\partial\langle\rho\rangle}{\partial t} + \frac{\partial}{\partial x_i}(\langle\rho\rangle\{u_i\}) = 0, \tag{2.5}$$

$$\frac{\partial}{\partial t}(\langle\rho\rangle\{u_i\}) + \frac{\partial}{\partial x_j}(\langle\rho\rangle\{u_j\}\{u_i\}) = \frac{\partial}{\partial x_j}\left(\langle\tau_{i,j}\rangle - \langle\rho\rangle\{u_i''u_j''\}\right) - \frac{\partial\langle P\rangle}{\partial x_i} + \langle\rho\rangle g_i, \tag{2.6}$$

$$\frac{\partial}{\partial t}(\langle\rho\rangle\{T\}) + \frac{\partial}{\partial x_j}(\langle\rho\rangle\{u_j\}\{T\}) = \frac{\partial}{\partial x_j}\left(\frac{\{\lambda\}}{c_p}\frac{\partial\{T\}}{\partial x_j} - \langle\rho\rangle\{u_j''T''\}\right) + \frac{\langle P_{rad}\rangle}{c_p}, \tag{2.7}$$

where c_p is assumed constant, g_i is the i-component of the acceleration gravity vector, $\{\lambda\}$ stands for the thermal conductivity evaluated at $\{T\}$, and the averaged Reynolds stresses $\langle\tau_{ij}\rangle$ are approximated by

$$\langle\tau_{ij}\rangle = \{\mu\}\left(\left(\frac{\partial\{u_i\}}{\partial x_j} + \frac{\partial\{u_j\}}{\partial x_i}\right) - \frac{2}{3}\delta_{ij}\frac{\partial\{u_k\}}{\partial x_k}\right), \tag{2.8}$$

where $\{\mu\}$ is the dynamic viscosity evaluated at $\{T\}$.
The numerical resolution of this set of equations is discussed in the following section.

2.2 Closure approaches to solve the RANS equations

A model is needed to solve the RANS problem defined by Eqs. 2.5 to 2.7 since the Reynolds stresses $\{u_i''u_j''\}$ and the turbulent heat flux $\{u_j''T''\}$ are unclosed terms.

2.2.1 Reynolds stresses closure

The terms $\{u_i''u_j''\}$ in Eq. 2.6 are additional unknowns in the well-established convective-diffusion problem. Thus, extra equations are required to solve the resulting system. Two main approaches can be distinguished.
On the one hand, the Algebraic Stress Models (ASM) (Naot and Rodi (1982)) and Reynolds Stresses Models (RSM) (Launder et al. (1975)) derive algebraic and transport equations, respectively, for each of the six independent Reynolds stresses (in three dimensions). The main strength of these approaches is their capability to account for anisotropy of the normal stresses, but several assumptions for modeling unknown turbulent process (pressure-strain correlations, turbulent diffusion of Reynolds stresses and dissipation) need to be done. Additionally, the memory and computational cost requirements are relatively large compared with other Reynolds stresses Closures.
On the other hand, turbulent viscosity models express the Reynolds stresses as a function of the averaged variables based on the turbulent-viscosity hipotesis, also called Boussinesq consideration:

$$\langle\rho\rangle\{u_i''u_j''\} = -\mu_t\left(\frac{\partial\{u_i\}}{\partial x_j} + \frac{\partial\{u_j\}}{\partial x_i} - \frac{2}{3}\delta_{i,j}\frac{\partial\{u_k\}}{\partial x_k}\right) + \frac{2}{3}\langle\rho\rangle k, \tag{2.9}$$

where k is the turbulent kinetic energy (TKE) expressed as $k = \frac{1}{2}\{u_i''^2\}$, δ_{ij} is the Kronecker delta operator, and μ_t is the turbulent viscosity which is an indicator of the local turbulent state of the flow. Turbulent viscosity models are further divided by the number of extra equations used to estimated μ_t, these are the zero-equation Mixing length model, the one-equation such as Spalart-Allmaras model (Spalart and Allmaras (1992)), and the two-equations models. The retained approach in this work is the two-equations models. This family of models considers two transport equations, one for the TKE (k) and another for the TKE dissipation ϵ (or a conceptually equivalent variable such as ω or τ) to compute μ_t. From dimensional analysis, the turbulent viscosity is generally expressed by

$$\mu_t = \langle\rho\rangle\ C_\mu f_\mu k^{1/2} l, \tag{2.10}$$

in which the local length scale l is obtained as a function of k and ϵ ($l \propto k^{3/2}/\epsilon$) in the $k-\epsilon$ model, and as a function of k and ω ($l \propto k^{1/2}/\omega$) in the $k-\omega$ model.
During the development of this thesis, five different variations of the two-equations viscosity models have been implemented. These are the $k-\epsilon$ JL model from Jones and Launder (1972), the $k-\epsilon$ LS model from Launder and Sharma (1974), the $k-\epsilon$ HH model from Henkes and Hoogendoorn (1995), the $k-\omega$ WX model from Wilcox et al. (1998) and Wilcox (1994), and the $k-\omega$ PD model from Peng and Davidson (1999), these models are described in the next subsections.

2.2.1.1 $k-\epsilon$ turbulent model

The turbulent viscosity and transport equations for k and ϵ are here modeled following the work of Pérez-Segarra et al. (1995) as

$$\mu_t = \langle\rho\rangle\, C_\mu f_\mu \frac{k^2}{\tilde{\epsilon}}, \tag{2.11}$$

$$\frac{\partial(\langle\rho\rangle k)}{\partial t} + \frac{\partial(\langle\rho\rangle\{u_i\}k)}{\partial x_i} = \frac{\partial}{\partial x_i}\left[\left(\{\mu\} + \frac{\mu_t}{\sigma_k}\right)\frac{\partial k}{\partial x_i}\right] + P_k - (\rho\tilde{\epsilon} + D)\,, \tag{2.12}$$

$$\frac{\partial(\langle\rho\rangle\tilde{\epsilon})}{\partial t} + \frac{\partial(\langle\rho\rangle\{u_i\}\tilde{\epsilon})}{\partial x_i} = \frac{\partial}{\partial x_i}\left[\left(\{\mu\} + \frac{\mu_t}{\sigma_\epsilon}\right)\frac{\partial \tilde{\epsilon}}{\partial x_i}\right] + C_{1,\epsilon} f_1 P_k \frac{\tilde{\epsilon}}{k} + E - C_{2,\epsilon} f_2 \frac{\rho\tilde{\epsilon}^2}{k}. \tag{2.13}$$

where P_k stands for the production of turbulent kinetic energy defined as $P_k = -\langle\rho u_i'' u_j''\rangle\partial\{u_i\}/\partial x_j$, and $\tilde{\epsilon}$ is a variable described by $\tilde{\epsilon} = \epsilon - D/\rho$. In Eqs. 2.12 and 2.13, gravitational effects are not considered since the focus of this thesis resides on non-buoyancy flows. All the experimental constants and dumping function characterizing the $k-\epsilon$ JL model from Jones and Launder (1972), the $k-\epsilon$ LS model from Launder and Sharma (1974) and the $k-\epsilon$ HH model are summarized in Tables 2.1, 2.2 and 2.3.

Table 2.1: *Constant values for the different $k-\epsilon$ models implemented.*

Model	C_μ	$C_{1,\epsilon}$	$C_{2,\epsilon}$	σ_k	σ_ϵ
HH	0.09	1.44	1.92	1.0	1.3
JL	0.09	1.55	2.0	1.0	1.3
LS	0.09	1.44	1.92	1.0	1.3

Table 2.2: *Dumping functions for the different $k-\epsilon$ models implemented.*

Model	f_μ	f_1	f_2
HH	1.0	1.0	1.0
JL	$exp\left(\dfrac{-2.5}{1+\frac{Re_t}{50}}\right)$	1.0	$1-0.3\ exp\left(-Re_t^2\right)$
LS	$exp\left(\dfrac{-3.4}{\left(1+\frac{Re_t}{50}\right)^2}\right)$	1.0	$1-0.3\ exp\left(-Re_t^2\right)$

Table 2.3: *Extra terms expressions for the $k-\epsilon$ models implemented.*

Model	D	E
HH	0.0	0.0
JL	$2\{\mu\}\left(\dfrac{\partial(k^{1/2})}{\partial x_j}\right)^2$	$\frac{2\{\mu\}\mu_t}{\rho}\left(\dfrac{\partial^2 u_i}{\partial x_j^2}\right)^2$
LS	$2\{\mu\}\left(\dfrac{\partial(k^{1/2})}{\partial x_j}\right)^2$	$\frac{2\{\mu\}\mu_t}{\rho}\left(\dfrac{\partial^2 u_i}{\partial x_j^2}\right)^2$

In Tables 2.2 and 2.3, Re_t is the local turbulent number defined as $Re_t = \frac{\langle\rho\rangle k^2}{\{\mu\}\tilde{\epsilon}}$.

2.2.1.2 $k-\omega$ turbulent model

First introduced by Kolmogorov (1942), ω is the rate of energy dissipation per unit of volume and per unit of time, $\omega \equiv \epsilon/k$. In the $k-\omega$ models, an equation for ω is used instead of the ϵ equation. Then,

$$\mu_t = \langle\rho\rangle\ C_\mu f_\mu \frac{k}{\omega}, \tag{2.14}$$

$$\frac{\partial(\langle\rho\rangle k)}{\partial t} + \frac{\partial(\langle\rho\rangle\{u_i\}k)}{\partial x_i} = \frac{\partial}{\partial x_i}\left[\left(\{\mu\}+\frac{\mu_t}{\sigma_k}\right)\frac{\partial k}{\partial x_i}\right] + P_k - C_k f_k \langle\rho\rangle\ k\ \omega, \tag{2.15}$$

$$\frac{\partial(\langle\rho\rangle\omega)}{\partial t} + \frac{\partial(\langle\rho\rangle\{u_i\}\omega)}{\partial x_i} = \frac{\partial}{\partial x_i}\left[\left(\{\mu\}+\frac{\mu_t}{\sigma_\omega}\right)\frac{\partial \omega}{\partial x_i}\right] + C_{1,\omega} f_1 P_k \frac{\omega}{k} - C_{2,\omega} f_2 \langle\rho\rangle\omega^2 + \\ + C_{r\omega}\frac{\mu_t}{k}\left(\frac{\partial k}{\partial x_i}\frac{\partial \omega}{\partial x_i}\right). \tag{2.16}$$

Again the gravitational effects have been neglected in Eqs. 2.15 and 2.16. The experimental constants and dumping functions for the $k-\omega$ WX model from

Wilcox (1994) and Wilcox et al. (1998), and the $k-\omega$ PD model from Peng and Davidson (1999) are summarized in Tables 2.4 and 2.5.

Table 2.4: *Constant values for the two different $k-\omega$ models implemented.*

Model	C_μ	C_k	$C_{1,\omega}$	$C_{2,\omega}$	$C_{r\omega}$	σ_K	σ_ω
PD	1	0.09	0.42	0.075	0.75	0.8	1.35
WX	1	0.09	0.56	0.075	0.0	2	2

Table 2.5: *Dumping functions for the different $k-\omega$ models implemented.*

	PD	WX
f_μ	$0.025 + \left(1 - e^{-\left(\frac{Re_t}{10}\right)^{3/4}}\right)\left(0.975 + \frac{10^{-3}}{Re_t} e^{-\left(\frac{Re_t}{200}\right)^2}\right)$	$\dfrac{0.025 + \frac{Re_t}{6}}{1 + \frac{Re_t}{6}}$
f_k	$1 - 0.722\, e^{-\left(\frac{Re_t}{10}\right)^4}$	$\dfrac{\frac{5}{18} + \left(\frac{Re_t}{8}\right)^4}{1 + \left(\frac{Re_t}{8}\right)^4}$
f_1	$1 + 4.3\, e^{-\left(\frac{Re_t}{1.5}\right)^{1/2}}$	$\dfrac{0.1 + \left(\frac{Re_t}{2.7}\right)}{1 + \left(\frac{Re_t}{2.7}\right)} f_\mu^{-1}$
f_2	1.0	1.0

In Tables 2.4 and 2.5, Re_t is the local turbulent number defined as $Re_t = \frac{\langle\rho\rangle k}{\{\mu\}\omega}$.

2.2.2 Turbulent heat flux closure

In the context of turbulent viscosity models, similar to the Boussinesq consideration (Eq. 2.9), the turbulent heat flux is commonly related to the mean flow characteristics by the expression

$$\langle\rho\rangle\{u_j''T''\} = -\frac{\mu_t}{\mathrm{Pr}_t}\frac{\partial\{T\}}{\partial x_j}, \tag{2.17}$$

where Pr_t is the turbulent Prandtl number. Rodi (1993) found through experimental investigation that for most of the cases the turbulent Prandtl number does not vary significantly along the flow. The value of the Pr_t is typicaly set to $\mathrm{Pr}_t = 0.9$ for boundary layers. However, for free shear layers, Wilcox et al. (1998) use $\mathrm{Pr}_t = 0.5$, while Pope (2001) considers the value of $\mathrm{Pr}_t = 0.7$ in a plane wake.

2.3 ConDiRa code: methodology for the numerical solution

ConDiRa (CONvection, DIfusion and RAdiation) is an in-house code developed in the course of this thesis, mainly during a summer stage conducted by Prof. J.

Xamán at the Department of Mechanical Engineering of CENIDET (National Center for Research and Technology Development), Mexico. In the ConDiRa code, the set of equations defining the RANS problem are discretized using the finite volume method (FVM) in a structured grid, and solved by an Alternating Direction Implicit (ADI) method.

FVM consists in integrating each governing equation over small control volumes (CV) (as the one shown in Fig. 2.1(a)), the ensemble of control volumes define the computational domain. In the present code, each CV or cell has a node at its geometrical center, i.e., the mesh is cell-centered. Moreover, the physical boundaries of the domain are set to match the CV interface as shown in Fig. 2.1(b).

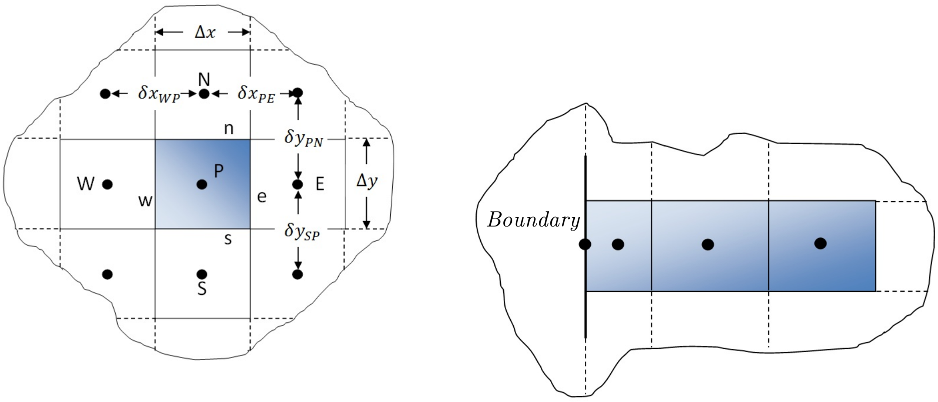

(a)

(b)

Figure 2.1: *(a) Control volume notation in a structured mesh used for the FVM discretization. Note that capital letters are used for nodes, while lower case letters are used for CV interfaces. (b) Details of the cell-centered mesh treatment at the boundary, a node is place at the physical domain boundary.*

2.3.1 Numerical discretization of the governing equations

As proposed in Patankar (1980), in order to facilitate the discretization procedure, all governing equations presented in the previous section can be expressed in the following general form:

$$\frac{\partial(\langle\rho\rangle\phi)}{\partial t}+\frac{\partial(\langle\rho\rangle\{u_i\}\phi)}{\partial x_i}=\frac{\partial}{\partial x_i}\left(\Gamma\frac{\partial\phi}{\partial x_i}\right)+S. \tag{2.18}$$

Table 2.6 shows the values of the generic variable ϕ, diffusion coefficient Γ and source term S to turn Eq. 2.18 into each of the governing equations.

Then, the FVM proceeds by performing a spatially integration in a CV and a

Table 2.6: *Equivalent generic variable ϕ, diffusion coefficient Γ and source term S in the general differential equation.*

Governing Eq.	ϕ	Γ	S
Mass	1	0	0
Momentum in x_i	$\{u_i\}$	$\{\mu\} + \mu_t$	$-\dfrac{\partial \langle P \rangle}{\partial x_i} + \langle \rho \rangle g_i$
Energy	$\{T\}$	$\frac{\{\lambda\}}{c_p} + \frac{\mu_t}{\mathrm{Pr}_t}$	$\dfrac{\langle P_{rad} \rangle}{c_p}$
TKE in $k-\epsilon$	k	$\{\mu\} + \frac{\mu_t}{\sigma_k}$	$P_k - (\rho\tilde{\epsilon} + D)$
TKE in $k-\omega$	k	$\{\mu\} + \frac{\mu_t}{\sigma_k}$	$P_k - C_k f_k \langle \rho \rangle \ k \ \omega$
ϵ	$\tilde{\epsilon}$	$\{\mu\} + \frac{\mu_t}{\sigma_\epsilon}$	$C_{1,\epsilon} f_1 P_k \frac{\tilde{\epsilon}}{k} + E - C_{2,\epsilon} f_2 \frac{\rho\tilde{\epsilon}^2}{k}$
ω	ω	$\{\mu\} + \frac{\mu_t}{\sigma_\omega}$	$C_{1,\omega} f_1 P_k \frac{\omega}{k} - C_{2,\omega} f_2 \langle \rho \rangle \omega^2 + C_{r\omega} \frac{\mu_t}{k} \left(\frac{\partial k}{\partial x_i} \frac{\partial \omega}{\partial x_i} \right)$

temporally integration from t to $t + \Delta t$ of the Eq. 2.18 in the form:

$$\int_t^{t+\Delta t} \int_{CV} \left[\frac{\partial(\langle \rho \rangle \phi)}{\partial t} + \frac{\partial(\langle \rho \rangle \{u_i\} \phi)}{\partial x_i} = \frac{\partial}{\partial x_i} \left(\Gamma \frac{\partial \phi}{\partial x_i} \right) + S \right] dV dt. \tag{2.19}$$

Integrating Eq. 2.19 in the two-dimensional CV presented in Fig. 2.1(a) and assuming an implicit scheme for the time integration, one can write

$$\begin{aligned} \frac{(\rho\phi)_P - (\rho\phi)_P^o}{\Delta t} \Delta x \Delta y + [(\rho u \phi)_e - (\rho u \phi)_w] \Delta y + [(\rho v \phi)_n - (\rho v \phi)_s] \Delta x = \\ [(\Gamma \frac{\partial \phi}{\partial x})_e - (\Gamma \frac{\partial \phi}{\partial x})_w] \Delta y + [(\Gamma \frac{\partial \phi}{\partial y})_n - (\Gamma \frac{\partial \phi}{\partial y})_s] \Delta x + \bar{S} \Delta x \Delta y, \end{aligned} \tag{2.20}$$

where $(\rho\phi)_P^o$ is the $\rho\phi$ value in the previous time step at point P, and $\bar{S}$ is the spatial average of S over the CV. Note that the mass fluxes $\rho u_i \phi$ and diffusives fluxes $\Gamma \partial\phi/\partial x_i$ are needed at the CV interfaces. An UPWIND scheme is used to approximate the value of ϕ at the interface, while a 2^{nd}-order centered finite-difference scheme is used to estimate $(\partial\phi)/(\partial x_i)$ at the CV interface. To determine Γ at the interface, a linear variation is assumed. Further accuracy from high order schemes is implemented using the source terms S_u^{DC} via deferred correction as discussed below. Finally, combining Eq. 2.20 with the mass conservation equation provides an algebraic equation for each variable ϕ in each node of the mesh as a function of the ϕ values at the neighbor nodes. This algebraic equation is called the discretization equation which, in a two-dimensional domain, can be expressed as

$$a_P \phi_P = a_W \phi_W + a_E \phi_E + a_N \phi_N + a_S \phi_S + b, \tag{2.21}$$

in which the coefficients are described by:

$$a_E = D_e + max[-F_e, 0], \tag{2.22a}$$
$$a_W = D_w + max[F_w, 0], \tag{2.22b}$$
$$a_N = D_n + max[-F_n, 0], \tag{2.22c}$$
$$a_S = D_s + max[F_s, 0], \tag{2.22d}$$
$$a_P = a_E + a_W + a_S + a_N + \rho_P^o \frac{\Delta x \Delta y}{\Delta t}, \tag{2.22e}$$
$$b = (\rho\phi)_P^o \frac{\Delta x \Delta y}{\Delta t} + \bar{S}\Delta x \Delta y + S_u^{DC}. \tag{2.22f}$$

where F and D are respectively the convective and diffusive fluxes at the CV interfaces. Recalling the nomenclature presented in Fig. 2.1(a), these fluxes are defined by:

$$F_e = (\rho u \phi)_e \Delta y, \quad F_w = (\rho u \phi)_w \Delta y, \quad F_n = (\rho v \phi)_n \Delta x, \quad F_s = (\rho v \phi)_s \Delta x, \tag{2.23}$$

$$D_e = \frac{\Gamma_e}{\delta x_{PE}} \Delta y, \quad D_w = \frac{\Gamma_w}{\delta x_{WP}} \Delta y, \quad D_n = \frac{\Gamma_n}{\delta y_{PN}} \Delta x, \quad D_s = \frac{\Gamma_s}{\delta y_{SP}} \Delta x. \tag{2.24}$$

The term S_u^{DC} in Eq. 2.21 has been added as a deferred correction source term which accounts for the contribution arising from the high-order scheme. If $S_u^{DC} = 0$ the discretization of the convective terms is achieved by using an UPWIND scheme, which is first-order accuracy and it is unconditionally stable. In this work six different second-order schemes have been implemented in the general form of the *Total Variation Diminishing* schemes (TVD). These are (i) the van Leer scheme (Van Leer (1977)), (ii) van Albada scheme (van Albada et al. (1982)), (iii) Min-Mod (Roe (1985)), (iv) SUPERBEE (Roe (1985)), (v) QUICK (Leonard (1988)) and (vi) UMIST (Lien and Leschziner (1994)). The TVD formulation avoids oscillation during the iterative process since it prevents instabilities while keeping a high-order of accuracy. Following the work of Versteeg and Malalasekera (2007), the source term S_u^{DC} is computed doing

$$S_u^{DC} = \frac{1}{2} F_e \left[(1-\alpha_e)\psi(r_e^-) - \alpha_e \psi(r_e^+)\right](\phi_E - \phi_P) \tag{2.25}$$
$$+ \frac{1}{2} F_w \left[\alpha_w \psi(r_w^+) - (1-\alpha_w)\psi(r_w^-)\right](\phi_P - \phi_W) \tag{2.26}$$
$$+ \frac{1}{2} F_n \left[(1-\alpha_n)\psi(r_n^-) - \alpha_n \psi(r_n^+)\right](\phi_N - \phi_P) \tag{2.27}$$
$$+ \frac{1}{2} F_s \left[\alpha_s \psi(r_s^+) - (1-\alpha_s)\psi(r_s^-)\right](\phi_P - \phi_S), \tag{2.28}$$

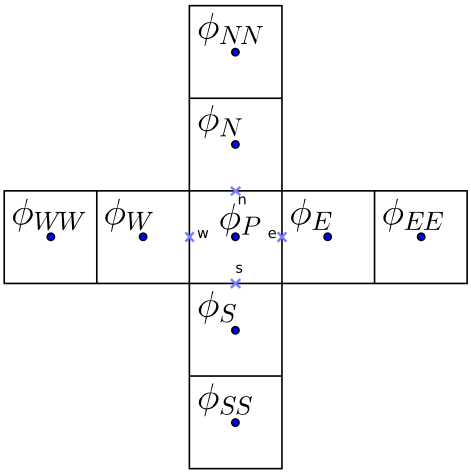

Figure 2.2

Figure 2.3: *Notation for the neighbor nodes of CV used in the derivation of high-order schemes*

Following the notation in Fig. 2.2, the variable r is defined as

$$
\begin{aligned}
r_e^+ &= \left(\frac{\phi_P - \phi_W}{\phi_E - \phi_P}\right), \quad r_e^- = \left(\frac{\phi_{EE} - \phi_E}{\phi_E - \phi_P}\right), \quad r_w^+ = \left(\frac{\phi_W - \phi_{WW}}{\phi_P - \phi_W}\right), \\
r_w^- &= \left(\frac{\phi_E - \phi_P}{\phi_P - \phi_W}\right), \quad r_n^+ = \left(\frac{\phi_P - \phi_S}{\phi_N - \phi_P}\right), \quad r_e^- = \left(\frac{\phi_{NN} - \phi_N}{\phi_N - \phi_P}\right), \\
r_s^+ &= \left(\frac{\phi_S - \phi_{SS}}{\phi_P - \phi_S}\right), \quad r_s^- = \left(\frac{\phi_N - \phi_P}{\phi_P - \phi_S}\right),
\end{aligned}
$$

and

$$
\begin{aligned}
\alpha_w &= \begin{cases} 1 & \text{if } F_w > 0 \\ 0 & \text{if } F_w \leq 0 \end{cases}, \quad \alpha_e = \begin{cases} 1 & \text{if } F_e > 0 \\ 0 & \text{if } F_e \leq 0 \end{cases}, \\
\alpha_s &= \begin{cases} 1 & \text{if } F_s > 0 \\ 0 & \text{if } F_s \leq 0 \end{cases}, \quad \alpha_n = \begin{cases} 1 & \text{if } F_n > 0 \\ 0 & \text{if } F_n \leq 0 \end{cases}.
\end{aligned}
$$

The function $\psi(r)$ is a flux limiter function that allows to generalize the high-order schemes solely as a function of $\psi(r)$. The value of the limiter function for each scheme is given in Table 2.7.

2.3.2 Momentum transport and mass conservation coupling

In order to deal with the non-linear coupling between mass and momentum equations, a non-uniform staggered marker-and-cell (MAC) mesh presented in Fig. 2.4 is used. In the MAC mesh (Harlow and Welch (1965)) the velocity

Table 2.7: *Expressions for the flux limiter function $\psi(r)$ for each of the second-order schemes implemented.*

High order Scheme	$\psi(r)$
Van Leer	$\psi(r) = \dfrac{r+\lvert r\rvert}{1+r}$
Van Albada	$\psi(r) = \dfrac{r+r^2}{1+r}$
Min-Mod	$\psi(r) = \begin{cases} \min(r,1) & \text{if } r>0 \\ 0 & \text{if } r \leq 0 \end{cases}$
SUPERBEE	$\psi(r) = \max\left[0, \min(2r,1), \min(r,2)\right]$
QUICK	$\psi(r) = \max\left[0, \min(2r,(3+r)/4,2)\right]$
UMIST	$\psi(r) = \max\left[0, \min(2r,(1+3r)/4,(3+r)/4,2)\right]$

components are calculated at a staggered grid (Figs. 2.4(a) and 2.4(b)), while the scalar variables (T, ρ, P, k, ϵ, ω, ...) are calculated at the main grid (not staggered) shown in Fig. 2.4(c). The first advantage of using this kind of mesh is that velocity in the computation of the convective fluxes defined in Eq. 2.23 is directly obtained at the CV interface of the main mesh without interpolation. Second, the computation of the momentum source term $-\partial P/\partial x_i$ in the staggered grid does not require interpolation at the CV interface, which leads to numerical stability and avoids physically unrealistic results.

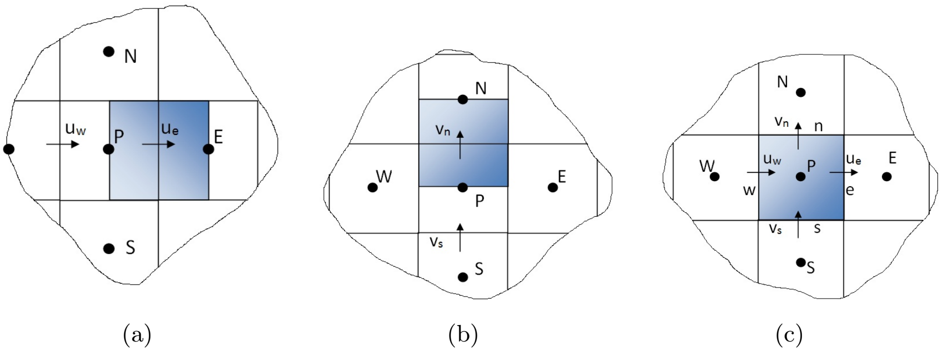

Figure 2.4: *The three meshes used to couple momentum transport and mass conservation. (a) Mesh for the x-component velocity u in which CV are displaced in the x-direction. (b)Mesh for the y-component velocity v in which CV are displaced in the y-direction. (c) Main grid where scalars are stored.*

The SIMPLE (Semi-Implicit Method for Pressure-Linked Equations) algorithm described in the work of Patankar and Spalding (1983) is used in this work to couple the mass conservation and the momentum transport equation. This method first consists in guessing a pressure field (p^*) by which an estimation of the velocity is computed (u_i^*) using the momentum transport equations. Then, from the mass conservation, a "pressure correction" field (p') is computed, which gives the rectification in pressure needed so that u_i^* fulfills the mass conservation equation. Once u_i^* and p^* are corrected, the process is iteratively repeated until a velocity field that simultaneously fulfills the mass conservation and momentum transport is obtained.

2.3.3 Variable density and transport properties

When large temperature differences are present in the domain, the computation of a density field varying over space is needed to accurately predict the flow dynamics. If the characteristic velocity of the flow is low when compared with the speed of sound, a low Mach number approximation can be applied. This approach avoids the need to account for acoustic propagation and still captures the relevant physics, being that the density is decoupled from the dynamic pressure so no acoustics are accounted for. Firstly, the total pressure is decomposed into the thermodynamic pressure P_0 and the dynamic pressure $\tilde{p}$ by the expression

$$P(x, y, t) = P_0 + \tilde{p}(x, y, t), \tag{2.29}$$

in which the thermodynamic pressure is assumed to be equal to the initial pressure P_0 and constant in time. The local density field can be computed from the ideal gas law as

$$\rho = \frac{P_0}{rT}. \tag{2.30}$$

For the case of variable properties, the matrices containing the local values of ρ, λ and μ are computed in every iteration for each temperature field, as shown in Fig. 2.5 in which a general overview of the code is presented. To interpolate the properties values at the control volume interfaces, a linear variation between two neighbor nodes is assumed.

2.3.4 Boundary conditions

Information of each variable ϕ at the boundaries is required in order to solve the problem. In this work, two kinds of boundary conditions are implemented. On the one hand, the Direchlet condition is used when a specific value (ϕ_a) is imposed at the boundary. Considering the discretization equation of ϕ in two-dimensions for a node ϕ_P placed at the boundary

$$a_P\phi_P = a_W\phi_W + a_E\phi_E + a_N\phi_N + a_S\phi_S + b, \tag{2.31}$$

a Direchlet condition is obtained by setting

$$a_E = a_W = a_N = a_S = 0,\ a_P = 1 \text{ and } b = \phi_a. \tag{2.32}$$

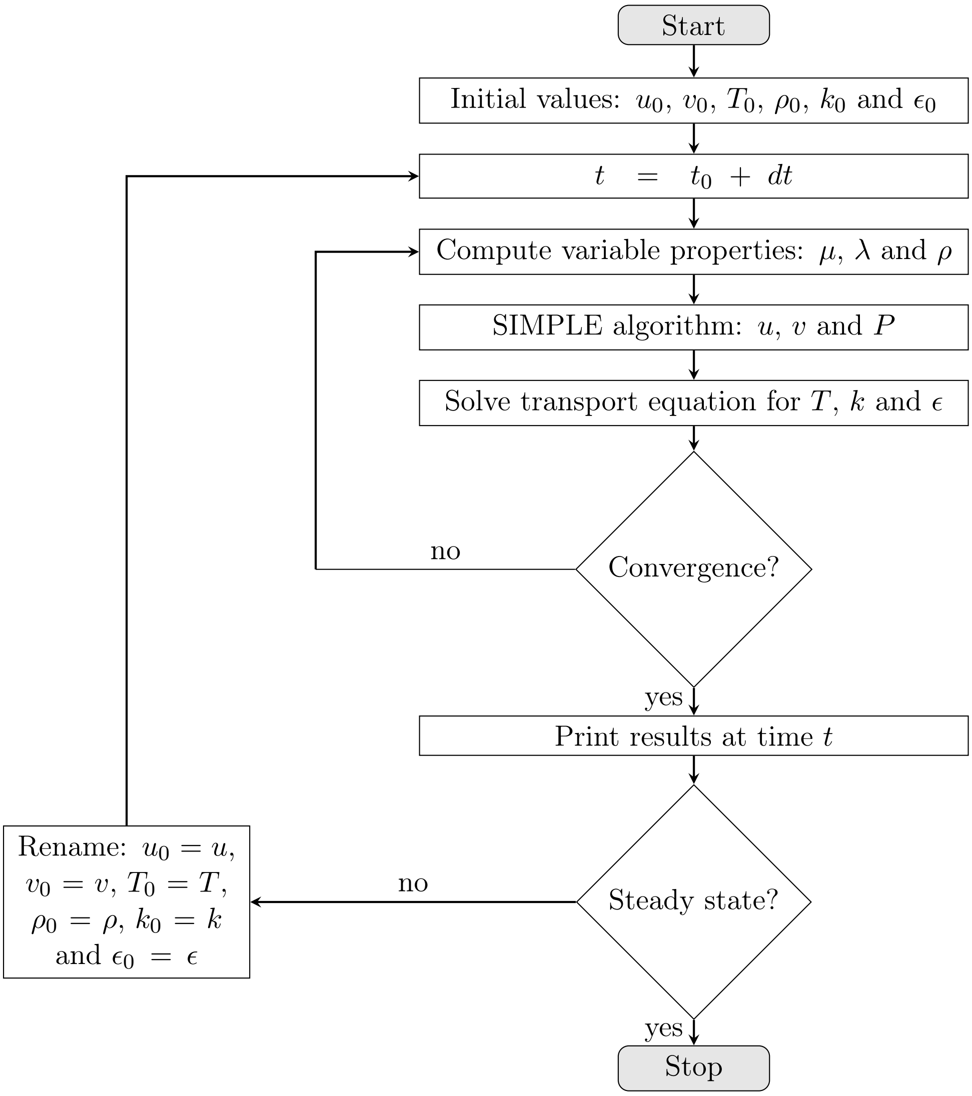

Figure 2.5: *Structure of the ConDiRa code for the $k-\epsilon$ model with variable properties.*

On the other hand, the Neumann condition is used when a variation (A) of a variable (ϕ) in a given direction (n) is specified in the form $\frac{\partial\phi}{\partial n} = A$. Recalling the nomenclature in Fig. 2.1(a) and assuminig linear variation of ϕ, a Neumann condition is imposed, for example in the south boundary, as

$$a_E = a_W = a_S = 0 \; a_P = a_N = 1 \text{ and } b = -A\delta y. \tag{2.33}$$

2.3.5 Numerical solution of the implicit system of equations

The set of algebraic equations resulting from the discretization is solved by an ADI iterative method (Peaceman and Rachford (1955)). In addition, under-relaxation parameters have been used in order to minimize the number of iterations required to obtain converged solutions.
When the residuals of the mass balance for every control volume, as well as the residual values for all other governing equations are sufficiently low, an overall convergence is achieved. Global residual values for each transport equation are computed based on Eq. 2.21 using the following quadratic mean

$$R_\phi = \sqrt{\sum_{all\ CV} \left[a_P\phi_P - (a_W\phi_W + a_E\phi_E + a_N\phi_N + a_S\phi_S + b)\right]^2}, \qquad (2.34)$$

The iterative process is considered converged when residuals scaled by its initial value are lower than 10^{-6} for each variable.

2.3.6 Code verification

In order to verify the numerical code, some benchmark problems are reproduced. Firstly, the high-order schemes are verified by reproducing pure convection in a diagonal flow. Secondly, the results for the laminar natural convection in steady state using constant properties are compared with the classical solutions of de Vahl Davis and Jones (1983); and Hortmann et al. (1990). Then, the variable-density laminar solutions with and without variable transport properties are compared with Le Quéré et al. (2005). Next, the laminar transient natural convection is compared with the results published in the work of Leal et al. (2000). Further details of the laminar natural convection solution using ConDiRa can be found in the Appendix D. Results for the turbulent simulation of free plane jets are presented in Chapter 9.

2.3.6.1 Pure convection in a diagonal flow

In order to verify the implementation of the high-order schemes, a simple problem presented in Patankar (1980) and illustrated in fig. 2.6(a) is computed in a uniform mesh of 121×121 nodes. This problem consists in a diagonal flow that purely convects a passive scalar ϕ through a constant velocity field defined by $u = v = 2$ m/s. The boundary conditions for the scalar are $\phi = 100$ in the west and north boundaries, and $\phi = 0$ in the east and south boundaries. In this problem the physical viscosity is set to zero, thus the analytical solution is known and it is shown in Fig. 2.6(b). Fig. 2.6(b) shows the value of the scalar ϕ along the diagonal $I - J$ (indicated in Fig. 2.6(a)) for the analitical solution, the 1^{st}-order UPWIND scheme, as well as for each implemented 2^{nd}-order scheme.

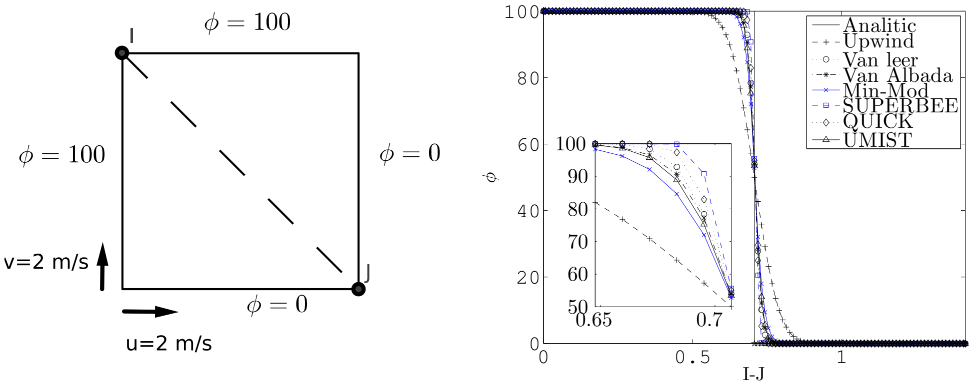

(a) (b)

Figure 2.6: *(a) Definition of the pure convection diagonal flow problem. (b) Comparison of the results of ϕ along the diagonal $I - J$ between the analytic solution and all the implemented schemes.*

From Fig. 2.6(b) it can be seen that high-order schemes estimate better the solution than the UPWIND first order scheme, which presents the largest values of numerical diffusion. In order to appropriately choose a high-order scheme for the present simulation, table 2.8 presents a comparison of CPU time and number of iteration spent to solve the diagonal flow problem for each scheme.

Table 2.8: *Comparison of numerical schemes in terms of CPU time and number of iteration to converge.*

	UPWIND	Van Leer	Van Albada	Min-Mod	SUPERBEE	QUICK	UMIST
num. of iter.	275	521	369	308	4465	2756	415
CPU time (s)	1.20	3.95	2.89	2.12	31.63	19.46	3.20

Van Albada scheme is retained since it is the second faster in terms of number of iteration and CPU time as presented in Table 2.8, while it is the fourth more accurate as shown in Fig. 2.6(b).

2.3.6.2 Laminar differently heated cavity: steady state with constant properties and Boussinesq approximation

A set of comparisons is performed for the constant properties case of the classical square cavity problem with differentially heated vertical walls under the Boussinesq approximation. A sketch of the square cavity with non-slip walls is presented in Fig. 2.7, in which temperature boundary conditions are indicated.

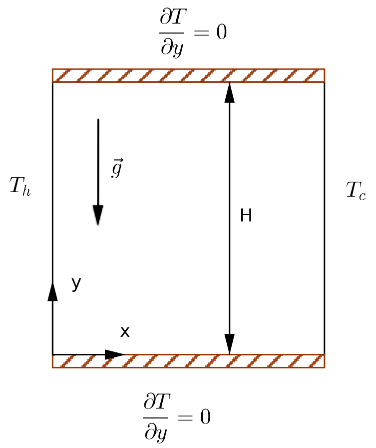

Figure 2.7: *Sketch of the differently heated cavity with non-slip walls.*

In the Boussinesq approximation, density is assumed constant and the source of motion is modeled by a source term in the momentum equation on the vertical direction. In Table 2.9, results for steady state regime for Rayleigh numbers between 10^3 and 10^6 are compared with the benchmark solutions of de Vahl Davis and Jones (1983); Hortmann et al. (1990) for $Pr = 0.71$. Prandt and Rayleigh numbers are defined as

$$Pr = \frac{c_p \mu_{ref}}{\lambda_{ref}} \quad \text{and} \quad Ra = Pr \frac{\rho_{ref}^2 g (T_h - T_c) H^3}{T_{ref} \mu_{ref}^2}, \tag{2.35}$$

where T_h and T_c are the temperatures at the hot and cold walls, respectively. T_{ref} is a reference temperature defined as $T_{ref} = (T_h + T_c)/2$; H is the cavity height and width; and λ_{ref}, ρ_{ref} and μ_{ref} are, respectively, the thermal conductivity, density and dynamic viscosity evaluated at T_{ref}. The following adimensionalized quantities are introduced for the sake of comparison with the literature results

$$T^* = \frac{T - T_c}{T_h - T_c}, \quad x^* = \frac{x}{H}, \quad y^* = \frac{y}{H}, \quad u^* = \frac{uH}{\alpha_0}, \quad v^* = \frac{vH}{\alpha_0}, \quad \text{and} \quad t^* = t\frac{\alpha_0}{H^2}, \tag{2.36}$$

where α_0 is the thermal diffusivity evaluated at the initial time, and the adimensionalized time t^* is chosen following the work of Leal et al. (2000).
The selected comparative results are: the maximum horizontal velocity, u^*_{max}, in the vertical mid-plane ($x^* = 0.5$); the maximum vertical velocity, v^*_{max}, in the horizontal mid-plane ($y^* = 0.5$); and the maximum, minimum and average Nusselt number in the hot wall, Nu_{max}, Nu_{min}, $\overline{Nu}$. The local Nusselt number at the hot wall, $Nu(y)|_{x=0}$, and the average Nusselt number, $\overline{Nu}|_{x=0}$, are determined as follows:

$$Nu(y)|_{x=0} = \frac{H}{\lambda_{ref}(T_h - T_c)} \lambda(T) || \frac{\partial T}{\partial x}|_{x=0}|| \quad \text{and} \quad \overline{Nu}|_{x=0} = \frac{1}{H} \int_0^H Nu(y)|_{x=0} dy.$$

(2.37)

As shown in Table 2.9, the overall agreement is quite reasonable with a maximum deviation of 1.99% with respect to de Vahl Davis and Jones (1983) and a 0.22% with respect to Hortmann et al. (1990).

Table 2.9: *Comparison between results obtained using the ConDiRa code and some steady state benchmark results for constant properties and Boussineq approximation.*

Ra		u^*_{max}	v^*_{max}	Nu_{max}	Nu_{min}	$\overline{Nu}$
10^3	de Vahl Davis and Jones (1983)	3.649	3.697	1.505	0.692	1.118
	Hortmann et al. (1990)	-	-	-	-	-
	Present work	3.6450	3.6998	1.5100	0.6935	1.1207
10^4	de Vahl Davis and Jones (1983)	16.178	19.617	3.528	0.586	2.243
	Hortmann et al. (1990)	16.1802	19.6295	3.53087	-	2.24475
	Present work	16.1838	19.6296	3.5319	0.5851	2.2452
10^5	de Vahl Davis and Jones (1983)	34.73	68.59	7.717	0.729	4.519
	Hortmann et al. (1990)	34.7399	68.6396	7.72013	-	4.52164
	Present work	34.7410	68.6212	7.7242	0.7280	4.5225
10^6	de Vahl Davis and Jones (1983)	64.63	219.36	17.925	0.989	8.800
	Hortmann et al. (1990)	64.8367	220.461	17.536	-	8.82513
	Present work	64.8473	220.5518	17.5752	0.9794	8.8300

2.3.6.3 Laminar differently heated cavity: steady state with a non-Boussinesq approach with and without variable transport properties

Le Quéré et al. (2005) published a benchmark solution for the variable-density case with and without variable transport properties. This reference solution is based on the results of five independent authors, whose methods and procedures are detailed in Becker et al. (1999); Guide (1997); Becker and Braack (2002); Vierendeels et al. (1999); Le Quéré et al. (1992). Three tests are available for the following conditions:
Test 1: $Ra = 10^6$, $\epsilon = 0.6$, $\mu = \mu_0$ and $\lambda = \lambda_0$,
Test 2: $Ra = 10^6$, $\epsilon = 0.6$, $\mu = \mu(T)$ and $\lambda = \lambda(T)$,
Test 3: $Ra = 10^7$, $\epsilon = 0.6$, $\mu = \mu(T)$ and $\lambda = \lambda(T)$,
where the initial conditions are $P_0 = 101325$ Pa and $T_0 = 600$ K. Viscosity and thermal conductivity are computed using Sutherland law as

$$\mu(T) = \mu' \left(\frac{T}{T'}\right)^{3/2} \frac{T' + S}{T + S} \quad \text{and} \quad \lambda(T) = \mu(T) \, \frac{\gamma R}{(\gamma - 1) Pr}, \tag{2.38}$$

where $T' = 273K$, $S = 110.5K$, $\gamma = 1.4$, $R = 287Jkg^{-1}K^{-1}$, $\mu' = 1.68 \cdot 10^{-5} m^{-1}s^{-1}kg$ and $Pr = 0.71$. Table 2.10 presents a comparison of the average Nusselt in the hot wall ($\overline{Nu_h}$) and the non-dimensional thermodynamic pressure ($\bar{P}(t)/P_0$ where $\bar{P}(t) = P_0 \int \frac{1}{T_0} dV / \int \frac{1}{T} dV$) obtained in this present work with the ones published in Le Quéré et al. (2005). The percentage deviation when comparing with the reference values are shown between parentheses. The results obtained for the non-Boussinesq approximation are in good agreement with previous solutions since the maximum deviation obtained is 0.129%.

Table 2.10: *Comparison of the present work with steady state benchmark results with a non-Boussinesq approach.*

		$\bar{P}(t)/P_0$	$\overline{Nu_h}$
Test 1	Quéré *et al.* (2005)	0.856338	8.85978
	Present work	0.8565 (0.019%)	8.8640 (0.048%)
Test 2	Quéré *et al.* (2005)	0.924487	8.6866
	Present work	0.9249 (0.045%)	8.6938 (0.083%)
Test 3	Quéré *et al.* (2005)	0.92263	16.2410
	Present work	0.92224 (0.042%)	16.2619 (0.129%)

2.3.6.4 Laminar differently heated cavity: transient regime with constant properties and Boussinesq approximation

Results for the unsteady regime are compared with previous publications (Leal et al. (2000)). Again, the Boussinesq approximation and constant properties formulation are used. Figures 2.8 and 2.9 show, for different physical times, non-dimensional temperature and dimensionless vertical velocity component distributions, respectively, in the cavity mid-plane ($y^* = 0.5$) for Rayleigh numbers between 10^3 and 10^6, $Pr = 0.71$ and $T_0 = T_c$. In addition, for the same Rayleigh range, the time evolution of the average Nusselt number is compared with the same authors in Fig. 2.10. Figures 2.8 to 2.10 show an excellent agreement, at least, at the graph scale. The expected increasing oscillations of the average Nusselt number as the Rayleigh number increases are also well reproduced. A distinguished agreement is achieved between every average Nusselt number at the end of the transient period and the ones found in the steady state formulation.

2.3.6.5 Turbulent isothermal plane free jet

The RANS implementation is here tested by solving an isothermal turbulent plane jet of water vapor discharging into a parallel low speed coflow of water vapor. The $k-\epsilon$ LS turbulent model and Van Albada scheme, both detailed in this Chapter, are used.

The plane jet is briefly detailed in this section, since an extensive explanation of the physical problem is further provided in Chapter 4. The turbulent statistics of a plane jet are two-dimensional. The streamwise direction is x while the cross-stream coordinate is y. The jet starts to develop at $x = 0$.

The setup for the present test is summarized in Table 2.11.

Table 2.11: *Configuration of the isothermal plane jet.*

δ [m]	U_1 [m/s]	U_2 [m/s]	Re	P_0 [atm]
$5 \cdot 10^{-2}$	4.176	$U_1/10$	3200	1

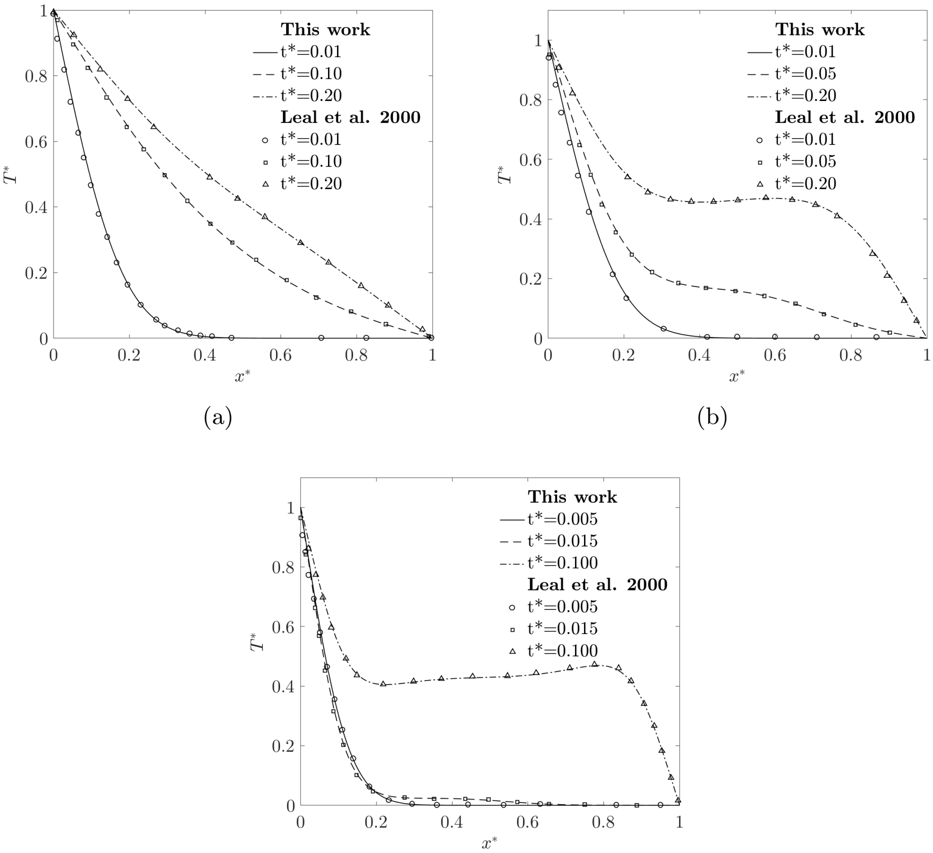

(a)

(b)

(c)

Figure 2.8: *Comparison of dimensionless temperature in the horizontal mid-plane for (a)* $Ra = 10^3$*, (b)* $Ra = 10^4$ *and (c)* $Ra = 10^5$*.*

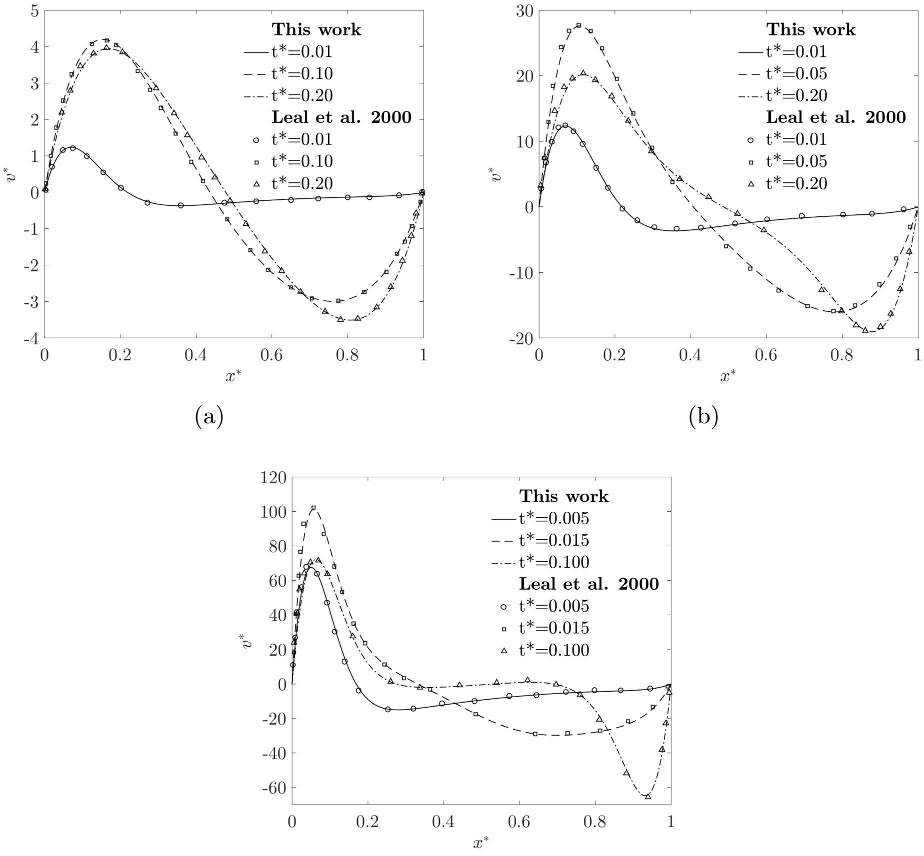

(a) (b)

(c)

Figure 2.9: *Comparison of dimensionless vertical velocity in the horizontal mid-plane for (a) $Ra = 10^3$, (b) $Ra = 10^4$ and (c) $Ra = 10^5$.*

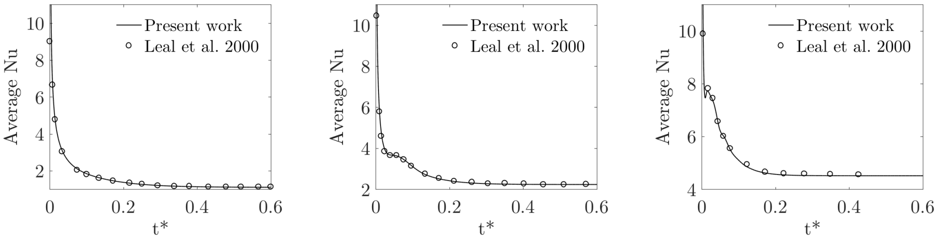

(a) (b) (c)

Figure 2.10: *Comparison of average Nusselt number in the hot wall over time for (a) $Ra = 10^3$, (b) $Ra = 10^4$ and (c) $Ra = 10^5$.*

where δ is the initial jet width opening, U_1 and U_2 are the mean inlet velocities for the jet and the coflow, respectively. P_0 stands for the mean pressure; and $\mathrm{Re} = \rho\Delta U_0\delta/\mu$ corresponds to the Reynolds number based on the initial jet width in which $\Delta U_0 = U_1 - U_2$. The jet spreading rate $y_{1/2}(x)$ is defined as the distance from the jet centerline at which the mean velocity corrected by the coflow velocity is half of the value at the jet centerline.
Mean profiles of the excess streamwise velocity ($\{U_e\} = \{u\} - U_2$) and the cross-stream velocity $\{v\}$ adimensionalized by the excess centerline velocity $\Delta\{U_c\} = \{U_c\} - U_2$ against $y/y_{1/2}$ become self-similar, that is, they collapse onto a single curve as long as the jet is developed. Fig. 2.11(a) and 2.11(b) show that velocity profiles at $x = 25\delta$ are in very good agreement with self-similar profiles from experimental (Gutmark and Wygnanski (1976)) and numerical (Stanley et al. (2002)) studies.

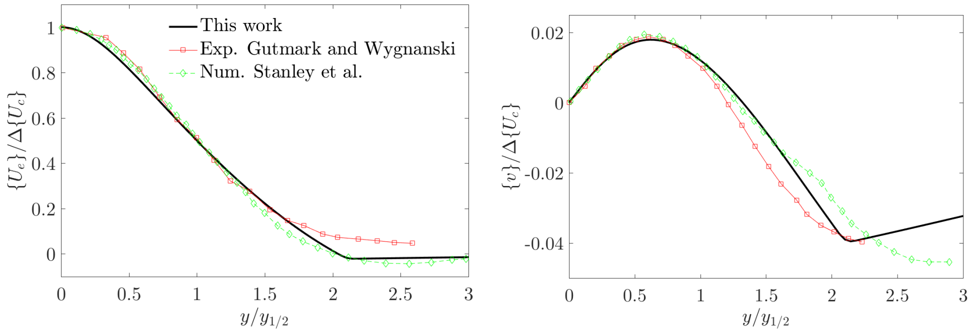

(a) (b)

Figure 2.11: *Self-similar profiles of (a) streamwise and (b) cross-stream velocities of the isothermal plane jet at $x = 25\delta$.*

Verification of the results is also performed by comparing the coefficients $K_{1,u}$, $K_{2,u}$, $C_{1,u}$ and $C_{2,u}$ from the linear fitting of the jet growth

$$\frac{y_{1/2}}{\delta} = K_{1,u}\left(\frac{x}{\delta} + K_{2,u}\right), \tag{2.39}$$

and the centerline velocity decay

$$\left(\frac{\Delta U_0}{\Delta\{U_c\}}\right)^2 = C_{1,u}\left(\frac{x}{\delta} + C_{2,u}\right), \tag{2.40}$$

Figure 2.12(a) presents the results of the growth of the jet half-width $y_{1/2}(x)$ along the streamwise coordinate. Additionally, the mean excess velocity decay $(\Delta U_0/\Delta\{U_c\})^2$ along the jet centerline is presented in Fig. 2.12(b). A linear regression in the zone $10\delta < x < 25\delta$ is shown. Also the experimental results from the work of Thomas and Chu (1989) are also presented for comparison.
The linear fitting coefficients in the zone $10\delta < x < 25\delta$ are summarized in Table 2.12 along with some experimental (Jenkins and Goldschmidt (1973);

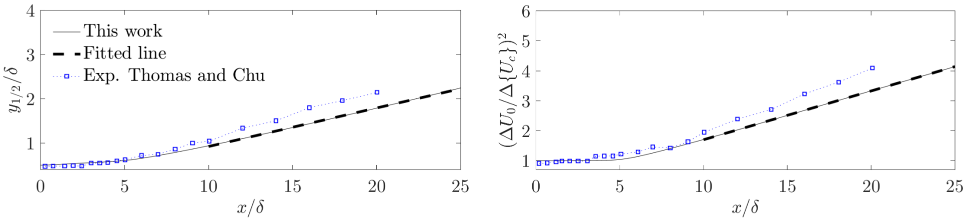

(a) (b)

Figure 2.12: *Comparison of the present RANS results for an isothermal plane jet with the experimental work of Thomas and Chu (1989): downstream evolution of (a) spread rate and (b) velocity decay.*

Goldschmidt and Young (1975); Gutmark and Wygnanski (1976); Thomas and Chu (1989)) and DNS (Stanley et al. (2002)) results. The results of the virtual origins ($K_{2,u}$ and $C_{2,u}$) differ among the referred works since they have a strong dependency on the inflow conditions (Stanley and Sarkar (2000); Klein et al. (2003)). However, the predicted slope coefficients ($K_{1,u}$ and $C_{1,u}$) compare generally well with previous results.

Table 2.12: *Comparison of the jet growth rate and the centerline velocity decay rate at the self-similar region between the current RANS results and some experimental and numerical reference values.*

	$K_{1,u}$	$K_{2,u}$	$C_{1,u}$	$C_{2,u}$
Jenkins and Goldschmidt (1973)	0.088	-4.5	0.160	4.0
Gutmark and Wygnanski (1976)	0.100	-2.00	0.189	-4.72
Goldschmidt and Young (1975)	0.0875	-8.75	0.150	-1.25
Thomas and Chu (1989)	0.110	0.14	0.220	-1.19
Stanley et al. (2002)	0.092	2.63	0.201	1.23
Current RANS results	0.0871	0.5646	0.1629	0.4291

To sum up, results obtained using RANS of cross-section profiles of velocity shown in Fig. 2.11, and the rates of jet spread and velocity decay compares reasonable well with previous experimental and numerical works.

2.4 Conclusions

This Chapter details the implementation of the variable-density $k-\epsilon$ and $k-\omega$ turbulent viscosity models in the ConDiRa (CONvection, DIfusion and RAdiation) RANS code.
The numerical discretization of the governing equations has been done following the Finite Volume Method and using high-order schemes in a Total Variation Diminishing (TVD) formulation keeping a reasonable accuracy and preventing instabilities during the iteration process.

In order to assess the accuracy of the implemented high-order schemes, results of pure convection in a diagonal flow problem, using a set of different high-order schemes, are discussed. Then, the laminar convection part of the code and the energy transport are checked computing natural convection in a square cavity for a set of conditions. Finally, an isothermal turbulent plane jet of water vapor discharging into a parallel low speed coflow of water vapor is computed to test the RANS implementation.

Chapter 3

Thermal Radiation Heat Transfer

In this Chapter, the fundamental concepts regarding thermal radiative transfer in participating media are introduced. Moreover, a detail description of the numerical tools used to solve the radiative problem is provided. Finally, the methods employed to carry out the couple DNS/Monte-Carlo and the RANS/Monte-Carlo coupling are described.

Contents

3.1 Introduction to thermal radiation

Thermal radiative transfer is the third mode of heat transfer in addition to convection and conduction energy transport modes. Thermal radiation occurs in the form of traveling electromagnetic waves principally in the infrared region. In contrast with convection and conduction which are described by local energy balances, radiation is characterized by long distance interactions among the

entire domain of study. Thus, the whole enclosure needs to be considered simultaneously in the radiation problem.
The radiation problem is further complicated by its directional and spectral dependency nature. Then, to describe the radiative heat flux, the spectral radiative intensity $I_\nu(\vec{x}, \vec{s})$ is defined as the radiative energy flow per unit solid angle and unit area normal to the direction $\vec{s}$ at a given wavenumber ν and at point $\vec{x}$. The equation governing the spectral intensity field inside a medium that emits, absorbs, and scatters radiation is the so called Radiative Transfer Equation (RTE). Omitting the time dependency and assuming local thermodynamic equilibrium, the RTE is expressed as

$$\frac{dI_\nu(\vec{x}, \vec{s})}{ds} = + \underbrace{\kappa_\nu(\vec{x}) I_{b\nu}(\vec{x})}_{\text{emission}} - \underbrace{\beta_\nu(\vec{x}) I_\nu(\vec{x}, \vec{s})}_{\text{absorption}} + \underbrace{\frac{\sigma_\nu(\vec{x})}{4\pi} \int_{4\pi} I_\nu(\vec{x}, \vec{s'}) \phi(\vec{s'}, \vec{s}) d\Omega'}_{\text{scattering}}, \tag{3.1}$$

which describes the change in intensity by emission, absorption and scattering along a line of sight into the direction $\vec{s}$. κ_ν, β_ν and σ_ν stand respectively for the absorption, extinction and scattering spectral coefficients. Vector $\vec{s'}$ represents all possible incoming directions towards position $\vec{x}$, while $\phi(\vec{s'}, \vec{s})$ is the scattering phase function that describes the probability that a ray coming from direction $\vec{s'}$ confined in the solid angle $d\Omega'$ scatters into the direction $\vec{s}$. Finally, $I_{b\nu}$ is the equilibrium spectral blackbody emitted intensity given by the Planck's law as

$$I_{b\nu} = \frac{2\pi h^{\text{planck}} c_0^2 \nu^3}{n^2 \left(e^{h^{\text{planck}} \nu / k_b T)} - 1 \right)}, \tag{3.2}$$

where h^{planck} is the Planck's constant, c_0 is the speed of light in vacuum, n is the refractive index and k_b is the Boltzmann's constant.
Assuming a non-scattering medium, the RTE can be simplified to

$$\frac{dI_\nu(\vec{x}, \vec{s})}{ds} = \kappa_\nu(\vec{x}) \left(I_{b\nu}(\vec{x}) - I_\nu(\vec{x}, \vec{s}) \right). \tag{3.3}$$

Once the spectral intensity field is known, the quantity of interest to couple convection and radiation modes of heat transfer is the volumetric radiative power P_{rad}, which acts as a source term in the Energy Transport Equation (Eq. 1.3) defined in Chapter 1. The radiative power is a balance over all the wavenumber spectrum between the power lost by radiative emission P_e, and the gained power due to absorption from all incoming directions P_a, that is

$$P_{rad} = \int_\nu \left(\kappa_\nu \int_{4\pi} I_\nu d\Omega - 4\pi \kappa_\nu I_{b\nu} \right) d\nu = \underbrace{\int_\nu \left(\kappa_\nu \int_{4\pi} I_\nu d\Omega \right) d\nu}_{P_a} - \underbrace{4\pi \int_\nu \kappa_\nu I_{b\nu} d\nu}_{P_e}.$$

(3.4)

To accurately obtain the volumetric radiative power from three-dimensional enclosures with variable temperature and species concentration fields is a complex task. The problem is further complicated if the dependency of κ_ν on the temperature, species concentration and wavenumber is taken into account. This is probably why several numerical models to solve the RTE as well as to account for detailed radiative properties have been developed during the last decades. The next section summarized those methods and highlights the main features of the ones used in this work.

3.2 Numerical methods to solve the radiative problem

Hardly any analytical solution of the RTE exists except for very simple cases such as the one-dimensional gray media problem. In the vast majority of research and industrial applications involving thermal radiation, numerical methods are used to solve the RTE.

The most common numerical methods to handle the RTE include the Spherical Harmonics Approximation (Evans (1998)), Discrete Ordinates (Fiveland (1984)) and Monte-Carlo (Howell (1998)) methods among others. The interest of using a specific method is often driven for the particularities of the problem and normally becomes a trade-off between accuracy and computational cost. A detailed description of these methods is beyond the scope of this section; instead, the main characteristics of the two methods employed in this work are highlighted.

On the one hand, the Monte-Carlo method is used in this work to take advantage of its capabilities to solve the RTE with detailed spectral radiative properties with a relatively low additional computational cost. Also, the use of the Monte-Carlo is justified since it provides a control of the convergence which determines the statistical error of the solution. Then, the Monte-Carlo method is employed within the thesis objectives of generating a high-fidelity database to quantify TRI and to set the modeling bases for free jets coupled with thermal radiation.

On the other hand, a DOM method has been implemented from scratch during the developing of this thesis. The principal motivation, just as for the implementation of the RANS, is to compare accuracy between simplified models and high-fidelity data. In this sense, the DOM implementation opens the way to further simulations using simplified radiation models to couple heated jets in order to quantify its accuracy by comparison with high-fidelity data. The DOM implementation is verified in Appendix E, further simulations using DOM are the subject of future works.

3.2.1 Discrete Ordinates Method

The Discrete Ordinates Method (DOM) uses numerical quadratures in order to integrate over directions. Then, any function $f(\vec{s})$ dependent on direction $\vec{s}$ can be integrated over the total solid angle range as

$$\int_{4\pi} f(\vec{s}) d\Omega \approx \sum_{k=1}^{M} W_k f(\Omega_k) \tag{3.5}$$

where M is the total number of discrete directions Ω_k, and W_k corresponds to the weight associated to each direction. Each specific quadrature defines its own discrete directions and its associated weight. Thus, the angular discretization substitutes the RTE for a set of M discrete equations, one for each discrete direction. Once the RTE is angularly discretized, it is further numerically integrated over the entire domain by means of a spatial discretization. In the present work, the finite volume method is used. In order to verify the implementation of the DOM, the numerical solution of combined heat transfer by radiation and natural convection in a square cavity filled with an absorbing-emitting and isotropic scattering medium has been verified with the numerical works of Yücel et al. (1989); Lari et al. (2011); Moufekkir et al. (2012). More details of the present DOM implementation and its verification can be found in Appendix E.

3.2.2 Monte-Carlo Method

The Monte-Carlo method consists in tracing a statistically meaningful number of photons from their points of emission to their points of absorption. This family of methods is known to provide benchmark results for the RTE, since it is suitable for complex radiative properties and the desired accuracy can be arbitrarily chosen. This method is used in the present work taking advantage of the in-house code Rainier which is described in the following section.

3.3 General description of the Rainier code

Rainier is an in-house code developed at EM2C laboratory (Zhang (2011); Refahi (2013); Zhang (2013); Koren (2016); Rodrigues (2018)). The Monte-Carlo method is optimized by using an Emission-based Reciprocity Method (ERM). In the ERM, only the bundles leaving a specific node are needed to estimate the local radiative power at this specific node. It is therefore possible to estimate the radiative power at one node without performing such estimation at all other nodes of the domain.

Moreover, a randomized Quasi Monte Carlo (QMC) (Lemieux (2008)) relying on low-discrepancy Sobol sequences (Joe and Kuo (2008)) that replace the pseudo-random number generator to accelerate the calculation is already implemented in Rainier (Palluotto et al. (2017)) and it is used in this work.

Rainier can also handle complex geometries since it uses unstructured meshes. Its scalability has been tested using up to 1920 processors with excellent results (Rodrigues (2018)). Despite three-dimensional radiative calculations with spectral radiative properties are computationally expensive, ERM is an efficient solver for this problem when compared with other deterministic solvers such as the Discrete Ordinates Method (DOM).
A description of the ERM used to solve the RTE, along with a brief explanation of the ck model to account for the detailed radiative properties of water vapor are provided in the following subsections.

3.3.1 Emission-based Reciprocity Monte-Carlo Method

The quantity of interest is the radiative power at a specific node i, denoted here as P_i^{rad}. It is computed as the sum of the exchanged radiative power $P_{i,j}^{exch}$ between i and all the other cells j of the domain, i.e.,

$$P_i^{rad} = \sum_j P_{ij}^{exch}. \tag{3.6}$$

Following the reciprocity principle, the Emission-based Reciprocity Method computes P_i^{rad} based on a large sample of rays (N_q) issued form node i exchanging energy with all cells (M_n) that the ray crosses before being absorbed or before it leaves the domain. The expression to compute the volumetric radiative power of a cell i writes:

$$P_i^{rad} = \frac{P_i^e}{N_q} \sum_{n=1}^{N_q} \sum_{m=1}^{M_n} \left[\frac{I_{b\nu_n}(T_m)}{I_{b\nu_n}(T_i)} - 1 \right] \tau_{\nu_n}(BF_m)\alpha_{n,m,\nu_n} \tag{3.7}$$

in which:

- $I_{b\nu}$ is the spectral blackbody emitted intensity described above in Eq. 3.2.
- P_i^e is the emitted power overall the wavenumber ν:

  $$P_i^e = 4\pi \int_\nu \kappa_\nu I_{b\nu}(T_i) d\nu, \tag{3.8}$$

- α_{n,m,ν_n} is the spectral absorptivity of the n^{th} ray in the m^{th} cell crossing. It is defined as

  $$\alpha_{n,m,\nu_n} = 1 - e^{-\kappa_\nu(T_m) l_{n,m}} \tag{3.9}$$

  where $l_{n,m}$ is the length that ray n goes across within cell m.
- $\tau_{\nu_n}(BF_m)$ is the spectral transmissivity associated with a given ray path from the source point B to the inlet point F_m in cell m. It corresponds

to 1 in the source point B and its value decays along the ray path due to absorption following the expression

$$\tau_{\nu_n}(BF_m) = \prod_{m=1}^{M_n} (1 - \alpha_{n,m,\nu_n}), \tag{3.10}$$

note that, in enclosed domains, it also includes wall reflexions.

The statistical behaviour of the computation is based on three Probability Density Functions (PDF): two to determine the direction (characterized by the azimuthal angle ϕ and the polar angle θ), and another to determine the wavenumber of the emitted ray, ν. Then, for each ray, three pseudo-random numbers need to be generated for the Monte-Carlo method, or equivalently a three-dimensional Sobol sequence is built for the randomized QMC. Optimized versions of the ERM - OERM (Zhang et al. (2012)) and OERM2 (Rodrigues (2018)) - can be derived by enhancing the PDF associated to the wavenumber. These optimized methods are both available in Rainier.

3.3.2 Detailed radiative properties

In Rainier, the spectral radiative properties for CO_2 and H_2O are modeled by means of the correlated-k (ck) narrow band model (Riviere et al. (1992); Goody and Yung (1995); Taine and Soufiani (1999)). Such a level of description is deemed very accurate for the targeted coupled simulations compared to Weighted-Sum-of-Gray-Gases (WSGG) global models or notoriously wrong gray-gas assumptions. This allows to capture as accurately as possible the detailed radiative transfer in the coupled simulation of the heated plane jet mixing.

The ck approach belongs to the more general kind of narrow band models (NB). In general, these NB models consist in discretizing the spectrum in intervals small enough such that $I_{b\nu}$ can be considered uniform in each narrow band. The absorption coefficient κ_ν remains however quite dynamic with rapid variations in the spectral bands. Simply averaging κ_ν yields erroneous results.

The key point of the ck approach is the way it handles the integration over a narrow band, on each narrow band $\Delta\nu$, the absorption coefficient is reordered by increasing values in a monotonic function $k(g)$, where g is a cumulative distribution function. In the Rainier implmentation, g can be understood as a dimensionless wavenumber (normalized by $\Delta\nu$) which takes values form 0 to 1. And, k goes from the minimal absorption coefficient value inside $\Delta\nu$ until its maximum value. Then, $k(0) = \kappa_{min}^{\Delta\nu}$ while $k(1) = \kappa_{max}^{\Delta\nu}$.

In the ck model, the spectral transmissivity of a homogeneous isothermal gas layer of thickness l (defined as $\tau_\nu = e^{-\kappa_\nu l}$) is computed as the averaged transmissivity over the band $\Delta\nu$ by numerical integration over the narrow band. The ck method implemented in Rainier uses Gaussian quadrature of order 7, then the averaged transmissivity over the band $\Delta\nu$ is computed as

$$\bar{\tau}^{\Delta\nu} = \sum_{i=1}^{7} \omega_i e^{-k_i l}, \tag{3.11}$$

where ω_i is the quadrature weight, and k_i is the reordered absorption coefficient evaluated at the quadrature point $k(g_i)$. Rainier follows the work of Soufiani and Taine (1997) to compute the reordered absorption coefficients k_i. For the case of pure H_2O, which is here the present case, the reordered absorption coefficients are computed as:

$$k_i = \frac{X_{H_2O}\ p\ k_i^*}{Q(T)\ T}, \tag{3.12}$$

where X_{H_2O} is the molar fraction of X_{H_2O}, p is the partial pressure of H_2O, T is the temperature and $Q(T)$ is a function that depends solely on temperature described in the work of Gamache et al. (1990). And, k_i^* are the parameters of the ck model, the ones used in Rainier are based on updated parameters of Rivière and Soufiani (2012). These parameters are tabulated by 16 temperatures, 5 molar fraction of H_2O, 44 narrow bands for H_2O with widths varying from 50 cm^{-1} to 400 cm^{-1}, and 7 Gauss-Lobatto quadrature points per band (g_i). Those parameters are generated for atmospheric pressure and for a temperature range between 300 and 4000 K. The accuracy of the ck model is further discussed in Chapter 6.

3.4 Coupling turbulence with thermal radiation

Since turbulence and thermal radiation have strong differences on their nature, each phenomenon has its own dedicated and optimized solver. The coupling method is the responsible to exchange the data needed for each solver, it should avoid instabilities on the solutions, be precise and minimize computer memory and CPU requirements.
The main difference between the implementation of the couple DNS/Monte-Carlo with respect to the RANS/Monte-Carlo coupling is that the former uses parallel coupling, meaning that both codes run simultaneously; while the latter uses a staggered scheme in which one code runs after the other. The main characteristics chosen for each coupling method are detailed in the next two sections.

3.4.1 Coupling thermal radiation with the DNS solver

Memory and time processing requirements should be carefully optimized when coupling the DNS and Monte-Carlo solvers. In this subsection, a discussion is provided regarding the main choices for such a coupling, which are the mesh for each solver, how data traffic is managed and how the load between parallel processors is distributed.

3.4.1.1 Fluid flow and Radiation Meshes

A first option is to compute both solvers on the same computational mesh. Despite the fact that it simplifies the task of coupling, this option does not take into account the specific requirements of each solver. While the flow field mesh should be more refined on velocity gradients, the radiative calculation are mainly sensitive to temperature and composition gradients. In DNS coupled simulations, the single-mesh option is rather out of reach because of the memory needed in the RTE solver. While a decomposition domain is performed in the fluid flow solver, the RTE solver needs information over all the domain to solve a single mesh node; thus, each processor needs to store the whole mesh.

However, considering separated meshes involves interpolation between them on each coupling iteration. These interpolations may lead to accumulating errors which reduces the accuracy of the coupling. Additionally, using two different meshes requires more CPU time to perform the interpolations and supplementary computer memory to store the extra mesh.

The retained approach in this study is to define the radiative mesh from the flow field mesh. On doing that, the radiative mesh cells are compounded of a certain number of flow field cells, and nodes form the radiative mesh are superposed to nodes from the flow field grid. That way, the interpolation scheme is very fast and the difficulties associated with the domain decomposition of the flow field can be directly managed. The only drawback is that the radiative mesh is limited to the topology of the flow field mesh. In the work of Zhang et al. (2013) this same approach is used and a discussion of it can be found in the study of Badinand and Fransson (2001).

3.4.1.2 Data exchange

All exchanged data between the two codes is handled by a direct Message Passing Interface (MPI) implementation. This method consists in dividing the total number of processors among the two codes while an extra processor is reserved to act as *coupler*. On each code, a structure *master/slaves* is implemented in a way that all communications are handled by MPI commands between the *master* of each code and the *coupler*. An schematic of the direct MPI approach is detailed on Fig. 3.1. On each couple iteration, the *master* of the fluid solver receives the radiative power (P_{rad}) from the *coupler*, and scatters it on each processor working in the fluid solver. After N_f iterations, the fluid solver computes a temperature field which needs to be gathered on the *master* of the fluid solver in order to be sent to the *coupler* (on a multi-specie simulation, concentration fields are also necessary). Once the *coupler* receives the temperature field, it is reordered so it can be sent to the radiative solver *master*. The RTE solver computes the P_{rad} for this specific temperature field, and is further sent to the *coupler* in order to restart the whole process. The main advantage of the direct MPI coupling method is that all elements on the process of coupling are controlled and can then be tested and optimized. This method is limited for the *coupler* processor which for large meshes can be inefficient. The current implementation has been carried out ensuring that the time spent on MPI communications (denoted as MPI time in Fig 3.1) is less than 0.5 % of the CPU time on every processor (except the *coupler* processor).

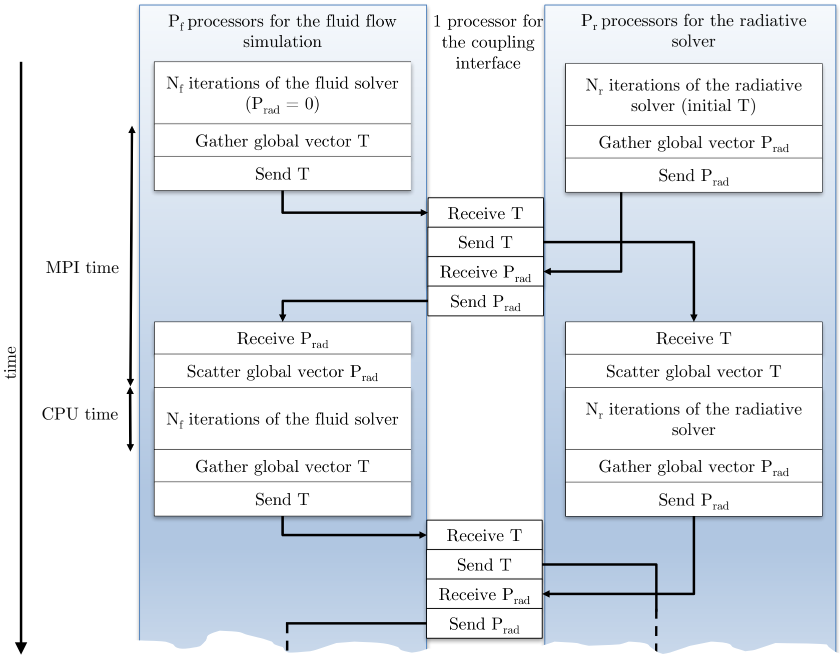

Figure 3.1: *Scheme for the coupling thermal radiation with the DNS solver using a parallel coupling method.*

3.4.1.3 Synchronization in CPU time

The time step of the fluid flow solver Δt_f has to be small enough to capture the acoustic (or pseudo-acoustic) waves crossing the domain without triggering any numerical instability. However, the radiative power field evolves along with the temperature field whose typical time scale is one or two orders smaller than the acoustic one in low-Mach number flows. Then, the radiative power field does not need to be updated after every fluid flow time step. Instead, it is updated every n_{cpl} iterations of the fluid flow solver. Consequently, the coupling period is defined by $\Delta t_{cpl} = n_{cpl}\Delta t_f$. To determine the optimal coupling parameter n_{cpl}, let us define the Euclidean norm of the difference between the radiative power in an iteration i, set as a reference (P^i_{rad}), with respect to the radiative power after N iterations (P^{i+N}_{rad}), that is

$$||P^{i+N}_{rad} - P^i_{rad}||_2 = \sqrt{\sum_{\vec{x}\epsilon\mathcal{D}} \left(P^{i+N}_{rad}(\vec{x}) - P^i_{rad}(\vec{x})\right)^2}, \tag{3.13}$$

where $\mathcal{D}$ is the computational domain. From the evolution of $||P^{i+N}_{rad} - P^i_{rad}||_2$ by increasing N, the error of coupling between N time steps of the fluid flow can be estimated. Then, n_{cpl} can be chosen based on the error estimated by the Euclidean norm of the difference between P^i_{rad} with respect to $P^{i+n_{cpl}}_{rad}$. Finally, the number of processors dedicated to each code should be set in order to minimize the time spent on waiting for MPI communications following the relations:

$$P_f \backsimeq \frac{P_{tot} T_f}{T_r/n_{cpl} + T_f} \quad \text{and} \quad P_r = P_{tot} - P_f - 1, \tag{3.14}$$

where T_f and T_r are the cpu time spent by one processor to compute one iteration on the fluid and the radiative solvers, respectively. P_{tot}, P_f and P_r are the total number of processors, and the number of processors dedicated to the fluid and radiative solvers, respectively. Note that ideal scalability is assumed in order to derive Eq. (3.14), i.e., T_f and T_r are inversely proportion to P_f and P_r, respectively.

3.4.2 Coupling thermal radiation with the RANS solver

Two-dimensional RANS computations are light when compared with the three-dimensional DNS and there is no need for the complexity that a parallel coupling implies. Then, a staggered scheme described in Fig. 3.2 is implemented to handle the coupling between the thermal radiation and RANS solvers. In this scheme, a RANS simulation is first carried out imposing a null radiative power field. Once the RANS steady state solution is converged, the average temperature field is further read from the Monte-Carlo solver which computes the corresponding radiative power field. Then, RANS solver computes again the steady state average temperature field, but this time accounting for the previously estimated radiative power. This process is repeat until P_{rad} differences before and after the Monte-Carlo solver are lower than a fixed tolerance ϵ. The RANS and Monte-Carlo solvers use exactly the same mesh since this option provides accuracy and it is affordable in terms of computational cost.

As already explained in Chapter 2, RANS solutions provide only the averaged flow fields, being that fluctuations of temperature are not solved. Unfortunately, those fluctuations may affect the radiation field since the emission of radiation ($I_{b\nu}$) and the radiative power are highly non-linear functions of temperature

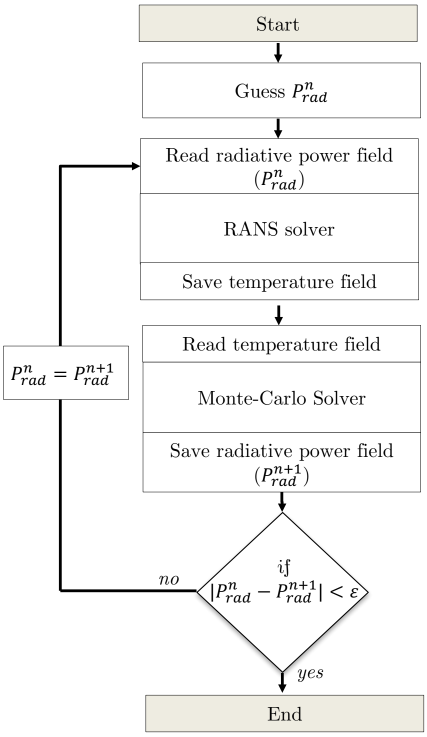

Figure 3.2: *Scheme for the coupling thermal radiation with the RANS solver using a coupling staggered method.*

and species concentration. The effects that fluctuations of temperature (and species concentration in a multi-species problem) cause in radiation are commonly called turbulent radiation interaction (TRI). A brief description of such interactions in the RANS framework is provided below.

Turbulence radiation interactions

When solving the radiation problem in the RANS context, the averaged form of the RTE is actually used, which for a non-scattering medium writes

$$\frac{d\langle I_\nu\rangle}{ds} = -\langle \kappa_\nu I_\nu\rangle + \langle \kappa_\nu I_{b\nu}\rangle. \tag{3.15}$$

Averaged emission $\langle \kappa_\nu I_{b\nu}\rangle$ and averaged absorption $\langle \kappa_\nu I_\nu\rangle$ are unclosed terms since their direct computation from averaged temperature and species concentration values, provided by the RANS solver, are not necessarily equal than its computation from instantaneous values. The complete expressions for the averaged emission and averaged absorption are

$$\langle \kappa_\nu I_{b\nu} \rangle = \langle \kappa_\nu \rangle \, \langle I_{b\nu} \rangle + \langle \kappa'_\nu I'_{b\nu} \rangle, \tag{3.16}$$

$$\langle \kappa_\nu I_\nu \rangle = \langle \kappa_\nu \rangle \, \langle I_\nu \rangle + \langle \kappa'_\nu I'_\nu \rangle, \tag{3.17}$$

In this work the global TRI effects on the radiative power P_{rad}^{TRI} are quantified as

$$P_{rad}^{TRI} = \langle P_{rad} \rangle - P_{rad}(\langle T \rangle) \tag{3.18}$$

where $\langle P_{rad} \rangle$ is the averaged radiative power from the coupled simulation and $P_{rad}(\langle T \rangle)$ corresponds to the radiative power computed from the averaged temperature field. Likewise, emission and absorption TRI powers are respectively defined by

$$P_e^{TRI} = \langle P_e \rangle - P_e(\langle T \rangle), \tag{3.19}$$

and

$$P_a^{TRI} = \langle P_a \rangle - P_a(\langle T \rangle), \tag{3.20}$$

where

$$P_e(\langle T \rangle) = 4\pi \int_\nu \kappa_\nu(\langle T \rangle) I_{b\nu}(\langle T \rangle) d\nu. \tag{3.21}$$

Most of the efforts in TRI modeling are dedicated to model the effects that fluctuations cause on the emission TRI while absorption TRI is usually not considered. This approach is supported by early works of Kabashnikov and Kmit (1979); Kabashnikov (1985) who show that, for moderate optical thicknesses, the fluctuations of the radiative intensity are mainly caused by distant points. Thus, the correlation between the spectral intensity and the local absorption coefficient is negligible, this consideration is the so-called optically thin fluctuation approximation (OTFA), that is

$$\langle \kappa_\nu I_\nu \rangle \approx \langle \kappa_\nu \rangle \, \langle I_\nu \rangle, \tag{3.22}$$

In that case, emission TRI can be easily accounted for since it fully depends on local values of temperature, pressure and species concentration. Mignon and coworkers (Mignon (1992); Soufiani et al. (1990a); Soufiani et al. (1990b)) proposed an attempt to closed the TRI problem by invoking the OTFA and assuming negligible radiative property fluctuations, then the averaged RTE writes:

$$\frac{d\langle I_\nu\rangle}{ds} = -\langle\kappa_\nu\rangle\ \langle I_\nu\rangle + \langle\kappa_\nu\rangle\ \langle I_{b\nu}\rangle, \tag{3.23}$$

followed by a development of the Plank function in series of order n around $\langle T\rangle$ of the form:

$$I_{b\nu}(T) = I_{b\nu}(\langle T\rangle + T') = \sum_{l=0}^{n} \frac{1}{l!} T' \frac{\partial^l I_{b\nu}}{\partial T^l}(\langle T\rangle). \tag{3.24}$$

Further extension of the development in Taylor series comprises the work of Snegirev (2004) who consider that the absorption coefficient depend solely on temperature and thus can be expressed:

$$\kappa_\nu(T) = \kappa_\nu(\langle T\rangle + T') = \sum_{l=0}^{n} \frac{1}{l!} T' \frac{\partial^l \kappa_\nu}{\partial T^l}(\langle T\rangle). \tag{3.25}$$

Doing some algebra and neglecting correlations higher than two yields:

$$\langle\kappa_\nu(T) I_{b\nu}(T)\rangle \approx \kappa_\nu(\langle T\rangle) I_{b\nu}(\langle T\rangle) \left(1 + 6\frac{\langle T'^2\rangle}{\langle T\rangle^2} + 4\frac{\langle T'^2\rangle}{\langle\kappa\rangle\langle T\rangle}\frac{\partial\kappa_\nu}{\partial T}(\langle T\rangle)\right). \tag{3.26}$$

Additional equations for the temperature variance are then required to close this model.
A more exact model to compute the terms $\langle\kappa_\nu(T) I_{b\nu}(T)\rangle$, and $\langle\kappa_\nu(T, Y_k)\rangle$ depending on species concentration is through Probability Density Functions (PDF). Either using presumed PDF shape models (Gore et al. (1992)) or transport PDF based methods (Coelho (2012); Coelho (2010); Li and Modest (2002)), it can be written:

$$\langle\kappa_\nu\rangle = \int_0^1 \kappa_\nu\left(T(z), Y_k(z)\right) \mathrm{PDF}(z) dz, \tag{3.27}$$

$$\langle\kappa_\nu I_{b\nu}\rangle = \int_0^1 \kappa_\nu\left(T(z), Y_k(z)\right)\ I_{b\nu}\left(T(z)\right)\ \mathrm{PDF}(z) dz, \tag{3.28}$$

where z is the mixture fraction which allows the direct determination of the temperature and the species concentration in the combustion framework. In the work of Burns (1999), a number of β PDF functions were studied concluding that the self-correlation of temperature ($\langle T^4\rangle/\langle T\rangle^4$) was weakly sensitive to the shape of the PDF.

Accounting for absorption TRI is much more complicated since it depends on the instantaneous solution of the whole domain. Optically thick and high turbulent flows compromise the validity of the OTFA. Thus, some attempts to address the modelling of the absorption TRI have been carry out. In the work of Tessé et al. (2004) the full effects of TRI are accounted for in a turbulent sooty flame. In order to model absorption and emission TRI a three-dimensional PDF comprising (i) the reaction progress variable, (ii) the mixture ratio and (iii) the soot volume fraction is considered together with a photon Monte Carlo Method to solve the RTE. To generate the joint PDF, they used a Lagrangian method applied to an a priori solution of the flow using a k-ϵ RANS solver. Their calculations relied on the assumptions that each turbulent structure (based on the turbulent integral lenght scale) is homogeneous and isothermal, so they can associate a single PDF on each "turbulent structure" rather than on each node of the mesh. Such an assumption is an estimation to account for the spatial correlation of the random variables composing the PDF.

Another approach, presented by Mehta and Modest (2006), for the modeling of the absorption TRI is based on the idea that in the parts of the spectrum that are optically thick, the diffusion approximation $q_{\nu,diff} = -\frac{1}{3\kappa_\nu}\nabla(4\pi I_{b\nu})$ can be applied assuming a non-scattering medium in the optically thick limit. In the other parts of the absorption coefficient, the OTFA is considered. This method could apply for turbulent sooty flame. However, there are some parts of the spectrum where the medium is neither optically thin nor in the thick limit.

The works of Coelho (2012); Coelho (2010) present an attempt to model the absorption TRI in a combustion framework through the mixture fraction (z). They use a two-dimensional clipped Gaussian joint probability density function of z and radiation intensity I_ν of the form:

$$\langle \kappa_\nu I_\nu\rangle = \int_0^\infty \int_0^1 \kappa_\nu\left(T(z), Y_k(z)\right)\ I_\nu\ \mathrm{PDF}(z, I_\nu)\ dz dI_\nu. \tag{3.29}$$

In order to compute the joint PDF(z, I_ν), two additional equations are needed to determine the variance of I_ν and the correlation coefficient between z and I_ν.

Additionally, a photon Monte Carlo approach to model absorption and emission TRI is proposed by Wang et al. (2008). Their approach uses a Particle Monte Carlo Method (Pope (1985)) to compute a composite PDF in which only species concentration and enthalpy are treated as random variables. Then, the only assumption made is that the instantaneous particle field in the PDF method represents an actual snapshot of the real turbulent flow field. Once the scalar fields are set, a Photon Monte Carlo (PMC) method able to compute the RTE in a media represented by particles is used to take into account the TRI effect of unresolved fluctuations. The details of such PMC method are detailed in the work of Wang and Modest (2006) in which different absorption models are proposed. Further application of this procedure in sooting flames can be found in the works of Mehta et al. (2010); Mehta et al. (2010).

3.5 Conclusions

In this Chapter the numerical tools used to solve the radiative problem and the methods employed to carry out the coupling between radiation and convection have been described.

The retained method to solve the RTE is the emission-based reciprocity Monte-Carlo (ERM) method. The spectral radiative properties are modeled by means of the ck model. The Monte-Carlo method is used in this work to take advantage of its capabilities to solve the RTE with detailed spectral radiative properties with a relatively low additional computational cost when compared with deterministic methods such as the Discrete Ordinates Method (DOM). Also, the use of the Monte-Carlo allows for controlling the computation error determined as the standard deviation of the Monte-Carlo statistical estimate.

Two coupling procedures are developed in this thesis, which are the coupled DNS/Monte-Carlo and the RANS/Monte-Carlo. The main difference between them is that the DNS/Monte-Carlo uses parallel coupling, meaning that both codes run simultaneously; while the RANS/Monte-Carlo uses a staggered scheme in which one code runs after the other.

In DNS/Monte-Carlo coupling, the memory and time processing requirements should be carefully optimized when coupling the solvers. A discussion has been provided regarding the main choices for such a coupling, which are the mesh for each solver, how data traffic is managed and how the load between parallel processors is distributed.

The implementation of the RANS/Monte-Carlo coupling is somewhat simpler. However, unclosed terms rise when computing the average radiative power from mean temperature fields, these terms are called emission and abosprtion TRI. A discussion regarding the modeling of these unclosed terms is provided, which highlights that most of the efforts in TRI modeling are dedicated to model the effects that fluctuations cause on the emission TRI; while absorption TRI is usually not considered due to its dependency on instantaneous solution from the whole domain.

Part II

Numerical setup dimensioning and validation of uncoupled simulations

Chapter 4

Dimensioning of plane jet cases based on Reynolds Average Navier-Stokes Solutions

The dimensioning of two different heated jets is here performed based on RANS computations coupled with the Monte-Carlo solver to account for the radiative heat transfer. The dimensioning envisages to determine the role of radiation on the energy balance equation. The setup for the RANS solutions as well as for the radiative solver is detailed. The influence of the main physical parameters of the jet on the role of radiation is discussed. Finally, a parametric study of the two desired jets is presented, and the choice of the retained setups is justified.

Contents

4.1 Introduction

The subject of this Chapter is to determine the setup to achieve two different desired turbulent plane jets. The choice of these jets is mainly based on the contribution of the radiative source term in the enthalpy transport and the further DNS processing time feasibility of its computation.

On the one hand, we seek to size up a turbulent jet based on values of inlet temperature found in modern steam turbines. In the present work a temperature of 860 K is choose based on values reported in the works of Jang et al. (2015); Tanuma (2017). We called this jet the **slightly heated jet**, which is prospecting for a modification of the temperature and density fields by the effects of radiation in the developing region affecting the jet downstream.

On the other hand, a **strongly heated jet** based on temperatures as high as the ones found in combustion systems (~ 2500 K) is further envisaged. We expect to find noticeable radiation effects all along the domain in order to analyze turbulent effects on radiation, as well as radiation effects on turbulence. Such situation will enable us to give some insight on turbulent radiation interactions (TRI) in free-shear flows, as well as to guide the developing of TRI models.

Since DNS have large computational cost, the parametric study to find the setup conditions that best fit the aforementioned heated jets is performed using RANS technique.

4.2 The physical model: the turbulent plane jet

The present work studies the radiative transfer in a heated turbulent plane jet of water vapor discharging into a parallel low speed coflow of cold water vapor. The principal direction of the mean flow is x, the cross-stream coordinate is y, and z is the spanwise coordinate for which all the statistics are homogeneous. There is statistical symmetry about the plane $y = 0$. The flow statistics are stationary and two-dimensional. Figure 4.1 shows a schematic representation in which the jet mixes with the surrounding slow coflow, which creates turbulence and increases the jet thickness.

At the inlet boundary, the jet width opening is defined by the parameter δ. The jet has an initial mean velocity U_1 and the mean coflow velocity is U_2. The jet temperature is T_1, while the temperature in the coflow is T_2.

The corresponding Reynolds number based on the width opening δ is defined by

$$\mathrm{Re} = \frac{\rho(T_1)\Delta U_0 \delta}{\mu(T_1)}, \tag{4.1}$$

where $\Delta U_0 = U_1 - U_2$.

The half width of the jet $y_{1/2}(x)$ displayed in Fig. 4.1 is a mean quantity useful to describe the jet spreading rate. It is defined as the distance from the jet centerline at which the mean velocity corrected by the coflow velocity $\{U_e\}$ is half of the value at the jet centerline $\Delta\{U_c(x)\}$, i.e., $\{U_e(x, y_{1/2})\} = \frac{1}{2}\Delta\{U_c(x)\}$. In the isothermal turbulent plane jet, the local Reynolds number based on $y_{1/2}$ and $\Delta\{U_c(x)\}$ grows downstream in the fully turbulent region as $x^{1/2}$.

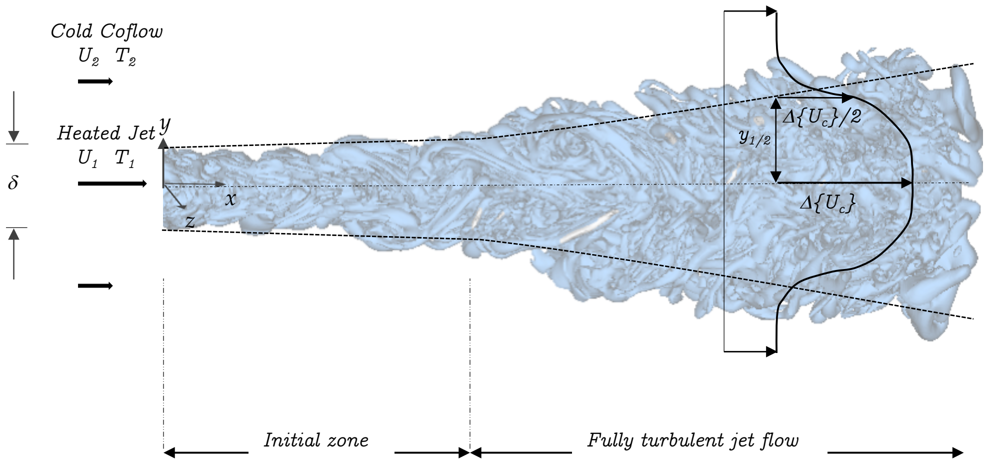

Figure 4.1: *Schematic representation of the turbulent structures of a heated plane jet identified by the Q-criterion.*

Experimental studies of the plane jet show that mean turbulent fields can be divided into two distinct regions along the x direction (Rajaratnam (1976)). The first region is the initial zone located in the vicinity of the nozzle. In this region the jet is surrounded by a mixing layer on top and bottom, and turbulence penetrates inwards toward the centerline of the jet. Until the growth of these mixing layers does not reach the jet centerline, there is a region called potential core, unaffected by the turbulence from these shear layers. In the potential core, the injected hot mixture remains uniform. The length of the initial zone is strongly affected by the inlet conditions as reported, for example, by the experimental work of Deo et al. (2007), and the numerical study of Klein et al. (2003). In the second region, called fully developed, turbulence has penetrated into the centerline of the jet and the mean streamwise velocity profile has a rounded shape. In this region, the mean fields of the isothermal plane jet become self-similar.

4.3 Numerical setup for the parametric study

In this Chapter, the jet described above is computed by means of the RANS method coupled with a Monte-Carlo solver to account for radiation. Tessé et al. (2004) show in their work that the radiative source terms in the energy balance tend to dissipate temperature fluctuations. Therefore, radiation effects relative to the other terms in the energy balance are expected to differ between a priori analysis and the coupled ones. This is the reason why, the dimensioning is performed using RANS fully coupled with the radiative solver. However, the coupled solution does not consider any TRI model, i.e., the radiative power field is directly computed from the averaged temperature given by the RANS solver. For further details in the coupling procedure see Chapter 3.

4.3.1 Setup for the RANS solution

The governing equations considering a two-dimensional flow for a Newtonian and slightly compressible fluid in turbulent regime presented in Chapter 2 are numerically solved using the $k-\epsilon$ LS turbulent model from Launder and Sharma (1974). A domain extension of $(L_x \times L_y/2) = (13.5\delta \times 5\delta)$ and a non-uniform mesh, shown in Fig. 4.2, of 141×81 nodes is considered. The turbulent Prandtl number is set to $\mathrm{Pr}_t = 0.6$. Numerical discretization of the governing equations is carried out using the Finite Volume method (FVM) and the Van Albada scheme (Van Albada et al. (1997)) in a Total Variation Diminishing (TVD) formulation keeping a high-order of accuracy and preventing instabilities during the iteration process. A detailed description of the RANS formulation can be found in Chapter 2.

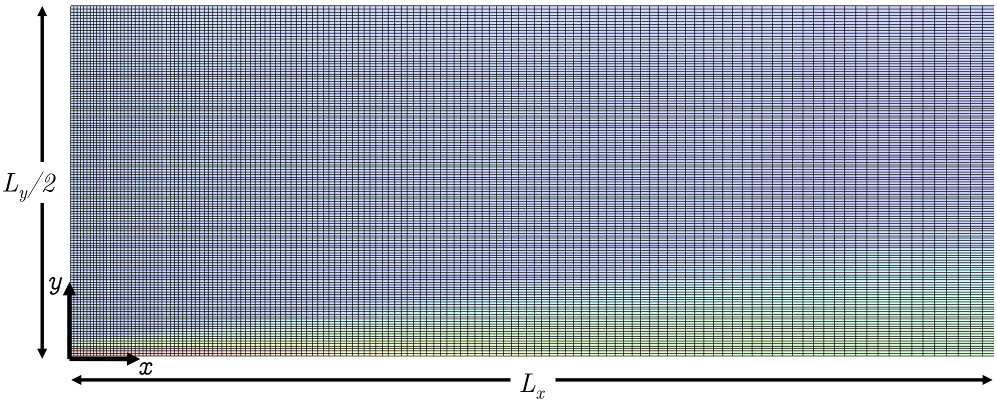

Figure 4.2: *Retained non-uniform structured mesh of* 141×81 *nodes to compute RANS solutions.*

Computation of the transport properties of water vapor is based on the data of Lemmon et al. (2005). Heat capacity at constant pressure is assumed constant since it varies less than 6.4% in the considered temperature range, while μ and λ vary around 163 % and 205%, respectively (Lemmon et al. (2005)). A polynomial regression of order two is then carried out in order to approximate the dynamic viscosity μ and thermal conductivity λ as follows

$$\mu(T) = a_0 + a_1\left(\frac{T}{T_{ref}}\right) + a_2\left(\frac{T}{T_{ref}}\right)^2, \text{ and } \lambda(T) = b_0 + b_1\left(\frac{T}{T_{ref}}\right) + b_2\left(\frac{T}{T_{ref}}\right)^2, \tag{4.2}$$

where T is in Kelvin, T_{ref} is a reference temperature $T_{ref} = 400$ K, $a_0 = -5.9340 \times 10^{-6} Pa \cdot s$, $a_1 = 1.9303 \times 10^{-5} Pa \cdot s$ and $a_2 = -7.4821 \times 10^{-7} Pa \cdot s$, $b_0 = 5.0855 \times 10^{-3} W/(m \cdot K)$, $b_1 = 1.5698 \times 10^{-2} W/(m \cdot K)$ and $b_2 = 8.5830 \times 10^{-3} W/(m \cdot K)$.

4.3.1.1 Boundary conditions

The flow is statistically symmetric in the plane $y = 0$. Additionally, all the statistics are homogeneous along the spanwise coordinate z. Thus, as shown in Fig. 4.3, the mathematical model is solved in a two-dimensional domain, and only the upper half domain is computed in order to speed up simulations. Boundary conditions are considered as follows:

West boundary, $0 < y < L_y/2$ **and** $x = 0$**.** Inlet velocity and temperature profiles are imposed in the west boundary. These profiles are defined using a hyperbolic function described as

$$U_{in}(y) = \frac{U_1 + U_2}{2} + \frac{U_1 - U_2}{2} \tanh\left(\frac{\delta/2 - |y|}{2\theta}\right), \tag{4.3}$$

$$T_{in}(y) = \frac{T_1 + T_2}{2} + \frac{T_1 - T_2}{2} \tanh\left(\frac{\delta/2 - |y|}{2\theta}\right). \tag{4.4}$$

with a corresponding shear layer momentum thickness of $\theta = 0.02\delta$ based on previous plane jet studies Stanley et al. (2002). Inlet boundary values for turbulent variables are calculated through the turbulent intensity I, which is defined as $I = k_{in}^{1/2}/U_{in}$ (here set to $I = 0.05$). Then, $k_{in}(y) = I^2 U_{in}(y)^2$. The dissipation of the turbulent kinetic energy inlet profile ϵ_{in} is based on the work of Heyerichs and Pollard (1996) defined as $\epsilon_{in}(y) = C_\mu k_{in}(y)^{3/2}/(0.03\delta/2)$.

East boundary, $0 < y < L_y/2$ **and** $x = L_x$**,** is an outflow condition with null gradients of all variables in the x-direction.

North boundary, $y = L_y/2$ **and** $0 < x < L_x$**,** corresponds to a far-field boundary condition, for stability reasons we consider symmetry in the north boundary and took the care to set this boundary far enough from the jet to ensure that this approximation has a negligible effect.

South boundary, $y = 0$ **and** $0 < x < L_x$**,** corresponds to a symmetry condition since the mean solution fields are symmetric at $y = 0$.

A schematic of the boundary conditions is presented in Fig. 4.3.

4.3.2 Setup for the Radiative Solver

The Monte-Carlo method computes the radiative power field from mean temperature solutions obtained using RANS. As detailed in Chapter 3, the ERM and a randomized Quasi Monte-Carlo relying on low-discrepancy Sobol sequences are used to account for the radiative heat transfer. Moreover, the spectral radiative properties for H_2O are modeled by means of the correlated-k (ck) narrow band model. Turbulence radiative interactions are neglected in this preliminary study.

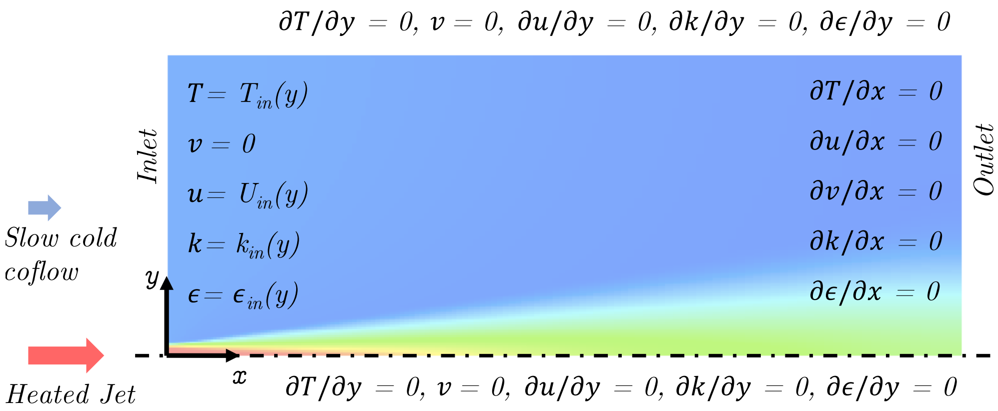

Figure 4.3: *Boundary conditions specifications for the heated turbulent plane jet for RANS computations.*

In the spanwise direction, periodic boundaries are set for the radiative solver; thus, if a ray gets off the domain, for example at the point (x, y, L_z), it will get in at the point $(x, y, 0)$ with the same propagation direction. All other boundaries, corresponding to the inflow and outflows, are treated as black-body at the local temperature of the node located in the boundary, this choice is further discussed in Chapter 6.

The mesh to compute the radiative solution has the same mesh refinement than the RANS grid, but the full domain (without the symmetry on $y = 0$) is considered. Additionally, since the Monte-Carlo solver is three dimensional, four nodes in the z-direction are added. Thus, radiative solution is computed in $282 \times 81 \times 4$ grid nodes in the x, y and z directions, respectively, which corresponds to approximately 9.1×10^4 nodes.

The radiative simulations are considered converged either when a local error lower than 1% of the radiative power is achieved or an absolute value of the error lower than $2 \cdot 10^3\ W/m^3$ is achieved. The value of $2 \cdot 10^3\ W/m^3$ corresponds to approximately 0.5% of the maximum value in magnitude of the radiative power in the slightly heated jet case. Finally, if these two criteria are not accomplished at a specific grid point, a maximum of 5×10^4 rays are considered. These criteria conditions are even more restrictive than further coupled DNS simulations since the processing time and the mesh size involved in the coupled RANS simulations are less restrictive.

4.4 DNS Dimensioning of radiative heated jets from coupled RANS computations

The purpose of the present coupled RANS analysis is to anticipate the role of radiation in the averaged energy balance before performing Direct Numercial Simulations. The averaged energy balance in terms of enthalpy can be simplified assuming statistically steady state and a low Mach number as

$$\underbrace{\frac{\partial\left(\langle\rho\rangle\{u_i\}\{h\}\right)}{\partial x_i}}_{\text{Mean flow advection}} + \underbrace{\frac{\partial\left(\langle\rho\rangle\{u_i''h''\}\right)}{\partial x_i}}_{\text{Turbulent convective heat flux}} = \underbrace{\frac{\partial}{\partial x_i}\left\langle\lambda\frac{\partial T}{\partial x_i}\right\rangle}_{\text{Molecular diffusion}} + \underbrace{\langle P_{rad}\rangle}_{\text{Radiative power}}. \tag{4.5}$$

Without radiation, the main terms for the turbulent plane jet are the mean flow advection, and the turbulent convective heat flux.Additionally, radiative power can also have a major contribution depending on the physical parameters of the heated jet. The main parameters that define the present jet are the opening width δ, the mean inlet velocities for the jet U_1 and the coflow U_2, as well as its corresponding temperatures T_1 and T_2, and the mean pressure P_0. Note that density and Reynolds number are consequently dependent parameters. The effects of each parameter on the radiation contribution in the energy balance with respect to the other terms are discussed below.

- Increasing the jet opening width δ increases the optical thickness of the system making the role of radiation more important. But at the same time, larger δ values implies larger Re. However, for the same Re, the relative effects of radiative transport increase as δ increases.
- When increasing the mean inlet jet velocity U_1, convective energy transport is strongly increased while there is not a direct impact on radiative heat transfer. The mean coflow velocity U_2 is set to be $U_2 = U_1/10$ which is a similar relation of a previous DNS study of a turbulent plane jet presented by Stanley et al. (2002).
- The inlet jet temperature T_1 has a major influence on the exchanged radiative power. Moreover, when increasing temperature, the Reynolds number computed as $\mathrm{Re} = \rho(T_1)\Delta U_0\delta/\mu(T_1)$ rapidly decreases when ΔU_0 and δ are kept constant due to a decrease of ρ and an increase in μ. Coflow temperature T_2 is set to be the minimal temperature at which water vapor remains in the gas state.
- Increasing P_0 increases the optical thickness, but implies a rise in density which increases the Reynolds number. Moreover, increasing P_0 implies larger values of T_2 to ensure gas state of the water vapor.

The desired heated jets to be simulated correspond to two different applications with its associated range of temperatures. The jet temperature for the slightly heated plane jet is set to $860K$, while for the strongly heated jet is set to $2500K$. The required CPU time strongly depends on the Re number, which determines the smallest length and time scales. Moreover, the ratio between the jet opening width and the jet velocity δ/U_1 is proportional to the required CPU time. On the one hand, δ defines the length L_x, which is here set to $L_x = 10\delta$ to observe self-similarity as reported by previous DNS results of Stanley et al. (2002). On the other hand, the ratio δ/U_1 defines the required physical time τ following the expression

$$\tau(U_1 + U_2)/(2L_x) = f.t.u, \tag{4.6}$$

where $f.t.u$ stands for the so-called flow time units, for which values greater than 10 are required in order to obtain a statistically meaningful amount of data to be averaged.

After performing some tests with the DNS mesh, we found that for $\delta = 0.05$ m, velocities greater than 4 m/s conform feasible δ/U_1 ratios in terms of CPU processing time at $Re = 1500$. Moreover, when defining the jet opening width $\delta = 0.05$ m, we also took the care to ensure that the associated cell sizes are not fully optically thick, since we envisaged radiative heat transfer among a wide variety of turbulent scales. Figure 4.4 present the spectral transmissivity of water vapor at 380 K for a cell size of $\delta/50$ which follows the same order of magnitude than previous DNS of turbulent plane jet performed by Stanley et al. (2002). In this Figure, temperature has been set to 380 K since it presents the largest optical thickness of the simulated temperature range. From Fig. 4.4, it can be seen that transmissivity is close to unity all along the wavenumber spectrum, ensuring radiative heat exchange among turbulent structures. Further analysis on the transmissivity of the water vapor for the problem scale is presented in Chapter 6.

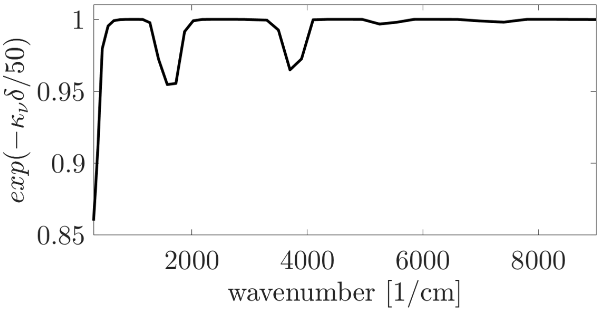

Figure 4.4: *Ck model results of the spectral transmissivity of an isothermal and homogeneous column* $X_{H_2O} = 1$ *of length* $l = \delta/50 = 1$ *mm at* 380 *K* .

4.4.1 Slightly heated plane jet

Temperature of the slightly heated jet is set to 860K based on inlet temperatures of modern steam turbines (Jang et al. (2015); Tanuma (2017)). The jet opening width δ is fixed to $\delta = 0.05$ m and the inlet pressure is set to 1 atm. Then, Reynolds number is varied from 750 to 3000 with its associated variation in the inlet velocity. The performed coupled RANS simulations for the slightly heated jet are described in Table 4.1.

Figure 4.5 shows the principal components of the energy balance for the $Re = 750$ case of the slightly heated jet. Given T_1, the pressure to achieve $U_1 = 2.09$

Table 4.1: *Setup for the different tested configurations for the slightly heated jet.*

Re	U_1 $[m/s]$	U_2 $[m/s]$	T_1 $[K]$	T_2 $[K]$	P_0 $[atm]$	δ $[m]$
750	2.090	0.2090	860	380	1.0	0.05
1500	4.176	0.4176	860	380	1.0	0.05
3000	8.360	0.8360	860	380	1.0	0.05

m/s at this Reynolds number is $P_0 = 1$ atm, which implies a coflow temperature of $T_2 = 380$ K to ensure gas state of the water vapor. The centerline evolution of the main terms in Eq. (4.5) is presented in Fig. 4.5(a), which shows that radiative power is larger than the turbulent convective heat flux almost until $x = 6\delta$. At the inlet section, radiative power is of the same order of magnitude than the mean flow advection. As envisaged, radiative power has a significant contribution in the developing region, specially at the jet centerline. Note that the turbulent term present larger magnitude in cross-section profiles due to the shear layers developed around the potential core as seen in Fig 4.5(b). Furthermore, at the developed region, radiative power is around 60% of the turbulent convective heat flux at the jet centerline and 9% of the mean flow advection at the jet centerline. Radiative power does not dominate the energy balance at the developed region ($x = 10\delta$), but still its effect is questionably negligible when compared with the other terms.

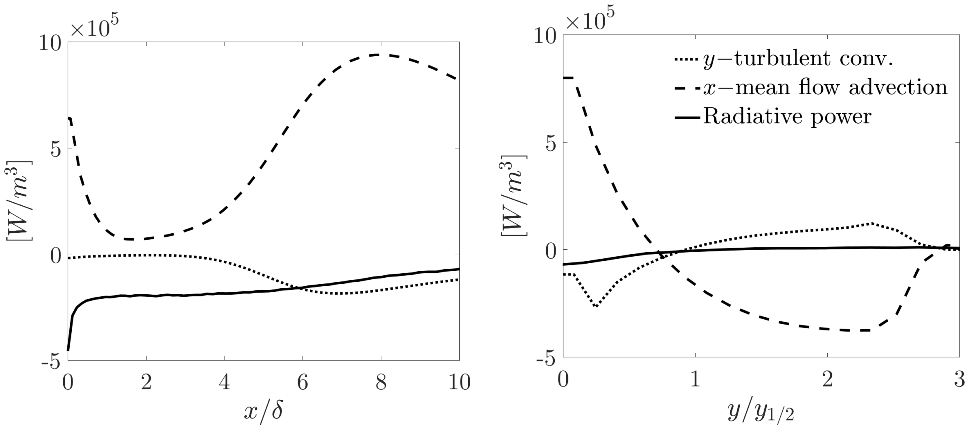

(a) (b)

Figure 4.5: *Enthalpy balance main components for the slightly heated jet at Re = 750. (a) Downstream evolution (b) and cross-section profile at $x = 10\delta$.*

Figure 4.6 shows the energy balance when the Reynolds number is set to 1500. The associated inlet velocity corresponds to $U_1 = 4.176$ m/s. As for the Re=750, the radiative power has a non-negligible contribution in the jet centerline at the developing region, since radiative power is larger than the turbulent convective heat flux until $x = 3.35\delta$ as shown in Fig. 4.6(a). The importance of the radiative power in the developed region ($x = 10\delta$) is less than for the case of Re=750, being that radiative power is 5% of the dominant mean flow advection at the jet centerline and it is around 30% of the turbulent convective heat flux at the jet centerline as it can be observed in Fig 4.6(b).

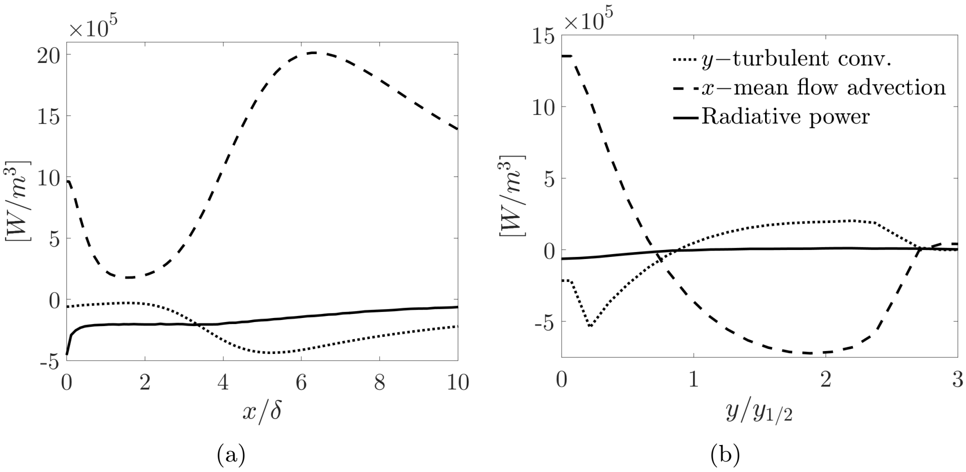

(a)

(b)

Figure 4.6: *Enthalpy balance main components for the slightly heated jet at $Re = 1500$. (a) Downstream evolution (b) and cross-section profile at $x = 10\delta$.*

Finally, the main terms of the energy balance for the case of $Re = 3000$ and $U_1 = 8.36$m/s are presented in Fig. 4.7. From Fig. 4.7(a) it can be observed that turbulent convective heat flux rapidly exceeds radiative power before $x = 2\delta$ at the jet centerline, which makes questionable that radiative power contributes indeed in the energy balance at the developing region. Nevertheless, as envisaged, radiative power at the developed region ($x = 10\delta$) is clearly negligible when compared with the other terms, since it is around 2% of the mean flow advection at the jet centerline and it is around 14% of the turbulent convective heat flux at the jet centerline as shown in Fig 4.7(b).

Based on the analysis varying the Reynolds number presented above, the retained case for the slightly heated jet is the one with $Re = 1500$. This case fulfill the envisaged requisites since radiation has a significant contribution in the energy balance at the developing region, specially at the jet centerline. And, at the same time, radiation has hardly any effects on the energy balance at the developed region. Moreover, the computational cost of the coupled DNS with thermal radiation is affordable for this Reynolds number and for the time scale δ/U_1.

4.4.2 Strongly heated plane jet

The water vapor inlet temperature for the strongly heated plane jet is set to $T_1 = 2500$ K based on temperature values found in combustion systems.

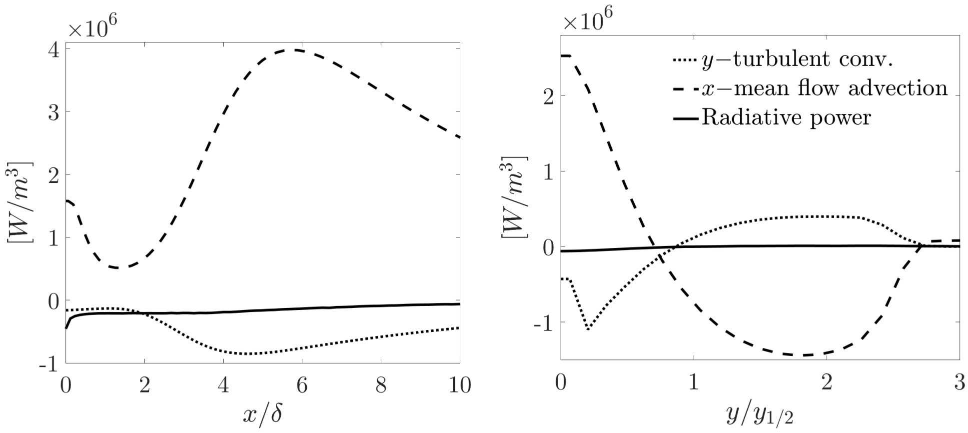

(a) (b)

Figure 4.7: *Enthalpy balance main components for the slightly heated jet at Re* $=$ 3000*. (a) Downstream evolution (b) and cross-section profile at* $x = 10\delta$*.*

Again, the jet opening width δ is fixed to $\delta = 0.05$ m and the Reynolds number is varied from 250 to 1000 at $P_0 = 2.576$ atm with its associated variation in the inlet velocity, while T_2 is set to be the minimal temperature at which water vapor remains in the gas state. The setup of the performed simulations for dimensioning the strongly heated jet are gathered at table 4.2.

Table 4.2: *Setup for the different tested configurations for the strongly heated jet.*

Re	U_1 $[m/s]$	U_2 $[m/s]$	T_1 $[K]$	T_2 $[K]$	P_0 $[atm]$
250	2.090	0.2090	2500	405	2.576
500	4.176	0.4176	2500	405	2.576
1000	8.360	0.8360	2500	405	2.576

Figure 4.8 presents the main terms in the energy balance for the case of $Re =$ 250. Radiative power significantly contributes to the energy balance at the jet centerline in the range $0 < x < 10\delta$ as shown in Fig. 4.8(a). Cross-section profile of the energy balance at $x = 10\delta$ presented in Fig. 4.8(b) shows that radiation is greater than the turbulent convective heat flux in the $y-$direction at the jet centerline.

Similarly, the downstream evolution of the energy balance at the jet centerline presented in Fig. 4.9(a) for the case of $Re = 500$ shows that radiation significantly contributes in the energy balance. However, observing the cross-section profiles at the developd region in Fig. 4.9(b), it can be observed that the turbulent convective heat flux is larger than for the case of $Re = 250$, being that radiation and the turbulent convective heat flux are almost equally at the jet centerline for $x = 10\delta$.

Figure 4.10 shows the energy balance when the Reynolds number is set to 1000.

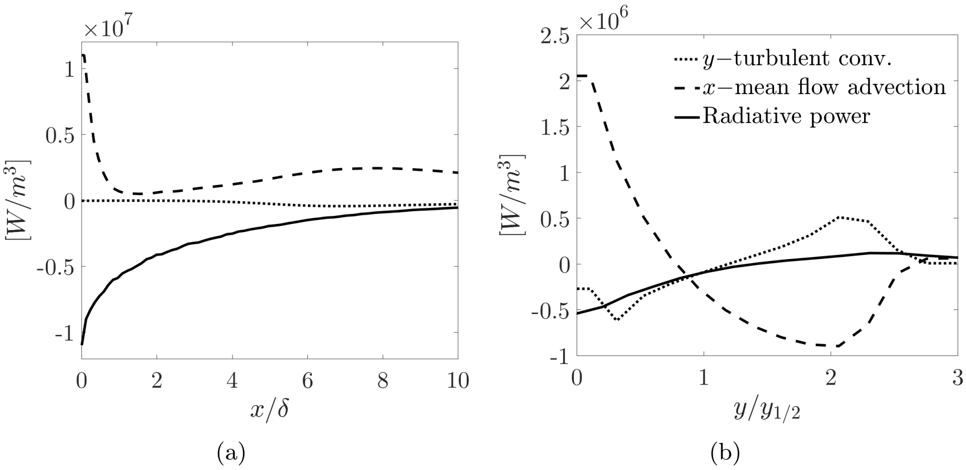

(a) (b)

Figure 4.8: *Enthalpy balance main components for the strongly heated jet at Re =250. (a) Downstream evolution and (b) cross-sections profile at $x = 10\delta$.*

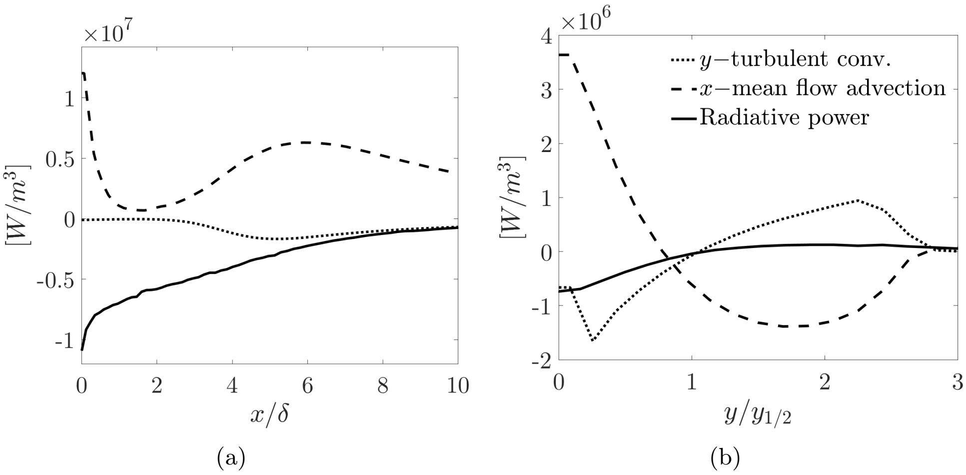

(a) (b)

Figure 4.9: *Enthalpy balance main components for the strongly heated jet at Re =500. (a) Downstream evolution and (b) cross-sections profile at $x = 10\delta$.*

It can be observed that radiation is still contributing in the energy balance all along the domain at the jet centerline as shown in Fig. 4.10(a) and even in the developed region as observed in Fig. 4.10(b). Nevertheless, radiation is noticeably less important in the energy balance when compared with the two other cases of the strongly heated jet.

A trade-off between a sufficiently high Reynolds number to ensure turbulent regime; and at the same time, a significant radiative power term in the energy balance is the case of $Re = 500$ based on the results of the coupled RANS simulations presented above. Then, the retained configuration for the strongly

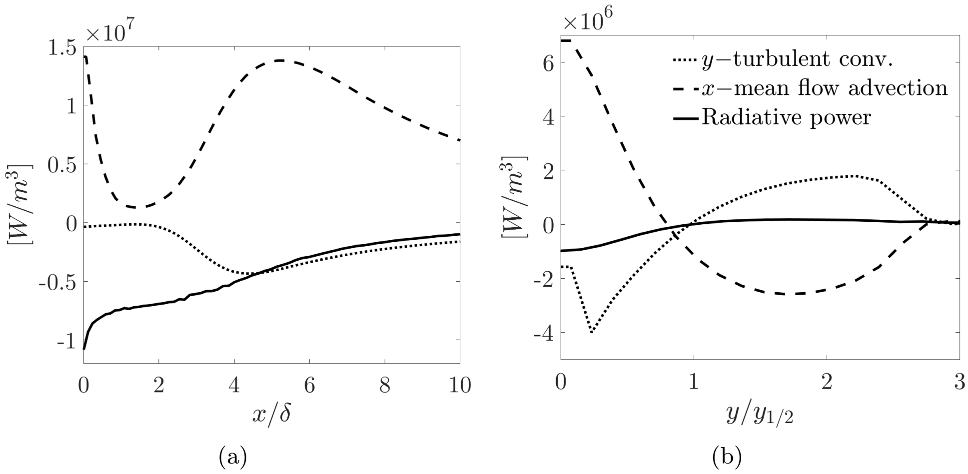

(a) (b)

Figure 4.10: *Enthalpy balance main components for the strongly heated jet at* $Re = 1000$. *(a) Downstream evolution and (b) cross-sections profile at* $x = 10\delta$.

heated jet is the case of $Re = 500$.

4.5 Conclusions

A parametric analysis of the main terms in the mean enthalpy balance has been carried out using the RANS solver coupled with the Mont-Carlo solver to account for thermal radiation. The dimensioning is based on the contribution of radiation in the enthalpy balance, as well as on obtaining an affordable computational cost for the coupled DNS. The retained setup for the slightly and the strongly heated jets are summarized in Table 4.3.

Table 4.3: *Final configurations for the slightly and strongly heated jets.*

	δ [m]	U_1 [m/s]	U_2 [m/s]	T_1 [K]	T_2 [K]	Re	P_0 [atm]
Slightly heated	$5 \cdot 10^{-2}$	4.176	$U_1/10$	860	380	1500	1
Strongly heated	$5 \cdot 10^{-2}$	4.176	$U_1/10$	2500	405	500	2.576

The Reynolds numbers of these jets (500 and 1500) are low compared with previous DNS studies of turbulent plane jets. For example, Klein et al. (2003) investigated the influence of the Reynolds number in the range of 1000 to 6000, and Stanley et al. (2002) simulated the plane jet using a Reynolds number of 3000. However, the retained Reynolds numbers are of the same order of the experimental study of Lemieux and Oosthuizen (1985), who reported a fully turbulent plane jet of a Reynolds number of 700. In our study, the Reynolds number is kept moderate in order to afford the computational cost of a coupled simulation with thermal radiation while featuring a turbulent flow as further discussed in Chapters 5, 7 and 8.

Chapter 5

Uncoupled Direct Numerical Simulations of plane jets

Direct numerical simulations of uncoupled isothermal and heated jets are analyzed to discuss the adequacy of the DNS numerical setup. First, the configuration and numerical setup of the simulations are detailed. Then, first and second orders of velocity are validated by comparison with previous experimental and numerical studies. For the heated jet without including radiation, the mean temperature and its fluctuations are compared with previous works. These uncoupled results demonstrate the suitableness of the DNS numerical setup.

Contents

5.1 DNS of the uncoupled isothermal plane jet

5.1.1 Introduction

Turbulent jets are one of the most commonly studied turbulent free shear flows. The fundamental understanding of the jet dynamics is necessary to comprehend and to predict the transport processes in many industrial applications such as combustion, propulsion and environmental flows. Greats efforts have been made to describe the dynamics of these flows at the developed region where turbulent statistics are assumed independent of initial conditions and present universal similarity solutions (Townsend (1956); Rajaratnam (1976); Abramovich (1963); Pope (2001)).

Early similarity solutions of the velocity field based on local velocity and length scales for constant-density free shear flows are derived in the work of Townsend (1956). Following this work, self-similarity on a constant density plane jet was reported in the experimental studies of Bradbury (1965) and Heskestad (1965) using hot-wire anemometry. They collected data of mean velocity, turbulent intensities and shear stresses fields, as well as the turbulent kinetic energy balance in the developed region. Further experimental work was conducted by Gutmark and Wygnanski (1976) applying conditional sampling techniques in order to provide data obtained exclusively within the turbulent zone. Despite some scatter among these experimental works (Bradbury (1965); Heskestad (1965); Gutmark and Wygnanski (1976)), data of the velocity field was found to be self-similar in the developed region when scaled using the classical parameters of Townsend (1956). More recent experimental works performed by Deo et al. (2008); Deo et al. (2007) underline the influence of the Reynolds number and the nozzle-exit geometric profile on self-similar solution of a plane jet. Accurate data of the constant-density plane jet has also been provided by numerical investigations including the work of Le Ribault et al. (1999) using Large Eddy Simulations (LES) and Stanley et al. (2002) through Direct Numerical Simulations (DNS). Both works obtained similarity profiles for mean velocity and Reynolds stresses. Proceeding with these studies, Klein et al. (2003) numerically investigated the influence of the Reynolds number and the inflow conditions in a constant-density plane jet using DNS. A recent study of Sadeghi et al. (2018) proposes new scaling laws for the higher moments in constant-density temporally evolving plane jet which were derived using Lie symmetry analysis.

For the constant-density round jets, the numerical work of Bogey and Bailly (2009) report reference solutions in the self-preserving region including the turbulence and energy budgets. Further similarity analysis in round jets include the theoretical and experimental work of Sadeghi et al. (2015) who derived a similarity law for the turbulent energy structure function; and the work of Thiesset et al. (2014) who discussed the similarity of the mean kinetic energy dissipation rate, and pointed out that assuming local isotropy and complete self-similarity, as well as considering only the production and advection in the energy budget, the virtual origin in one configuration should be the same independently of the flow quantity under consideration.

5.1.2 Configuration and numerical setup

The isothermal jet of water vapor is defined by the jet width opening ($\delta = 0.05$ m), the initial mean velocity ($U_1 = 4.176$ m/s) and the mean coflow velocity ($U_2 = U_1/10$). The simulation is carried out at atmospheric pressure (1 atm) and at a constant temperature of 610 K. Transport properties of water vapor are computed using Eq. 4.2. Then, the corresponding Reynolds number based on the width opening δ is

$$\mathrm{Re} = \frac{\rho(T_1)\Delta U_0 \delta}{\mu(T_1)} = 3200, \tag{5.1}$$

where $\Delta U_0 = U_1 - U_2$. The present setup for the isothermal plane jet is summarized in Table 5.1, a schematic representation of the plane jet has been already presented in Fig. 4.1.

Table 5.1: *Setup configuration of the isothermal turbulent plane jet.*

δ [m]	U_1 [m/s]	U_2 [m/s]	T_1 [K]	T_2 [K]	Re	P_0 [atm]
$5 \cdot 10^{-2}$	4.176	$U_1/10$	610	610	3200	1

5.1.2.1 Numerical tools

As explained in Chapter 1, the governing equations are numerically solved on a structured mesh using a 4^{th}-order centered finite-difference scheme for the spatial derivatives and an explicit 4^{th}-order Runge-Kutta method for the time integration, an overview of such methods can be found in the work of Kennedy and Carpenter (1994). In addition, an implicit filter of 8^{th}-order proposed in the work of Gaitonde and Visbal (1999) is used for stability purposes. More details of the implementation can be found in the work of Coussement (2012).

5.1.2.2 Boundary conditions

Following the study of Poinsot and Lele (1992), the inflow and outflow boundaries are formulated as subsonic partially non-reflecting boundary conditions using the Navier-Stokes Characteristic Boundary Conditions (NSCBC) for the modified ASR system of equations, as explained in Chapter 1.

Outflow boundary. In the outflow boundaries, atmospheric pressure is enforced with a partially reflecting characteristic boundary condition. The presence of turbulent structures on the outflow boundary bring instabilities in the solution. When mass is coming into the domain from an outflow boundary, no physical input values of velocity, pressure and temperature can be possible imposed. This issue can eventually lead to divergence, specially during the time at which the flow is developing. To deal with this issue, a sponge layer is set at the near region of the outflow boundary. To this purpose, the fluid viscosity used to compute the solution μ_{tot} is artificially increased by the expression:

$$\mu_{tot} = \begin{cases} \mu_{physic} & \text{if } 0 \le x < (x_0 - L_\mu) \\ \mu_{physic} \cdot \left(1 + \frac{N_\mu}{2}\left[1 + \tanh\left(\frac{x - x_0}{L_\mu/2}\right)\right]\right) & \text{if } x \ge (x_0 - L_\mu) \end{cases} \tag{5.2}$$

where x_0 defines the coordinate in which the viscosity patch is centred, L_μ is half the sponge layer width, and N_μ stands for the value of the artificial patch as $\mu_{tot} = N_\mu \mu_{physic}$. In the present study x_0 is set to $11.4h$, while $L_\mu = 0.4h$ and $N_\mu = 200$. The resulting value of μ_{tot} along the x axis is shown in Fig. 5.1

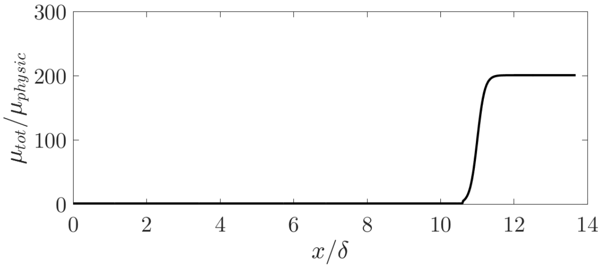

Figure 5.1: *Total viscosity along the jet centerline defining the sponge layer at the outflow boundary.*

Such technique enhance the robustness of the solution by preventing negative streamwise velocities through dissipation of turbulent kinetic energy.

Inlet boundary: The inlet velocity profile that defines the jet is specified by the hyperbolic function:

$$U_{in}(y) = \frac{U_1 + U_2}{2} + \frac{U_1 - U_2}{2} \tanh\left(\frac{\delta/2 - |y|}{2\theta}\right), \tag{5.3}$$

the shear layer momentum thickness θ is set to $\theta = 0.07\delta$. This value has been chosen following the work of Stanley et al. (2002) to ensure numerical stability. Low values of the shear layer momentum thickness promote the jet growth but required more mesh refinement to well describe the velocity gradients in the jet edge.

The averaged velocity profile at the inlet section is shown in Fig. 5.2(a) where $\{U_e\}$ denotes the Favre average velocity excess $\{U_e\} = \{U\} - U_2$, and $\Delta\{U_c\}$ is the Favre average velocity excess at the jet centreline $\Delta\{U_c\} = \{U_c\} - U_2$. Synthetic turbulence generated using the model of Passot and Pouquet (1987) is combined with the mean inlet velocity profile at the jet region. This technique promotes turbulent instabilities and reduces the initial region of the jet. The Passot Pouquet model defined in §1.3.2 is here used. The kinetic energy spectrum is defined by fixing the auto-correlation integral scale L_c and the *turbulent velocity* u'. In the present simulation, these values are set to $L_c = \delta/2$

and $u' = U_1/20$. Velocity fluctuations have its maximum value at the jet centerline while are set to zero at the coflow following an hyperbolic profile analogous to the one of the inlet streamwise velocity. The resultant inlet averaged root-mean-square (rms) velocity fluctuations are shown in Fig. 5.2(b).

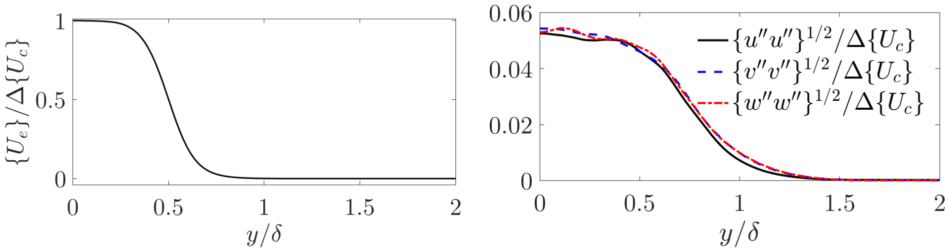

(a) (b)

Figure 5.2: *Cross-section profiles of mean (a) streamwise velocity and (b) Reynolds stresses profiles at the inlet boundary.*

5.1.2.3 Computational mesh and domain

The grid is non-uniform in the x and y directions while it is uniform in the spanwise direction. Computations are performed in a domain extension of $13.5\delta \times 10\delta \times 3\delta$ in x, y and z directions, respectively, while a domain extension of $10\delta \times 10\delta \times 3\delta$ is considered to compute the statistics of the flow. The spanwise box size is determined from an estimation of the integral length scale based on the work of Klein et al. (2003). The flow solution is computed using a structured grid with $566 \times 469 \times 149$ nodes, in the x, y and z directions, respectively, which corresponds to approximately 39.5×10^6 nodes.

The grid spacings, relevant for direct numerical simulations, can be anticipated from the known behavior of turbulent plane jets. Indeed, from the scaling law for decaying centerline velocity profile from Jenkins and Goldschmidt (1973), it is possible to estimate $U_c(x)$ for the present inlet values. Estimating the dimensionless turbulent kinetic energy dissipation ϵ^* from the previous DNS results of Stanley et al. (2002), ϵ can be scaled for the present simulation. Then, the grid spacing along x-axis is set to be locally maximum four times the local Kolmogorov scale $\eta \equiv \left(\frac{(\mu/\rho)^3}{\epsilon}\right)^{1/4}$. The grid spacing along y-axis is such that the inner region of the jet ($y < y_{1/2}(x)$) is as much refined as in the x direction. Finally, the grid spacing along z-axis is uniform and equal to $\Delta z = \delta/50$, which is a close value to the Δx and Δy averages.

5.1.2.4 The Acoustic Speed Reduction method

The acoustic speed reduction method introduced in Chapter 1 is used setting $\alpha = 8$. This value of α sets the Courant-Friedrichs-Lewy and Fourier conditions within the same order of magnitude for the current simulation.

5.1.3 DNS results of the uncoupled isothermal jet

In order to accelerate convergence of statistical values, all mean quantities have been averaged in the spanwise direction. In addition, the symmetry plane about $y = 0$ is used to double the averaging samples. The statistics are obtained by averaging the data over approximately $\tau = 2.4$s of physical time. This time corresponds to approximately 11 flow time units defined as in the work of Stanley et al. (2002) as $\tau(U_1 + U_2)/(2L_x) = 11$, where L_x is the domain size in the x direction $L_x = 10\delta$.

In the developed region of the isothermal plane jet, the jet half-width $y_{1/2}(x)$ has a linear relationship with the streamwise coordinate (Rajaratnam (1976)),

$$\frac{y_{1/2}}{\delta} = K_{1,u}\left(\frac{x}{\delta} + K_{2,u}\right), \tag{5.4}$$

while the mean streamwise velocity excess at the jet centerline $\Delta\{U_c\} = \{U_c\} - U_2$ is found to vary as $x^{-1/2}$,

$$\left(\frac{\Delta U_0}{\Delta\{U_c\}}\right)^2 = C_{1,u}\left(\frac{x}{\delta} + C_{2,u}\right), \tag{5.5}$$

where $\Delta U_0 = U_1 - U_2$. The slope coefficients, $K_{1,u}$ and $C_{1,u}$, in the fully developed region are known to be universal for the isothermal jet; that is to say that, for large Reynolds number, they are independent of the jet conditions. Similarly, properly scaled non-dimensional profiles become self-similar in the same region.

Figure 5.3(a) presents the results of the growth of the jet half-width $y_{1/2}(x)$, while the adimensionalized mean excess velocity decay $(\Delta U_0/\Delta\{U_c\})^2$ along the jet centerline is presented in Fig. 5.3(b). In both figures, the linear regression in the fully developed region and the experimental results from the work of Thomas and Chu (1989) are also shown for the sake of comparison. Figure 5.3 shows that both the jet half-width and the mean velocity decay have a linear dependency on x/δ beyond $x = 8\delta$, which is the same value reported by Stanley *et al.* Stanley et al. (2002). Hence, the coefficients for the linear fitting shown in Fig. 5.3 are computed using values in the range $8\delta < x < 10\delta$.

The present results of the linear fitting coefficients in the self-similar zone are summarized in Table 5.2 along with some experimental (Jenkins and Goldschmidt (1973); Goldschmidt and Young (1975); Gutmark and Wygnanski (1976); Thomas and Chu (1989)) and DNS (Stanley et al. (2002)) results. The results of the virtual origins ($K_{2,u}$ and $C_{2,u}$) differ among the referred works since they have a strong dependency on the inflow conditions (Stanley and Sarkar (2000); Klein et al. (2003)). On the other hand, the predicted

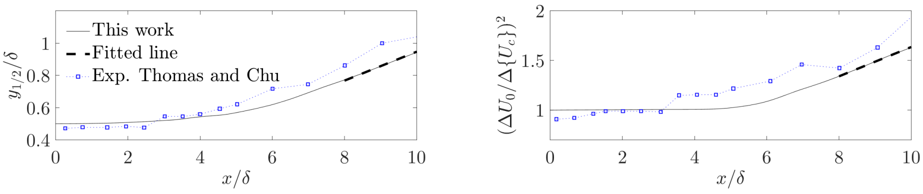

(a)

(b)

Figure 5.3: *Comparison of the present isothermal plane jet results with the experimental work of Thomas and Chu (1989): downstream evolution of (a) spread rate and (b) velocity decay.*

slope coefficients ($K_{1,u}$ and $C_{1,u}$) compare generally well with previous results, although $C_{1,u}$ is somewhat lower.

Table 5.2: *Comparison of the jet growth rate and the centerline velocity decay rate at the self-similar region between the current results and some experimental and numerical reference values.*

	$K_{1,u}$	$K_{2,u}$	$C_{1,u}$	$C_{2,u}$
Jenkins and Goldschmidt (1973)	0.088	-4.5	0.160	4.0
Gutmark and Wygnanski (1976)	0.100	-2.00	0.189	-4.72
Goldschmidt and Young (1975)	0.0875	-8.75	0.150	-1.25
Thomas and Chu (1989)	0.110	0.14	0.220	-1.19
Stanley et al. (2002)	0.092	2.63	0.201	1.23
This work	0.088	0.721	0.146	1.181

Mean profiles of the excess streamwise velocity ($\{U_e\} = \{u\} - U_2$) and the cross-stream velocity $\{v\}$ adimensionalized by $\Delta\{U_c\} = \{U_c\} - U_2$ against $y/y_{1/2}$ become self-similar, that is, they collapse onto a single curve as long as the jet is developed. Fig. 5.4(a) and 5.4(b) show that velocity profiles at $x = 10\delta$ are in good agreement with self-similar profiles from experimental (Gutmark and Wygnanski (1976)) and numerical (Stanley et al. (2002)) studies. The beginning of the developed zone associated with the self-similarity of streamwise velocity profiles is considered to begin at $x = 8\delta$ where profiles of streamwise velocity collapse onto almost the same curve, as shown in Fig. 5.5. This is the same value reported by Le Ribault et al. (1999). Likewise, the numerical study of Stanley et al. (2002) obtained similar values, they found that the streamwise velocity profiles collapse around $x = 10\delta$. Nevertheless, experimental studies report much larger values, for example, Gutmark and Wygnanski (1976) estimate that self-similarity begins beyond $x = 40\delta$ while Bradbury (1965) reports a value of $x = 30\delta$. As mentioned earlier, inlet boundary conditions have a strong influence on the length of the jet potential core. Therefore, the injection of artificial turbulence in the inlet boundary can modify the beginning of the self-similar region. Despite the short considered domain length (10δ) in the streamwise direction which is limited; the good agreement of velocity profiles with previous self-similar data, and the linear growth of the jet half-width and the velocity decay indicate that the numerical domain between $x = 8\delta$ and $x = 10\delta$ is inside the developed region of the jet where self-similarity applies quite satisfactorily.

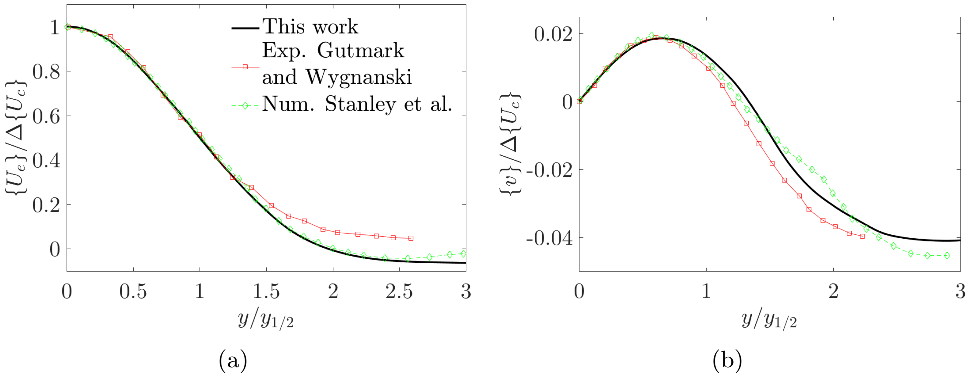

(a) (b)

Figure 5.4: *Self-similar profiles of (a) streamwise and (b) cross-stream velocities of the isothermal plane jet at $x = 10\delta$.*

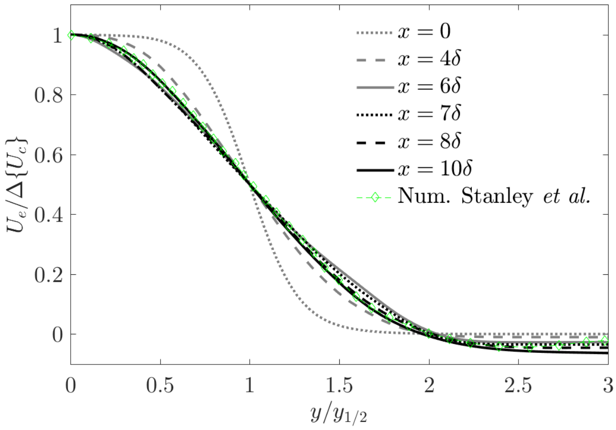

Figure 5.5: *Cross-section profiles of streamwise velocity at several distances for the isothermal jet.*

Reynolds stresses in the fully turbulent zone are also expected to become self-similar when adimensionalized by $\Delta\{U_c\}$ and plotted against $y/y_{1/2}$. Figure 5.6 compares the Reynolds stresses results at $x = 10\delta$ with experimental data of Thomas and Prakash (1991), Ramaprian and Chandrasekhara (1985) and Bradbury (1965) as well as numerical results of Stanley et al. (2002). Predicted

Reynolds stresses profiles are satisfactory although one can notice the spread of the reported profiles in the literature.

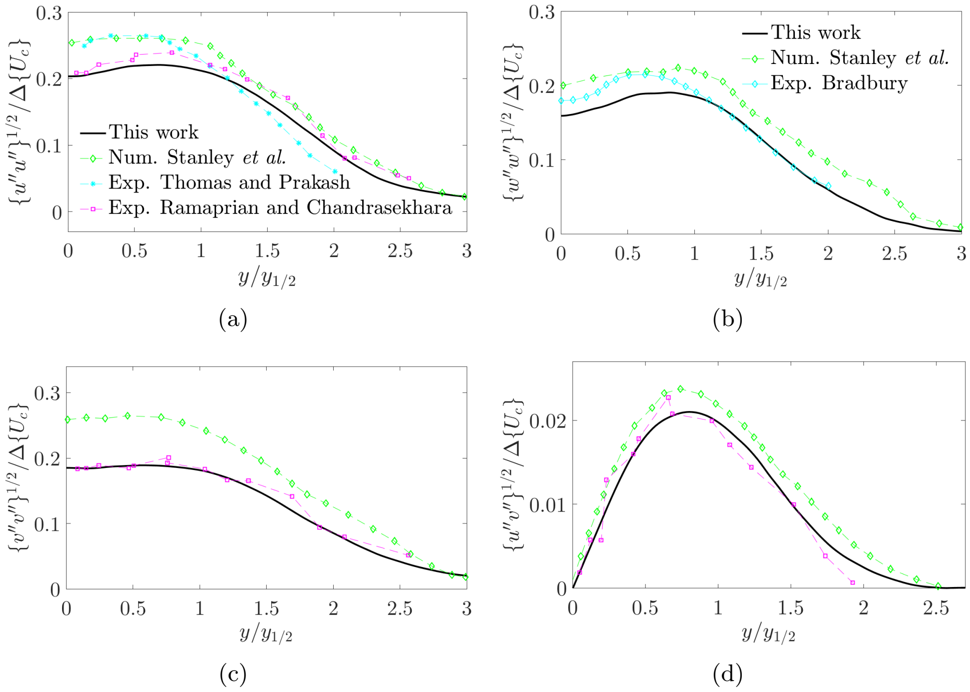

(a) (b)

(c) (d)

Figure 5.6: *Self-similar Reynolds stresses profiles of the isothermal plane jet in the (a) x direction, (b) z direction, (c) y direction; and (d) shear stress at* $x = 10\delta$.

The general definition of turbulent kinetic energy for a variable density flow is a Favre average of the mass-weighted fluctuations u_i'', i.e, $k = \frac{1}{2}\{u_i''^2\} = \frac{1}{2}\langle \rho u_i''^2\rangle / \langle \rho \rangle$. Following the work of Chassaing et al. (2013) or Huang et al. (1995), the transport equation of the turbulent kinetic energy is expressed as

$$\underbrace{\frac{1}{2}\frac{\partial \langle \rho u_i''^2\rangle}{\partial t} + \frac{\partial}{\partial x_j}\left(\frac{1}{2}\langle \rho u_i''^2\rangle\{u_j\}\right)}_{\text{Advection, } \langle\rho\rangle \frac{\bar{D}k}{Dt}} = -\underbrace{\langle \rho u_i'' u_j''\rangle \frac{\partial \{u_i\}}{\partial x_j}}_{\text{Production, } \mathcal{P}} - \underbrace{\langle \tau_{i,j} \frac{\partial u_i''}{\partial x_j}\rangle}_{\text{Viscous dissipation, } \epsilon}$$
$$\underbrace{-\frac{\partial\left(\langle P\rangle\langle u_i''\rangle\right)}{\partial x_i} - \frac{\partial \langle P' u_i''\rangle}{\partial x_i} + \frac{\partial \langle \tau_{i,j} u_i''\rangle}{\partial x_j} - \frac{\partial}{\partial x_j}\langle \rho u_j'' \frac{u_i''^2}{2}\rangle}_{\text{Diffusion terms, } \nabla\cdot T} + \underbrace{\langle P \frac{\partial u_i''}{\partial x_i}\rangle.}_{\text{Pressure-Dilatation, } \Pi} \quad , \tag{5.6}$$

where the different diffusive fluxes (pressure diffusion, viscous diffusion and turbulent diffusion) have been gathered in the quantity denoted as T. The numerical computation of each term in Eq. 5.6 is detailed in Appendix A.

Since velocity and Reynolds stresses profiles adimensionalized by $\Delta\{U_c\}$ are self-similar and independent of Re in the developed region for the isothermal jet, so are the different terms in the transport equation for turbulent kinetic energy profiles when they are adimensionalized by the scaling factor $y_{1/2}/(\Delta\{U_c\}^3\langle\rho\rangle)$. The dimensionless transport equation of the turbulent kinetic energy is then expressed as:

$$\frac{\bar{D}k^*}{\bar{D}t} + \nabla \cdot T^* = \mathcal{P}^* - \epsilon^* + \Pi^*, \tag{5.7}$$

where * denotes adimensionalized quantities. The budget of the turbulent kinetic energy in the self-similiar zone is presented in Fig. 5.7(a), while Figs. 5.7(b) to 5.7(e) show the results of each term in the turbulent kinetic energy equation compared with experimental data of Terashima et al. (2012) and numerical results of Stanley et al. (2002). The profiles are obtained by averaging the scaled simulation fields in the range $9\delta < x < 10\delta$. The pressure-dilatation term (Π^*) has a negligible contribution; in consequence, it is not included in Fig. 5.7. All trends in the budget are well captured and compare reasonably good with experimental results, even improving the results from past numerical simulations.

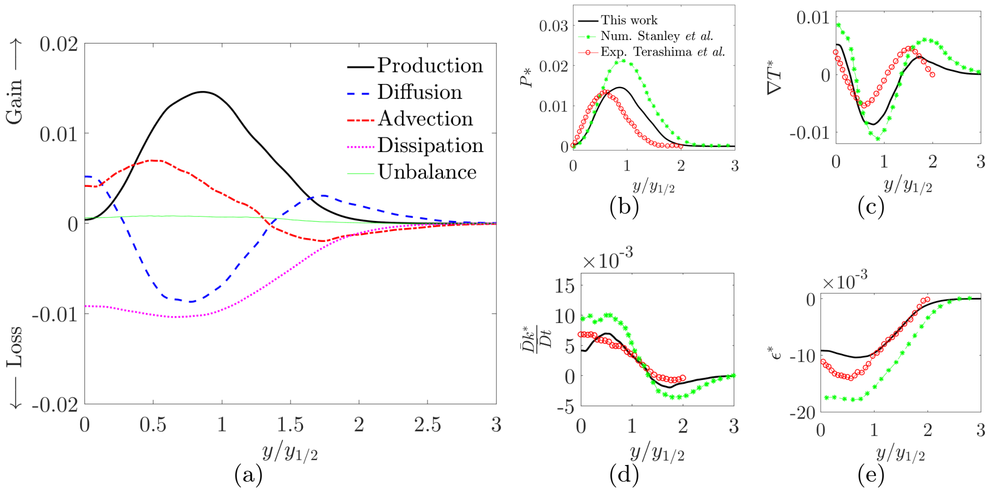

Figure 5.7: *(a) Budget of dimensionless turbulent kinetic energy of the isothermal plane in the self-similar zone. Components of the turbulent kinetic energy budget: (b) production, (c) turbulent diffusion, (d) advection and (e) dissipation compared with experimental data of Terashima, Sakai and Nagata (2012) and numerical results of Stanley, Sarkar and Mellado (2002).*

The two main terms in the energy budget are production and dissipation. Viscous dissipation is almost constant in the core of the jet ($y < y_{1/2}$) while production has a strong peak around $y = 0.8y_{1/2}$ in agreement with the Reynolds stresses presented in Fig. 5.6. The turbulent kinetic energy generated at the peak of production is advected to the jet centerline through entrainment velocity while turbulent diffusion spread the turbulent kinetic energy to both the jet centerline and the jet edge. At the center of the jet, turbulent fluctuations are maintained solely through advection and turbulent diffusion. The low value of the unbalance among all terms (—Unbalance, in Fig. 5.7(a)) points out that the simulation is capturing all the physical mechanism in which turbulence is produced, dissipated and transported.

A 8^{th}-order filter described in Gaitonde and Visbal (1999) is used in order to damp high-wavenumber noise enhancing the robustness of the solution. High-order filters in direct numerical solutions have been used in other studies (Shan et al. (2005); Gruber et al. (2012); Yoo et al. (2011); Garmann and Visbal (2014); Castela et al. (2016)). Such an approach is preferred instead of replacing the 4th-order centerered numerical scheme by more dissipative numerical scheme for all wavelength. The fact that the balance of kinetic energy in Fig. 5.7 satisfactorily closes is already a good indicator that most of the dissipation can be attributed to the physical viscous dissipation, and not to the numerical dissipation introduced by the retained discretization scheme or filtering. However, a look at the spectra is also a safe check. Thus, the spectrum of the isothermal jet along the homogeneous spanwise direction of the streamwise velocity fluctuations at $x = 10\delta$ in the jet centerline adimensionalized by the centerline excess velocity ΔU_c and the jet half width $y_{1/2}$ is compared with the spectra results of a plane jet from Stanley et al. (2002) in Fig. 5.8(a). Since Stanley et al. (2002) reported temporal spectra and assumed the Taylor hypothesis to obtain $E(k)$, the fact that their spectra captures wavenumbers lower than the present spectra corresponds to the choice of the averaged period. This same Figure shows that the present DNS simulation improves the resolution of the dissipative region of the spectrum when compared with the results of Stanley et al. (2002). Moreover, Fig. 5.8(b) shows the dissipation spectra (scaled by the Kolmogorov length $\eta \equiv \left(\frac{(\mu/\rho)^3}{\epsilon}\right)^{1/4}$ and velocity $u_\eta = (\epsilon\nu)^{1/4}$ scales), in which the dive of the profile occurs at a location close to the expected wavenumber when compared to reference spectra presented in Fig. 5.8(c) from Pope (2001). Note that the highest wavenumbers of the present dissipation spectra consistently correspond to the highest wavenumbers of the dissipation spectra presented in Pope (2001). This is a demonstration that, yet again, the impact of the high-order filter is negligible on the reported results.

5.2 DNS of the uncoupled heated plane jet

5.2.1 Introduction

Variable-density free shear flows, as opposed to the constant-density ones, have received less attention despite its broad engineering importance associated with

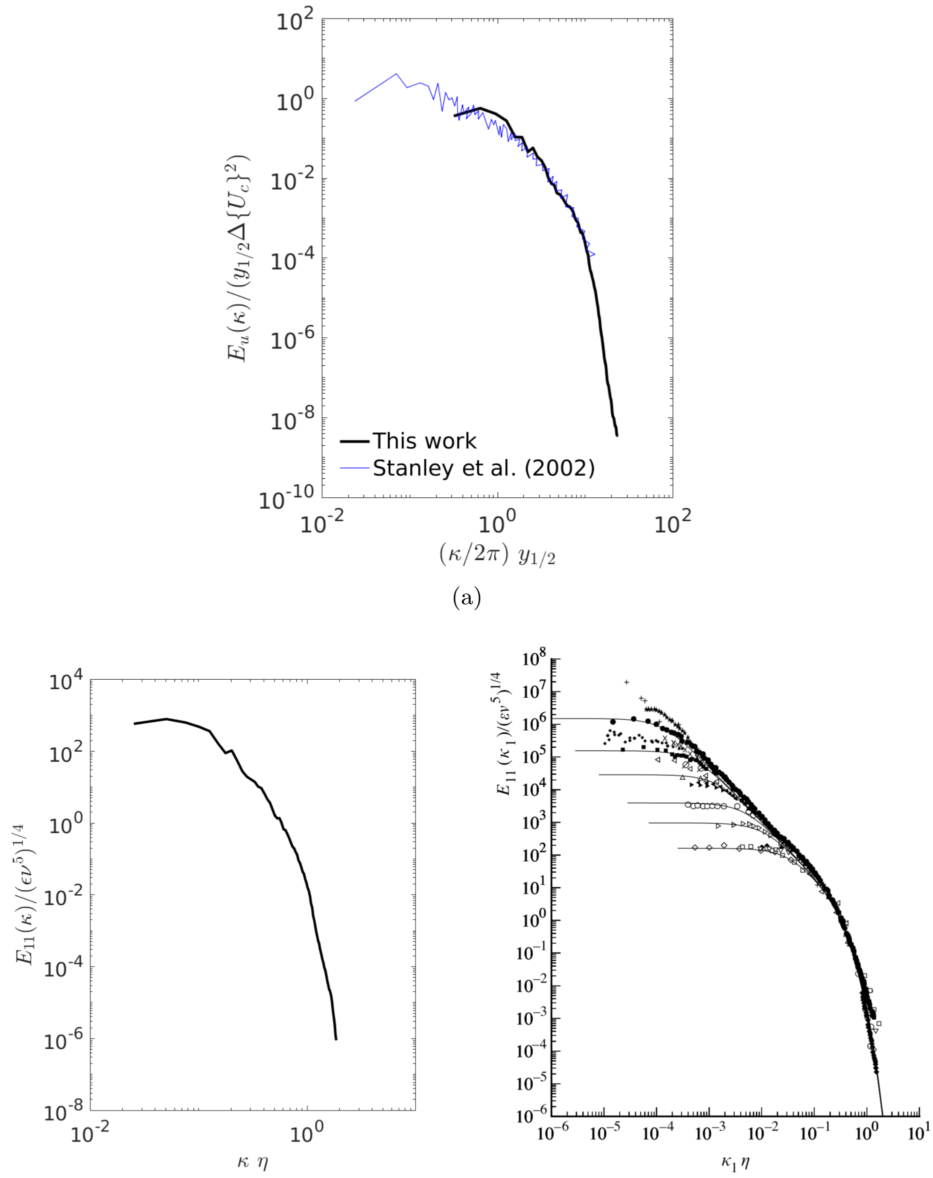

(a)

(b)

(c)

Figure 5.8: *(a) One-dimensional spectrum along the homogeneous spanwise direction of the centerline longitudinal velocity fluctuations at $x = 10\delta$ adimensionalized by the centerline excess velocity ΔU_c and the jet half-width $y_{1/2}$. (b) Dissipative spectra scaled by the Kolmogorov length scale $\eta \equiv \left(\frac{(\mu/\rho)^3}{\epsilon}\right)^{1/4}$ and velocity scale $u_\eta \equiv (\epsilon\nu)^{1/4}$ of the centerline spanwise velocity fluctuations at $x = 10\delta$. (c) Reference dissipation spectrum showing previous results from several sources (extracted from Pope (2001)).*

the mixing process. For the case of free jets, initial density differences are typically imposed by jet gas composition or by heating the jet fluid. The work of Chen and Rodi (1980) showed that when jet and ambient densities differ significantly self-similarity is not achieved. Nevertheless, for a sufficient distance downstream, density gradients across the flow decreases and thus the solution asymptotically approaches self-similarity if scaled by an effective radius which compensates the effects of density as explained in the work of Thring and Newby (1953). Richards and Pitts (1993) experimentally investigated variable-density axisymmetric jets with density ratio between 0.138 and 1.552. They analyzed data from downstream distances at which the local density ratio of the jet to ambient fluid approached unity achieving to characterize the self-similar solution of both mean and fluctuations values of a passive scalar field. Experimental works of Jenkins and Goldschmidt (1973), Davies et al. (1975) and Antonia et al. (1983) addressed the variable-density plane jet considering slightly heated jets with density ratios between 0.8 and 0.9, i.e., temperature is considered as a passive scalar causing little effects on the evolution of the flow field. They found similarity profiles of temperature using the classical scaling law since density gradients were low. All these authors found that the spreading rate based on temperature is larger than the one based on velocity. The stability of variable-density plane jets has been experimentally studied by Yu and Monkewitz (1993) for density ratio between 0.73 and 1, and Raynal et al. (1996) within a range for the density ratio of 0.14 - 1. They found that the oscillating regime disappears above a critical value of the density ratio which increases with the Reynolds number.

In the case of the studied heated jet, one is interested in the turbulent mixing of the temperature field. Additionally, the associated variable density field can modify the turbulent transfer of momentum and make the temperature mixing deviate from the behavior of a passive scalar in a turbulent jet.

5.2.2 Configuration and numerical setup

The current heated jet of water vapor has a very similar configuration than the isothermal one and uses the same numerical tools. Thus, in this section the new features introduced by the heated jet are hihglighted and some relevant aspects of the simulation are recalled. For more details of the configuration and numerical setup see §5.1.2.

The current setup for the heated jet is detailed in Table 5.3 which corresponds to the slightly heated jet setup discussed in Chapter 4.

Table 5.3: *Setup configuration of the isothermal turbulent plane jet.*

δ [m]	U_1 [m/s]	U_2 [m/s]	T_1 [K]	T_2 [K]	Re	P_0 [atm]
$5 \cdot 10^{-2}$	4.176	$U_1/10$	860	380	1500	1

As for the RANS simulations presented in Chapter 4, the inlet temperature profile that defines the heated jet is

$$T_{in}(y) = \frac{T_1 + T_2}{2} + \frac{T_1 - T_2}{2} \tanh\left(\frac{\delta/2 - |y|}{2\theta}\right). \tag{5.8}$$

The inlet profile of the Favre average excess temperature defined as $\{T_e\} = \{T\} - T_2$ adimensionalized by the Favre average excess temperature at the jet centerline $\Delta\{T_c\} = \{T_c\} - T_2$ is presented in Fig. 5.9(a). Similarly, the mean density profile at the inlet is shown in Fig. 5.9(b).

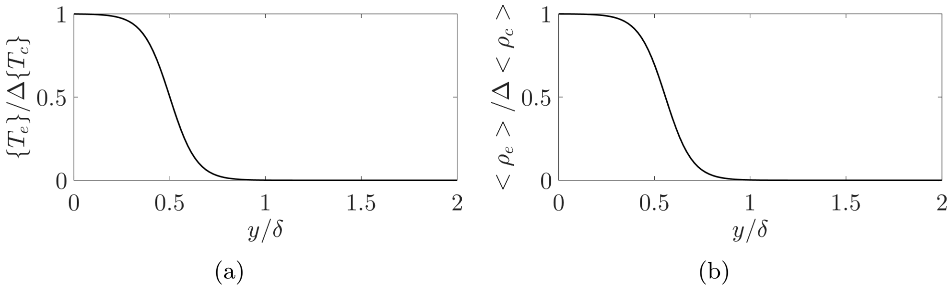

Figure 5.9: *Cross-section profiles of mean (a) temperature and (b) density at the inlet boundary.*

Specifications of the boundary conditions and the computation domain for the heated jet are presented in Fig. 5.10.

The retained mesh for the uncoupled heated jet is anticipated from scaling laws of both the decaying temperature and velocity reported by Jenkins and Goldschmidt (1973). Similar to the isothermal jet, $T_c(x)$ and $U_c(x)$ are predicted for the present inlet values. Then, estimating the dimensionless turbulent kinetic energy dissipation ϵ^* from previous DNS results (Stanley et al. (2002)), ϵ can be scaled for the present simulation. The local grid spacing along x-axis is set to be shorter than twice the local Kolmogorov scale. The grid spacing along y-axis is such that the inner region of the jet ($y < y_{1/2}(x)$) is as much refined as in the x direction. Finally, the grid spacing along z-axis is uniform and equal to $\Delta z = \delta/50$, which is a close value to the Δx and Δy averages.

The paramater α needed to setup the the acoustic speed reduction method is set to $\alpha = 8$.

5.2.3 DNS results of the uncoupled heated jet

In this section, the solution of the heated jet is compared with reported experimental data of the slightly heated plane jet and numerical data of the evolution of a passive scalar field in a plane jet. Mean results of the uncoupled heated jet are computed by averaging the data over approximately $\tau = 2.4$ s of physical time, which is equivalent to 11 flow time units.

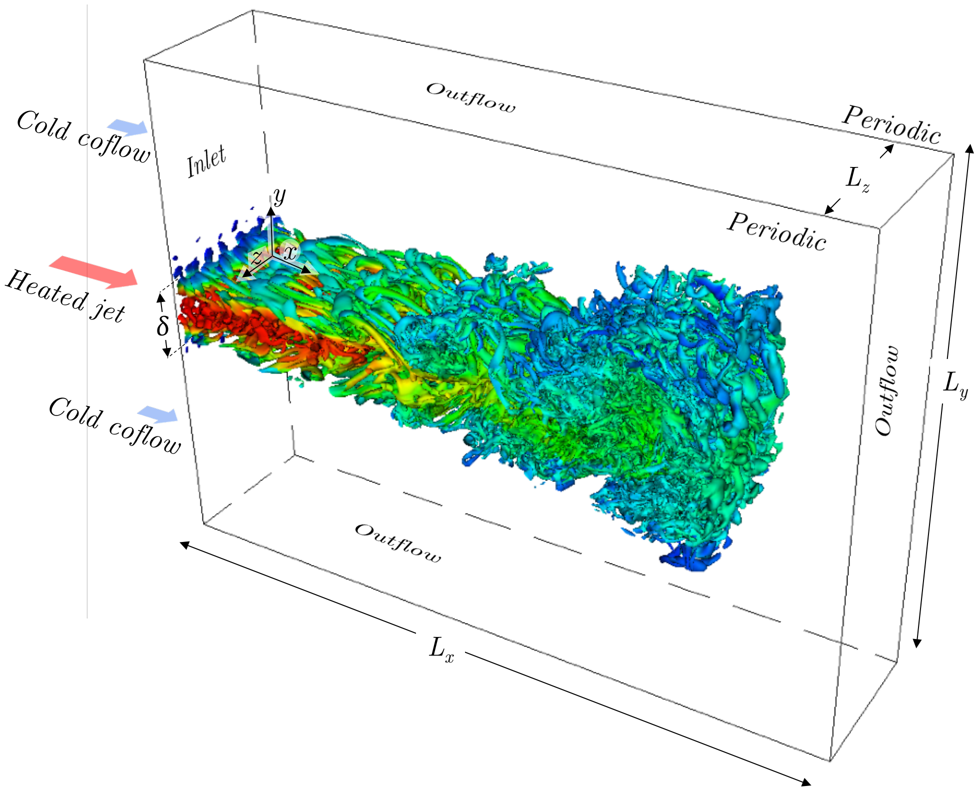

Figure 5.10: *Schematic representation of boundary conditions in a snapshot of turbulent eddies identified by the Q-criterion coloured by temperature.*

Figure 5.11 describes key features of the downstream evolution of mean temperature and compares them with numerical results of Stanley et al. (2002) who analyzed the evolution of a passive scalar field using a unity Schmidt number, and with experimental results of a heated plane jet of Browne et al. (1983) who set an initial excess temperature of $\Delta T_0 = T_1 - T_2 = 25$ K. Similar to the jet half-width based on the mean streamwise velocity $y_{1/2}$, the half-width based on temperature $y_{1/2,T}$ is the distance from the center of the jet where the corrected temperature $\{T_e\} = \{T\} - T_2$ is half the corrected temperature at the jet center $\Delta\{T_c\} = \{T_c\} - T_2$. In Figure 5.11(a), results of the evolution of the half-width of the jet based on temperature are compared with the numerical results of Stanley et al. (2002) and the experimental data of Browne et al. (1983). The results of the current heated jet show a slow initial developing when compared with the data of Browne et al. (1983) and Stanley et al. (2002) in which the half-width linear growth appears beyond $x = 4\delta$ and $x = 6\delta$, respectively; while for the present results linear growth is shown beyond $x = 7\delta$. As for the results of the velocity fields in the isothermal plane jet, the strong dependency of the initial developing zone on the inflow conditions explains the scatter among the different works, while the slope of the downstream evolution of $y_{1/2,T}$ compares well with previous works. Figure 5.11(b) shows the temperature decay in the jet centerline in which $\Delta T_0 = T_1 - T_2$ and $\Delta\{T_c\} = \{T_c\} - T_2$. The results of the temperature decay are in good agreement with the mean scalar decay of Stanley et al. (2002). Results of the temperature decay of Browne et al. (1983) have a faster initial developing, probably due to the inflow conditions, while the decay rate is greater than the decay predicted by both the current numerical results and the simulation of Stanley et al. (2002).

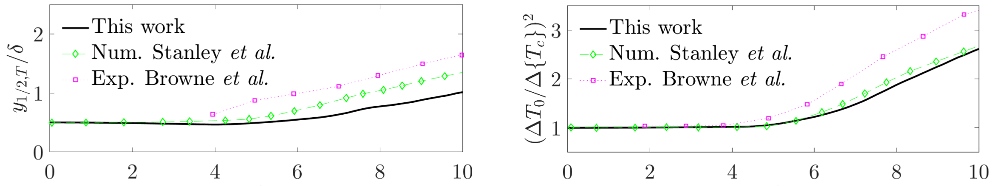

(a) (b)

Figure 5.11: *Downstream evolution of mean temperature field: (a) jet spread based on temperature and (b) temperature decay along the jet centerline.*

In Figure 5.12(a), the Favre averaged temperature corrected by the coflow temperature $\{T_e\} = \{T\} - T_2$ adimensionalized by $\Delta\{T_c\} = \{T\}_{y=0} - T_2$ is plotted against $y/y_{1/2,T}$ at $x = 10\delta$ and compared with experimental results from Davies et al. (1975) who set an initial excess temperature of $\Delta T_0 = 14.6$ K, the experimental study of Jenkins and Goldschmidt (1973) that fixed this value to $\Delta T_0 = 20.7$ K, and the experimental results of Antonia et al. (1983) with an excess temperature at the inlet section of $\Delta T_0 = 25$ K; while the excess temperature in the current simulation is $\Delta T_0 = T_1 - T_2 = 480$ K. Despite the ΔT_0 disparity among the present work and the values found in the literature, the dimensionless temperature profile is in good agreement with experimental results. Additionally, Figure 5.12(b) compares the downstream evolution of the temperature fluctuations along the jet centerline with experimental results of Browne et al. (1983), and numerical data of Stanley et al. (2002). Results from Browne et al. (1983) have a faster initial developing and a higher fluctutions intensity, this may explain the results of the temperature decay presented in Fig. 5.11(b). The current results of temperature fluctuations have the same tendency as previous data, which is a strong growth of the fluctuations at the end of the initial developing zone followed by a slow decay downstream.

Integrating the x-momentum boundary-layer equation with respect to y, the momentum flow rate per unit span, defined as $\int_{-\infty}^{+\infty} \langle \rho u^2 \rangle dy$, is constant along the streamwise direction of the plane jet. Due to the presence of a coflow stream, this quantity is infinite and is here replaced by

$$M_x = \int_{-\infty}^{+\infty} \left(\langle \rho u^2 \rangle - \rho_2 U_2^2 \right) dy, \tag{5.9}$$

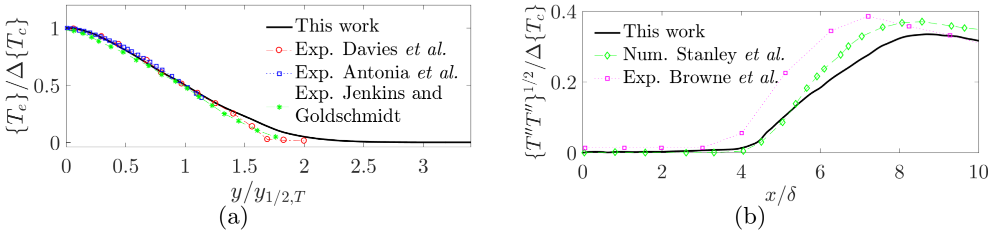

Figure 5.12: *(a) Dimensionless Favre averaged temperature profiles of the heated plane jet without including radiation at $x = 10\delta$. (b) Downstream evolution of temperature fluctuations at the jet centerline.*

Results of the momentum flow rate adimensionalized by its value at the initial cross-section are presented in Fig. 5.13 for both the isothermal and the heated jets. Additionally, an horizontal dashed line corresponding to the ideal behaviour of the jet is included in Fig. 5.13. As expected, the momentum flow rate is almost constant along the streamwise direction for both cases, i.e., M_x deviations from the ideal plane jet are less than 1.3%.

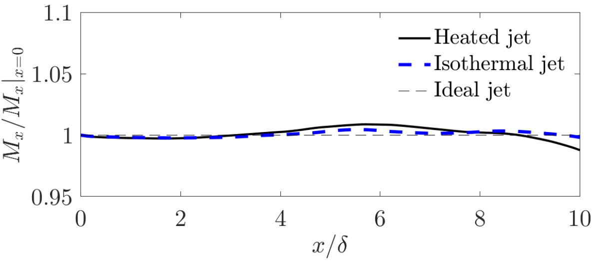

Figure 5.13: *Evolution of momentum flow rate per unit span along x direction.*

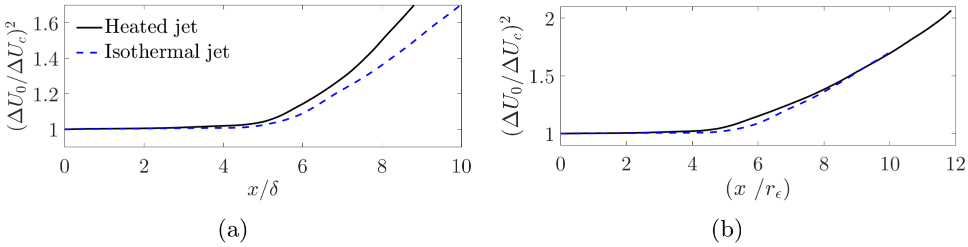

Figure 5.14: *Centerline velocity decay against (a) x/δ and (b) x/r_ϵ.*

As detailed in the work of Foysi et al. (2010), the conservation of momentum flux in the developed region yields that the ratio between $\langle\rho_c\rangle\Delta\{U_c\}^2 y_{1/2}$ and $\rho_0\Delta U_0^2\delta$ is constant, where $\langle\rho_c\rangle$ is the mean density at the jet centerline and ρ_0 is the jet density at the exit nozzle. Defining an equivalent jet opening of $r_\epsilon = \delta\left(\overline{\rho_0}/\langle\rho_c\rangle\right)$, in which the exit nozzle density is considered as $\overline{\rho_0} = \frac{1}{\delta}\int_\delta \rho_{|x=0}\,dy$, since the density at the exit nozzle is not constant. As reported in the work of Richards and Pitts (1993), r_ϵ can be interpreted physically as the width opening of a hypothetical jet of density $\langle \rho_c \rangle$ with the same initial mass and momentum fluxes as the jet under consideration. Then, the conservation of momentum flux can be written as

$$\frac{\Delta \{U_c\}^2 y_{1/2}}{\Delta U_0^2 r_\epsilon} \sim constant, \tag{5.10}$$

As shown in Fig. 5.14, the velocity decays of the heated and isothermal jets almost collapse on the same curve when $(\Delta U_0 / \{U_c\})^2$ is plotted against x/r_ϵ (Fig. 5.14(b)), while these curves have a clearly different slope when plotted against x/δ (Fig. 5.14(a)). Note, that the scaled velocity decay of the heated jet in Fig. 5.14(b) has values beyond $x = 10 r_\epsilon$ since $r_\epsilon < \delta$.

5.3 Conclusions

The suitableness of the DNS numerical setup has been demonstrated by analyzing in detail uncoupled isothermal and heated jets. First, velocity and Reynolds stresses profiles of the isothermal plane jet are validated by comparison with previous experimental and numerical studies. Additionally, the turbulent kinetic energy balance of the isothermal jet is checked and each term is compared with available data. The spectrum of turbulent kinetic energy adimensionalized by the large scales of the flow compares very well with previous works of Stanley et al. (2002); while the dissipation spectra show that the impact of the high-order filter is negligible on the reported results.

Regarding the heated jet without including radiation, the profile of mean temperature and the downstream evolution of temperature fluctuations are compared with previous experimental works. The constancy of the momentum flow rate per unit span is checked for the isothermal and heated jets. Moreover, the scaled velocity decay of the heated and isothermal jets collapses almost onto the same curve.

The inlet velocity profile is here combined with artificial turbulence to shorten the domain with a quick destabilization of the potential core to yield a reduced computational time. Despite the limited extent of the present domain; the obtained profiles of first and second order moments of velocity fields beyond $x = 8\delta$ compare quite well with previous self-similar profiles, and besides, linearity in the velocity decay rate and the jet half-width growth is observed in the region $8\delta \leq x \leq 10\delta$.

Chapter 6

Accuracy assessment of uncoupled radiative power field computations

Stand-alone Monte-Carlo computations are here presented in order to assess the accuracy of the exchanged radiative energy solution. Firstly, the spectral radiative properties of water vapor computed using the ck model are validated by comparison with line-by-line (LBL) results. Then, results varying key parameters of the Monte-Carlo solver are analyzed in order to ensure the accuracy of the radiative power field calculations. The analyzed parameters are the maximum number of rays issued from a node, the choice of the boundary conditions for the radiative solver, and the effects of considering a coarser mesh for the radiative computations. After that, the transmissivity of the water vapor for the problem scale is analyzed together with the emitted intensity as a function of temperature and wavenumber. Finally, the criteria for the statistical convergence of the Monte-Carlo are discussed for the slightly and strongly heated jets.

Contents

6.1 Ck accuracy

Detailed spectral data provides the absorption coefficient for up to one million wavenumbers. The most detailed radiative calculation consists in solving the radiative transfer problem for each line in the spectrum followed by integration over the spectrum, this is the so-called "line-by-line" (LBL) method. In most of the cases, LBL calculations are too computationally intensive in coupled three-dimensional simulations. However, such calculations yields high-resolution computations useful to quantify the accuracy of simplified methods. Thus, the ck model used to estimate the spectral radiative properties of water vapor described in Chapter 3 is first validated by comparison with LBL results presented in the work of Soufiani and Taine (1997) and the LBL database HITEMP from Rothman et al. (2010) updated by Rivière and Soufiani (2012). Figure 6.1 compares LBL results from the aforementioned works of the transmissivity of an isothermal and homogeneous $H_2O - N_2$ ($X_{H_2O} = 0.5$) column of length $l = 0.5$ m at a pressure of 1 atm and a temperature of 1000 K, with the results obtained using the present ck model. For this specific mixture, a good agreement between the ck and the LBL computations is observed over all the spectrum.

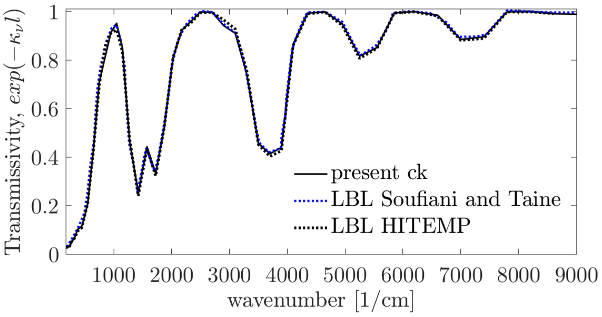

Figure 6.1: *Comparison of ck model results of the spectral transmissivity of an isothermal and homogeneous column $X_{H_2O} = 0.5$ of length $l = 0.5$ m at 1000 K with LBL data from Soufiani and Taine (1997) and HITEMP (2010).*

Once a reference test case is validated, the current ck model is compared with LBL results for representative conditions of the slightly heated jet, involving temperature between 380 and 860 K. Figures 6.2(a), 6.2(b) and 6.2(c) compare the transmissivity of a water vapor column of lenght $l = 0.05$ m at a pressure of 1 atm and temperatures of 860, 620 and 380 K, respectively, between the current ck model and the LBL database HITEMP Rothman et al. (2010) updated by Rivière and Soufiani (2012). For the three analyzed temperatures the current ck model is in very good agreement with LBL results over all the spectrum.

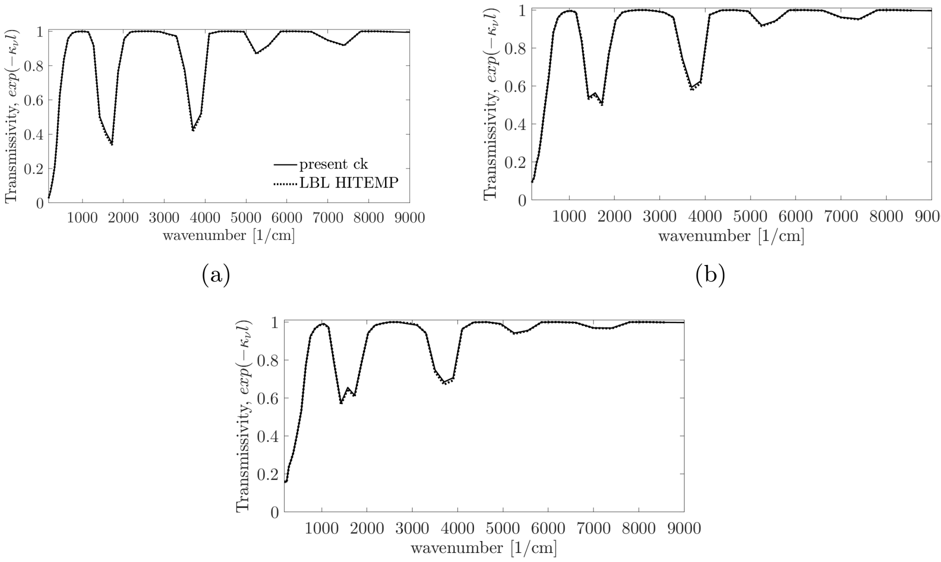

(a)

(b)

(c)

Figure 6.2: *Comparison of ck model results of the spectral transmissivity of an isothermal and homogeneous water vapor (X_{H_2O} = 1) column of length l = 0.05 m at a pressure of 1 atm and temperatures of (a)* 380 *K, (b)* 620 *and (c)* 860 *K.*

6.2 Effects of increasing the maximum number of rays issued from a node

The effects of increasing the maximum number of rays issued from a node are analyzed for the slightly and the strongly heated jets in the framework of the Emission-based Reciprocity Monte-Carlo Method. To do so, the radiative power field has been computed for a given instantaneous temperature field setting the maximum number of rays to 2.5×10^3 and 5×10^3 while keeping constant all other parameters.

Figure 6.3 shows instantaneous slices of the radiative power for the slightly heated jet when a maximum number of rays of 2.5×10^3 and 5×10^3 are set. Analogously, Fig. 6.4 shows instantaneous slices of the radiative power for the strongly heated jet. No significant qualitative differences can be observed between the 2.5×10^3 and 5×10^3 cases for both jets.

Additionally, for the slightly heated jet, downstream and cross-section profiles of the instantaneous radiative power are shown in Fig. 6.5 for a maximum number of 2.5×10^3 and 5×10^3.

Figure 6.6 show again the downstream evolution of the instantaneous radiative power at the jet centerline, and its cross-section profile at $x = 10\delta$ for the strongly heated jet.

From these results, it can be seen that despite some small relative difference can

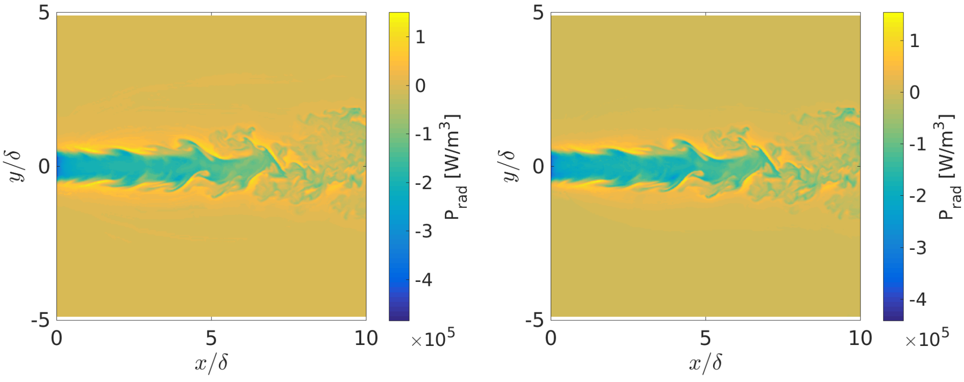

(a)

(b)

Figure 6.3: *Instantaneous radiative power field at* $z = 0$ *for the slightly heated jet when a maximum number of (a)* 2.5×10^3 *and (b)* 5×10^3 *are issued from each node.*

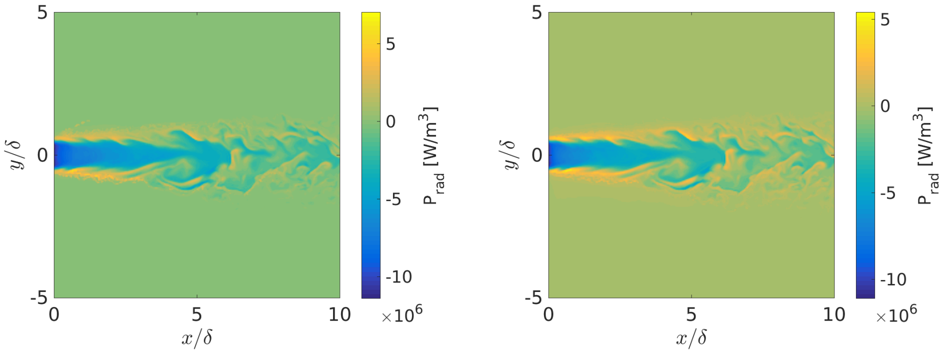

(a)

(b)

Figure 6.4: *Instantaneous radiative power field at* $z = 0$ *for the strongly heated jet when a maximum number of (a)* 2.5×10^3 *and (b)* 5×10^3 *are issued from each node.*

be observed when varying the maximum number of rays, a maximum number of 2.5×10^3 rays captures accurately the trends of the radiative power. Hence, a maximum number of 2.5×10^3 rays is retained for the slightly and the strongly heated jets in order to keep a feasible amount of computational time.

6.3 Accuracy of thermal radiative boundary conditions

Inlet and outflow boundary conditions are not straightforward and need strong assumptions to close the radiative transfer equation in open boundaries. Physically, the open boundary conditions would have to let the ray get outside the

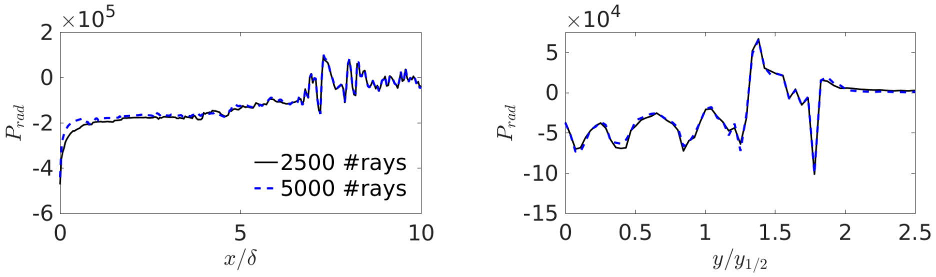

(a) (b)

Figure 6.5: *Radiative power results comparison for the slightly heated jet between a maximum number of* 2.5×10^3 *and* 5×10^3 *issued from each node. (a) Downstream evolution of the radiative power and (b) cross-section profiles of radiative power at* $x = 10\delta$.

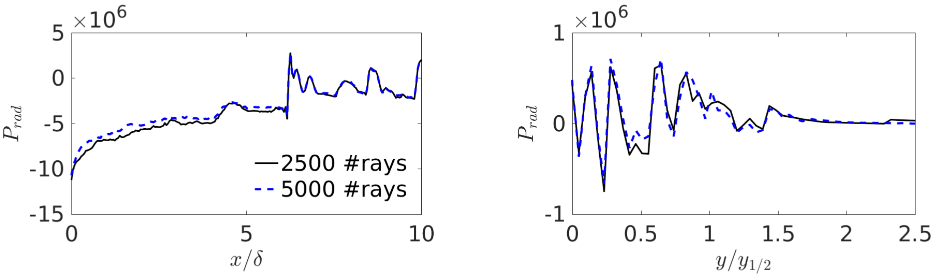

(a) (b)

Figure 6.6: *Radiative power results comparison for the strongly heated jet between a maximum number of* 2.5×10^3 *and* 5×10^3 *issued from each node. (a) Downstream evolution of the radiative power and (b) cross-section profiles of radiative power at* $x = 10\delta$.

domain without reflexion, while accounting for all the emission corresponding to the outer infinite extension outside the computational domain. To approach this behavior, two different boundary conditions have been implemented and a comparison between them using the Emission-based Reciprocity Monte-Carlo Method is here presented in order to justify our choice. The first approach is to set black-body boundary conditions at the local temperature, hereinafter referred as variable temperature boundary conditions. The second approach consists in setting black-body boundary condition at the coflow temperature, hereinafter referred as isothermal boundary conditions.

Figure 6.7 presents instantaneous slices at $z = 0$ of the radiative power for the case of isothermal black boundaries for the slightly and the strongly heated jets in Figs. 6.7(a) and 6.7(b), respectively. Comparing theses fields with the corresponding radiative power fields using variable temperature boundary conditions already presented in Fig. 6.3(a) for the slightly heated jet and Fig.

6.4(a) for the strongly heated jet, it can be seen that the effect of isothermal boundaries is restricted to the surroundings of the inlet jet region.

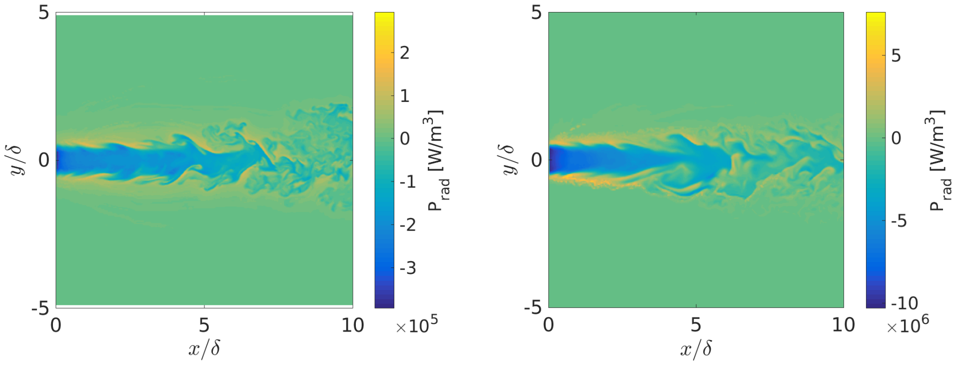

(a) (b)

Figure 6.7: *Instantaneous radiative power field at $z = 0$ when isothermal black boundaries are considered in (a) the slightly heated jet and (b) strongly heated jet.*

In order to quantify the effect of the boundary condition choice, Fig. 6.8 shows the radiative power along the jet centerline for the slightly and the strongly heated jets. On both cases, the boundary condition specification have a strong effect at the initial region of the jets. However, such effect is restricted at the very beginning of the jet. As shown in Fig. 6.9, the effect of the radiative boundary condition on the cross-section profiles at $x = 10\delta$ is negligible for both the slightly and the strongly heated jets.

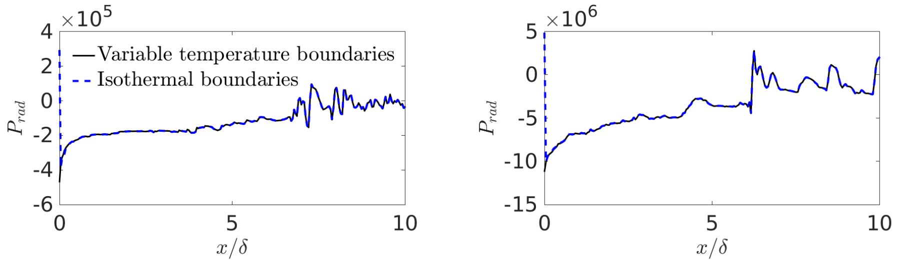

(a) (b)

Figure 6.8: *Radiative power results comparison between variable temperature and isothermal approaches for the radiative conditions on the open boundaries. Downstream evolution of the radiative power for (a) the slightly heated jet and (b) the strongly heated jet.*

In order to avoid the unphysical peak at the surroundings of the inlet jet region, the variable temperature boundary condition approach for the inlet and outflow boundaries is retained in this work.

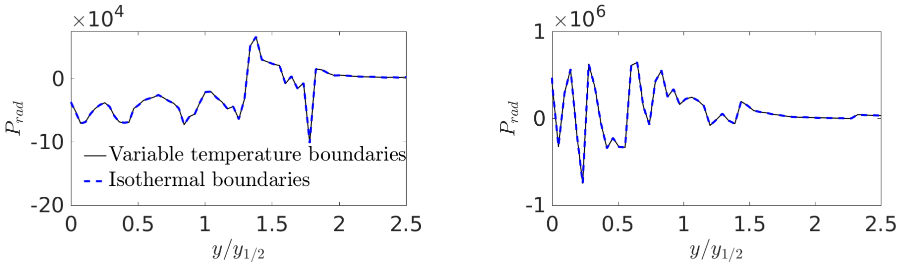

(a) (b)

Figure 6.9: *Radiative power results comparison between variable temperature and isothermal approaches for the radiative conditions on the open boundaries. Cross-section profiles of radiative power at $x = 10\delta$ for (a) the slightly heated jet and (b) the strongly heated jet.*

6.4 Radiative mesh independence study

The effects of considering a coarser mesh for the radiative computations in the framework of the Emission-based Reciprocity Monte-Carlo Method are analyzed in this section. The coarser radiative mesh consists in taking one out of two nodes in each direction from the DNS mesh. In Table 6.1 all the information regarding the DNS and radiative meshes for the slightly and the strongly heated jets is gathered.

Table 6.1: *Mesh size for the slightly and the strongly heated jets.*

		Slightly heated	**Strongly heated**
DNS Mesh	Nodes on $x \times y \times z$	566×469×149	$514 \times 401 \times 121$
	Total num. nodes	39.5×10^6	24.9×10^6
Rad. Mesh	Nodes on $x \times y \times z$	$282 \times 235 \times 75$	$257 \times 201 \times 61$
	Total num. nodes	4.97×10^6	3.15×10^6

In order to assess the independence of the radiative solution from the used mesh, radiative power fields have been computed for both jets using the aforementioned DNS and coarser radiative meshes for a given instantaneous temperature field. Then, a comparison of the instantaneous radiative power downstream evolution along the jet centerline for both meshes is presented in Fig. 6.10(a) for the slightly heated jet, while cross-section profiles of instantaneous radiative power at $x = 10\delta$ computed on both meshes are shown in Fig. 6.10(b). Analogously, the same comparison for the strongly heated jet is presented in Fig. 6.11.

From the results presented in Figs. 6.10 and 6.11, it can be seen that despite some small relative difference between both meshes are observed, the coarse mesh is able to correctly capture the trends of the radiative power. Also note that the impact of using a coarser mesh for the radiative solver is more im-

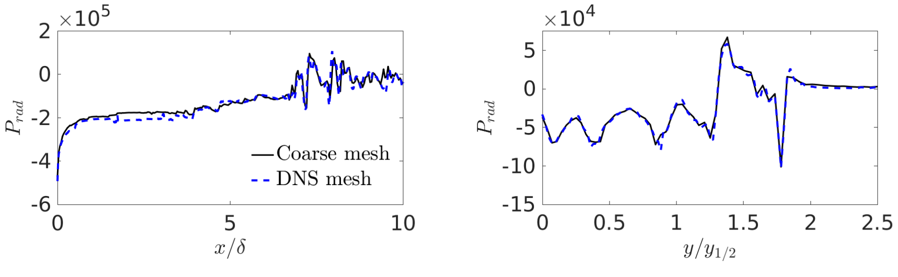

(a) (b)

Figure 6.10: *Radiative power results for the slightly heated jet comparison between the coarse and refined meshes for the radiative computations. (a) Downstream evolution of the radiative power and (b) Cross-section profiles of radiative power at* $x = 10\delta$

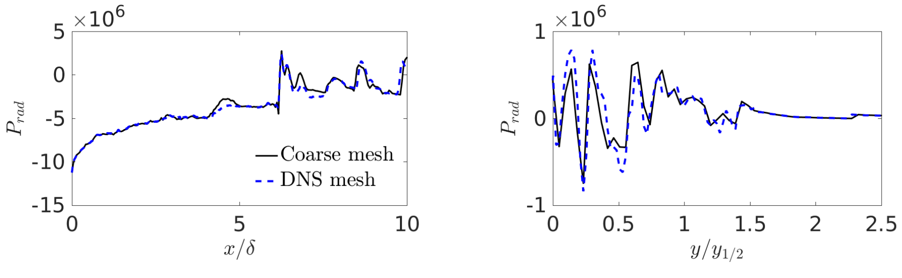

(a) (b)

Figure 6.11: *Radiative power results for the strongly heated jet comparison between the coarse and refined meshes for the radiative computations. (a) Downstream evolution of the radiative power and (b) Cross-section profiles of radiative power at* $x = 10\delta$

portant for the strongly heated jet. Despite the degradation on accuracy, the coarse mesh is retained in this study since radiative computations in the DNS mesh increases by a factor of 8 the required computational memory and the processing time when compared with the coarse mesh.

6.5 Radiative transfer nature of water vapor under the studied conditions

The radiative properties of a medium strongly affect the exchanged radiation and the behavior of TRI effects as explained in the works of Coelho (2007); Modest and Haworth (2016). In order to characterize the nature of the radiative transfer in the configuration under study, the spectral transmissivity of water vapor based on the initial jet width ($\delta = 0.05$ m) is computed following Eq. 3.11 using the present ck model for the slightly and strongly heated jets.

Figure 6.12 characterizes the radiative properties of the slightly heated jet by showing in Fig. 6.12(a) the spectral transmissivity based on the initial jet width for the maximum (860 K) and minimum (380 K) temperatures at a pressure of 1 atm. Additionally, the spectral Planck functions for these temperatures are presented in Fig. 6.12(b) adimensionalized by its maximum value.

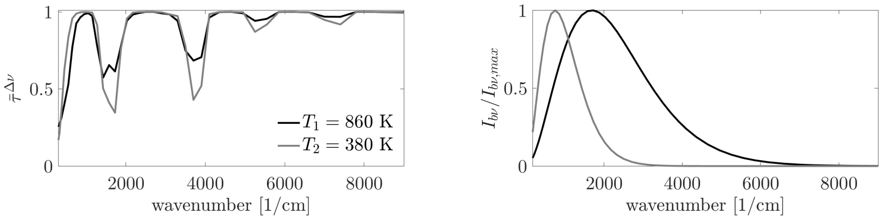

(a) (b)

Figure 6.12: *For a pressure of 1 atm and the maximum and minimum temperatures of the slightly heated jet: (a) comparison of the spectral transmissivity of water vapor based on the initial jet width, and (b) spectral Planck functions adimensionalized by its maximum value.*

Likewise, the spectral transmissivity based on the initial jet width for the maximum (2500 K) and minimum (405 K) temperatures at a pressure of 2.87 atm characterizing the strongly heated jet are presented in Fig. 6.13(a) and the corresponding dimensionless spectral Planck functions for these temperatures are plotted in Fig. 6.13(b).

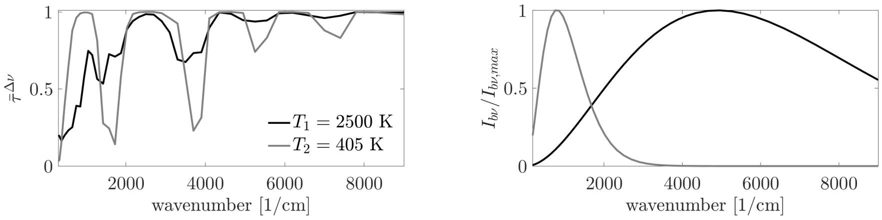

(a) (b)

Figure 6.13: *For a pressure of 2.87 atm and the maximum and minimum temperatures of the strongly heated jet: (a) comparison of the spectral transmissivity of water vapor based on the initial jet width, and (b) spectral Planck functions adimensionalized by its maximum value.*

From Figs. 6.12(a) and 6.13(a), it can be seen that regardless of the temperature, water vapor tends to be optically thick at low wavenumbers ($\lesssim 500\ 1/cm$), and it presents two "peaks" of moderate optical thickness around wavenumbers of 1500 cm^{-1} and 3800 cm^{-1}. As temperature increases, these "peaks" of optical thickness decrease; while, as expected, when pressure increases, the transmissivity decreases. Additionally, Figs. 6.12(b) and 6.13(b) show that temperature shifts the peaks of emission towards higher wavenumbers and smooths the Planck function. Then, most of the emitted radiation comes from hot regions of the fluid (corresponding to the peaks of 1500 cm^{-1} and 3800 cm^{-1}). If the rays emitted in hot regions are not reabsorbed in the vicinity of the emission point, they are likely to be absorbed in the colder region, being that low temperature fluid parcels have low transmissivity at those wavenumbers (1500 cm^{-1} and 3800 cm^{-1}), as shown in Figs. 6.12(a) and 6.13(a).

Note that the radiative properties dependency on wavenumber can be even stronger than the dependency on temperature for the present temperature range, which points out the need for an spectral model rather than a gray gas model to accurately account for radiative heat transfer.

6.6 Monte-Carlo statistical convergence

An interesting feature of the Monte-Carlo method for solving the RTE is that it provides a local control of the convergence which determines the statistical error of the solution. In the present simulations, several criteria for considering the statistical convergence of the radiative simulations are defined. First, if the relative standard deviation of the local estimated radiative power is lower than 5 %, the solution is considered converged. However, in regions where this criterion is not achieved, an absolute value of the standard deviation of the local estimated radiative power is considered. This value has been chosen to be approximately 0.5% of the maximum value in magnitude of the radiative power in the domain. Finally, if these two criteria are not accomplished at a specific grid point, a maximum of 2.5×10^3 rays are considered as discussed before in this Chapter.

For a given instantaneous field of temperature and the convergence criteria specified above, the local number of rays issued to compute the radiative power using the Emission-based Reciprocity Monte-Carlo Method is shown in 6.14(a) for the slightly heated jet; while the relative statistical error of convergence, computed as the relative standard deviation of the local estimated P_{rad} (here denoted as P_{rad} rms), is presented in Fig. 6.14(b).

Similarly, the local number of rays to compute the radiative field for the strongly heated jet, as well as its associated relative standard deviation of the local estimated radiative power are shown in Figs. 6.15(a) and 6.15(b), respectively. As it can be seen in Figs. 6.14(a) and 6.15(a), the jet edges are the hardest regions to converge the radiative power. This is because its radiative power value is close to zero, which implies large values of relative standard deviation of the local estimated radiative power. And, at the same time, this region has a strong radiative heat exchange with inner regions of the jet. Furthermore, regions with more than 5% of relative standard deviation of the local estimated radiative power in Figs. 6.14(b) and 6.15(b) correspond to regions with P_{rad} close to zero that have been assumed converged either due to its absolute standard deviation of the local estimated radiative power or because the maximum number of rays issued from a point has been reached.

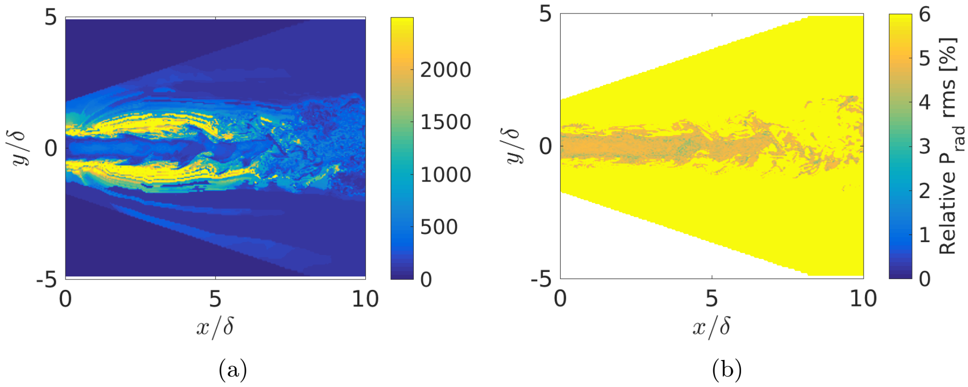

Figure 6.14: *Contour fields at* $z = 0$ *for the slightly heated jet related to the Monte-Carlo solution and its convergence. (a) Local number of rays and (b) relative standard deviation of the local estimated* P_{rad}.

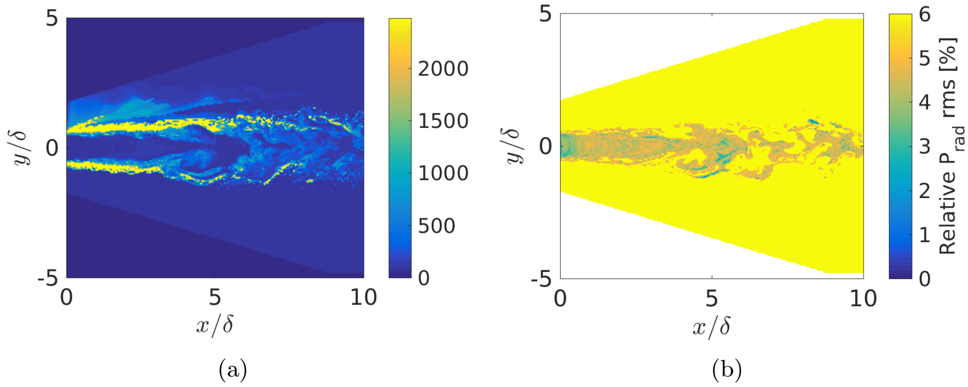

Figure 6.15: *Contour fields at* $z = 0$ *for the strongly heated jet related to the Monte-Carlo solution and its convergence. (a) Local number of rays and (b) relative standard deviation of the local estimated* P_{rad}.

6.7 Conclusions

In this Chapter, the accuracy of the Emission-based Reciprocity Monte-Carlo Method applied to the present configuration is discussed. A clear advantage of Monte Carlo methods is its inherent estimation of the remaining error, allowing to control it and attribute the necessary resources. The choices defining the setup are listed below.

- A maximum number of 2.5×10^3 rays issued from each node is retained in order to keep a feasible amount of computational time.
- Black-body boundary conditions at the local temperature are set to model the open boundaries.
- A coarser mesh to solve the radiative problem consisting in taking one

out of two nodes in each direction from the DNS mesh is retained to keep feasible coupled simulation in terms of computational cost.

- The solutions is considered converged when either the relative standard deviation of the local estimated radiative power is lower than 5 %, or the absolute standard deviation of the local estimated radiative power is lower than the 0.5% of the maximum value in magnitude of the radiative power in the domain.

Moreover, in this chapter, the ck model used to estimate the spectral radiative properties of water vapor has been validated by comparison with LBL results for three different temperatures. And, the nature of the radiative transfer has been assessed for the slightly and strongly heated jets.

Part III

Multiphysics simulation of free jets

Chapter 7

Scaling of heated plane jets with moderate radiative heat transfer in coupled DNS

The effects of thermal radiation in the slightly heated jet of water vapor are studied with a direct numerical simulation coupled to a Monte-Carlo solver. Radiative energy transfer is then accounted for with spectral dependency of the radiative properties described by the Correlated-k (ck) method. Between the direct impact through modification of the temperature field by the additional radiative transfer and the indirect one where the varied flow density changes the turbulent mixing, the present study is able to clearly identify the second one in the jet developed region by considering conditions where effects of thermal radiation are moderate. When using standard jet scaling laws, the different studied cases without radiation and with small-to-moderate radiative heat transfer yield different profiles even when thermal radiation becomes locally negligible. By deriving another scaling law for the decay of the temperature profile, self-similarity is obtained for the different turbulent jets. The results of this Chapter allow for distinguishing whether thermal radiation modifies the nature of heat transfer mechanisms in the jet developed region or not while removing the indirect effects of modified density.

Contents

7.1 Introduction

Radiative heat transfer can modify the jet scaling laws in two ways: first, a different nature and balance of the different heat transfer mechanisms, and secondly a variation in density due to the modified temperature field. In order to fully characterize the first phenomenon of high interest, it is necessary to establish scaling laws that can distinguish both mechanisms.

The present Chapter aims then at analyzing the scaling laws of turbulent heated jets without radiation and with moderate radiative transfer to consider mainly the second mechanism. The results will indeed show that moderate radiation effects can change the classical jet scaling laws in the fully developed region although thermal radiation can be locally negligible in this region. Without any adaptation of the jet scaling laws for variable density, one wrongly concludes about the modified balance of heat transfers in the studied case. This Chapter considers then another set of scaling laws and derives a new one for the mean temperature field in particular to make cases without radiation and with small-to-moderate radiative effects self-similar. These results allow for a future clear identification of larger radiation effects of the first kind.

In the considered case of this Chapter, a heated water vapor mixture discharges into a parallel low-speed coflow of cold water vapor. The numerical study is carried out with state-of-the-art fidelity to be as representative as possible of an actual jet in a participating medium. The turbulent jet is described by a direct numerical simulation (DNS) coupled to a reciprocal Monte-Carlo method to solve the radiative transfer equation. The spectral dependency of the radiative properties is accounted for with an accurate Correlated-k (ck) method.

7.2 Configuration

The jet studied in this Chapter corresponds to the slightly heated jet dimensionalized in Chapter 4 , which is prospecting for a modification of the temperature and density fields by the effects of radiation in the developing region affecting the jet downstream. But, at the same time, envisaging negligible radiation effects in the developed region in order to still achieving nearly self-similarity. The dimensioning also accounts for a feasible amount of CPU time.

At the inlet boundary, the jet width opening is set to $\delta = 0.05$ m. The jet has an initial mean velocity $U_1 = 4.176$ m/s and the mean coflow velocity is set to $U_2 = U_1/10$. The jet temperature is fixed to $T_1 = 860$ K, while the temperature in the coflow is $T_2 = 380$ K, this temperature range has been chosen based on typical values found in modern steam turbines (Tanuma (2017)). All simulations are carried out at atmospheric pressure (1 atm).
The corresponding Reynolds number based on the width opening δ is

$$\mathrm{Re} = \frac{\rho(T_1)\Delta U_0 \delta}{\mu(T_1)} = 1500, \tag{7.1}$$

where $\Delta U_0 = U_1 - U_2$.
Physical parameters describing the slightly heated jet computed in the present Chapter are summarized in Table 7.1, a schematic representation of the plane jet has been already presented in Fig. 4.1.

Table 7.1: *Configuration of the slightly heated jet.*

δ [m]	U_1 [m/s]	U_2 [m/s]	T_1 [K]	T_2 [K]	Re	P_0 [atm]
$5 \cdot 10^{-2}$	4.176	$U_1/10$	860	380	1500	1.0

7.3 Numerical setup

7.3.1 Fluid simulation

The current Numerical setup for the fluid simulation is the same than the one for uncoupled heated jet presented in Chapter 5. Then, numerical tools, fluid flow boundary conditions, computational mesh, domain size as well as the parameters for the ASR corresponds to ones retained for the uncoupled heated jet.

7.3.1.1 Radiation simulation settings

Because the computational cost of the Monte-Carlo method remains large, the grid to compute the radiative solution fields is based on a coarser mesh than the DNS one: one out of two points is considered in each direction. Then, the radiative solution is computed in 282 × 235 × 75 grid nodes in the x, y and z directions, respectively. The effects of considering a coarser mesh for the radiative computations are analyzed in Chapter 6.
One of the advantages of the retained ERM method is that only the bundles leaving a specific node are needed to estimate the local radiative power at this specific node. It is therefore possible to estimate the radiative power at one node without performing such estimation at all other nodes of the domain. In order to save computational power, the radiative power is only computed at

relevant points. The cross-stream coordinate y of these points is restricted to the range $[-4y_{1/2}(x), 4y_{1/2}(x)]$. Then, radiative calculations are performed in a volume that surrounds the jet and follows its growth.

Periodic boundary conditions are set in the spanwise direction: if a ray gets off the domain, for example at the point (x, y, L_z), it will get in at the point $(x, y, 0)$ with the same propagation direction. All other boundaries are treated as black-body at the local temperature of the node located in the boundary, this choice is discussed in Chapter 6.

An additional advantage of ERM is to allow the Monte-Carlo convergence to be locally controlled. The present radiative simulations are considered converged when a local error lower than 5 % of the radiative power is achieved. The error is characterized in terms of statistical standard deviation of the estimated quantity of interest. In regions where the mean radiative power is close to 0 and so the relative error is difficult to converge, an absolute value of the error of 2000 W/m^3 is considered to achieve convergence. This value corresponds to approximately 0.5% of the maximum value in magnitude of the radiative power in the domain. Finally, if these two criteria are not accomplished at a specific grid point, a maximum of 2.5×10^3 rays are considered. The choice of the convergence criteria are analyzed in Chapter 6.

7.3.2 Determination of the coupling period and computational load distribution among processors

A parallel coupling between the fluid flow solver and the radiative solver is used as discussed in Chapter 3. The optimal coupling period n_{cpl} is determined based on the Euclidean norm of $||P_{rad}^{i+N} - P_{rad}^{i}||_2$ adimensionalized by $||P_{rad}^{i}||_2 = \sqrt{\sum_{\vec{x} \epsilon \mathcal{D}} \left(P_{rad}^{i}(\vec{x})\right)^2}$ when increasing N. In Figure 7.1, it can be observed that after 58 iterations the radiative power field changes by around 5%. Because the radiative solution is considered converged when a local error lower than 5 % of the mean radiative power is achieved, a coupling period corresponding to $n_{cpl} = 58$ is retained.

Once the value n_{cpl} is fixed, the number of processors dedicated to each code should be set in order to minimize the time spent on waiting for MPI communications as explained in Chapter 3. The present simulation has been performed with a total of 216 processors. In the case of the coupled slightly heated jet simulation, 64 processors are attributed to the fluid flow solver while 151 are assigned to the radiation solver. The one processor left is in charge of the coupling procedure. The computational time to compute the coupled jet is approximately 3.5 times greater than the uncoupled simulation.

7.3.3 CPU cost

The statistics are obtained by averaging the data over approximately $\tau = 1$ s of physical time. This time corresponds to approximately 4.6 flow time units

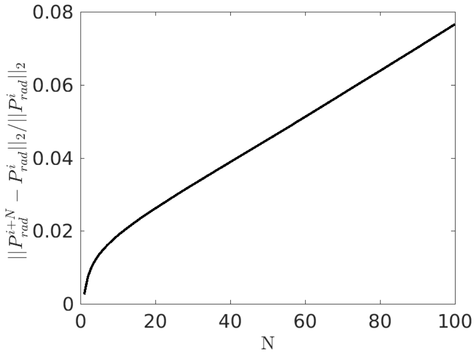

Figure 7.1: *Euclidean norm of the evolution of the radiative power with respect to a reference radiative power field.*

defined as $\tau(U_1{+}U_2)/(2L_x) = 4.6$, where L_x is the domain size in the x direction $L_x = 10\delta$. The approximate cpu cost using Intel Xeon CPU E5-2670 v3 24 cores @ 2.30 GHz is of 150000 h for the uncoupled simulation. The computational resources to compute the coupled jet are approximately 3.5 times greater than the uncoupled simulation.

7.4 Radiative power field

A slice of the instantaneous radiative power at $z = 0$ is presented in Fig. 7.2(a), while Fig. 7.2(b) shows the averaged radiative power $\langle P_{rad} \rangle$. Radiative power is a balance between the power lost by emission and the power gained due to absorption, thus regions with negative values of P_{rad} are cooling down by the effect of radiation, while regions with positive values are heating up due to radiation. As expected, Fig. 7.2 shows that the centerline of the jet, which is the hottest region of the flow, loses heat by radiation. On the other hand, thermal radiation energy is further absorbed at colder regions of the jet, tending to a null radiative power as the distance to the jet centerline increases. In Fig. 7.2(b), the emission dominated region has been delimited from the absorption dominated region by a solid black line corresponding to the isoline of $P_{rad} = 0$. The initial zone in which the jet develops is the most affected region by radiation due to the large temperature gradients. Then, radiative power at the jet centerline tends to zero downstream. Regarding a cross-section profile of the jet, a large radiative power is emitted in the centerline, then radiative power tends to zero in the jet edge while an absorption dominated zone is developed at the outer region of the jet. In the fully turbulent zone the temperature and its gradients are lower and the heat transport by radiation decreases significantly.

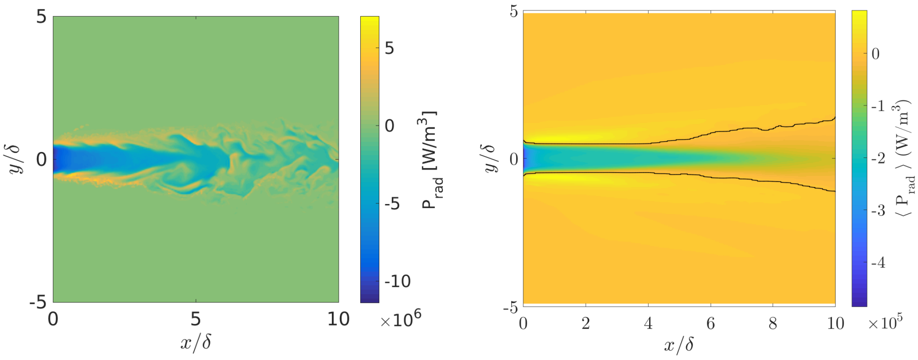

(a)

(b)

Figure 7.2: *(a) Instantaneous radiative power field at $z = 0$. (b) Mean exchanged radiative power field, solid black lines delimit the emission dominated region from the absorption dominated region.*

.

7.5 Radiation effects on temperature using classical adimensionalization

Mean temperature fields are slightly modified by radiation as shown in Figs. 7.3(a) and 7.3(b). Radiation enhances the energy transport specially in the entrance zone at which large temperature gradients are present. Then, radiation slightly shortens the temperature potential core and smooths the gradients of mean temperature. Comparing the temperature *rms* adimensionalized by the local Favre averaged temperature shown in Figs. 7.4(a) with Fig. 7.4(b), it can be seen that the fields are similar. The maximum difference in temperature fluctuations is approximately 10%.

To characterize the effects of radiation in the heat transport, the averaged energy balance in terms of enthalpy for the plane jet is analyzed. It can be simplified assuming statistically steady state and a low mach number as

$$\underbrace{\frac{\partial\left(\langle\rho\rangle\{u_i\}\{h\}\right)}{\partial x_i}}_{\text{Mean flow advection}} + \underbrace{\frac{\partial\left(\langle\rho\rangle\{u_i''h''\}\right)}{\partial x_i}}_{\text{Turbulent convective heat flux}} = \underbrace{\frac{\partial}{\partial x_i}\left\langle\lambda\frac{\partial T}{\partial x_i}\right\rangle}_{\text{Molecular diffusion}} + \underbrace{\langle P_{rad}\rangle}_{\text{Radiative power}}. \tag{7.2}$$

The enthalpy balance for both the radiative and non-radiative cases is analyzed in the developing zone in Fig. 7.5 in which cross-section profiles at $x = \delta$ of terms in Eqs. 7.2 are adimensionalized by the factor $y_{1/2}/\left(\Delta\{U_c\}C_p\Delta\{T_c\}\langle\rho\rangle\right)$. In the developing zone, the transport of enthalpy occurs around the jet edge for the non-radiative jet (Fig. 7.5(a)); while in the radiative jet, showed in Fig. 7.5(b), a significant enthalpy transport occurs in the jet core due to radiation

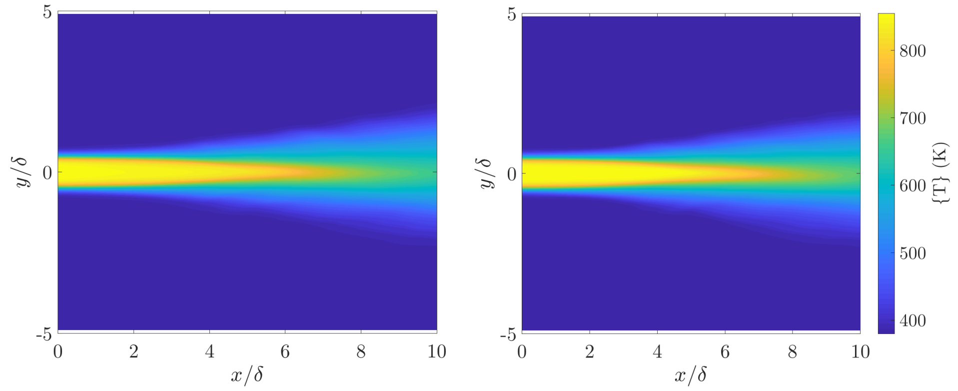

(a) (b)

Figure 7.3: *Comparison of temperature fields between the radiative (a) and the non-radiative (b) heated plane jet. (a) Favre averaged temperature of the heated jet including radiation. (b) Favre averaged temperature of the heated jet without radiation.*

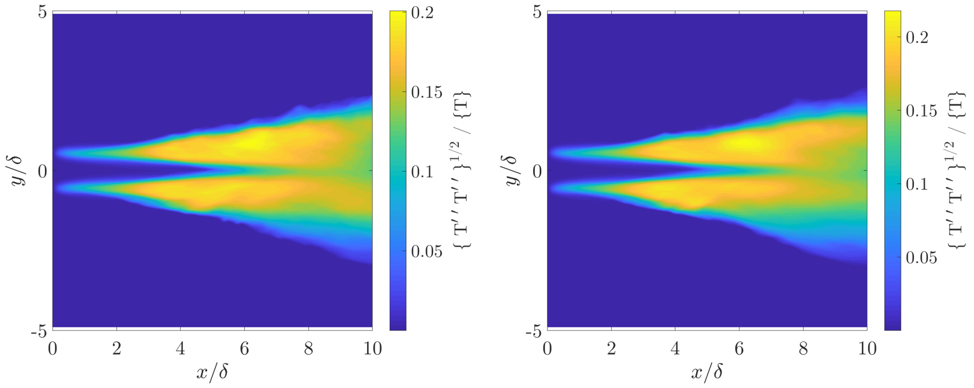

(a) (b)

Figure 7.4: *Comparison of temperature fluctuations fields between the radiative (a) and the non-radiative (b) heated plane jet. (a) Favre averaged temperature fluctuations of the heated jet including radiation. (b) Favre averaged temperature fluctuations of the heated jet without radiation.*

and it is compensated by mean flow advection. Mean flow advection and turbulent convective heat flux have opposite effects. However, because turbulence has not yet penetrated in the jet centerline in the developing zone, turbulent convective heat flux has null effects in the jet core.

Figure 7.6 shows an analysis of the enthalpy balances in the developed region ($x = 10\delta$). Again, all terms of the balances have been adimensionalized by the factor $y_{1/2}/\left(\Delta\{U_c\}C_p\Delta\{T_c\}\langle\rho\rangle\right)$. It can be seen that the mean flow advection and the turbulent convective heat flux term strongly dominate the enthalpy balance in the studied case. The radiation term in the balance of Eq. 7.2 has a

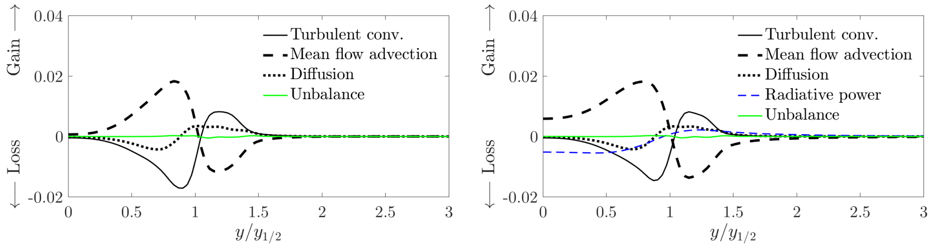

(a) (b)

Figure 7.5: *Cross-section profiles of the enthalpy budget main terms at $x = \delta$ for (a) the non-radiative and (b) the radiative jets.*

negligible contribution at the developed zone but it is significant in the developing zone. This situation is produced due to the lower temperature gradients involved in the developed zone and the increased turbulent fluctuations in the developed zone which enhance the turbulent convective heat flux.

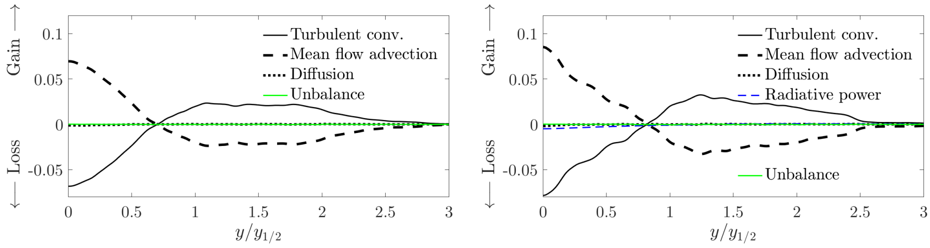

(a) (b)

Figure 7.6: *Cross-section profiles of the enthalpy budget main terms at $x = 10\delta$ for (a) the non-radiative and (b) the radiative jets.*

Mean temperature decay which provides a measure of the overall cooling of the jet is shown in Fig. 7.7(a) where $\Delta T_0 = T_1 - T_2$ and $\Delta\{T_c\} = \{T\}_{y=0} - T_2$. Surprisingly, despite the fact that radiation has no effects on the developed zone, as shown in Fig. 7.6, the mean temperature at the jet centerline decays faster in the radiative case than in the non-radiative case. Fig. 7.7(a) shows that the jet half-with based on temperature for the radiative case is slightly larger than for the non-radiative case. Temperature profiles of the uncoupled and coupled heated jets, shown in Fig. 7.7(c), collapse almost in the same curve when the y coordinate is adimensionalized by $y_{1/2,T}$.
Figure 7.8(a) shows the root-mean-square of temperature fluctuations along the jet centerline adimensionalized by the local Favre average excess temperature. While for the non-radiative jet, temperature fluctuations start to develop beyond $x = 4\delta$, in the radiative case, temperature fluctuations start further downstream and its intensity remains slightly lower than in the non-radiative jet. Dimensionless cross-section profiles of temperature fluctuations at $x = 10\delta$

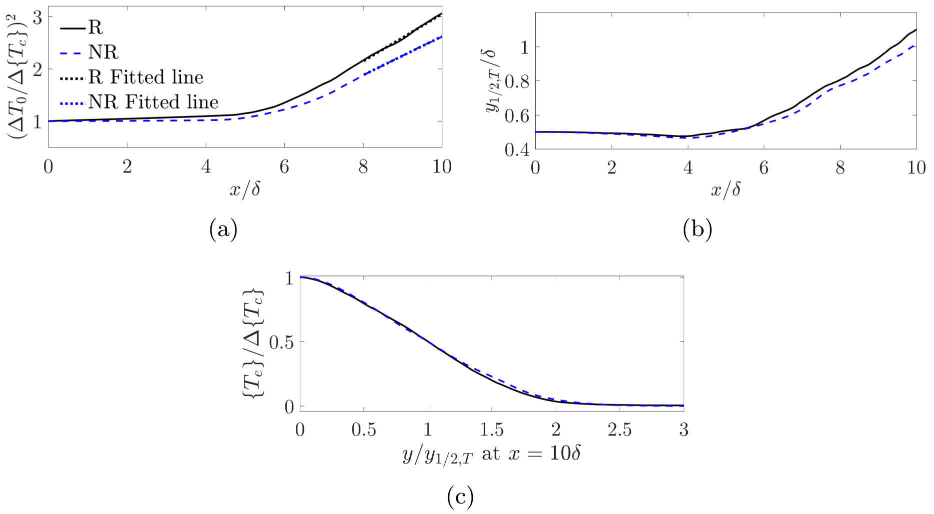

(a) (b)

(c)

Figure 7.7: *Comparison of mean temperature-related quantities between the radiative (R) and the non-radiative (NR) jets. (a) Downstream jet spread based on temperature. (b) Downstream temperature decay along the jet centerline. (c) Cross-section profile of mean excess temperature adimensionalized by the mean excess centerline temperature at* $x = 10\delta$.

are presented in Fig. 7.8(b). Temperature fluctuations almost collapse onto the same curves with classical adimensionalization although slightly different trends can be observed.

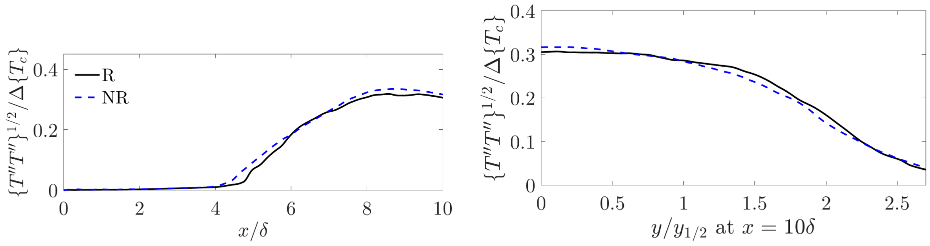

(a) (b)

Figure 7.8: *Comparison of temperature fluctuations-related quantities between the radiative and the non-radiative plane jet. (a) Downstream evolution of dimensionless temperature fluctuations along the jet centerline. (b) Cross-section profile of dimensionless temperature fluctuations at* $x = 10\delta$.

7.6 A novel adimensionalization for the mean temperature field to correct variable density effects

As observed in Fig. 7.7(a), the classical adimensionalization fails to give the same slope for the temperature decay between radiative and non-radiative cases despite the negligible contribution of radiation in the developed region. In this section, a novel adimensionalization based on approximate conservation of the convective heat flux is derived in order to collapse the temperature decay of different heated jets even though developing conditions are different. This assumption is exact for negligible coflow and radiative effects. It allows here to correct variable density effects for the investigated cased with moderate radiative transfer. This adimensionalization can then be used to distinguish whether radiation changes the dynamic mechanisms in the developed region or not.

Conservation of the convective heat flux in a free jet can be expressed by the equation

$$\frac{\partial}{\partial x}\int_{-\infty}^{+\infty}\langle\rho\rangle\{u\}\Delta\{T_e\}dy = 0, \tag{7.3}$$

For the new scaling, temperature and density fields are assumed self-similar in the form $\Delta\{T_e\} = \Delta\{T_c\}f_T(\eta)$ and $\langle\rho\rangle = \langle\rho_c\rangle f_\rho(\eta)$. Considering a strong jet with minor co-flow effects, velocity self-similarity is expressed in the form $\{u\} = \{U_c\}f_u(\eta)$. Note that $\Delta\{T_c\}$, $\langle\rho_c\rangle$ and $\{U_c\}$ are respectively temperature, density and velocity scales that depend only on downstream position, while $f_T(\eta)$, $f_\rho(\eta)$ and $f_u(\eta)$ are distribution functions depending on the dimensionless coordinate $\eta = y/y_{1/2,T}$. The choice of a unique length scale, in this case $y_{1/2,T}$, implies that self-similarity on temperature, density and velocity can be described with the same local length scale, which is consistent since the jet growths are proportional among them. Then, Eq. 7.3 can be written as

$$\langle\rho_c\rangle\{U_c\}\Delta\{T_c\}y_{1/2,T}\int_{-\infty}^{+\infty} f_T(\eta)f_\rho(\eta)f_u(\eta)d\eta = \text{constant}, \tag{7.4}$$

which implies that the product $\langle\rho_c\rangle\{U_c\}\Delta\{T_c\}y_{1/2,T}$ is independent of x in the self-similar region. Then, in this region, the convective heat flux conservation can be expressed as

$$\frac{\langle\rho_c\rangle\{U_c\}\Delta\{T_c\}y_{1/2,T}}{\overline{\rho_0}\;\overline{u_0}\Delta T_0\delta} = \text{constant}. \tag{7.5}$$

where $\overline{u_0} = \frac{1}{\delta}\int_\delta U_{in}(y)dy$ is analogous to $\overline{\rho_0}$ defined in Chapter 5

Similar to the derivation of the scaling for the velocity decay in the jet centerline (Foysi et al. (2010)), it is possible to deduce a scaling for the temperature decay.

Defining an equivalent heat jet opening characterizing thermal transfer, $r_{\epsilon,T}$, as

$$r_{\epsilon,T} = \frac{\delta^2}{y_{1/2,T}} \left(\frac{\overline{\rho_0}}{\langle \rho_c \rangle} \right)^2 \left(\frac{\overline{u_0}}{\{U_c\}} \right)^2, \tag{7.6}$$

the convective heat flux conservation presented in Eq. (7.5) can be expressed as

$$\left(\frac{\Delta\{T_c\}}{\Delta T_0} \right)^2 \frac{y_{1/2,T}}{r_{\epsilon,T}} = \text{constant}. \tag{7.7}$$

Then, similar to Eqs. (5.4) and (5.5), the temperature decay $(\Delta T_0/\Delta\{T_c\})^2$ in the self-similar region has a linear relationship with the streamwise coordinate in the form

$$\left(\frac{\Delta T_0}{\Delta\{T_c\}} \right)^2 = Q_{1,T} \left(\frac{x}{r_{\epsilon,T}} + Q_{2,T} \right), \tag{7.8}$$

assuming self-preserving temperature, density and velocity distributions; the temperature decay of heated jets has a universal behavior in the self-similar region when adimensionalized by the equivalent heat jet opening introduced in Eq. 7.6.

7.7 Radiation effects on temperature using the new scaling

Figure 7.9 shows again the centerline temperature decay and temperature profiles of the uncoupled and coupled jets but this time using the equivalent heat jet opening based on the convective heat flux conservation to scale the results. Additionally, the linear regressions of the centerline temperature decay in the fully developed region ($8\delta < x < 10\delta$) is shown in Fig. 7.9(a). In contrast with Fig. 7.7(a), it can be observed that in Fig. 7.9(a) the temperature decays of the radiative and the non-radiative jets collapse into almost the same curve presenting nearly the same slope when the x-coordinate is scaled by $r_{\epsilon,T}$. Figure 7.9(b) shows the collapse of temperature profiles for the radiative and non-radiative jets at the same $x = 9r_{\epsilon,T}$ which actually corresponds to $x = 9.76\delta$ for the non-radiative jet and to $x = 9.15\delta$ for the radiative jet, although the classical scaling was already collapsing mean temperature profiles onto almost the same curve.

In order to quantitatively compare the behavior of the temperature decay between the radiative and non-radiative jets, results of the linear fitting coefficients in the self-similar zone (beyond $x = 7\delta$) for both the new scaling (using

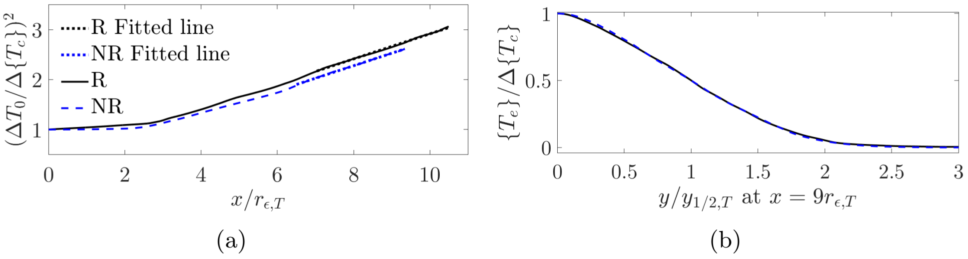

(a)

(b)

Figure 7.9: *Comparison of mean temperature-related quantities between the radiative and the non-radiative jets scaled using $r_{\epsilon,T}$. (a) Scaled downstream temperature decay along the jet centerline. (b) Cross-section profile of mean excess temperature adimensionalized by the mean excess centerline temperature at $x = 9r_{\epsilon,T}$.*

$r_{\epsilon,T}$ in Eq. 7.8) and the classical scaling (using δ instead of $r_{\epsilon,T}$ in Eq. 7.8) are summarized in Table 7.2.

On the one hand, values of $Q_{2,T}$ differ between R and NR cases for both scalings due to the inclusion of the radiative heat exchange which affects the developing zone. On the other hand, while $Q_{1,T}$ coefficients are significantly different (22.2%) when comparing R and NR cases using the classical scaling, they have a small difference (0.32 %) using the new scaling based on the equivalent heat jet opening.

Table 7.2: *Comparison of decay and spread of temperature fitted coefficients for the radiative and non-radiative slightly heated jets using scaling based on the convective heat flux conservation.*

Scaling	Jet case	$Q_{1,T}$	$Q_{2,T}$
Classic scaling	Non-radiative	0.3697	-2.9090
	Radiative	0.4517	-3.2460
New scaling	Non-radiative	0.2505	1.0962
	Radiative	0.2513	1.6099

Temperature fluctuations along the jet centerline for the radiative and non-radiative jets are shown in Fig. 7.10(a) adimensionalized using $r_{\epsilon,T}$. The intensity of the temperature fluctuations is first slightly lower for the radiative case at the developing region in which radiation has a significant impact on the flow. However, once in the developed region, the intensity of temperature fluctuations at the jet centerline collapses almost into the same value. Additionally, the collapse of cross-section temperature fluctuation profiles for the radiative and non-radiative jets at the same $x = 9r_{\epsilon,T}$ is presented in Fig. 7.10(b).

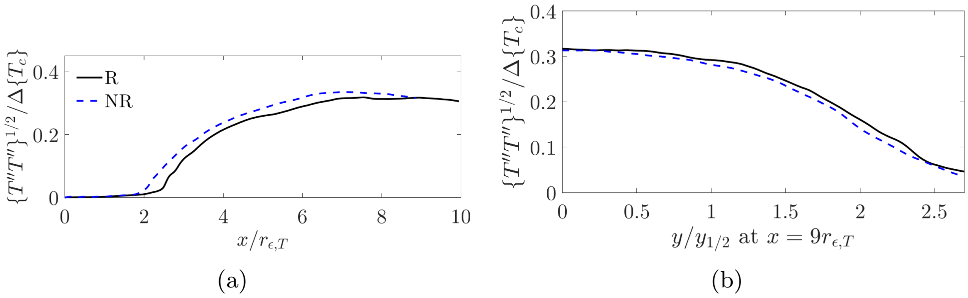

(a) (b)

Figure 7.10: *Comparison of temperature fluctuations-related quantities between the radiative and the non-radiative plane jets scaled using* $r_{\epsilon,T}$*. (a) Downstream evolution of dimensionless temperature fluctuations along the jet centerline. (b) Cross-section profile of dimensionless temperature fluctuations at* $x = 9r_{\epsilon,T}$*.*

7.8 Conclusions

An analysis of the enthalpy balance at the initial zone of the slightly heated jet shows that radiation has a major contribution of heat transport modifying temperature and density fields. On the other hand, a negligible radiative contribution is found in the developed region. Thus, for both uncoupled and coupled heated jets, the nature of heat transfer remain the same, which is here the turbulent heat transport. However, despite this minor contribution of radiation in the developed region, the classical jet scaling law fails to give the same temperature decay slope between the radiative and non-radiative cases. This could wrongly lead to conclude on a modified balance of heat transport mechanisms in the studied case. In fact, thermal radiation can have two kind of effects on the temperature profile: a direct one from radiative energy transfer and an indirect one due to the modified flow density.

The proposed equivalent heat jet opening deduced from the convective heat flux conservation equation has shown to compensate density differences to collapse both radiative and non-radiative jets profiles onto the same temperature decay rate in the developed region. This scaling accounts for the indirect effects of variable density in cases with radiation. It allows for distinguishing whether radiation modifies the heat transfer mechanisms in the developed region or not. In the studied case, it is now clearly identified that it does not.

Chapter 8

Physical study of radiation effects in a strongly heated turbulent jet using Direct Numerical Simulations

DNS of a heated jet of water vapor discharging into a parallel low speed coflow of cold water vapor is fully coupled with a reciprocal Monte-Carlo method. The spectral dependency of the radiative properties is accounted for using the ck method. A strongly heated case in which radiation has a noticeable impact is considered in this Chapter. The effects of radiation on mean temperature and velocity fields are analyzed. Additionally, temperature fluctuations and Reynolds stresses for the radiative and non-radiative jets are discussed through the enthalpy variance and turbulent kinetic balances. Finally, results of the radiative power field and specific contributions of absorption and emission powers are presented.

Contents

8.1 Introduction

Radiation can modify the heat transport and the fluid dynamics, while turbulence fluctuations can significantly alter the radiative heat transfer. Several works have quantified turbulence effects on radiation (the so-called TRI) through uncoupled computations and a priori analysis in a variety of configurations such as turbulent diffusion jet flames (Coelho (2004)), homogeneous isotropic turbulence (Kritzstein and Soufiani (1993); da Silva et al. (2009); Roger et al. (2009); Roger et al. (2010)), and temporally evolving jet (Roger et al. (2011)).

Coupled simulations solving both fluid dynamics and radiation allow for capturing these interactions, as well as radiation effects on turbulence, although additional modeling can be necessary depending on the turbulence description. Early coupled simulations using Reynolds average Navier-Stokes (RANS) include the studies of diffusion jet flames of Tessé et al. (2004) who pointed out the important role of soot particles in global radiative loss; and the work of Li and Modest (2003) in which was found that TRI reduces the total drop in flame peak temperature caused by radiative heat losses. Additionally, a recent RANS coupled simulation in a high-pressure gas turbine combustion chamber was reported by Ren et al. (2018).

In the coupled LES framework, Gupta et al. (2013) characterized contributions of subfilter-scale fluctuations to TRI in a diffusion flame; Ghosh et al. (2011) observed that radiation counteract the effects of compressibility in a nonreactive supersonic channel flow; and Poitou et al. (2012) showed how radiation can change the flame brush structure. Still in the LES formulation, coupled simulations in complex geometries of combustion chambers include the works of Jones and Paul (2005), Berger et al. (2016), Koren et al. (2018).

Several coupled DNS works, for which all interactions are fully captured, have been performed on different systems: statistically 1-dimensional premixed (Wu et al. (2005); Wu et al. (2007)) and nonpremixed (Deshmukh et al. (2008)) flames; natural convection in a differentially heated cubical cavity (Soucasse et al. (2016)); and nonreactive channel flow (Zhang et al. (2013); Vicquelin et al. (2014)); leading to an understanding of the mechanisms in which radiation modifies turbulence, and a direct quantification of TRI.

These studies relied on different numerical solvers for the radiative transfer equation (discrete ordinates (Coelho (2004); Jones and Paul (2005); Ghosh et al. (2011); Poitou et al. (2012); Berger et al. (2016)), ray tracing (Coelho (2004); da Silva et al. (2009); Roger et al. (2009); Roger et al. (2010); Roger et al. (2011); Soucasse et al. (2016)), spherical harmonics (Li and Modest (2003); Gupta et al. (2009)), and Monte-Carlo (Tessé et al. (2004); Gupta et al. (2013); Koren et al. (2018); Wu et al. (2005); Wu et al. (2007); Deshmukh et al. (2008); Zhang et al. (2013); Vicquelin et al. (2014)) methods) and models for radiative properties (gray gas (Gupta et al. (2009); Jones and Paul (2005); Wu et al. (2005); Wu et al. (2007); Deshmukh et al. (2008)), SNB-CK and its variants (Kritzstein and Soufiani (1993); Li and Modest (2003); Coelho (2004); Ghosh et al. (2011); Poitou et al. (2012); Berger et al. (2016)), Absorption Distribution Function (Soucasse et al. (2016)), correlated k-distribution (ck) models (Coelho (2004); da Silva et al. (2009); Roger et al. (2009); Roger et al. (2010); Roger et al. (2011); Tessé et al. (2004); Koren et al. (2018); Zhang et al. (2013); Vicquelin et al. (2014)), and Line-by-line computations (Gupta et al. (2013); Ren et al. (2018)).

All these studies indicate that, when considering heated free shear flows such as jets, radiation can play an important role on heat transport and may modify the thermal fields and fluid dynamics in participating medium. Given the complexity of combustion systems, it is desirable to simplify the problem by considering non-reactive free shear flows to understand the isolated impact of radiation in a more canonical configuration without wall interactions. With the exception of the LES study of Ghosh and Friedrich (2015), most coupled works addressing free shear flows problems correspond however to combustion systems.

The effects of thermal radiation in nonreactive turbulent jets deserves then further investigation. As far as we know, the present set of simulations are the first DNS of a free shear flow to be fully coupled with a spectral radiative heat transfer solver.

The present Chapter analyzes the radiation effects on the strongly heated plane jet, which is a canonical system of free shear flows. The goal is to isolate the gas-gas radiative contribution to give insight not only on radiation effects on free jets, but also on the behaviour of turbulent flows in general. The effects of radiation on first and second orders of velocity and temperature are addressed. Results of the radiative power field and specific contributions of absorption and emission powers are presented. Additionally, a quantification of the effects that turbulence causes on radiation is discussed.

8.2 Configuration

The strongly heated water vapor jet studied in this chapter has been dimensionalized based on the RANS parametric study presented in Chapter 4. Such study determined a CPU feasible turbulent heated jet in which radiative heat transfer is of the same order than both the turbulent convective flux and the mean flow advection. The retained inlet velocities (U_1, U_2) and temperatures (T_1, T_2) represented in Fig. 8.1 are specified in Table 8.1. The mean pressure (P_0) and the Reynolds number based on the initial jet width $\mathrm{Re} = \rho(T_1)\Delta U_0 \delta / \mu(T_1)$ (where $\Delta U_0 = U_1 - U_2$, and $\rho(T_1)$ and $\mu(T_1)$ stand for density and viscosity evaluated at T_1) are also specified in Table 8.1.

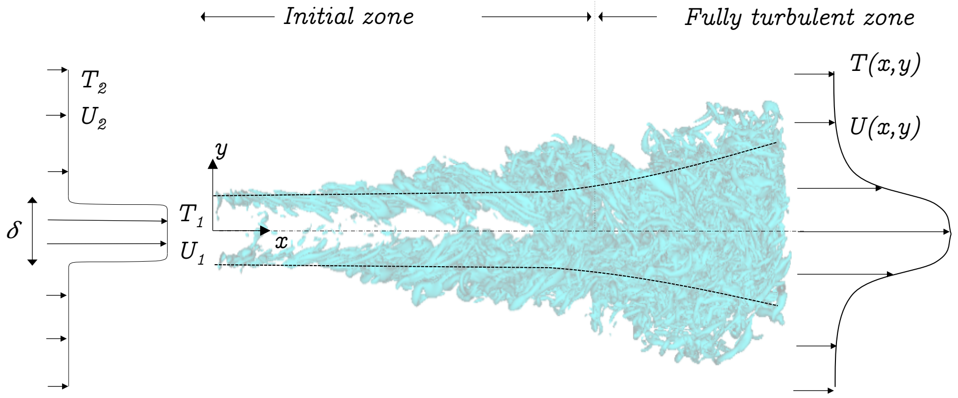

Figure 8.1: *Schematic representation of the turbulent structures of a heated plane jet identified by the Q-criterion.*

Table 8.1: *Configuration of the strongly heated jet.*

δ [m]	U_1 [m/s]	U_2 [m/s]	T_1 [K]	T_2 [K]	Re	P_0 [atm]
$5 \cdot 10^{-2}$	4.176	$U_1/10$	2500	405	500	2.576

8.3 Numerical setup

8.3.1 Fluid simulation

8.3.1.1 Inlet boundary conditions

Inlet velocity and temperature profiles are defined using an hyperbolic function described in Chapter 5 with a corresponding shear layer momentum thickness of $\theta = 0.02\delta$. The synthetic turbulence described in Chapter 1 is added to the inlet mean velocity following an hyperbolic profile, the synthetic turbulence field is fully defined by the parameters $L_c = \delta/2$ and $u' = U_1/20$.

8.3.1.2 Computational mesh and domain

The grid spacing in the x- and y- axis has been chosen to be the Kolmogorov scale following the temperature and velocity decays as explained in Chapter 5. The grid spacing along z-axis is uniform and equal to $\Delta z = \delta/40$, which is a close value to the Δx and Δy averages.
The flow solution is computed in a domain extension of $13.5\delta \times 10\delta \times 3\delta$ in x, y and z directions, respectively, using a structured grid with $514 \times 401 \times 121$ nodes, in the x, y and z directions, respectively, which corresponds to approximately 24.9×10^6 nodes. The statistics of the flow are computed in a domain extension of $10\delta \times 10\delta \times 3\delta$.

8.3.1.3 The Acoustic Speed Reduction method

The acoustic speed reduction method introduced in Chapter 1 is used with the value of the factor α set to $\alpha = 6.82$. This value sets the Courant- Friedrichs-Lewy and the Fourier conditions within the same order of magnitude for the current simulation.

8.3.2 Radiation simulation

Emission-based Reciprocity Monte-Carlo method (ERM) and a randomized Quasi Monte Carlo relying on low-discrepancy Sobol sequences are used to account for the radiative heat transfer. The spectral radiative properties for H_2O are modeled by means of the correlated-k (ck) narrow band model as explained in Chapter 3.
As discussed in Chapter 6, the grid to compute the radiative solution field is based on a coarser mesh than the DNS one: one out of two points is considered in each direction. Then, the radiative solution is computed in $257 \times 201 \times 61$ grid nodes in the x, y and z directions, respectively, which corresponds to approximately 5×10^6 nodes.
The current radiative simulations are considered converged either when a local error lower than 5% of the radiative power is achieved or an absolute value of the error lower than $5 \cdot 10^4$ W is achieved. The absolute value of the error corresponds to approximately 0.5% of the maximum value in magnitude of the radiative power in the domain. Finally, if these two criteria are not accomplished at a specific grid point, a maximum of 2.5×10^3 rays are considered. A discussion of the accuracy of these parametrs can be found in Chapter 6.

8.3.3 Determination of the coupling period and computational load distribution among processors

As described in Chapter 3, the optimal coupling parameter n_{cpl} is determined by the Euclidean norm of the difference between the radiative power in a iteration i set as a reference P^i_{rad} with respect to the radiative power after N iterations

P_{rad}^{i+N}. Figure 8.2 shows the evolution of $||P_{rad}^{i+N} - P_{rad}^{i}||_2$ adimensionalized by $||P_{rad}^{i}||_2 = \sqrt{\sum_{\vec{x} \epsilon \mathcal{D}} \left(P_{rad}^{i}(\vec{x})\right)^2}$ when increasing N. From this figure, it can be observed that after 30 iterations the radiative power field changes by around 5%. Because the radiative solution is considered converged when a local error lower than 5 % of the mean radiative power is achieved, a coupling period corresponding to $n_{cpl} = 30$ is retained.

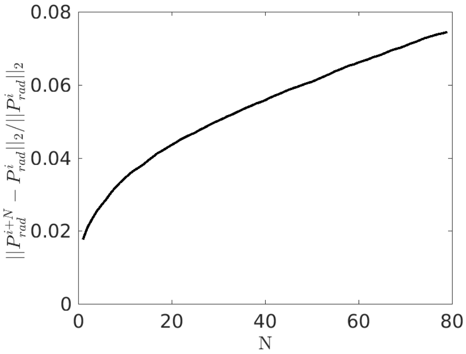

Figure 8.2: *Euclidean norm of the evolution of the radiative power with respect to a reference radiative power field.*

Analogous to §7.3.2, the processors distribution between the fluid and radiative solvers is done following Eq. 3.14. The present simulation has been performed with a total of 720 processors. In the case of the strongly heated jet coupled simulation, 216 processors are attributed to the fluid flow solver while 503 are assigned to the radiation solver. The one processor left is in charge of the coupling procedure. The computational time to compute the coupled jet is approximately 3.3 times greater than the uncoupled simulation.

8.3.4 CPU cost

The statistics are obtained by averaging the data over approximately $\tau = 1$ s of physical time. This time corresponds to approximately 4.6 flow time units defined as $\tau(U_1 + U_2)/(2L_x) = 4.6$, where L_x is the domain size in the x direction $L_x = 10\delta$. The approximate total cpu cost of the coupled simulation using Intel Xeon CPU E5-2670 v3 24 cores @ 2.30 GHz is of 270000 h.
In Table 8.2, the CPU time of the current coupled simulation is compared with this same simulation without radiation, and the coupled and uncoupled simulations of the slightly heated jet. In Table 8.2, η corresponds to the Kolmogorov scale.

Table 8.2: *Comparison of CPU among the different simulation of this work.*

Case	Re	Δx_i	Relative CPU cost
Uncoupled sligthly heated jet	1500	$\sim 2\eta$	1.0
Coupled sligthly heated jet	1500	$\sim 2\eta$	3.5
Uncoupled strongly heated jet	500	$\sim 1\eta$	0.55
Coupled strongly heated jet	500	$\sim 1\eta$	1.8

8.4 Uncoupled results of the heated jet

Before presenting results of the strongly heated jet coupled with thermal radiation, the uncoupled strongly and slightly heated jets are briefly comapred in this section.

Figure 8.3(a) shows the cross-section profiles at $x = 10\delta$ of the streamwise velocity for the strongly and slightly heated jets, while Fig. 8.3(b) presents the profiles of mean temperature at this same cross-section. Despite some discrepancies are observed in the scaled profiles, trends are very similar for both mean temperature and mean velocity at the developed region.

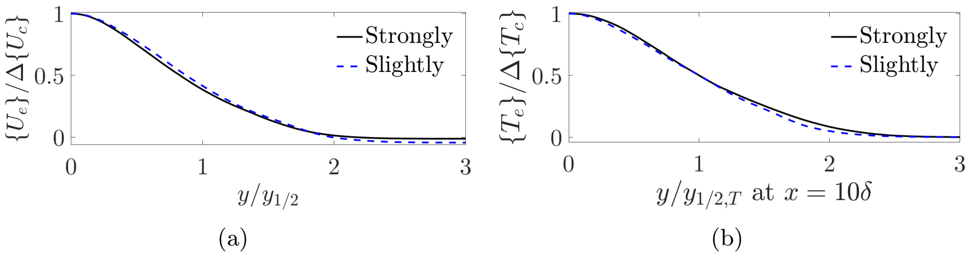

(a)

(b)

Figure 8.3: *Comparisons of (a) mean streamwise velocity and (b) mean temperature profiles at $x = 10\delta$ between the strongly and slightly heated jets.*

The velocity decay shown in Fig. 8.4(a) indicates that temperature differences strongly impact on the velocity decay. However, when scaled using the equivalent jet opening r_ϵ the decays have a similiar slope although the strongly heated jet decay is slightly larger.

A turbulent quantity of high interest is the turbulent Prandtl number Pr_t which is generally used to model energy transport in turbulent flows. From the present DNS data, the value of Pr_t has been explicitly computed using the following expression, valid for thin layer flows,

$$\mathrm{Pr}_t = \frac{-\langle\rho\rangle\{u''v''\}}{-\langle\rho\rangle\{v''h''\}/c_p}\frac{\partial\{T\}/\partial y}{\partial\{u\}/\partial y}, \tag{8.1}$$

In Figures 8.5(a) and 8.5(b) the downstream evolution of Pr_t is presented for the strongly and slightly heated jets for the lines defined by $y = y_{1/2}$ and

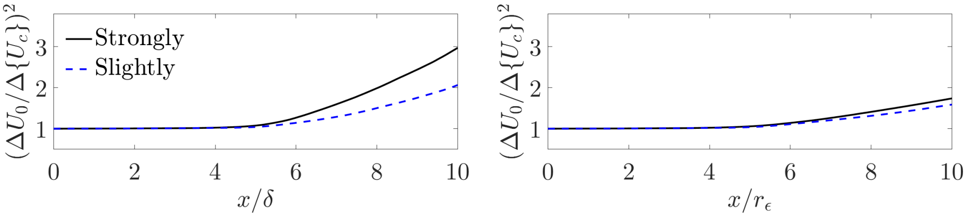

(a) (b)

Figure 8.4: *Comparisons of the (a) velocity decay and (b) scaled velocity decay between the strongly and slightly heated jets.*

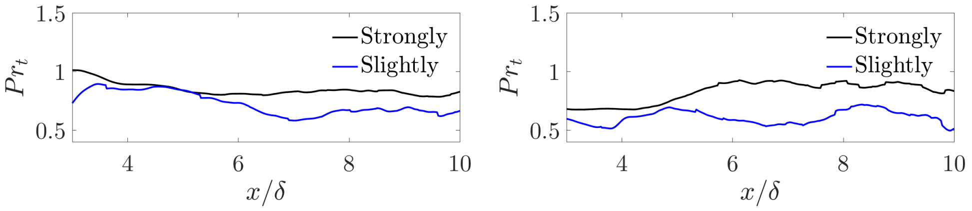

(a) (b)

Figure 8.5: *Comparison of Pr_t results computed from DNS data of the strongly and slightly heated jets along two different lines of equal $y_{1/2}$: (a) $Pr_t(x, y = y_{1/2}/2)$, (b) $Pr_t(x, y = y_{1/2})$.*

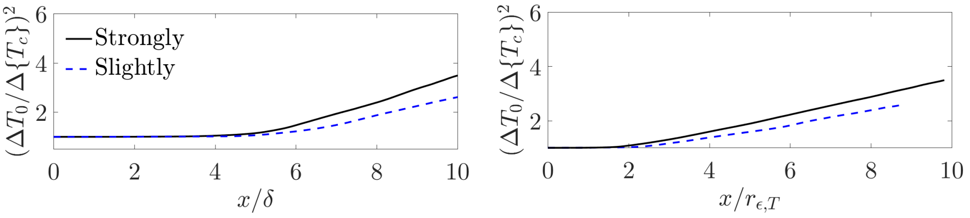

(a) (b)

Figure 8.6: *Downstream temperature decay along the jet centerline for the strongly and slightly heated jets using (a) classical scaling (b) scaling based on convective heat flux conservation.*

$y = y_{1/2}/2$. As it can be seen in Fig. 8.5, the Pr_t is significantly larger in the strongly heated jet.

Centerline temperature decay for the strongly and slightly heated jets is shown in Fig. 8.6. In accordance with the turbulent Prandt number, a greater decay rate for the strongly heated jet is observed, since the turbulent Prandt number corresponds to the ratio between the turbulent diffusion of momentum and the heat transfer by turbulent diffusion. However, when the new scaled is used to compensate the density effects of temperature, different slopes are obtained for the strongly and slightly heated jets. In the next Chapter, the role of the new scaling in constant turbulent Prandt number computations using RANS simulations will be analyzed.

8.5 Radiation effects on temperature fields

When accounting for radiation in the energy transport, the instantaneous temperature fields are significantly modified as shown in Fig. 8.7. Despite there is not a clear difference in the turbulent structures identified by the Q-criterion, it can be seen qualitatively that the energy mixing process is enhance by the presence of radiation.

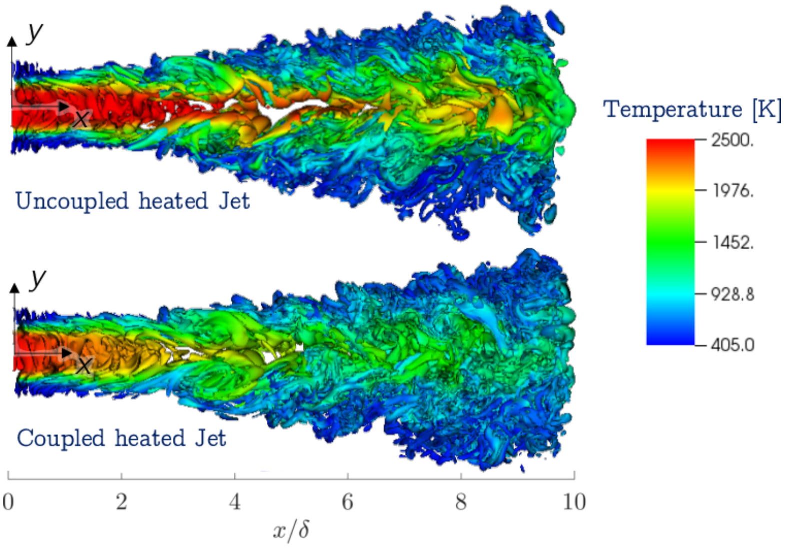

Figure 8.7: *Snapshots of turbulent eddies identified by the Q-criterion colored by temperature for the heated jet without including radiation, and the heated jet coupled with the radiative solver.*

8.5.1 Mean temperature field

Mean temperature fields are modified by radiation as shown in Fig. 8.8. Radiation enhances the energy transport specially in the entrance zone at which large temperature gradients are present. Then, radiation shortens the temperature potential core and smooths the gradients of mean temperature.

Figure 8.9 shows the jet half-width based on temperature $y_{1/2,T}$ adimensionalized by the initial jet width δ for the radiative and the non-radiative cases. From this figure, it can be observed that the jet starts spreading beyond $x = 3\delta$ when radiation is included. On the other hand, for the non-radiative jet, the jet start spreading afterwards around $x = 5\delta$. Such difference is caused by the

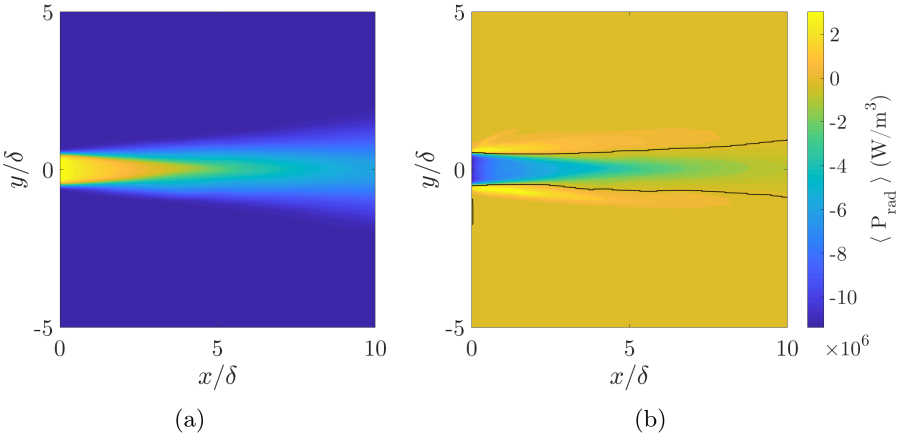

Figure 8.8: *Comparison of Favre averaged temperature fields between (a) the radiative and the (b) non-radiative heated plane jets.*

enhanced energy transport when including radiation effects.

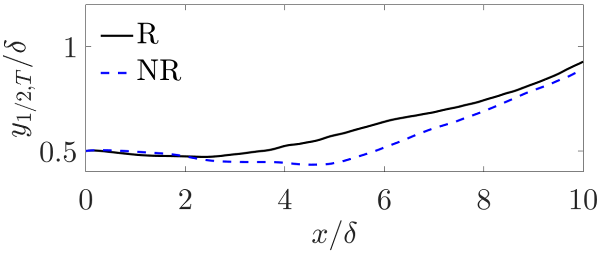

Figure 8.9: *Downstream jet spread based on temperature for the radiative and non-radiative jets.*

Excess Favre averaged temperature profiles ($\{T_e\} = \{T\} - T_2$) of the radiative and the non-radiative jets are presented in Fig. 8.10 adimensioalized by $\Delta\{T_c\}$ at $x = 10\delta$. When adimensionalized, temperature profiles of the radiative and non-radiatice cases are very similar.

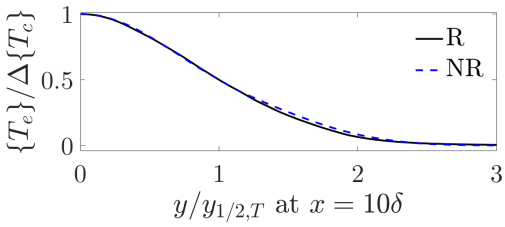

Figure 8.10: *Comparison of Cross-section profiles of mean excess temperature adimensionalized by the mean excess centerline temperature at $x = 10\delta$ for the radiative and non-radiative jets.*

Just as for the slightly heated jet, the radiation role in the heat transport is assessed by means of the average enthalpy balance. Recalling Eq. 7.2 for a statistically steady state and a low mach number flow:

$$\underbrace{\frac{\partial\left(\langle\rho\rangle\{u_i\}\{h\}\right)}{\partial x_i}}_{\text{Mean flow advection}} + \underbrace{\frac{\partial\left(\langle\rho\rangle\{u_i''h''\}\right)}{\partial x_i}}_{\text{Turbulent convective heat flux}} = \underbrace{\frac{\partial}{\partial x_i}\left\langle\lambda\frac{\partial T}{\partial x_i}\right\rangle}_{\text{Molecular diffusion}} + \underbrace{\langle P_{rad}\rangle}_{\text{Radiative power}}. \tag{8.2}$$

Figure 8.11 presents the cross-section profiles of the terms in Eq. (8.2) at the developing region ($x=\delta$) adimensionalized by the factor $y_{1/2}/\left(\Delta\{U_c\}C_p\Delta\{T_c\}\langle\rho\rangle\right)$. Figure 8.11(b) shows that radiation has a major contribution in the developing zone, specially in the jet centerline. Analogous to the slightly heated jet, radiation effects at the jet centerline are compensated by the mean flow advection.

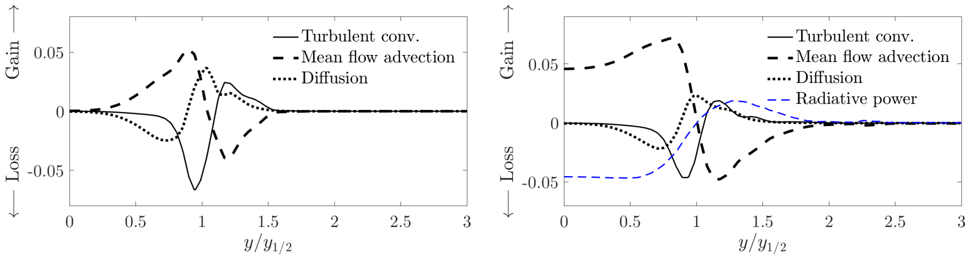

(a) (b)

Figure 8.11: *Cross-section profiles of the enthalpy budget main terms at $x=\delta$ for (a) the non-radiative and (b) the radiative jets.*

Figure 8.12 shows an equivalent analysis at the developed region. Again, all terms of the balance have been adimensionalized by the factor $y_{1/2}/\left(\Delta\{U_c\}C_p\Delta\{T_c\}\langle\rho\rangle\right)$.

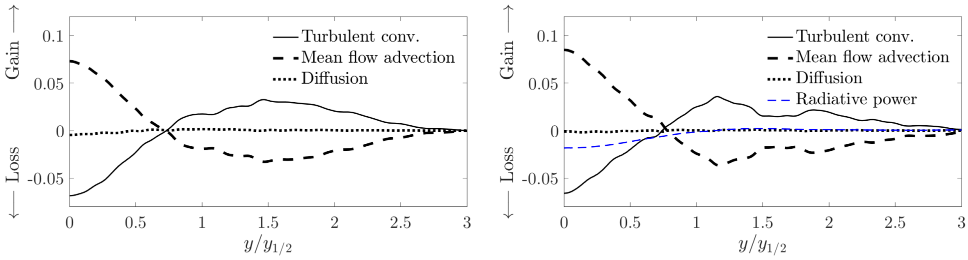

(a) (b)

Figure 8.12: *Cross-section profiles of the enthalpy budget main terms at $x=10\delta$ for (a) the non-radiative and (b) the radiative jets.*

In contrast with the slightly heated jet, radiation has a noticeable contribution for $y < y_{1/2}$ in the enthalpy balance at the developed region as shown in Fig. 8.12(b).

The temperature in the jet centerline decays faster in the radiative case (R) than in the non-radiative case (NR) as shown in Fig. 8.13(a), in which $\Delta T_0 = T_1 - T_2$ and $\Delta\{T_c\} = \{T\}_{y=0} - T_2$. The temperature decay provides a measure of the overall cooling of the jet. As expected, radiation enhances the overall cooling of the jet since an extra mode of energy transport is included. Additionally, in Fig. 8.13(b), the streamwise coordinate is scaled based on convective heat flux conservation using the $r_{\epsilon,T}$ as explained in Chapter 7. A linear fitting of the form

$$\left(\frac{\Delta T_0}{\Delta\{T_c\}}\right)^2 = Q_{1,T}\left(\frac{x}{r_{\epsilon,T}} + Q_{2,T}\right), \tag{8.3}$$

is included in Fig. 8.13(b) for both cases.

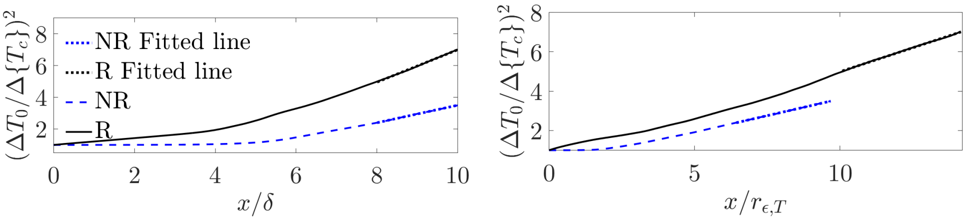

(a)

(b)

Figure 8.13: *Downstream temperature decay along the strongly heated jet centerline for the radiative (R) and non-radiative (NR) jets using (a) classical scaling (b) scaling based on convective heat flux conservation.*

Similarly to Table 7.2, results of the linear coefficients using both the classical and the new scaling are presented in Table 8.3 for the strongly heated jet.

Table 8.3: *Comparison of decay and spread of temperature fitted coefficients for the radiative and non-radiative strongly heated jets using scaling based on the convective heat flux conservation.*

Scaling	Jet case	$Q_{1,T}$	$Q_{2,T}$
Classic scaling	Non-radiative	0.552	-3.650
	Radiative	1.022	-3.218
New scaling	Non-radiative	0.3386	0.645
	Radiative	0.4867	0.251

As for the slightly heated jet, the temperature decay rate using the classical scaling is greater for the radiative jet; although a larger relative difference of 46% is found for the strongly heated case. However, when using the new scaling in the strongly heated jet with the goal of counteracting the density effects in the decay rate, Table 8.3 shows that the temperature decay rate using the equivalent heat jet opening is significantly different between the radiative and the non-radiative cases, with a relative difference of 30.4 %. Thus, it is shown that for strongly heated jets the general scaling based on convective heat flux conservation for variable-density jets presented in Chapter 7 is no longer valid when large radiation effects are accounted for. This analysis is in accordance with the average enthalpy balance in the developed region presented in Fig. 8.12(b), which states that the nature of the heat transfer is modified by the inclusion of radiation. Note that when comparing the decay rate without accounting for radiation for the strongly and heated jets, as done in section 8.4, a disagreement between them is found.

8.5.2 Fluctuations of enthalpy

Comparing the temperature fluctuations adimensionalized by the local Favre averaged temperature shown in Figs. 8.14(a) with Fig. 8.14(b), it can be seen that radiation tends to decrease temperature fluctuations; although similar patterns of the temperature fluctuations field are obtained in spite of the inclusion of radiation.

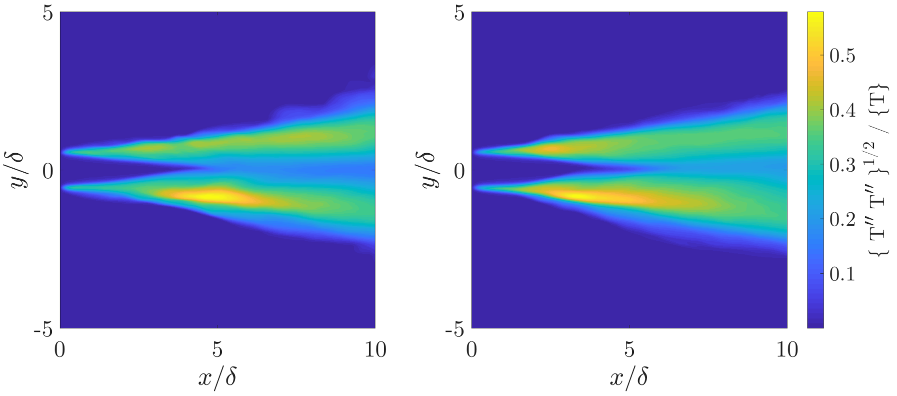

(a) (b)

Figure 8.14: *Comparison of Favre averaged temperature fluctuations between (a) the radiative and the (b) non-radiative strongly heated plane jets.*

Figure 8.15(a) shows the temperature fluctuations along the jet centerline adimensionalized by the excess Favre average temperature. For both cases, temperature fluctuations start to develop beyond $x = 3.5\delta$. However, in the radiative case, temperature fluctuations intensity remains lower than in the non-radiative jet. At the developed region ($x > 8\delta$), radiation decreases the temperature fluctuations around 38 % in the jet centerline.

The dimensionless cross-section profiles of temperature fluctuations at $x = 10\delta$ are presented in Fig. 8.15(b). In accordance with Fig. 8.15(a), temperature fluctuations at the jet centerline are lower for the radiative jet. However, temperature fluctuations are almost equal on both cases beyond $y = 1.2y_{1/2}$ at the developed zone when adimensionalized by $\Delta\{T_c\}$.

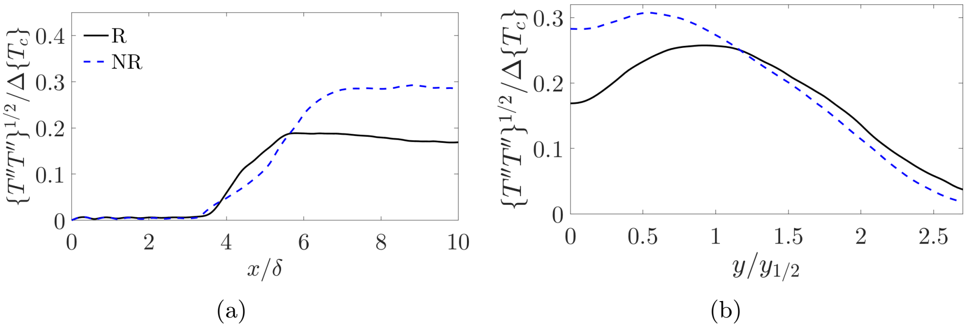

Figure 8.15: *Comparison of temperature fluctuations between the radiative and the non-radiative jets. (a) Downstream evolution of dimensionless temperature fluctuations along the jet centerline. (b) Cross-section profile of dimensionless temperature fluctuations at* $x = 10\delta$.

The effect of radiation on the temperature fluctuations is further analyzed through the transport equation of Favre averaged enthalpy variance, $\Theta = \frac{1}{2}\{h''^2\}$. Following the development in the work of Vicquelin et al. (2014), for a low-Mach flow, the enthalpy variance transport equation can be expressed as:

$$\begin{aligned}
\underbrace{\frac{1}{2}\frac{\partial}{\partial t}\left(\langle\rho\rangle\{h''^2\}\right) + \frac{\partial}{\partial x_j}\left(\frac{1}{2}\langle\rho\rangle\{u_j\}\{h''^2\}\right)}_{\text{Advection, } \langle\rho\rangle\frac{\bar{D}\Theta}{\bar{D}t}} = - \underbrace{\frac{\partial\left\langle q_j' h'\right\rangle}{\partial x_j}}_{\text{Molecular diffusion , } \mathcal{D}_\Theta} \\
+ \underbrace{\left\langle q_j' \frac{\partial h'}{\partial x_j}\right\rangle}_{\text{Molecular dissipation, } \epsilon_\Theta} - \underbrace{\langle\rho\rangle\{u_j''h''\}\frac{\partial\{h\}}{\partial x_j}}_{\text{Production, } \mathcal{P}_\Theta} - \underbrace{\frac{\partial}{\partial x_j}\langle\rho\rangle\{u_j''\frac{h''^2}{2}\}}_{\text{Turbulent difusion, } \nabla\cdot T_\Theta'} \qquad (8.4) \\
- \underbrace{\langle h''\rangle\frac{\partial\langle q_j\rangle}{\partial x_j}}_{\text{I}} + \underbrace{\langle h''\rangle\langle P_{rad}\rangle}_{\text{II}} + \underbrace{\langle h'' P_{rad}'\rangle}_{\text{III}}
\end{aligned}$$

To enhance convergence when computing the budged of enthalpy variance all correlations involving fluctuations are expressed as functions of its mean values as detailed in Appendix A. The molecular diffusion, and Terms I and II are neglected in the following analysis since they do not contribute significantly in the present enthalpy fluctuations balance. Then, adimensionalizing all terms in the enthalpy fluctuations budget by the factor $\dfrac{y_{1/2}}{\Delta U_c (C_p \Delta T_c)^2 \langle\rho\rangle}$, Eq. 8.4

can be rewritten as

$$\frac{\bar{D}\Theta^*}{\bar{D}t} = \epsilon_\Theta^* + \mathcal{P}_\Theta^* + \nabla \cdot T_\Theta'^* + \left\langle h'' P_{rad}' \right\rangle^* \tag{8.5}$$

where * denotes adimensionalized quantities.

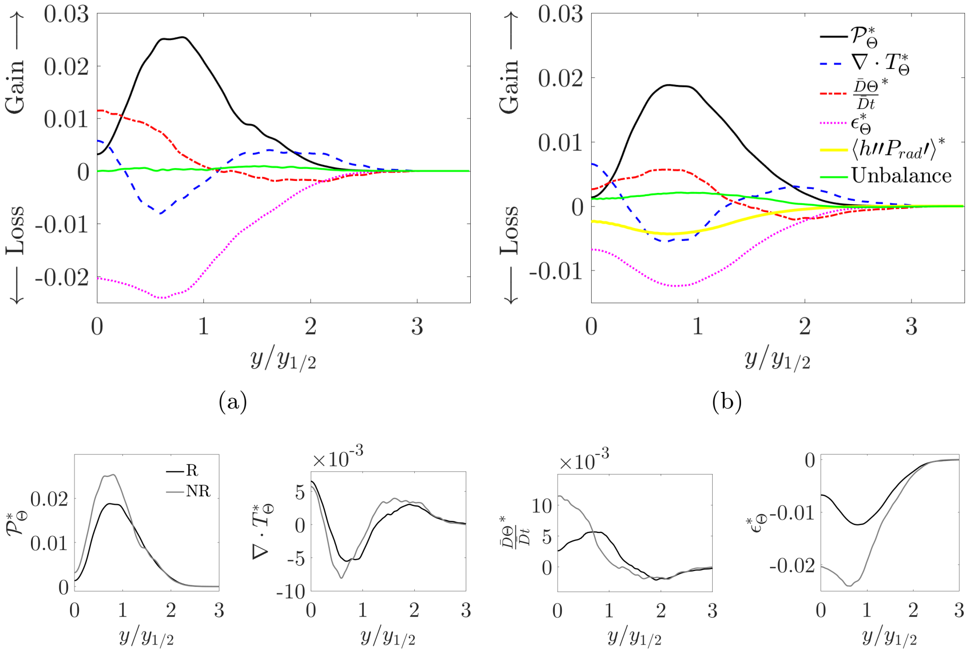

(a) (b)

(c) (d) (e) (f)

Figure 8.16: *Budget of dimensionless enthalpy fluctuations of the heated jet in the developed region. (a) Uncoupled heated jet. (b) Accounting for radiative heat transfer. Comparison of the components of the enthalpy fluctuations budget: (c) production, (d) turbulent diffusion, (e) advection and (f) dissipation between the radiative and the non-radiative jet cases.*

The budget of the enthalpy fluctuations for the radiative and non-radiative jets are presented in Figs. 8.16(b) and 8.16(a), respectively. A comparison of each term in the balance between both cases is presented in Figs. 8.16(c) to 8.16(f). As expected, in the non-radiative jet, production and dissipation terms dominate the budget. However, when radiation is included, a new term corresponding to the correlation between enthalpy fluctuations and radiative power fluctuations significantly contributes to an additional dissipation mechanism of enthalpy variance, that is why we called this term radiative dissipation as in the work of Vicquelin et al. (2014). Despite the fact that the unbalance terms remain quite small in both budgets; it must be said that for the radiative case, the budget is not completely close. This may be attributed to numerical

dissipation introduced in the resolution of the RTE in a coarser mesh. Moreover, note that because of the parallel coupling scheme, the computation of the radiative dissipation term (term III) is not straightforward and care must be taken when computing $\langle hP_{rad} \rangle$, in which both enthalpy and radiative power fields must correspond to the same physical time.
When radiation is taken into account, production decreases since temperature gradients are smoother. Due to the decrease in production and the additional radiative dissipation mechanism, enthalpy variance decreases as shown in Fig. 8.15. Then, because of the acting radiative dissipation mechanism and the decreased enthalpy variance, the molecular dissipative term nearly decreases by a factor of two when radiation is considered.

8.6 Radiation effects on velocity fields

Radiation effects on velocity fields are expected to be smaller than in temperature fields; since effects on velocity are indirectly caused by density and viscosity changes, while effects on temperature are directly caused by radiation.

8.6.1 Mean velocity field

The downstream growth of the jet half-width $y_{1/2}(x)$ is presented for the radiative and non-radiative cases in Fig. 8.17. For the radiative case, the jet half-width is shrinking in the developing region. This phenomenon occurs due to the decrease of temperature potential core size which reduces velocity in this region and specially at the jet edges. In the present simulation, the jet half-width for the non-radiative jet remains greater all along the simulated domain.

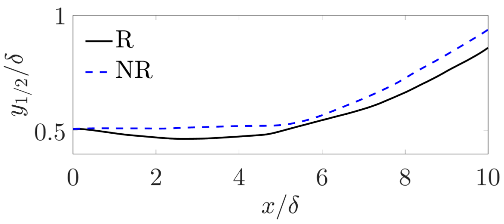

Figure 8.17: *Comparisons of the jet half-width between the radiative (R) and the non-radiative (NR) cases.*

Figure 8.18(a) shows the comparison of the centerline mean excess velocity decay adimensionalized by $\Delta U_0 = U_1 - U_2$ between the radiative and the non-radiative cases. The downstream velocity decay of the radiative case is greater than the non-radiative case. Nevertheless, when the streamwise coordinate is scaled by ρ_c/ρ_0 in Fig. 8.18(b) as explained in Chapter 5, this behavior is inversed and the scaled velocity decays rate are significantly different. This difference shows that radiation and its effects on density can change the dynamics of heated jets. Thus, it is shown that for strongly heated jets the general scaling law of variable-density jets is no longer valid when radiation is accounted for.

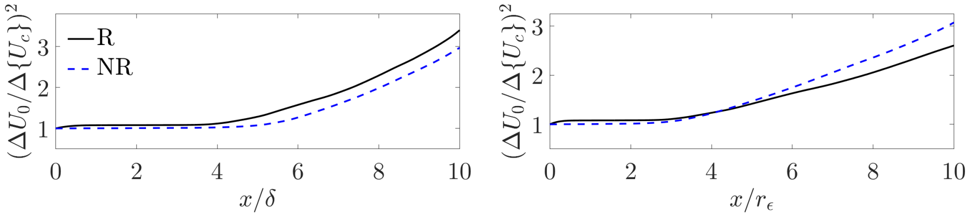

(a) (b)

Figure 8.18: *Comparisons (a) velocity decay and (b) scaled velocity decay between the radiative and the non-radiative cases.*

The local Reynolds number based on $y_{1/2}$ defined as $Re_{y_{1/2}} = \frac{\langle\rho_c\rangle\Delta\{U_c\}2y_{1/2}}{\mu(\{T_c\})}$ is shown in Fig. 8.19. Despite the fact that the mean excess velocity decay is larger for the radiative case, the local Reynolds number is significantly larger for the radiative case since $\langle\rho\rangle$ increases while μ decreases by the effects of radiation on temperature.

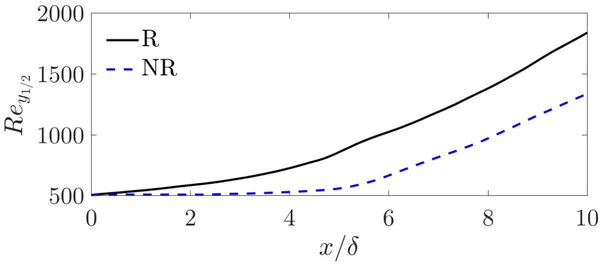

Figure 8.19: *Comparisons of local Reynolds number between the radiative and the non-radiative cases.*

Favre averaged velocity profiles at $x = 10\delta$ are shown in Figure 8.20 for the radiative and non-radiative cases. The profile trends are similar between both cases. In a jet, the cross-stream velocity is equivalent to the entrainment velocity which is significantly greater in the radiative case as observed in Fig. 8.20(b).

8.6.2 Velocity fluctuations

Figure 8.21 shows the Reynolds stresses downstream evolution at the centerline of the jet adimensionalized by $\Delta\{U_c\}$. The Reynolds stresses grow strongly in the region $4 < x/\delta < 8$, then its growth moderate in the developed region. The intensity of the Reynolds stresses at the developed region turns to be almost the same for both cases. This trend was also observed in the mixing layer studied by Ghosh and Friedrich (2015). Additionally, Fig. 8.22 shows profiles of the Reynolds stresses at $x = 10\delta$, which are not significantly affected by

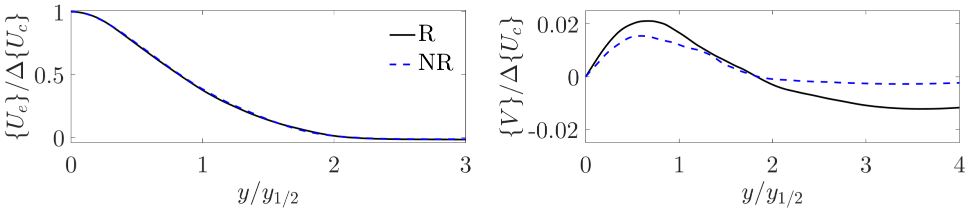

(a) (b)

Figure 8.20: *Comparisons of (a) streamwise and (b) cross-stream velocities profiles at $x = 10\delta$ between the radiative and the non-radiative cases adimensionalized by the non-radiative mean excess centerline velocity.*

radiation. These results indicate that radiation slightly modifies scaled second order moments of velocity for the present strongly heated jet.

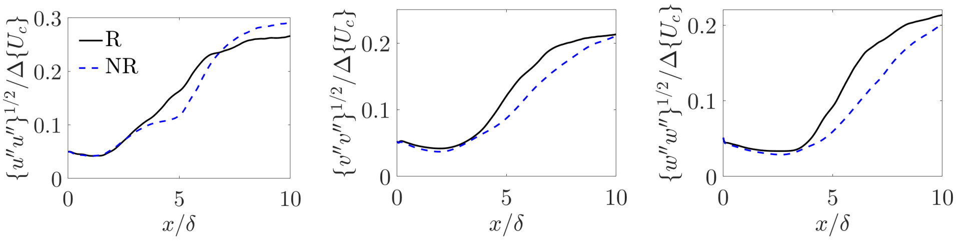

(a) (b) (c)

Figure 8.21: *Comparison of dimensionless Reynolds stresses along the jet centerline in the (a) streamwise, (b) cross-stream and (c) spanwise directions between the radiative and the non-radiative cases.*

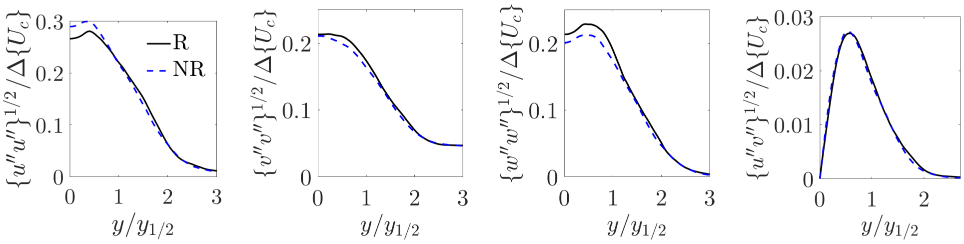

(a) (b) (c) (d)

Figure 8.22: *Comparisons of the dimensionless Reynolds stresses profiles at $x = 10\delta$ in the (a) streamwise, (b) cross-stream and (c) spanwise directions, and (d) Reynolds shear stress profiles between the radiative and the non-radiative cases.*

This point is further investigated by analyzing the transport equation for the turbulent kinetic energy. The transport equation of the turbulent kinetic energy, already presented in Chapter 5 is expressed as

$$\begin{aligned}
&\underbrace{\frac{1}{2}\frac{\partial\langle\rho u_i''^2\rangle}{\partial t}+\frac{\partial}{\partial x_j}\left(\frac{1}{2}\langle\rho u_i''^2\rangle\{u_j\}\right)}_{\text{Advection, }\langle\rho\rangle\frac{\bar{D}k}{\bar{D}t}}=-\underbrace{\langle\rho u_i''u_j''\rangle\frac{\partial\{u_i\}}{\partial x_j}}_{\text{Production, }\mathcal{P}}-\underbrace{\langle\tau_{i,j}\frac{\partial u_i''}{\partial x_j}\rangle}_{\text{Viscous dissipation, }\epsilon}\\
&\underbrace{-\frac{\partial\left(\langle P\rangle\langle u_i''\rangle\right)}{\partial x_i}-\frac{\partial\langle P'u_i''\rangle}{\partial x_i}+\frac{\partial\langle\tau_{i,j}u_i''\rangle}{\partial x_j}-\frac{\partial}{\partial x_j}\langle\rho u_j''\frac{u_i''^2}{2}\rangle}_{\text{Diffusion terms, }\nabla\cdot T'}+\underbrace{\langle P\frac{\partial u_i''}{\partial x_i}\rangle.}_{\text{Pressure-Dilatation, }\Pi}\qquad,
\end{aligned}\tag{8.6}$$

A detailed explanation of how each term on Eq. (8.6) has been computed to enhance convergence can be found in Appendix A. Scaling Eq. (8.6) by the factor $y_{1/2}/(\Delta\{U_c\}^3\langle\rho\rangle)$, one can write

$$\frac{\bar{D}k^*}{\bar{D}t}+\nabla\cdot T'^*=\mathcal{P}^*-\epsilon^*+\Pi^*,\tag{8.7}$$

where * denotes adimensionalized quantities.
The turbulent kinetic energy balance at the developed region for the strongly heated jet is presented in Fig. 8.23(b) for the radiative jet, and in Fig. 8.23(a) for the non-radiative jet. Moreover, Figs. 8.23(c) to 8.23(f) show a comparison of each term in the turbulent kinetic energy equation between the radiative and non-radiative jets. The profiles are obtained by averaging the scaled simulation fields in the range $9\delta < x < 10\delta$. The pressure-dilatation term (Π^*) has a negligible contribution; in consequence, it is not included in Fig. 8.23. Turbulent kinetic energy balances for the radiative and non-radiative jets are very similar in magnitude and in trends. As noted with the Reynolds stresses, radiation slightly modifies the budget of second order moments of velocity through the indirect effect of the modified fields of density and viscosity.

8.7 Radiative power field

Turbulent structures identified by the Q-criterion, and colored by instantaneous emitted and absorbed power fields are shown in Fig. 8.24. A region with strong emission is identified close to the nozzle, while a peak of absorption is located δ downstream from the nozzle, around the jet centerline. As discussed in Chapter 3, radiative power is a balance between emission and absorption. In order to analyze the exchanged radiation in the mean flow, the averaged radiative power $\langle P_{rad}\rangle$ is presented in Fig. 8.25. Regions with negative P_{rad} are loosing energy by the effect of radiation, while regions with positive values are gaining energy due to radiation. The same behavior as in the slightly heated jet is found, which is that the centerline of the jet mainly emits thermal radiation and part

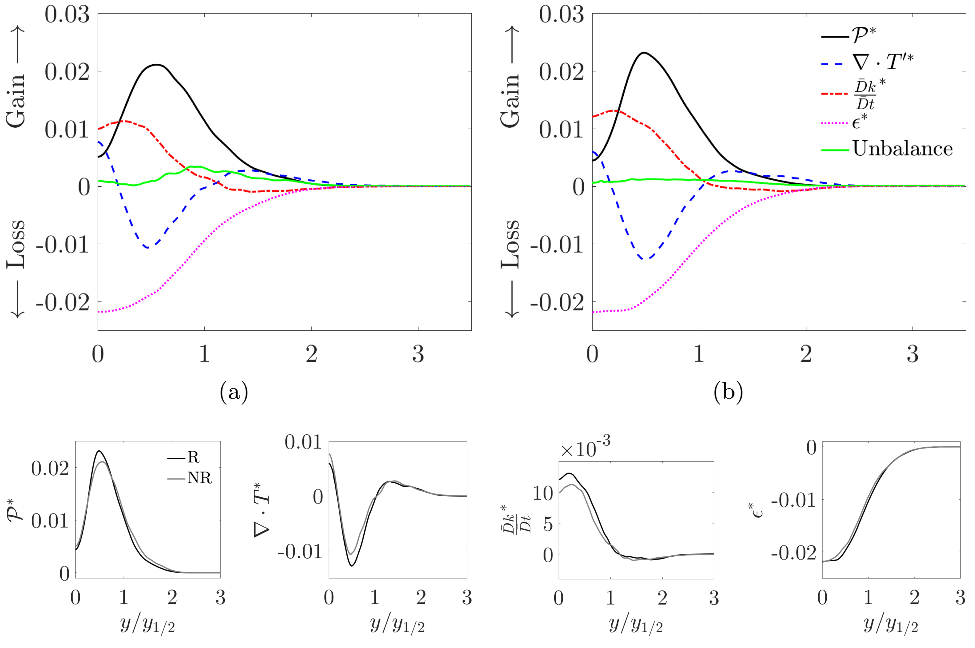

(a) (b)

(c) (d) (e) (f)

Figure 8.23: *Budget of dimensionless turbulent kinetic energy of the heated jet in the developed region: (a) uncoupled heated jet, and (b) accounting for radiative heat transfer. Comparison of the components of the turbulent kinetic energy budget: (c) production, (d) turbulent diffusion, (e) advection and (f) dissipation between the radiative and the non-radiative jet cases.*

of this radiation is further absorbed at colder regions of the jet. The emission dominated region has been delimited from the absorption dominated region by solid black lines corresponding to the isoline of $P_{rad} = 0$.

Figure 8.27(a) shows the downstream variation of the mean emission and mean absorption radiative powers along the centerline of the jet, both decrease in magnitude beyond $x = \delta$ along with the temperature decay. In the initial region of the jet, around $x < 5\delta$, radiative heat transfer is dominated by emission power yet the absorption is around 61% of the emitted power at $x = 5\delta$. As the flow evolves downstream, the difference between emitted and absorbed power decreases. Then, beyond $x > 9\delta$, in the fully turbulent region, absorption is around 80% of the emitted power. The spectral transmissivity based on the initial jet half-width length and the temperature downstream evolution computed using Eq. 3.11 is shown in Fig. 8.26 by means of the ck method. Since the optical thickness does not vary significantly downstream, the strong absorption observed beyond $x > 9\delta$ is because there is a considerable reabsorption, i.e., most of the emitted energy is reabsorbed in the immediate vicinity of the emission point; but also because there is, in some extend, a noticeable absorption from the emission at the inlet region. The nature of this energy exchange

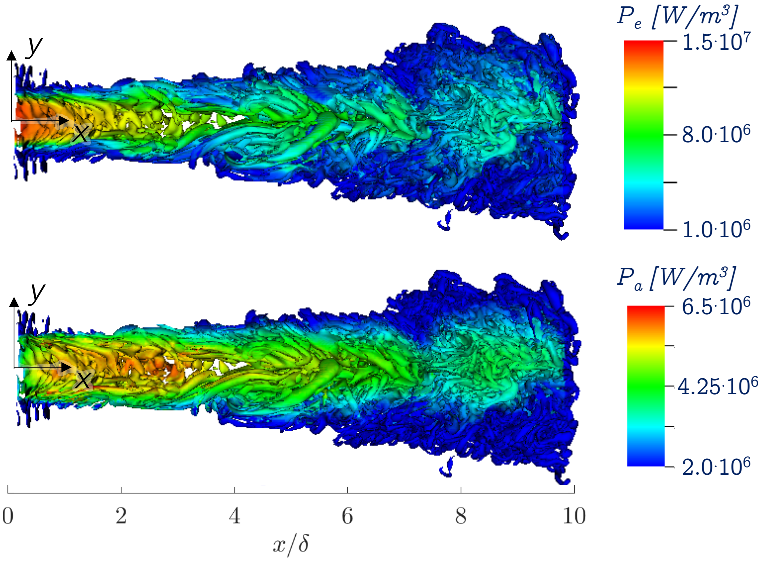

Figure 8.24: *Snapshots of turbulent eddies identified by the Q-criterion colored by P_e and P_a.*

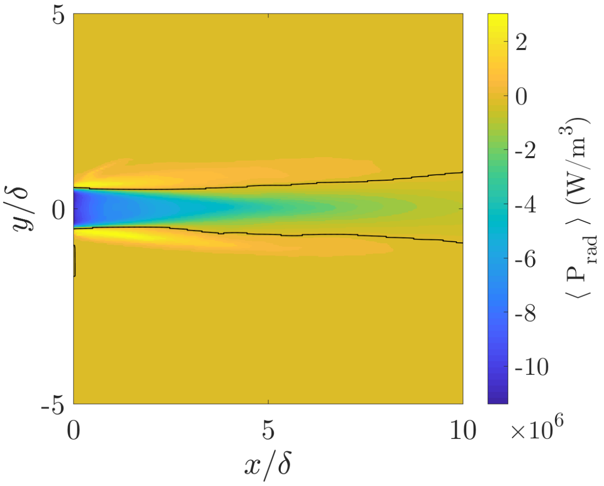

Figure 8.25: *Contour of the mean exchanged radiative power of the strongly heated jet. A solid black line delimits the emission dominated region from the absorption dominated region.*

has not been characterized in this work and it needs further information to complete the analysis.

The mean radiative power along the jet centerline, resulting from the difference between the mean emission and mean absorption radiative powers, is presented in Fig. 8.27(b). The initial zone is the most affected region by radiation due to the large radiative power emitted. Then, radiative power at the jet centerline tends to zero downstream.

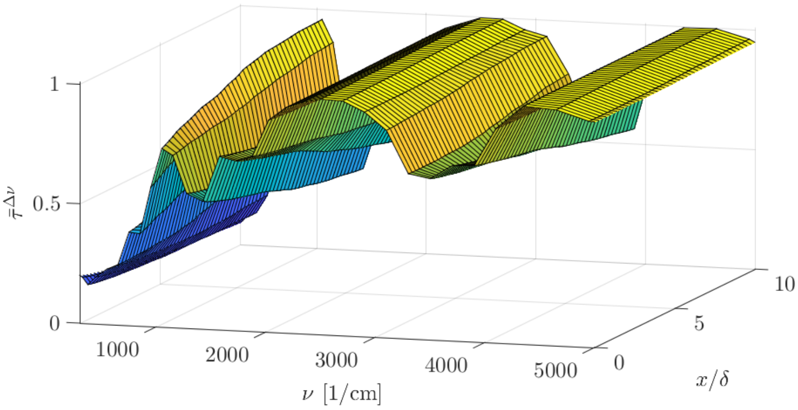

Figure 8.26: *Spectral transmissivity of water vapor based on the initial jet half-width length and the temperature downstream evolution for the strong heated jet conditions.*

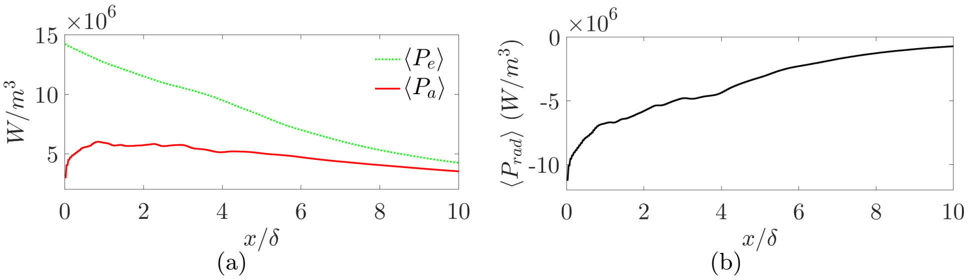

(a) (b)

Figure 8.27: *Downstream evolution along the jet centerline of (a) $\langle P_a \rangle$ and $\langle P_e \rangle$, and (b) $\langle P_{rad} \rangle$.*

The cross-section profiles of mean emission and mean absorption radiative powers in the initial zone ($x = \delta$) are shown in Fig. 8.28(a) in which a maximum relative difference of around 53% between the emitted and the absorption powers at the jet centerline is observed. The resulting mean radiative power at $x = \delta$ is presented in Fig. 8.28(b). This Figure shows a strong emitted radiative power corresponding to the jet potential core, how the radiative power tends to zero in the jet edge, and an absorption dominated zone in the outer region of the jet. In the fully turbulent zone, the temperature and its gradients are lower and the heat transport by radiation decreases significantly. This considerable reduction of the radiative power at $x = 10\delta$ is illustrated in Fig. 8.28(c) which shows that the relative difference between mean emission and absorption powers is around 17%. These values are reflected in the mean radiative power cross-section at $x = 10\delta$ presented in Fig. 8.28(d).

Despite the fact that the mean radiative power decreases significantly downstream, its cross-section profiles have similar trends. Having this in mind, an adimensionalization is proposed in order to characterize the cross-section profiles of mean radiative power in the fully developed turbulent region. The

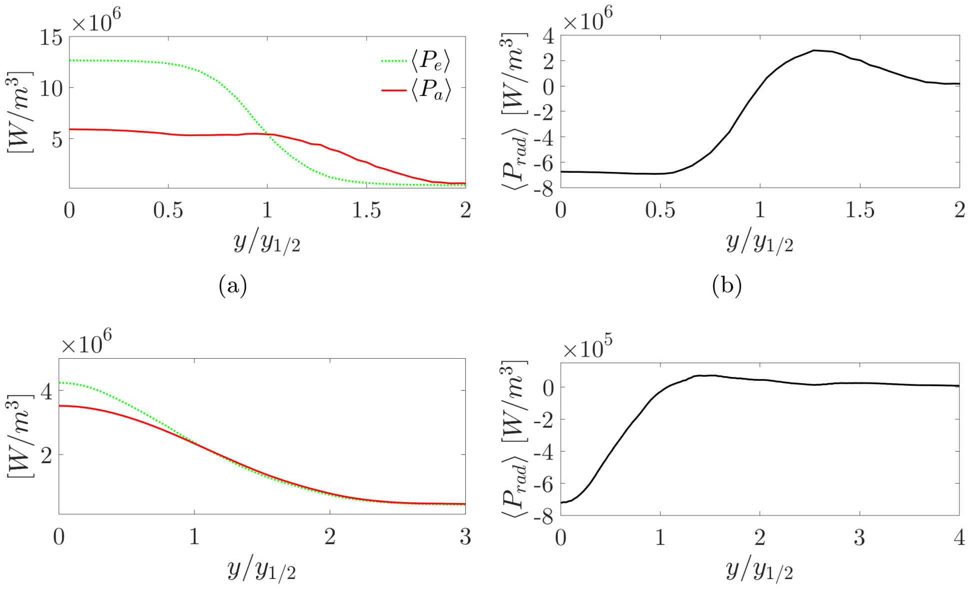

(a) (b) (c) (d)

Figure 8.28: *Mean emission, mean absorption and mean radiative powers cross-sections at the initial ($x = \delta$) and fully turbulent ($x = 10\delta$) regions. (a) $\langle P_a\rangle$ and $\langle P_e\rangle$ at $x = \delta$, (b) $\langle P_{rad}\rangle$ profile at $x = \delta$, (c) $\langle P_a\rangle$ and $\langle P_e\rangle$ at $x = 10\delta$, and (d) $\langle P_{rad}\rangle$ profile at $x = 10\delta$.*

adimensionalization is based on the distance from the centerline of the jet at which the mean radiative power is null $y_{1/2,P_{rad}}(x)$ and the magnitude of mean radiative power at the jet centerline $\langle P_{c,rad}\rangle$. On the one hand, Fig. 8.29(a) shows how dimensional radiative power profiles versus the cross-stream coordinate adimensionalized by the half-width based on velocity do not collapse into the same profile and how they decrease in magnitude downstream. On the other hand, Fig. 8.29(b) shows the adimensionalized radiative power profiles at $x = 8\delta$, $x = 9\delta$ and $x = 10\delta$. This adimensionalization induces reasonable self-similar profiles of mean radiative power beyond $x = 8\delta$. A reason to observed self-similarity in the radiative power would be due to self-similarity in the temperature profiles in addition to a strong reabsorption which would imply that the radiative power is essentially determined by local properties.

8.8 Turbulence effects on radiative heat transfer

An analysis of the effects that turbulence causes on radiation is presented in this section. These effects arise due to radiation nonlinearities: the average radiation heat transfer in a fluctuating temperature field may differ from the one obtained from the averaged temperature. To quantify the turbulence effects on radiation, a non-coupled Monte-Carlo computation of the radiative heat

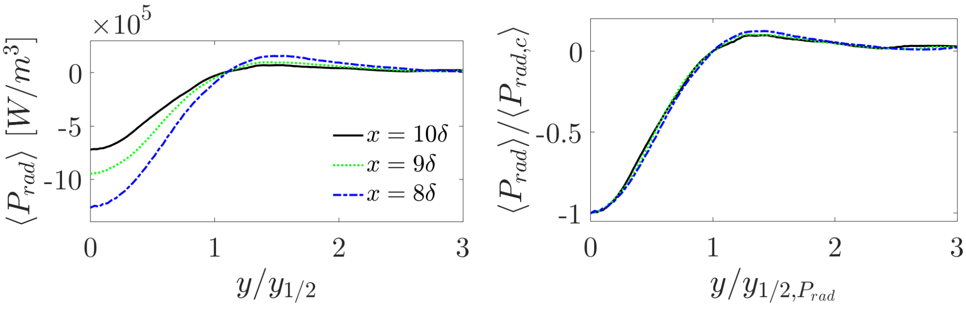

(a) (b)

Figure 8.29: *Adimensionalized radiative power profiles at different cross-sections.*

transfer from the averaged temperature field $P_{rad}\left(\langle T\rangle\right)$ is compared with the averaged radiative power from the coupled simulation $\langle P_{rad}\left(T\right)\rangle$ presented in §8.7.

The downstream evolution of $P_{rad}\left(\langle T\rangle\right)$ and $\langle P_{rad}\left(T\right)\rangle$ at the jet centerline are presented in Fig. 8.30(a), while in Fig. 8.30(b) the jet centerline differences between $P_e\left(\langle T\rangle\right)$ and $\langle P_e\left(T\right)\rangle$ are shown.

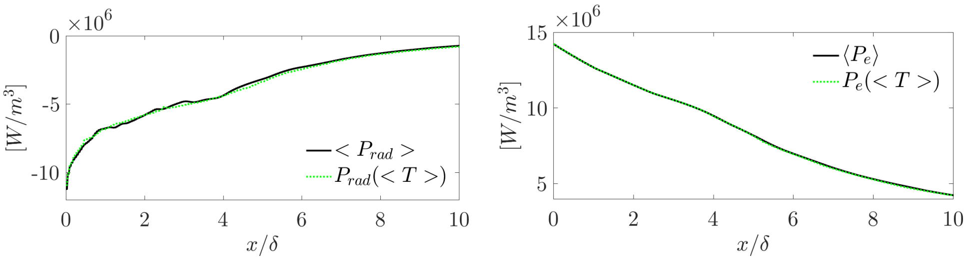

(a) (b)

Figure 8.30: *Comparison between average radiative power field and radiative power from averaged temperature field. (a) Downstream evolution of $P_{rad}\left(\langle T\rangle\right)$ and $\langle P_{rad}\left(T\right)\rangle$ along the jet centerline and (b) $P_e\left(\langle T\rangle\right)$ and $\langle P_e\left(T\right)\rangle$ downstream evolution along the jet centerline.*

In order to quantify the TRI in the radiative power, Fig. 8.31 shows the relative difference between the radiative heat transfer computed from the averaged temperature field $P_{rad}\left(\langle T\rangle\right)$ and the averaged radiative power from the coupled simulation $\langle P_{rad}\left(T\right)\rangle$ along the jet centerline. From Fig. 8.31 it can be observed that TRI, in the emission dominated jet centerline, does not exceed the relative difference of 10%.

Finally, in Figure 8.32(a) a comparison between cross-section profiles of $P_{rad}\left(\langle T\rangle\right)$ and $\langle P_{rad}\left(T\right)\rangle$ at $x = 10\delta$ is presented. Likewise, cross-section profiles of the averaged emitted and absorption radiative powers, $\langle P_e\rangle$ and $\langle P_a\rangle$, as well as the emitted and absorbed powers from averaged temperature, $P_e\left(\langle T\rangle\right)$ and

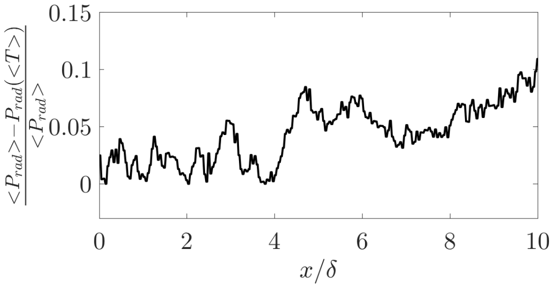

Figure 8.31: *Relative difference between* $< P_{rad} >$ *and* $P_{rad}(< T >)$ *along the strongly heated jet centerline.*

$P_a(\langle T \rangle)$, at $x = 10\delta$, are shown in Figs. 8.32(b) and 8.32(c), respectively.

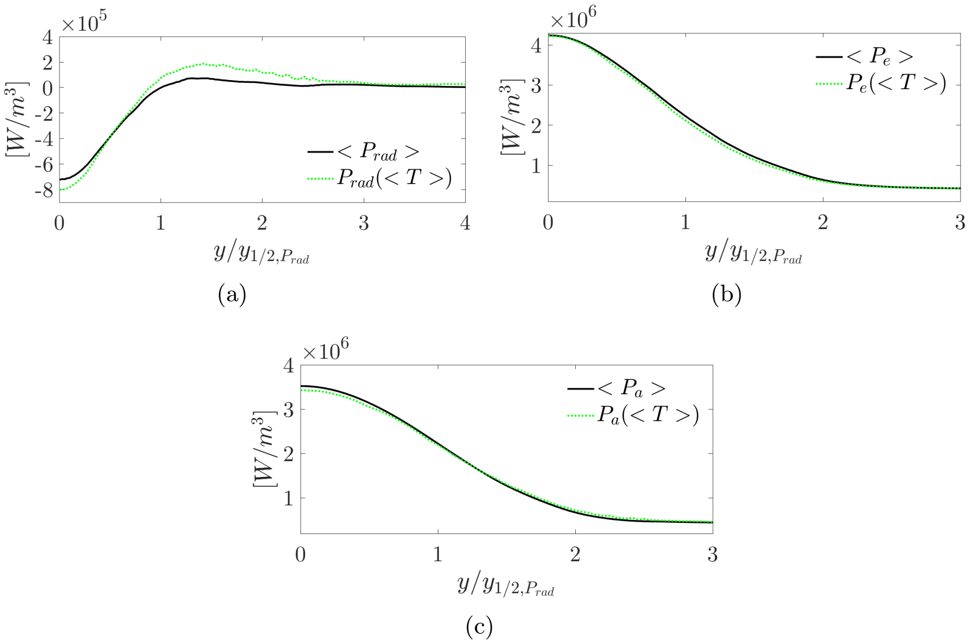

Figure 8.32: *Comparison between average radiative power field and radiative power from averaged temperature field. (a) Cross-section profile of* $P_{rad}(\langle T \rangle)$ *and* $\langle P_{rad}(T) \rangle$ *at* $x = 10\delta$, *(b) cross-section profile of* $P_e(\langle T \rangle)$ *and* $\langle P_e(T) \rangle$ *at* $x = 10\delta$, *and (c) cross-section profile of* $P_a(\langle T \rangle)$ *and* $\langle P_a(T) \rangle$ *at* $x = 10\delta$.

According with the TRI results at the jet centerline, shown in Figs. 8.30, the effects of turbulence on radiation for the case under study are small. A relative quantification has shown that such effects are lower than 10% at the jet centerline. However, a closer look at the TRI along cross-section profiles at the developed region, presented in Fig. 8.32, has shown a difference between $P_{rad}(\langle T \rangle)$ and $\langle P_{rad}(T) \rangle$. As observed in Fig. 8.32(b), radiative emitted power is always slightly unpredicted when computed from averaged temperature; while absorption is underpredicted at the inner region of the jet, and over predicted at the outer region when computed from averaged temperature. Thus, the resultant cross-section profile of P_{rad} TRI shown in Fig. 8.32(a) is correlated with the abosrption TRI rather than the emisson TRI. The observed small-to-moderate turbulent effects on radiation under the present configuraton are in accordance with the literature which stands that for most non-reactive flows the TRI effects are negligible (Mazumder and Modest (1999); Gupta et al. (2009); Zhang et al. (2013); Vicquelin et al. (2014); Fraga et al. (2017)).

8.9 Conclusions

In this Chapter, the impact of radiation has been analyzed in a non-reactive strongly heated jet. When looking at the enthalpy balance at the developed region, radiation has a noticeable contribution for $y < y_{1/2}$; thus, the nature of the heat transfer is modified by the inclusion of radiation. The main effect on mean temperature is that radiation shortens the temperature potential core and smooths the gradients of mean temperature. Additionally, it is shown that for strongly heated jets the general scaling for the temperature decay based on convective heat flux conservation for variable-density jets presented in Chapter 7 is no longer valid when large radiation effects are accounted for.

Regarding the second order moments of temperature, it is found through the analysis of the enthalpy variance budget; that when radiation is taken into account, production decreases since temperature gradients are smoother. Due to the decrease in production and the additional radiative dissipation mechanism, enthalpy variance decreases. Then, because of the acting radiative dissipation mechanism and the decreased enthalpy variance, the molecular dissipative term nearly decreases by a factor of two when radiation is considered.

Although lower than in mean temperature, a noticeable effect of radiation on the mean velocity field is found for the current configuration. It has been found that when accounting for radiation the general scaling law of variable-density jets is no longer valid; thus, radiation and its effects on density can change the dynamics of strongly heated jets. However, a slightly effect has been found in second order moments of velocity by analyzing Reynolds stresses and the budget of turbulent kinetic energy.

An adimensionalization to characterize the cross-section profiles of mean radiative power in the fully developed turbulent region of the jet has been proposed. The adimensionalization is based on the distance from the centerline of the jet at which the mean radiative power is null $y_{1/2,P_{rad}}(x)$, and the magnitude of mean radiative power at the jet centerline $\langle P_{c,rad} \rangle$. It has been found that for the strongly heated jet under study, profiles of mean radiative power become reasonable self-similar beyond $x = 8\delta$.

Finally, as already pointed out in the literature, the effects of turbulence on radiation for the nonreactive case under study has found to be small, being that the relative difference between the radiative heat transfer computed from the averaged temperature field $P_{rad}\left(\langle T\rangle\right)$ and the averaged radiative power from the coupled simulation $\langle P_{rad}\left(T\right)\rangle$, in the emission dominated jet centerline, does not exceed the relative difference of 10%.

Chapter 9

Reynolds Average Navier-Stokes results of free jets

This Chapter presents results using RANS technique of the isothermal plane jet, the uncoupled heated jet and the heated jet coupled with thermal radiation. These results are compared with the DNS data presented in Chapters 5, 7 and 8. Once the accuracy of the RANS results is assessed, uncoupled and coupled computations are analyzed to discuss the role of the novel scaling based on the convective heat flux conservation taking advantage of the relatively low time processing of RANS computations.

Contents

9.1 Comparison between RANS solutions and DNS data

This section assesses the accuracy of RANS computations by comparison with DNS data previously presented in Chapters 5, 7 and 8.

RANS solutions in the following subsections are computed using the $k-\epsilon$ LS model from Launder and Sharma (1974), second order Van Albada scheme

(Van Albada et al. (1997)) and variable transport properties as described in Chapter 4. The turbulent Prandtl number is set to $\mathrm{Pr}_t = 0.6$. To appropriately compare the RANS solver with the DNS data, RANS boundary conditions for k and ϵ are based on results of the DNS simulations.

9.1.1 Results of the isothermal plane jet

The present setup for the isothermal plane jet summarized in Table 9.1 corresponds to the one presented in Chapter 5.

Table 9.1: *Setup configuration of the isothermal turbulent plane jet.*

δ [m]	U_1 [m/s]	U_2 [m/s]	T_1 [K]	T_2 [K]	Re	P_0 [atm]
$5 \cdot 10^{-2}$	4.176	$U_1/10$	610	610	3200	1

In order to check the effect of confinement due to the domain size, two RANS simulations are considered for the isothermal jet:

- A RANS setup with the same domain extend than the DNS domain, i.e., $(L_x \times L_y/2) = (13.5\delta \times 5\delta)$ with 141 × 81 nodes as in Chapter 4, referred in this section as RANS-10δ.
- Another setup, with the same refinament than in the RANS-10δ mesh, but considering a total extension of $(L_x \times L_y/2) = (35\delta \times 15\delta)$ with a grid of 241 × 141 nodes, referred in this section as RANS-35δ

Figure 9.1 compares the jet half-width growth $y_{1/2}$, in Fig. 9.1(a), and the centerline mean excess velocity decay $(\Delta U_0/\Delta\{U_c\})^2$, in Fig. 9.1(b), between DNS data presented in Chapter 5 and the current RANS results. For the DNS and the RANS-10δ, a linear regression in the fully developed region is plotted. The coefficients for the linear fitting are computed using values between $8\delta < x < 10\delta$ for both the RANS and the DNS data. Additionally, results from the experimental work of Thomas and Chu (1989) are also shown as a reference.

In order to quantify the accuracy of the RANS modeling, Table 9.2 compares the present RANS results of the linear fitting coefficients of the jet growth and the velocity decay with the DNS data along with the experimental studies of Jenkins and Goldschmidt (1973); Goldschmidt and Young (1975); Thomas and Chu (1989); Gutmark and Wygnanski (1976), and the numerical work of Stanley et al. (2002). The effect of considering a larger domain are also analyzed in Table 9.2. The linear fitting coefficients corresponding to the simulation RANS-35δ are computed using values between $8\delta < x < 10\delta$ (as in the DNS and RANS-10δ), but also using values between $10\delta < x < 25\delta$ in order to check that the fully developed region is reached in the reduced domain.

As observed in Table 9.2, the results of the virtual origins ($K_{2,u}$ and $C_{2,u}$) strongly differ among the referred works since they have strong dependency on the inflow conditions as explained by Klein et al. (2003). Despite RANS solutions are in good agreement with previous data, there is an effect of confinement on the RANS solutions as shown in Table 9.2. Moreover, velocity

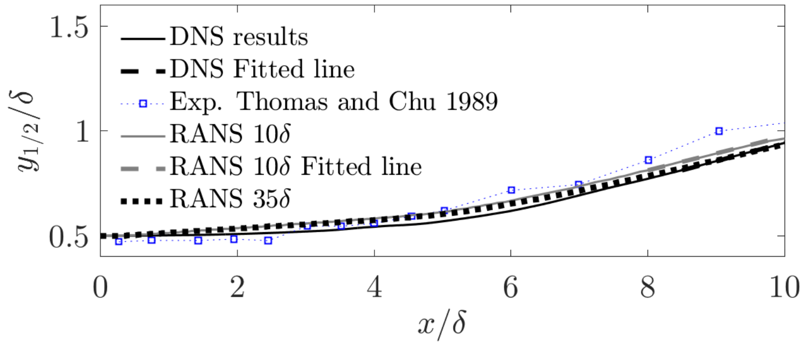

(a)

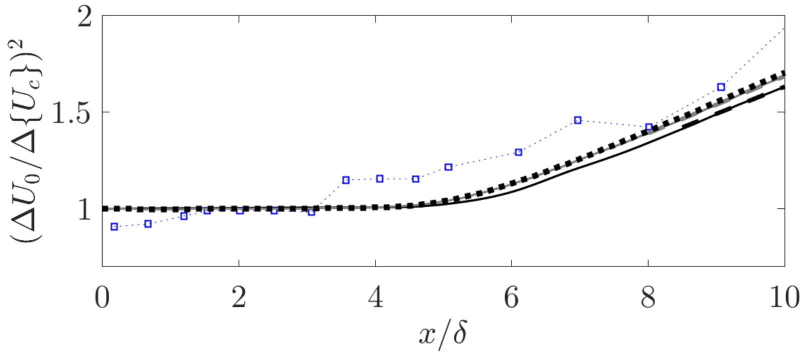

(b)

Figure 9.1: *Comparison of the present isothermal plane jet results with the experimental work of Thomas and Chu (1989): downstream evolution of (a) spread rate and (b) velocity decay.*

decay rate and the slope of the jet spread are slightly different when fitted between $8\delta < x < 10\delta$ or between $10\delta < x < 25\delta$. However, despite the observed changes in the RANS solutions, predicted slope coefficients ($K_{1,u}$ and $C_{1,u}$) for both domain sizes compare reasonable well with the DNS data.

Table 9.2: *Comparison of the jet growth and the centerline velocity decay linear fitting coefficients computed using beyond $x = 8\delta$ for the RANS and the DNS data, along with experimental and numerical reference data.*

	$K_{1,u}$	$K_{2,u}$	$C_{1,u}$	$C_{2,u}$
Jenkins and Goldschmidt (1973)	0.088	-4.5	0.160	4.0
Gutmark and Wygnanski (1976)	0.100	-2.00	0.189	-4.72
Goldschmidt and Young (1975)	0.0875	-8.75	0.150	-1.25
Thomas and Chu (1989)	0.110	0.14	0.220	-1.19
Stanley et al. (2002)	0.092	2.63	0.201	1.23
DNS results	0.088	0.721	0.146	1.181
RANS 10δ	0.080	2.176	0.148	1.365
RANS 35δ $8\delta < x < 10\delta$	0.075	2.465	0.151	1.284
RANS 35δ $10\delta < x < 25\delta$	0.087	0.565	0.163	1.429

Figure 9.2 compares the cross-section profiles at $x = 10\delta$ of streamwise velocity, in Fig. 9.2(a), and of cross-stream velocity, in Fig. 9.2(b), between the present RANS-10δ results and the DNS data presented in Chapter 5. Moreover, results from the RANS-35δ at x=25δ, experimental data by Gutmark and Wygnanski (1976), and numerical results from Stanley et al. (2002) are also plotted as a reference. From Fig. 9.2, it can be observed that RANS-10δ roughly describes velocity cross-section profiles when compared with DNS, although general trends are captured. Additionally, RANS-35δ is in very good agreement with DNS data.

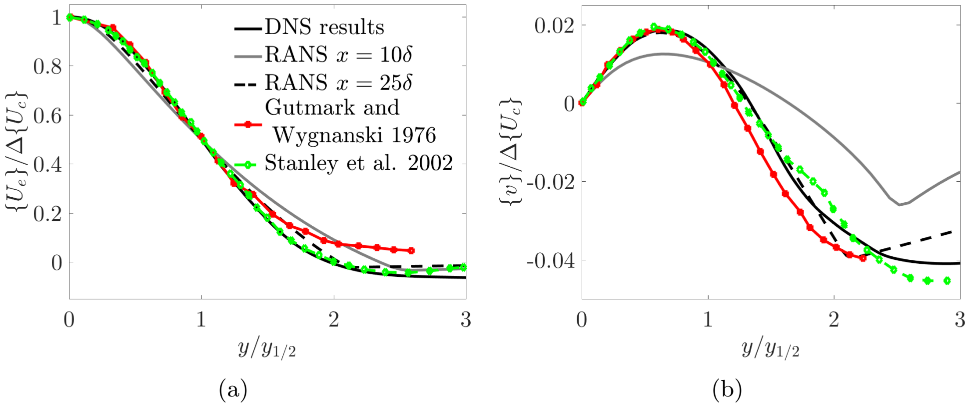

(a) (b)

Figure 9.2: *Comparison between RANS and DNS results of the self-similar profiles of (a) streamwise and (b) cross-stream velocities of the isothermal plane jet.*

Figure 9.3 compares the Reynolds stresses of the RANS-10δ results with the DNS data in the developed region at $x = 10\delta$. Moreover, results from the RANS-35δ at x=25δ are shown. As a reference, data from Thomas and Prakash (1991), Ramaprian and Chandrasekhara (1985), Bradbury (1965); and Stanley et al. (2002) are also plotted. Despite normal Reynolds stresses are underpredicted at the jet centerline for the RANS-10δ simulation, RANS results of Reynolds stresses show good agreement with DNS data.

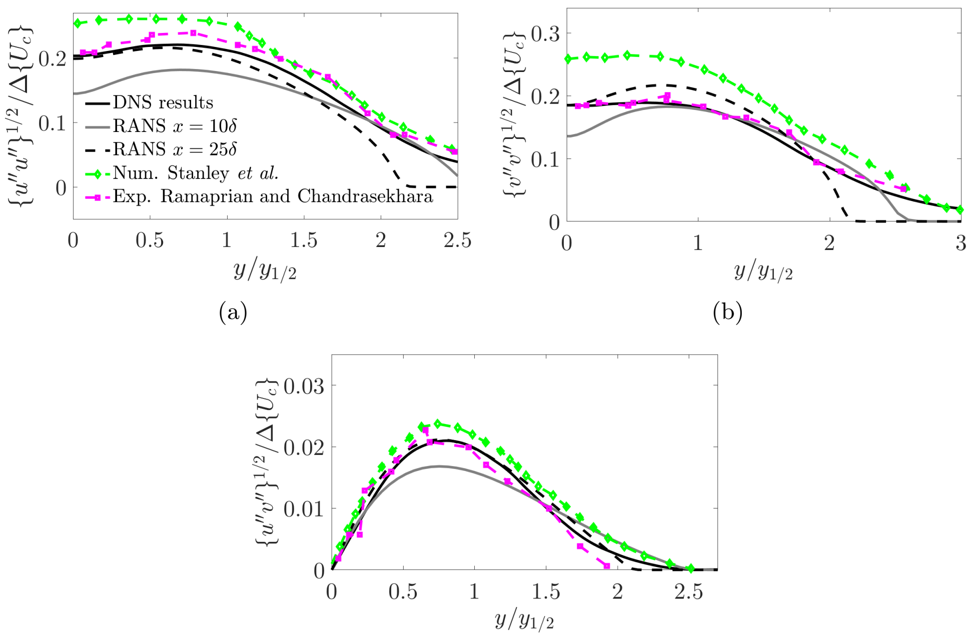

(a) (b)

(c)

Figure 9.3: *Self-similar Reynolds stresses profiles of the isothermal plane jet in the (a) x direction, (b) y direction; and (c) shear stress at $x = 10\delta$ and $x = 25\delta$ for the RANS-10δ and RANS-35δ simulations, respectively.*

As stated in Chapter 2, the transport equation of the turbulent kinetic energy in the RANS context is expressed as

$$\underbrace{\frac{\partial(\langle\rho\rangle k)}{\partial t} + \frac{\partial(\langle\rho\rangle\{u_i\}k)}{\partial x_i}}_{\text{Advection, } \langle\rho\rangle\frac{\bar{D}k}{Dt}} = \underbrace{\frac{\partial}{\partial x_i}\left[\left(\{\mu\} + \frac{\mu_t}{\sigma_k}\right)\frac{\partial k}{\partial x_i}\right]}_{\text{Diffusion terms, } -\nabla\cdot T} + \underbrace{\mathcal{P}}_{\text{Production}} - \underbrace{(\rho\tilde{\epsilon} + D)}_{\text{Viscous dissipation, } \epsilon}, \tag{9.1}$$

where D is defined as $D = 2\mu\left(\frac{\partial k^{1/2}}{\partial x_j}\right)^2$ following the $k - \epsilon$ LS model from Launder and Sharma (1974).

When adimensionalized by the scaling factor $y_{1/2}/(\Delta\{U_c\}^3\langle\rho\rangle)$, the turbulent kinetic energy balance can be expressed as

$$\frac{\bar{D}k^*}{\bar{D}t} + \nabla \cdot T^* = \mathcal{P}^* - \epsilon^*, \tag{9.2}$$

where * denotes adimensionalized quantities.
Figure 9.4(a) presents the budget of the turbulent kinetic energy in the self-similiar zone obtained by both the RANS-10δ and RANS-35δ computations at two different cross-sections: $x = 10\delta$ for the RANS-10δ simulation and $x = 25\delta$ for the RANS-35δ. Each term of the budget is modeled following Eq. 9.1. Additionally, Figs. 9.4(b) to 9.4(e) show a comparison of each term of the turbulent kinetic energy equation between the DNS data presented in Chapter 5, and the RANS-10δ and RANS-35δ simulations. For the adopted RANS model, production and dissipation trends are well captured. However, RANS-10δ results of production and dissipation are slightly lower in magnitude than DNS data. Despite trends of advection and turbulent diffusion are somehow correct, RANS-10δ results poorly captured its value all along the cross-section when compared with the DNS data.

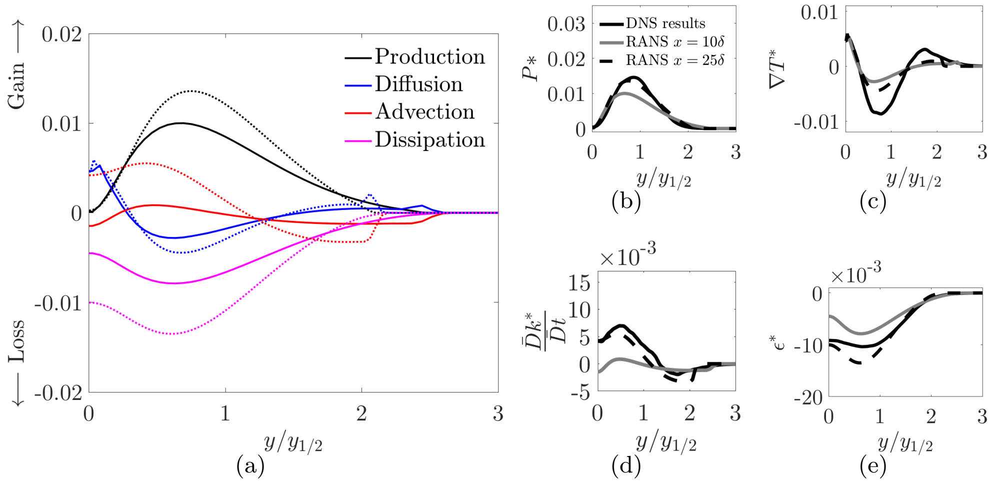

Figure 9.4: *(a) Budget of dimensionless turbulent kinetic energy of the isothermal jet at different cross-sections; RANS-10δ simulation (solid line) , RANS-35δ simulation (dotted line). Components of the turbulent kinetic energy budget: (b) production, (c) turbulent diffusion, (d) advection and (e) dissipation compared with DNS results at the developed region.*

9.1.2 Results of the heated jet

The present setup for the heated jet corresponds to the one presented in Chapter 5, its main features are recalled in Table 9.3.

Table 9.3: *Setup configuration of the slightly heated jet.*

δ [m]	U_1 [m/s]	U_2 [m/s]	T_1 [K]	T_2 [K]	Re	P_0 [atm]
$5 \cdot 10^{-2}$	4.176	$U_1/10$	860	380	1500	1

As shown in Figure 9.5, good agreement is found in the cross-section profile of temperature corrected by the coflow temperature $\{T_e\} = \{T\} - T_2$ adimensionalized by $\Delta\{T_c\}$ between the DNS, and the RANS computed in DNS domain extend. Therefore, hereinafter this domain size for the RANS simulation is used to continue the discussion. In Figure 9.5, as a reference, results from Davies et al. (1975), Jenkins and Goldschmidt (1973) and Antonia et al. (1983) are also plotted.

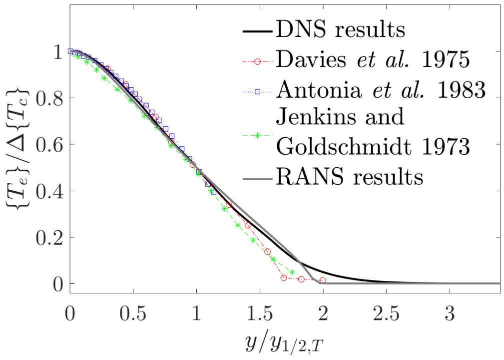

Figure 9.5: *DNS and RANS dimensionless Favre averaged temperature profiles of the heated plane jet at $x = 10\delta$ compared with reference experimental data.*

In Figure 9.6, RANS results of the evolution of the half-width of the jet based on temperature are compared with the DNS results presented in Chapter 5. Additionally, as a reference, the numerical results of Stanley et al. (2002) and the experimental data of Browne et al. (1983) are also presented. It is worth to mention that numerical results of Stanley et al. (2002) are based on a passive scalar, i.e., the passive scalar has null effects on the flow field. Similarly, Browne et al. (1983) set an initial excess temperature of $\Delta T_0 = T_1 - T_2 = 25$ K causing little effects on density. In contrast, the initial excess temperature of the present simulation is $\Delta T_0 = 480$ K.

RANS initial developing region is shorter than the one from DNS data. However, the slope of the downstream evolution of $y_{1/2,T}$ computed using RANS is in good agreement with the DNS data. This is the same behavior found for the half-width based on velocity in §9.1.1.

Figure 9.7 shows the temperature decay in the jet centerline in which $\Delta\{T_c\} = \{T_c\} - T_2$. As for the velocity decay, RANS results and DNS data slopes have a very close value.

As explained in Chapter 5, the conservation of momentum flux in the developed

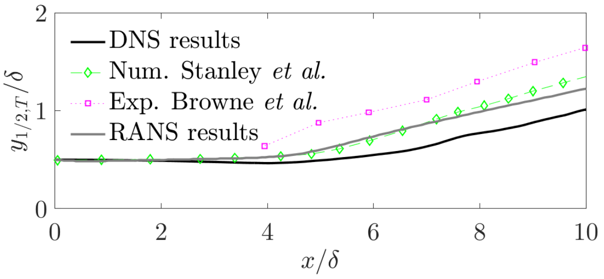

Figure 9.6: *Comparison of the results for the downstream evolution of the jet spread based on temperature between RANS and DNS.*

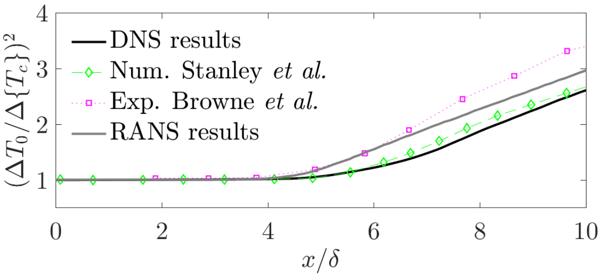

Figure 9.7: *Comparison of the temperature decay along the jet centerline between RANS and DNS results for the uncoupled slightly heated jet.*

region yields

$$\frac{\Delta\{U_c\}^2 y_{1/2}}{\Delta U_0^2 r_\epsilon} \sim constant, \tag{9.3}$$

where $r_\epsilon = \delta\left(\overline{\rho_0}/\langle\rho_c\rangle\right)$, $\langle\rho_c\rangle$ is the mean density at the jet centerline and $\overline{\rho_0}$ is the mean jet density at the exit nozzle $\overline{\rho_0} = \frac{1}{\delta}\int_\delta \langle\rho\rangle_{|x=0}\, dy$.

Figure 9.8(a) clearly shows that the velocity decay of the isothermal and heated jets have different slopes. However, when ploted against x/r_ϵ density effects are compensated and velocity decays collapse into almost the same curve as shown in Fig. 9.8(b).

9.1.3 Heated jet coupled with radiative heat transfer

In order to assess the accuracy of the RANS computations coupled with radiative heat transfer, temperature and radiative power fields from RANS solutions are compared with the DNS data of the slightly and strongly heated coupled jets obtained in Chapters 7 and 8 , respectively. Setup for these jets are summarized in Table 9.4.

The staggered procedure described in Chapter 3 is used in order to couple RANS and MC codes. The setup for the Monte-Carlo solver is the same that the one used for the jet dimensioning presented in §4.3.2. Considering that the

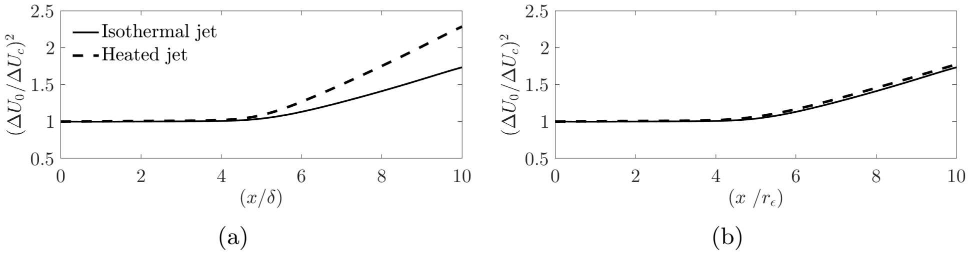

(a) (b)

Figure 9.8: *RANS results of the centerline velocity decay for the isothermal and heated jets against (a) x/δ and (b) x/r_ϵ.*

Table 9.4: *Configuration of the slightly and strongly heated jets.*

	δ [m]	U_1 [m/s]	T_1 [K]	T_2 [K]	Re	P_0 [atm]
Slightly heated	$5 \cdot 10^{-2}$	4.176	860	380	1500	1
Strongly heated	$5 \cdot 10^{-2}$	4.176	2500	405	500	2.576

turbulent effects on radiation are small-to-moderate as shown in Chapter 8, no TRI model is used to computed the coupled solution, i.e., the radiative power field is directly computed from the averaged temperature given by the RANS solver.

9.1.3.1 Slightly heated jet coupled with the Monte-Carlo solver

Before comparing the radiative power between RANS and DNS results, the temperature decay between both approaches is presented in Fig. 9.9. RANS results present a shorter potential core and the temperature decay rate is in good accordance, as for the uncoupled slightly heated jet, which is an expected result since radiation has a minor effect in the developed region as shown in Chapter 7.

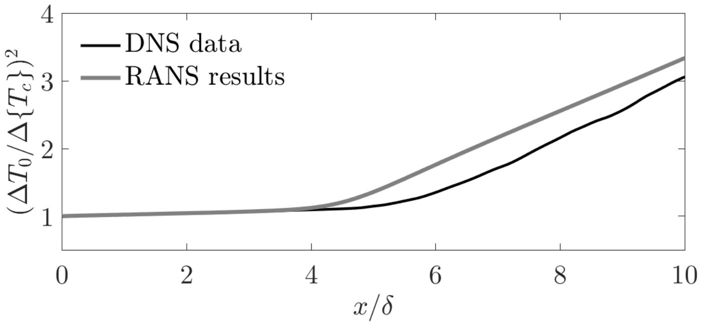

Figure 9.9: *Downstream evolution of temperature decay along the jet centerline between RANS and DNS results for the coupled slightly heated jet.*

In order to compare the mean radiative power between the DNS and the RANS solutions, Figure 9.10 shows the contours of $\langle P_{rad} \rangle$ for the coupled slightly heated jet using both approaches. The radiative power contour shown in Fig. 9.10(a) corresponds to DNS data and it has been already presented in Chapter 7. Figure 9.10(b) shows the radiative power computed by coupling the RANS code to the Monte-Carlo solver. Despite the predicted temperature potential core is narrower for the coupled RANS results, the RANS coupled solution of the slightly heated jet estimates well the radiative power field given reasonably good trends when compared with the DNS data.

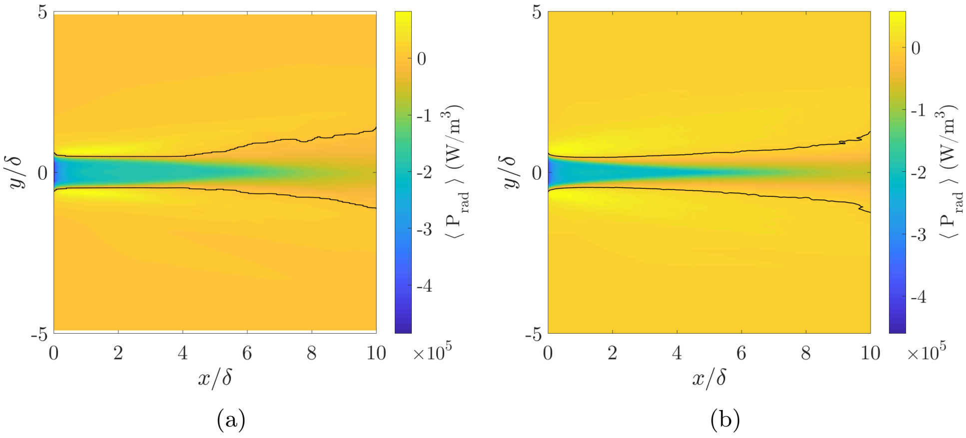

Figure 9.10: *Contour of the mean exchanged radiative power. A solid black line delimits the emission dominated region from the absorption dominated region. (a) Coupled DNS data and (b) coupled RANS results.*

Figure 9.11 compares the radiative power at the jet centerline between the DNS data presented in Chapter 7 and the current RANS results. Moderate, discrepancies are found in Fig. in 9.11, since the fact of neglecting TRI at the jet centerline has shown little impact on the resultant P_{rad}, those discrepancies are rather caused by the differences in the computed RANS temperature field. A greater emitted radiative power is obtained for the RANS results until the temperature at the jet centerline starts to drop, at around $x = 4\delta$. Then, because the absolute temperature at the jet centerline is lower for the RANS solution, as shown in Fig. 9.9, the radiative power from the RANS computation accounts for less emitted radiative power which implies that radiative power is smaller in magnitude beyond $x = 5\delta$.

Figure 9.12 compares the cross-section profiles at $x = 10\delta$ between the DNS data presented in Chapter 7 and the current RANS results for the slightly heated jet. Fig. 9.12 shows that trends of the cross-section profile are reasonably well captured by the RANS coupled computations in spite of small differences are observed. Because the temperature cross-section is reasonably well predicted by the RANS solver as shown in Fig. 9.5, and because a noticeable moderate effect was predicted in the cross-section profiles of radiative power at

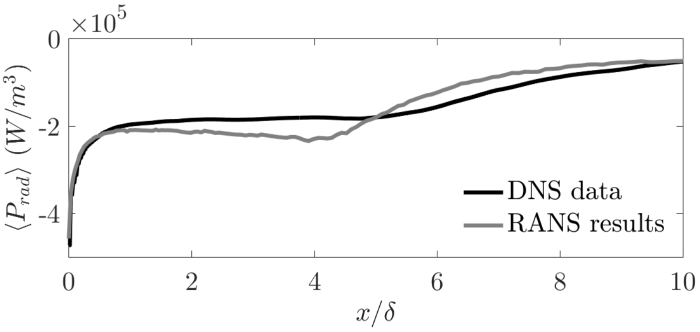

Figure 9.11: *Comparison of the downstream evolution of the mean radiative power along the jet centerline between RANS solution and DNS data for the slightly heated coupled jet.*

$x = 10\delta$ due to TRI effects (although the study refers to the strongly heated jet); those small differences observed in Fig. 9.12 are caused, in some extend, to the fact that TRI effects are not considered in this coupled simulations.

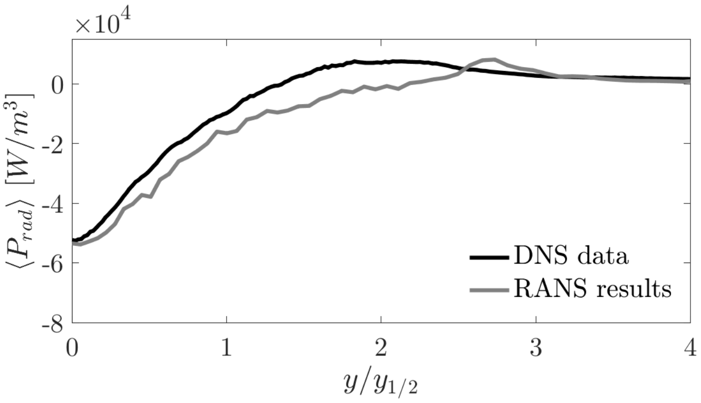

Figure 9.12: *Comparison of cross-section profiles at $x = 10\delta$ of the mean radiative power between RANS solution and DNS data for the slightly heated coupled jet.*

9.1.3.2 Strongly heated jet coupled with the Monte-Carlo solver

In contrast with the slightly heated jet, coupled RANS results for the temperature decay rate for the strongly heated case do not match DNS data as shown in Fig. 9.13. As explained in Chapter 2, the turbulent heat flux in the RANS framework is closed using an analogy between momentum and heat transfer in the form

$$\langle \rho \rangle \{u_j'' h''\} = -\frac{\mu_t}{\mathrm{Pr}_t} \frac{\partial \{h\}}{\partial x_j} \tag{9.4}$$

where Pr_t is the turbulent Prandtl number. A common approach is to consider a constant value for Pr_t, in this work we set until now $\mathrm{Pr}_t = 0.6$ following

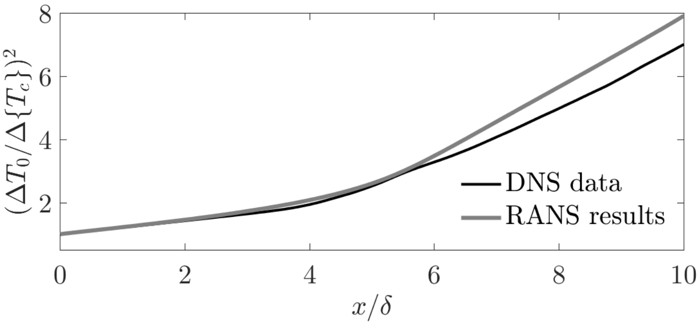

Figure 9.13: *Comparison of the temperature decay along the jet centerline between RANS and DNS results for the coupled strongly heated jet using $Pr_t = 0.6$.*

typical values for a free shear layer (Wilcox et al. (1998) and Pope (2001)). However, considering the disagreement of the temperature decay rate between RANS and DNS data shown in Fig. 9.13, the value of Pr_t from DNS data has been explicitly computed using the following expression, valid in thin layers,

$$\mathrm{Pr}_t = \frac{-\langle\rho\rangle\{u''v''\}}{-\langle\rho\rangle\{v''h''\}/cp}\frac{\partial\{T\}/\partial y}{\partial\{u\}/\partial y}, \tag{9.5}$$

for the radiative (R) and non-radiative (NR) strongly heated jets. Figure 9.14 shows numerical results of the turbulent Prandtl number computed from the DNS data presented in Chapter 8. In Figures 9.14(a) to 9.14(c) the downstream evolution of Pr_t for three constant $y_{1/2}$-lines are plotted, which are respectively $\mathrm{Pr}_t(x, y = y_{1/2}/2)$, $\mathrm{Pr}_t(x, y = y_{1/2})$ and $\mathrm{Pr}_t(x, y = 3y_{1/2}/2)$. While turbulent Prandtl number close to the jet centerline (Fig. 9.14(a)) for the R case has a close value to the NR case and even lower, in the outer region of the jet $y = 3y_{1/2}/2$ (Fig. 9.14(c)) it has significant higher values. The increase in the turblent Prandt Number due to the effects of radiation has already been reported in the work of Vicquelin et al. (2014) in wall bounded flows.

In order to quantify the increase in the turbulent Prandtl number due to radiation, the spatial averages of Pr_t computed in the range $5\delta < x < 10\delta$ for the iso-$y_{1/2}$-lines are reported in Table 9.5. As an initial approach, the variation on the Prandtl number due to the inclusion of radiation is not modeled but, based on the values presented in Table 9.5, a constant $\mathrm{Pr}_t = 0.9$ is now set for the RANS simulation. Then, the temperature decay along the jet centerline using $\mathrm{Pr}_t = 0.9$ is presented in Fig. 9.15. The decay rate for the strongly heated jet computed by RANS is now in agreement with the DNS data.

Figure 9.16 shows the same analysis of the turbuent Prandt number done in Fig. 9.14 but for the DNS results of the slightly heated jet presented in Chapter 7. As expected, Pr_t does not vary significantly due to the consideration of radiation in the slightly heated jet as shown in Fig. 9.16.

Then, following the RANS simulations with $\mathrm{Pr}_t = 0.9$, Fig. 9.17 compares the contours of $\langle P_{rad}\rangle$ for the strongly heated jet between DNS data, in Fig.

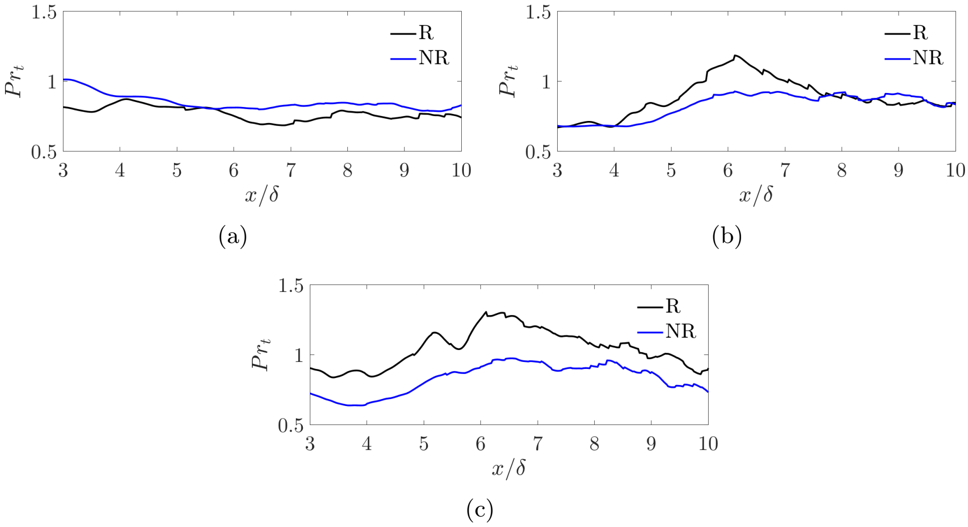

(a)

(b)

(c)

Figure 9.14: *Comparison of* Pr_t *results computed from DNS data of the strongly heated jet between the radiative (R) and non-radiative (NR) cases along three different lines of equal* $y_{1/2}$*: (a)* $Pr_t(x, y = y_{1/2}/2)$*, (b)* $Pr_t(x, y = y_{1/2})$ *and (c)* $Pr_t(x, y = 3y_{1/2}/2)$*.*

Table 9.5: *Turbulent Prandtl number spatially averaged along lines of equal* $y_{1/2}$ *for the Radiative (R) and the Non-radiative (NR) cases of the strongly heated jet.*

Case	$\overline{\mathrm{Pr}_t(x, y = y_{1/2}/2)}$	$\overline{\mathrm{Pr}_t(x, y = y_{1/2})}$	$\overline{\mathrm{Pr}_t(x, y = 3y_{1/2}/2)}$
R	0.5613	0.8249	1.1006
NR	0.7779	0.8811	0.8848

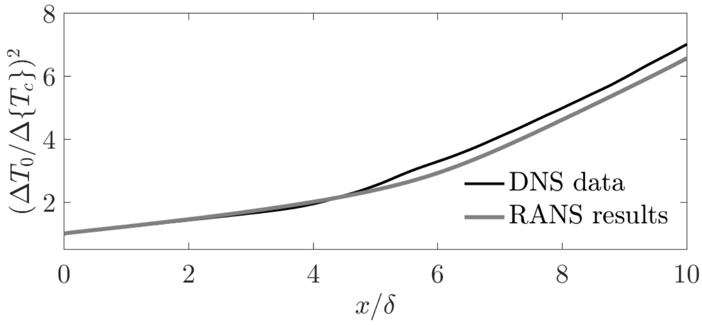

Figure 9.15: *Comparison of the temperature decay along the jet centerline between RANS and DNS results for the coupled strongly heated jet using* $Pr_t = 0.9$*.*

9.17(a), and the RANS solution, in Fig. 9.17(b). The coupled RANS solution estimates reasonably well the radiative power field when compared with the DNS data of the strongly heated jet.

A comparison of the radiative power downstream evolution at the jet centerline

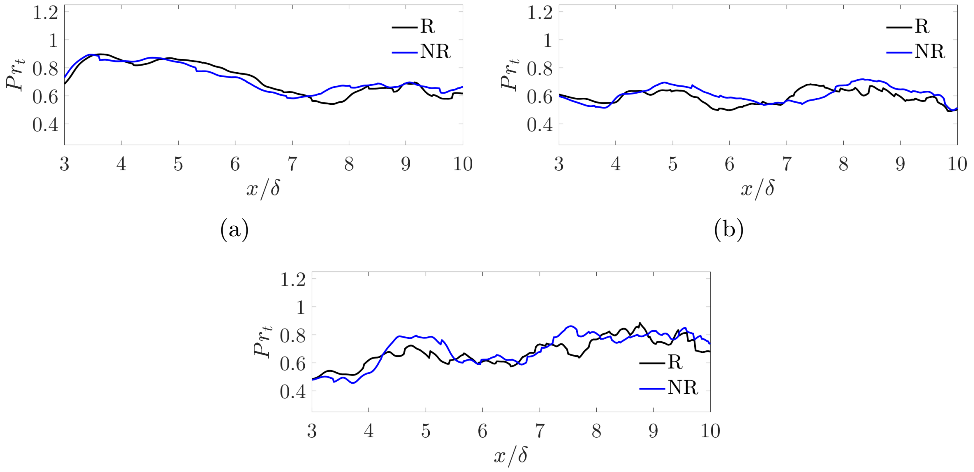

(a)

(b)

(c)

Figure 9.16: *Comparison of Pr_t results computed from DNS data of the slightly heated jet between the radiative (R) and non-radiative (NR) cases along three different lines of equal $y_{1/2}$: (a) $Pr_t(x, y = y_{1/2}/2)$, (b) $Pr_t(x, y = y_{1/2})$ and (c) $Pr_t(x, y = 3y_{1/2}/2)$.*

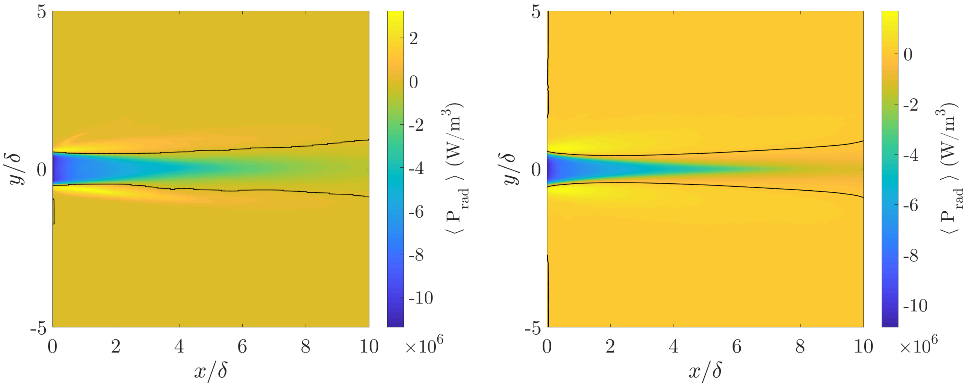

(a)

(b)

Figure 9.17: *Contour of the mean exchanged radiative power. A solid black line delimits the emission dominated region from the absorption dominated region. (a) Coupled DNS data and (b) coupled RANS results.*

between DNS and RANS results for the strongly heated case is presented in Fig. 9.18. A good prediction by RANS is found, despite the radiative power from RANS computation is slightly greater in magnitude all along the jet centerline.

Figure 9.19 compares the cross-section profiles at $x = 10\delta$ between the DNS data and the current RANS results. Analogous to Fig. 9.12, radiative power trends of the cross-section profile at $x = 10\delta$ are also reasonably well captured

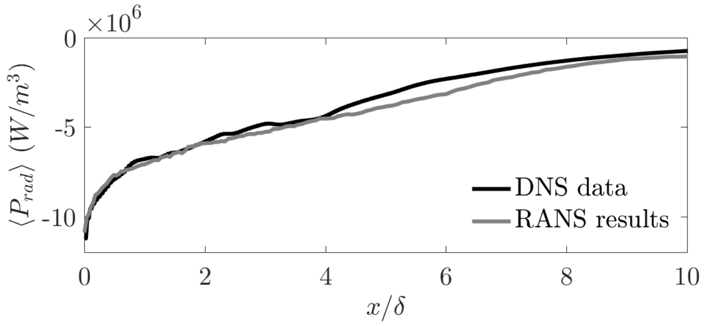

Figure 9.18: *Comparison between RANS solution and DNS data of downstream evolution of the mean radiative power along the jet centerline for the strongly heated jet.*

in spite of small differences can be observed. Due to the fact that a noticeable moderate TRI effect was predicted in Chapter 8 in the cross-section profiles of radiative power at $x = 10\delta$; those small differences are caused, in some extend, to the fact that TRI effects are not considered in this coupled simulation. Additionally, the differences between the DNS and the RANS solutions of P_{rad} shown in Fig. 9.19 present similar trends that the ones due to not consider TRI effects, presented in Fig. 8.32(a). These trends are a slightly over-prediction in magnitude of the radiative power at the inner region of the jet, and an over-prediction of the radiative power at the jet outer region.

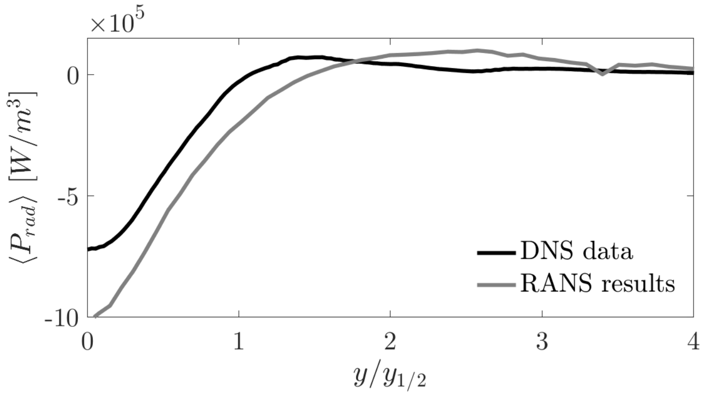

Figure 9.19: *Comparison between RANS solution and DNS data of cross-section profiles at $x = 10\delta$ of the mean radiative power for the strongly heated jet.*

9.2 Assessing the scaling based on convective heat flux conservation in the RANS context

Taking advantage of the relatively low time processing of the RANS solutions, the novel adimensionalization based on convective heat flux conservation presented in Chapter 7 is here analyzed for various differently heated jets uncoupled and coupled with radiative heat transfer. The turbulent Prandtl number is set to a constant value of $\mathrm{Pr}_t = 0.6$. The jets used to check the adimensionalization are presented in table 9.6, in which initial jet temperature T_1 is varied from 500 to 2500 K and the Reynolds number is changed accordingly to set $U_1 = 4.176$ m/s, $P_0 = 1$ atm and $\delta = 0.05$ m. The coflow is keep for all cases at temperature $T_2 = 380K$ and velocity $U_2 = 0.1U_1$. The jet corresponding to the Run # 1 is expected to have smaller density effects than the slightly heated jet presented in Chapter 7, while the rest of the jets are expected to increasingly have stronger effects. Mesh and domain sizes, as well as the Monte-Carlo setup are the same than the ones used in Chapter 4.

Table 9.6: *Main characteristics of the heated jets used to check the adimensionalization based on convective heat flux conservation.*

Run	T_1 (K)	*Re*
Run # 1	500	4851
Run # 2	1000	1097
Run # 3	1500	492
Run # 4	2000	287
Run # 5	2500	193

9.2.1 Uncoupled heated jets

Temperature decays of the jets defined in table 9.6 using the classic adimensionalization are presented in Fig. 9.20. When using the classical adimensionalization the temperature decay rate increases along with the initial jet temperature. As it can be seen in Fig. 9.20 the slopes of the temperature decay clearly have different values.

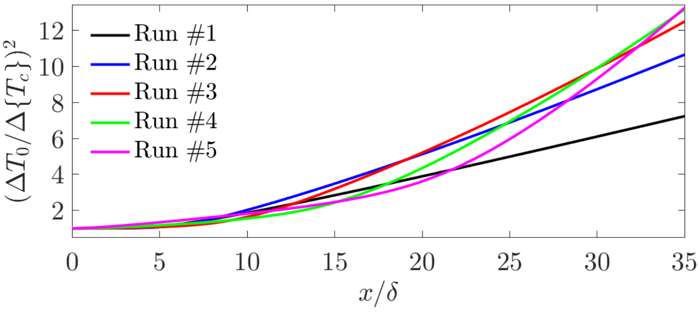

Figure 9.20: *Downstream evolution of the temperature decay along the jet centerline using the classical adimensionalization for five different heated jets.*

As demonstrated in Chapter 7, the conservation of convective heat flux together with the self-similar assumption bring to the following expression for the temperature decay

$$\left(\frac{\Delta\{T_c\}}{\Delta T_0}\right)^2 \frac{y_{1/2,T}}{r_{\epsilon,T}} = \text{constant}, \tag{9.6}$$

where

$$r_{\epsilon,T} = \frac{\delta^2}{y_{1/2,T}} \left(\frac{\overline{\rho_0}}{\langle\rho_c\rangle}\right)^2 \left(\frac{\overline{u_0}}{\{u_c\}}\right)^2. \tag{9.7}$$

Figure 9.21 shows again the centerline temperature decay of heated jets defined in Table 9.6, but this time using the equivalent heat jet opening based on the convective heat flux conservation ($r_{\epsilon,T}$) to scale the results. In contrast with Fig. 9.20, the temperature decays shown in Fig. 9.21 have almost the same slope for the five tested heated jets.

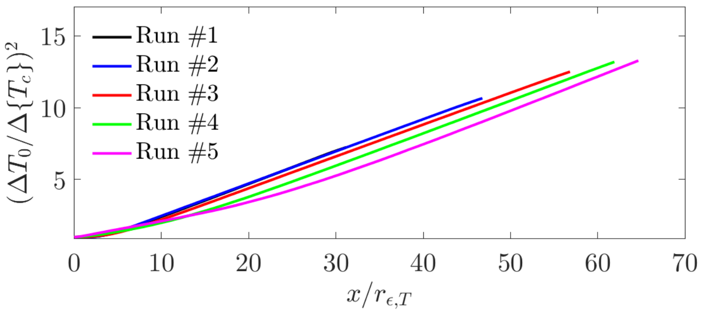

Figure 9.21: *Downstream evolution of the temperature decay along the jet centerline using the adimensionalization of the equivalent heat jet opening based on the convective heat flux conservation for five different heated jets.*

Fig. 9.21 presents a general temperature decay of heated jets with a constant turbulent Prandtl number. In order to quantify such behavior, the linear fitting coefficients ($Q_{1,T}$ and $Q_{2,T}$) of the form

$$\left(\frac{\Delta T_0}{\Delta\{T_c\}}\right)^2 = Q_{1,T}\left(\frac{x}{r_{\epsilon,T}} + Q_{2,T}\right) \tag{9.8}$$

are summarized in Table 9.6
As expected, the slope coefficients ($Q_{1,T}$) have small differences among the computed jets, being that the maxim relative difference is 4.4% (observed between RUN # 1 and # 3).
The equivalent heat jet opening deduced from the convective heat flux conservation equation has shown to compensate density differences collapsing onto almost the same slopes and trends the temperature decay at the developed region. Thus, the equivalent heat jet opening allows to capture the dynamics of the jet within a general behavior for the five studied jets.

Table 9.7: *Comparison of decay temperature fitted coefficients for five different heated jets using the convective heat flux conservation adimensionalization.*

Run	$Q_{1,T}$	$Q_{2,T}$
Run # 1	0.2309	0.3536
Run # 2	0.2225	1.3040
Run # 3	0.2207	-0.0288
Run # 4	0.2256	-3.5158
Run # 5	0.2239	-6.1638

9.2.2 Coupled heated jets with thermal radiation

Figure 9.22 presents again the temperature decay with the classical adimensionalization for the heated jets of Table 9.6, but this time radiative heat transfer has been coupled with the RANS solver. Again the turbulent Prandtl number is fixed to $\mathrm{Pr}_t = 0.6$. As it can be seen in Fig. 9.22, when compared with Fig. 9.20, temperature decay is increased in all cases when radiation is taken into account. As expected, the increase in the decay rate due the inclusion of radiation is greater when higher inlet jet temperatures are considered.

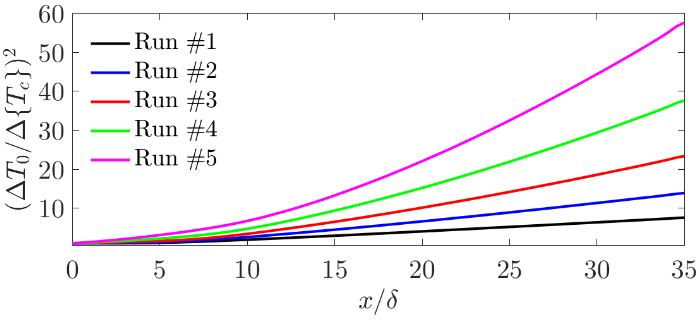

Figure 9.22: *Downstream evolution of the temperature decay along the jet centerline using the classical adimensionalization for five different heated jets including radiative heat transfer.*

Figure 9.23 shows the temperature decay adimensionalized by the equivalent heat jet opening based on the convective heat flux conservation ($r_{\epsilon,T}$) of the heated jets defined in Table 9.6. From Fig. 9.23 it can be seen clearly that the equivalent heat jet opening adimensionalization fails to collapse temperature decay into the same curve when radiation is accounted for.

To quantify this difference, linear fitting coefficients ($Q_{1,T}$ and $Q_{2,T}$) of Eq. 9.8 from the uncoupled and coupled heated jets are detailed in Table 9.8.

Results for the slope coefficient ($Q_{1,T}$) between uncoupled and coupled cases from the same RUN may differ significantly whether radiation is an important mode of heat transfer or not. On the one hand, when using the new scaling in the jet corresponding to the Run # 1, which is expected to have smaller radiation effects than the slightly heated jet presented in Chapter 7, slope

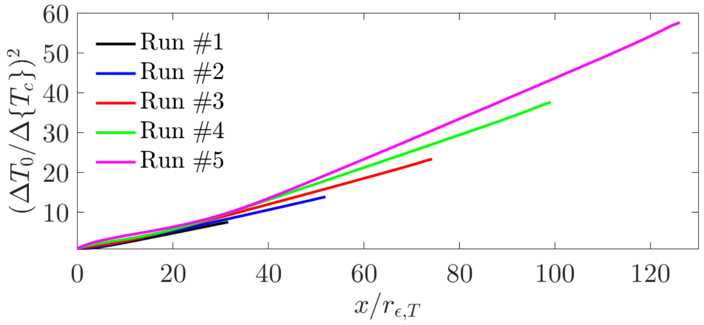

Figure 9.23: *Downstream evolution of the temperature decay along the jet centerline using the adimensionalization of the equivalent heat jet opening based on the convective heat flux conservation for five different heated jets including radiative heat transfer.*

Table 9.8: *Comparison of decay temperature fitted coefficients using the convective heat flux conservation based adimensionalization between the uncoupled and coupled cases for five different heated jets.*

		Non-radiative		**Radiative**	
Run	T_1 (K)	$Q_{1,T}$	$Q_{2,T}$	$Q_{1,T}$	$Q_{2,T}$
Run # 1	500	0.2309	0.3536	0.2406	0.0885
Run # 2	1000	0.2225	1.3040	0.2696	-0.3425
Run # 3	1500	0.2207	-0.0288	0.3286	-3.3288
Run # 4	2000	0.2256	-3.5158	0.4129	-8.4190
Run # 5	2500	0.2239	-6.1638	0.5151	-14.8560

coefficient ($Q_{1,T}$) does not vary significantly and is a close value to the one found for the slightly heated jet using DNS data (0.2513) in Chapter 7. On the other hand, the rest of the tested jets (Run #2, #3, #4, #5), which are expected to have stronger radiation effects than the slightly heated jet, present increasingly different temperature decays rates using the new scaling. Which shows, as already pointed out in Chapter 8, that for strongly heated jets the general scaling based on convective heat flux conservation for variable-density jets is no longer valid when important thermal radiation effects are present.

9.3 Conclusions

This Chapter has presented a comparison between results using RANS and the DNS data presented in Chapters 5, 7 and 8. Besides, the role of the novel scaling based on the convective heat flux conservation is also discussed taking advantage of the relatively low time processing of RANS computations.

For the isothermal jet, RANS predicted slope coefficients of velocity decay and spread rate compare very well with the DNS data. General trends of cross-sections profiles of first and second order of velocity are well captured by

RANS when compared with DNS data, although some discrepancies are found, especially in the budget of turbulent kinetic energy.

Regarding the heated jet, the RANS results of the $y_{1/2,T}$ slope and temperature decay rate are in very good agreement with the DNS data setting a $\mathrm{Pr}_t = 0.6$. Moreover, temperature RANS cross section-profile has the expected trends.

Given that the turbulent effects on radiation are small-to-moderate as shown in Chapter 8, no TRI model has been considered to computed the coupled solution. RANS coupled solution of the slightly heated jet estimates well the radiative power field given reasonably good trends when compared with the DNS data, althoguh the predicted temperature potential core is somewhat narrower for the coupled RANS results.

In contrast with the slightly heated jet, coupled RANS results of the temperature decay rate for the strongly heated case do not match DNS data when $\mathrm{Pr}_t = 0.6$ is set. By explicitly computing the turbulent Prandtl number from DNS data, it has been found that radiation increases Pr_t for the strongly heated jet, while no significant variation is found for the slightly heated jet. Once Pr_t is set to 0.9, the temperature decay rate for the strongly heated jet computed by RANS is in very good agreement with the DNS data. Moreover, the radiative power is in reasonable good agreement with the DNS data presented in Chapter 8.

Taking advantage of the relatively low time processing of the RANS solutions, the novel equivalent heat jet opening scaling based on the convective heat flux conservation has proved to compensate density differences collapsing onto almost the same slopes and trends the temperature decay at the developed region of five different uncoupled heated jets. When including radiation, results for the temperature decay rate differ significantly whether radiation is an important mode of heat transfer or not.

Conclusion

Uncoupled Simulations

- Direct numerical simulations of uncoupled isothermal and heated jets have been suitably computed. The velocity and Reynolds stresses profiles of the isothermal plane jet have been validated by comparison with previous experimental and numerical studies. Additionally, the turbulent kinetic energy balance of the isothermal jet has been checked and each term has been compared with available data. Regarding the heated jet without including radiation, the profile of mean temperature and the downstream evolution of temperature fluctuations have been compared with previous experimental works. The constancy of the momentum flow rate per unit span has been checked for the isothermal and heated jets. Moreover, the scaled velocity decay of the heated and isothermal jets collapses almost onto the same curve.
- The Acoustic Speed Reduction method has been found to be suitable for increasing the time step without a significant lost in accuracy in the current direct numerical simulations. Through an analysis of a pressure wave for different values of the accelerator paramater α, the ASR has been found to be solely applicable in low Mach numbers flows in which pressure waves are small enough to induce minor changes in velocity, temperature and density.
- Results of the Monte-Carlo solver by varying the maximum number of rays issued from a node, the choice of the boundary conditions for the radiative solver, and the effects of considering a coarser mesh for the radiative computations have demonstrated its accuracy in the present jet simulations. Moreover, the spectral radiative properties of water vapor computed using the ck model have been validated by comparison with line-by-line results.
- A RANS solver able to handle variable-density flows has been successfully implemented using the Finite Volume Method and high order schemes. On the one hand, RANS results for the isothermal jet have been checked by comparison with the previously obtained DNS data. The computed slopes for the downstream evolution of spread rate and velocity decay from RANS are found to be in accordance with the DNS results. Velocity

cross-section profiles trends have been well captured by the RANS model. Additionally, Reynolds stresses have shown good agreement with DNS data and the trends of the turbulent kinetic energy balance have been well reproduced by RANS. On the other hand, results for the RANS heated jet have been compared with the DNS data obtaining satisfactory results for the mean temperature field.

Coupled Direct Numerical Simulations

A parallel coupling between the radiative Monte-Carlo solver and the fluid flow DNS solver has been successfully implemented. The coupling period has been optimized based on the Euclidean norm of the difference between the radiative power from two consecutive coupling periods.

Slightly heated jet

- An analysis of the enthalpy balance at the initial zone shows that radiation has a major contribution to heat transport, modifying temperature and density fields. On the other hand, a negligible radiative contribution is found in the developed region. Thus, for both uncoupled and coupled slightly heated jets, the nature of heat transfer remain the same, which is here the turbulent heat transport. However, despite this minor contribution of radiation in the developed region, the classical jet scaling law fails to give the same temperature decay slope between the radiative and non-radiative cases. This could wrongly lead to conclude on a modified balance of heat transport mechanisms in the studied case. In fact, thermal radiation can have two kind of effects on the temperature profile: a direct one from radiative energy transfer and an indirect one due to the modified flow density. The proposed equivalent heat jet opening deduced from the convective heat flux conservation equation has shown to compensate density differences to collapse both radiative and non-radiative jets profiles onto the same temperature decay rate in the developed region. This scaling accounts for the indirect effects of variable density in cases with radiation. It allows for distinguishing whether radiation modifies the heat transfer mechanisms in the developed region or not. In the studied slightly heated jet, it is now clearly identified that it does not.

Strongly heated jet

- Radiation has a significant contribution in the mean enthalpy balance on both the developing and the developed zones. Then, mean temperature fields are strongly affected by radiation in the strongly heated jet. The temperature decay rate scaled with the equivalent heat jet opening gives significantly different results between the radiative and non-radiative jets.

This difference shows that for strongly heated jets, the general scaling based on the convective heat flux conservation for variable-density jets is no longer valid when radiation contribution in the enthalpy balance is significant in the developed region.

- Further analysis of temperature fluctuations through the enthalpy fluctuations balance has shown that the correlation between enthalpy fluctuations and radiative power fluctuations significantly contributes to the dissipation of the enthalpy variance. When radiation is taken into account, the molecular dissipative term nearly decreases by a factor of two. This is because production decreases with radiation since temperature gradients are smoother, but also because enthalpy variance is dissipated by radiation.
- An adimensionalization to characterize the cross-section profiles of mean radiative power in the fully developed turbulent region of the jet has been proposed. The adimensionalization is based on the distance from the centerline of the jet at which the mean radiative power is null $y_{1/2,P_{rad}}(x)$, and the magnitude of mean radiative power at the jet centerline $\langle P_{c,rad} \rangle$. It has been found that for the strongly heated jet under study, profiles of mean radiative power become reasonable self-similar beyond $x = 8\delta$.
- An analysis of the effects that turbulence causes on radiation has been performed by comparing the non-coupled Monte-Carlo computation of the radiative heat transfer from the averaged temperature field $P_{rad}\left(\langle T \rangle\right)$ with the averaged radiative power from the coupled simulation $\langle P_{rad}\left(T\right) \rangle$. It has been found that, for this specific case, such effects do not exceed 10% at the jet centerline.

Coupled Reynolds Average Navier-Stokes Simulations

- The accuracy of the coupled RANS solution in strongly heated jets has shown to depend on the choice of the turbulent Prandtl number. From explicit computation in DNS data, the turbulent Prandtl number has found to increase due to the effects of radiation in free jets.
- Taking advantage of the relatively low time processing of the RANS solutions, the novel equivalent heat jet opening scaling based on the convective heat flux conservation has proved to compensate density differences collapsing onto almost the same slopes and trends the temperature decay at the developed region of five different uncoupled heated jets. When including radiation, results for the temperature decay rate differ significantly whether radiation is an important mode of heat transfer or not.

Perspectives

- The implementation carried out in this work of the Smagorinsky model for LES, and the DOM to solve the RTE, opens the way to further coupled simulations of high Reynolds number jets in larger domain extensions. Moreover, the present results achieved with DNS coupled to a ck model and Monte-Carlo to describe radiation may serve as a reference case to compare simplified approaches such as LES for the turbulence model, or Weighted Sum of Gray Gases (WSGG) and its modern variants for modeling radiative properties combined with deterministic approaches to solve the RTE like DOM.
- The turbulent Prandtl number has found to be a key parameter to account for radiation effects in coupled RANS simulations. In this work, it has been manually adjusted based on DNS data. The derivation of a model to automatically adjust the turbulent Prandtl number in coupled RANS simulation is indeed a promising perspective.
- This works deals with a non-reactive flow in a canonical configuration. Further effects of radiation while accounting for more complex phenomena such as combustion or soot formation, could give valuable insight on interactions between turbulence and radiation.
- Using the coupled RANS described in this work, an exploration of coupled cases could be performed to characterize radiation effects in a wider variety of setups.

Part IV

Appendices

Appendix A

Numerical computation of second order moments

To enhance convergence when computing the balances of turbulent kinetic energy and enthalpy fluctuations, all correlations involving fluctuations are expressed as functions of its mean values. This appendix provides a detailed description on how the budges have been computed in the present work from mean variables.

A.1 Turbulent kinetic energy balance

The general definition of turbulent kinetic energy for a variable density flow is a Favre average of the mass-weighted fluctuations u_i'', i.e, $k = \frac{1}{2}\{u_i''^2\} = \frac{1}{2}\langle \rho u_i''^2 \rangle / \langle \rho \rangle$. Following the work of Chassaing, Antonia, Anselmet, Joly, and Sarkar (2013) or Huang, Coleman, and Bradshaw (1995), the transport equation of the turbulent kinetic energy is expressed as

$$\underbrace{\frac{1}{2}\frac{\partial \langle \rho u_i''^2 \rangle}{\partial t} + \frac{\partial}{\partial x_j}\left(\frac{1}{2}\langle \rho u_i''^2 \rangle \{u_j\}\right)}_{\text{Advection, } \langle \rho \rangle \frac{\bar{D}k}{\bar{D}t}} = -\underbrace{\langle \rho u_i'' u_j'' \rangle \frac{\partial \{u_i\}}{\partial x_j}}_{\text{Production, } \mathcal{P}} - \underbrace{\langle \tau_{i,j} \frac{\partial u_i''}{\partial x_j} \rangle}_{\text{Viscous dissipation, } \epsilon} \tag{A.1}$$

$$-\underbrace{\frac{\partial \left(\langle P \rangle \langle u_i'' \rangle\right)}{\partial x_i} - \frac{\partial \langle P' u_i'' \rangle}{\partial x_i} + \frac{\partial \langle \tau_{i,j} u_i'' \rangle}{\partial x_j} - \frac{\partial}{\partial x_j}\langle \rho u_j'' \frac{u_i''^2}{2} \rangle}_{\text{Diffusion terms, } \nabla \cdot T'} + \underbrace{\langle P \frac{\partial u_i''}{\partial x_i} \rangle.}_{\text{Pressure-Dilatation, } \Pi} \quad , \tag{A.2}$$

In order to build the energy budget, the terms in Eq. (A.2) have been computed as follows:

Advection of turbulent kinetic energy, or convection due to the mean flow, has been computed as

$$\langle\rho\rangle\frac{\bar{D}k}{\bar{D}t}=\frac{\partial}{\partial x_j}\left(\langle\rho\rangle k\{u_j\}\right)=\frac{\partial}{\partial x_j}\left(\langle\rho\rangle\frac{1}{2}\left(\{u_i^2\}-\{u_i\}^2\right)\{u_j\}\right), \tag{A.3}$$

The flux of turbulent kinetic energy where the different diffusive fluxes (pressure diffusion $\varphi_{\mathcal{D},P}$, viscous diffusion $\varphi_{\mathcal{D},visc}$ and turbulent diffusion $\varphi_{\mathcal{D},turb}$) have been gathered in the quantity denoted as T':

$$\nabla\cdot T'=\frac{\partial}{\partial x_j}\left(\varphi_{\mathcal{D},turb}+\varphi_{\mathcal{D},P}+\varphi_{\mathcal{D},visc}\right), \tag{A.4}$$

where the different diffusive fluxes hav been computes as follows:

$$\begin{aligned}
\varphi_{\mathcal{D},turb}&=\langle\rho u_j''\frac{u_i''^2}{2}\rangle=\frac{1}{2}\langle\rho\rangle\left[\{u_ju_i^2\}+2\{u_j\}\{u_i\}^2-\left(\{u_j\}\{u_i^2\}+2\{u_i\}\{u_ju_i\}\right)\right],\\
\varphi_{\mathcal{D},P}&=\langle P'u_j''\rangle-\langle P\rangle\langle u_j''\rangle=\langle Pu_j\rangle-\langle P\rangle\langle u_j\rangle-\langle P\rangle\left(\langle u_j\rangle-\{u_j\}\right)\\
\varphi_{\mathcal{D},visc}&=-\langle u_i''\tau_{i,j}\rangle=\{u_i\}\langle\tau_{i,j}\rangle-\langle u_i\tau_{i,j}\rangle
\end{aligned} \tag{A.5}$$

Turbulent kinetic energy dissipation represents the increase in internal energy due to the work of the fluctuating velocity gradients, it has been computed as

$$\epsilon=-\langle\tau_{i,j}\frac{\partial u_i''}{\partial x_j}\rangle=\langle\tau_{i,j}\rangle\frac{\partial\{u_i\}}{\partial x_j}-\langle\tau_{i,j}\frac{\partial u_i}{\partial x_j}\rangle \tag{A.6}$$

Production , or also called "shear production", express the turbulent kinetic energy transformed into kinetic energy of the mean flow, it has been computed as

$$\mathcal{P}=-\langle\rho u_i''u_j''\rangle\frac{\partial\{u_i\}}{\partial x_j}=-\langle\rho\rangle\left(\{u_iu_j\}-\{u_i\}\{u_j\}\right)\frac{\partial\{u_i\}}{\partial x_j} \tag{A.7}$$

Pressure dilatation , also called pressure-fluctuation dilatation correlation, expressed the transformation of turbulent kinetic energy into internal energy due to compressible effects, and can be computed as

$$\Pi=-\langle P\frac{\partial u_i''}{\partial x_i}\rangle=\langle P\rangle\frac{\partial\{u_i\}}{\partial x_i}-\langle P\frac{\partial u_i}{\partial x_i}\rangle \tag{A.8}$$

A.2 Enthalpy fluctuations balance

The transport equation of Favre averaged enthalpy variance, $\Theta=\frac{1}{2}\{h''^2\}$. Following the development in the work of Vicquelin, Zhang, Gicquel, and Taine

(2014), for a low-Mach flow, the enthalpy variance transport equation can be expressed as:

$$\underbrace{\frac{1}{2}\frac{\partial}{\partial t}\left(\langle\rho\rangle\{h''^2\}\right)+\frac{\partial}{\partial x_j}\left(\frac{1}{2}\langle\rho\rangle\{u_j\}\{h''^2\}\right)}_{\text{Advection, } \langle\rho\rangle\frac{\bar{D}\Theta}{\bar{D}t}} = -\underbrace{\frac{\partial\left\langle q'_j h'\right\rangle}{\partial x_j}}_{\text{Molecular diffusion , } \mathcal{D}_\Theta}$$
$$+\underbrace{\left\langle q'_j\frac{\partial h'}{\partial x_j}\right\rangle}_{\text{Molecular dissipation, } \epsilon_\Theta} \underbrace{-\langle\rho\rangle\{u''_j h''\}\frac{\partial\{h\}}{\partial x_j}}_{\text{Production, } \mathcal{P}_\Theta} - \underbrace{\frac{\partial}{\partial x_j}\langle\rho\rangle\{u''_j\frac{h''^2}{2}\}}_{\text{Turbulent difusion, } \nabla\cdot T'_\Theta} \tag{A.9}$$
$$-\underbrace{\langle h''\rangle\frac{\partial\langle q_j\rangle}{\partial x_j}}_{\text{I}}+\underbrace{\langle h''\rangle\langle P_{rad}\rangle}_{\text{II}}+\underbrace{\langle h''P'_{rad}\rangle}_{\text{III}}$$

The terms in Eq. (A.9) are rewritten and gathered in the following quantities for the numerical computation:

Advection, because the plane jet is statistically stationary, convection due to the mean flow is computed as

$$\langle\rho\rangle\frac{\bar{D}\Theta}{\bar{D}t}=\frac{\partial}{\partial x_j}\left(\frac{1}{2}\langle\rho\rangle\{u_j\}\{h''^2\}\right) \tag{A.10}$$

where $\{h''^2\}$ is computed as

$$\{h''^2\}=\frac{\langle\rho hh\rangle-\langle\rho h\rangle\langle\rho h\rangle/\langle\rho\rangle}{\langle\rho\rangle} \tag{A.11}$$

Molecular diffusion has been computed as

$$\mathcal{D}_\Theta=-\frac{\partial\left\langle q'_j h'\right\rangle}{\partial x_j}=-\frac{\partial}{\partial x_j}\left(\langle q_j h\rangle-\langle q_j\rangle\langle h\rangle\right) \tag{A.12}$$

Molecular dissipation has been calculated as

$$\epsilon_\Theta=\left\langle q'_j\frac{\partial h'}{\partial x_j}\right\rangle=\left\langle q_j\frac{\partial h}{\partial x_j}\right\rangle-\langle q_j\rangle\left\langle\frac{\partial h}{\partial x_j}\right\rangle \tag{A.13}$$

Production has been computed as

$$\mathcal{P}_\Theta=\langle\rho\rangle\{u''_j h''\}\frac{\partial\{h\}}{\partial x_j}=\langle\rho\rangle\frac{\partial\{h\}}{\partial x_j}\left(\{u_j h\}-\{u_j\}\{h\}\right) \tag{A.14}$$

Turbulent diffusion has been calculated as

$$\nabla\cdot T'_\Theta=\frac{\partial}{\partial x_j}\langle\rho\rangle\{u''_j\frac{h''^2}{2}\}=\frac{1}{2}\frac{\partial}{\partial x_j}\langle\rho\rangle\Big(\{u_j h^2\}+2\{u_j\}\{h\}^2-\left(\{u_j\}\{h^2\}+2\{h\}\{u_j h\}\right)\Big) \tag{A.15}$$

Term I has been computed as

$$I = \left\langle h'' \right\rangle \frac{\partial \left\langle q_j \right\rangle}{\partial x_j} = \left(\left\langle h \right\rangle - \left\{ h \right\} \right) \frac{\partial \left\langle q_j \right\rangle}{\partial x_j} \tag{A.16}$$

Term II has been calculated as

$$II = \left\langle h'' \right\rangle \left\langle P_{rad} \right\rangle = \left(\left\langle h \right\rangle - \left\{ h \right\} \right) \left\langle P_{rad} \right\rangle \tag{A.17}$$

Term III has been computed as

$$III = \left\langle h'' P'_{rad} \right\rangle = \left\langle h P_{rad} \right\rangle - \left\langle h \right\rangle \left\langle P_{rad} \right\rangle \tag{A.18}$$

Appendix B

Large eddy simulation

While the larger and more energetic turbulent structures of the flow have strong dependency on the geometry and the boundary conditions, the smaller scales of turbulence are nearly isotropic and then somehow more predictable. Large eddy simulations (LES) try to take advantage of this fact by resolving the largest turbulent structures and modeling the smaller ones. A model for the Subgrid scale effects has been implemented in the frame of the YWCx code. This implementation opens the way to further coupled simulations of high Reynolds number jets.
To this end, three dimensional and unsteady computations are necessary to capture the behavior of the most energetic eddies. In order to separate the larger from the smaller eddies, LES uses a spatial filtering operation.

B.1 Filter operations

The filtered quantity f can be defined as in the work of Pope (2001)

$$\overline{f}(\mathbf{x}) = \int f(\mathbf{x}')F(\mathbf{x\text{-}x'})d\mathbf{x'} \tag{B.1}$$

Typically filter operations are made in spectral space or in physical space. In our case, we use a box filter in physical space defined by:

$$F(\mathbf{x}) = \begin{cases} 1/\Delta^3 \text{ if } |x_i| \leq \Delta/2,\ i\ =\ 1,2,3 \\ 0 \text{ otherwise} \end{cases} \tag{B.2}$$

This filter actually corresponds to an averaging over a cubic box of size Δ of the form:

$$\overline{f}(x,y,z,t) = \frac{1}{\Delta^3}\int_{x'=x-\Delta/2}^{x'=x+\Delta/2}\int_{y'=y-\Delta/2}^{y'=y+\Delta/2}\int_{z'=z-\Delta/2}^{z'=z+\Delta/2} f(x',y',z',t)dz'\ dy'\ dx'$$

(B.3)

The mass-weighted spatial filter (similar to Favre in RANS) is defined as:

$$\tilde{f} = \frac{\overline{\rho\, f}}{\bar{\rho}} \tag{B.4}$$

which is useful for simplifying equations of variable density flows, since we can write:

$$\overline{\rho\, f} = \frac{\bar{\rho}}{\bar{\rho}}\, \overline{\rho\, f} = \bar{\rho}\tilde{f} \tag{B.5}$$

Similarly to the RANS formulation, we can decompose the quantity f as a resolved part, $\bar{f}$, and a unresolved part, f^{sgs}, related to the sub-grid scale flow motions:

$$f = \bar{f} + f^{sgs} \tag{B.6}$$

B.2 Filtered N-S equations

Filtering the instantaneous N-S equations using the Favre spatial filter operation defined above, we obtain:

a. Mass. Making use of the relation defined in eq. (B.5) :

$$\frac{\partial\bar{\rho}}{\partial t} + \frac{\partial(\bar{\rho}\tilde{u}_j)}{\partial x_j} = 0, \tag{B.7}$$

b. Momentum. Again making use of eq. (B.5); adding and subtracting non-linear terms due to the filtering operation, we have:

$$\frac{\partial(\bar{\rho}\tilde{u}_i)}{\partial t} + \frac{\partial(\bar{\rho}\tilde{u}_i\tilde{u}_j)}{\partial x_j} = -\frac{\partial\overline{P}}{\partial x_i} + \frac{\partial}{\partial x_j}\left[\hat{\tau}_{i,j} + \underbrace{\overline{\tau_{i,j}} - \hat{\tau}_{i,j}}_{\text{b1}} - \underbrace{\bar{\rho}\left(\widetilde{u_i u_j} - \tilde{u}_i\tilde{u}_j\right)}_{\text{b2}}\right] \tag{B.8}$$

b1. Non linear viscous terms appear since the directly filtered stress tensor $\overline{\tau_{i,j}}$ is not formally equal to $\hat{\tau}_{i,j}$ which stands for:

$$\hat{\tau}_{i,j} = \mu(\tilde{T})\left(2\tilde{S}_{ij} - \frac{2}{3}\delta_{ij}\tilde{S}_{kk}\right). \tag{B.9}$$

where $\tilde{S}_{i,j}$ is the resolved shear stress $\tilde{S}_{i,j} = \frac{1}{2}\left(\frac{\partial\tilde{u}_i}{\partial x_j} + \frac{\partial\tilde{u}_j}{\partial x_i}\right)$. Nevertheless, the works of Vreman, Geurts, and Kuerten (1995); Vreman

(1995); Martin, Piomelli, and Candler (2000) show that $\dfrac{\partial}{\partial x_j}\left(\overline{\tau_{i,j}} - \hat{\tau}_{i,j}\right)$ is small or negligible; so we assume here that this terms have a negligible effect on the filtered momentum transport equation.

b2. Unresolved Reynolds stresses, $\overline{\rho}\left(\widetilde{u_i u_j} - \tilde{u}_i\tilde{u}_j\right)$. For the sake of simplicity, let us define the turbulent stress tensor as:

$$\tau^t_{i,j} = -\overline{\rho}\left(\widetilde{u_i u_j} - \tilde{u}_i\tilde{u}_j\right). \tag{B.10}$$

Then, this term is expressed according the Boussinesq approximation as:

$$\tau^t_{i,j} = -\overline{\rho}\left(\frac{\delta_{i,j}}{3}\tau^t_{kk} - 2\nu_t\left(\tilde{S}_{i,j} - \frac{\delta_{i,j}}{3}\tilde{S}_{k,k}\right)\right), \tag{B.11}$$

where τ^t_{kk} corresponds to twice the sub-grid scale turbulent kinetic energy which is absorbed into the filtered pressure $\bar{P}$ (Poinsot and Veynante (2005)), leading then to

$$\tau^t_{i,j} = 2\overline{\rho}\nu_t\left(\tilde{S}_{i,j} - \frac{\delta_{i,j}}{3}\tilde{S}_{k,k}\right) \tag{B.12}$$

and ν_t is a sub-grid scale viscosity modeled following the Smagorinsky model as

$$\nu_t = (C_s\Delta)^2\left(2\tilde{S}_{i,j}\tilde{S}_{i,j}\right)^{1/2} \tag{B.13}$$

where C_s is a model constant set to $C_s \approx 0.2$ and the filter size Δ is computed from the grid spacing as $\Delta = (\mathrm{dx\ dy\ dz})^{1/3}$.

Then, we can rewrite eq. (B.8) as:

$$\frac{\partial(\overline{\rho}\tilde{u}_i)}{\partial t} + \frac{\partial(\overline{\rho}\tilde{u}_i\tilde{u}_j)}{\partial x_j} = -\frac{\partial\overline{P}}{\partial x_i} + \frac{\partial}{\partial x_j}\left(\hat{\tau}_{i,j} + \tau^t_{i,j}\right) \tag{B.14}$$

c. Energy. Filtering the original equation, and by adding and subtracting non-linear terms, we have:

$$\frac{\partial\overline{\rho}\tilde{e}}{\partial t} + \frac{\partial\left(\overline{\rho}\tilde{u}_j\tilde{e}\right)}{\partial x_j} = -\frac{\partial\overline{p}\tilde{u}_j}{\partial x_j} + \frac{\partial\tilde{\tau}_{i,j}\tilde{u}_i}{\partial x_j} \tag{B.15}$$

$$+\frac{\partial}{\partial x_j}\left[\underbrace{\overline{\lambda\frac{\partial T}{\partial x_j}}}_{\text{c1}} - \underbrace{\overline{\rho}\left(\widetilde{u_j e} - \tilde{u}_j\tilde{e}\right) - \left(\overline{p u_j} - \overline{p}\tilde{u}_j\right)}_{\text{c2}} + \underbrace{\overline{\tau_{i,j}u_i} - \tilde{\tau}_{i,j}\tilde{u}_i}_{\text{c3}}\right]. \tag{B.16}$$

c1. The molecular heat flux, $\overline{\lambda \frac{\partial T}{\partial x_j}}$, as suggested by apriori test (Vreman, Geurts, and Kuerten (1995); Vreman (1995); Martin, Piomelli, and Candler (2000)), it is approximated by a simple gradient assumption as $\overline{\lambda \frac{\partial T}{\partial x_j}} = \overline{\lambda} \frac{\partial \tilde{T}}{\partial x_j}$ where $\overline{\lambda} = \lambda(\tilde{T})$

c2. Unresolved convected energy, $\overline{\rho}\left(\widetilde{u_j e} - \tilde{u}_j \tilde{e}\right) - \left(\overline{p u_j} - \overline{p}\tilde{u}_j\right)$, as in Garnier, Adams, and Sagaut (2009) this term can be regrouped in the following form:

$$\overline{\rho}\left(\widetilde{u_j e} - \tilde{u}_j \tilde{e}\right) - \left(\overline{p u_j} - \overline{p}\tilde{u}_j\right) = c_p Q_j + J_i \tag{B.17}$$

where $Q_j = \bar{\rho}\left(\widetilde{u_j T} - \tilde{u}_j \tilde{T}\right)$ which is commonly modeled assuming that the energy transfered from the resolved scales to the sub-grid scales is proportional to the gradient of resolved temperature in the following form:

$$Q_j = \frac{\bar{\rho}\nu_t}{Pr_t}\frac{\partial \tilde{T}}{\partial x_j}. \tag{B.18}$$

where ν_t is defined in eq. (B.13), Pr_t is sub-grid scale Prandtl number which is set to 0.9. For simplicity, let us define the $\lambda_t = \frac{\bar{\rho} c_p \nu_t}{Pr_t}$ which stands for the sub-grid thermal conductivity or turbulent thermal conductivity. The term J_i corresponds to the turbulent diffusion and writes (Garnier, Adams, and Sagaut (2009)):

$$J_i = \frac{1}{2}\left(\bar{\rho}\widetilde{u_j u_i u_i} - \bar{\rho}\tilde{u}_j \widetilde{u_i u_i}\right) = \frac{1}{2}\left(\bar{\rho}\widetilde{u_j u_i u_i} - \bar{\rho}\tilde{u}_j \tilde{u}_i \tilde{u}_i - \tau^t_{kk}\right) \tag{B.19}$$

Since our case is placed in the framework of low Mach and Reynolds numbers, we assume that turbulent diffusion is negligible when compare to internal energy.

c3. Non-linear viscous terms Similarly to the term b1 in eq. (B.8), the term $\overline{\tau_{i,j} u_i} - \tilde{\tau}_{i,j}\tilde{u}_i$ is small or negligible; so we assume here that this terms have a negligible effect on the filtered energy transport equation.

Finally, we can rewrite eq. (B.16) as:

$$\frac{\partial \overline{\rho}\tilde{e}}{\partial t} + \frac{\partial\left(\overline{\rho}\tilde{u}_j \tilde{e}\right)}{\partial x_j} = -\frac{\partial \overline{p}\tilde{u}_j}{\partial x_j} + \frac{\partial \tilde{\tau}_{i,j}\tilde{u}_i}{\partial x_j} + \frac{\partial}{\partial x_j}\left[\left(\overline{\lambda} + \lambda_t\right)\frac{\partial \tilde{T}}{\partial x_j}\right] \tag{B.20}$$

B.2.1 Turbulent kinetic energy of the resolved scales

Before deducing the formulation for the resolved turbulent kinetic energy, let us defined the time averaging of a filtred time-dependent quantity $\tilde{f}(t)$ as

$$\langle \tilde{f} \rangle = \frac{1}{T}\int_T \tilde{f}(t)dt, \tag{B.21}$$

where T is the time-averaged period, which should be much larger than the characteristic time of the fluctuations, such fluctuations are defined by:

$$f' = \tilde{f} - \langle \tilde{f} \rangle. \tag{B.22}$$

Similarly, we define the time density-weighted averaging or time Favre averaging as:

$$\{\tilde{f}\} = \frac{\langle \bar{\rho}\tilde{f} \rangle}{\langle \bar{\rho} \rangle}, \tag{B.23}$$

and its fluctuations as

$$f'' = \tilde{f} - \{\tilde{f}\}. \tag{B.24}$$

For the deduction of the transport equation of the resolved turbulent kinetic energy we follow the book of Chassaing, Antonia, Anselmet, Joly, and Sarkar (2013) who developed this equation for the instantaneous quantities, recently Atoufi, Fathali, and Lessani (2015) developed it for the filtered quantities in a similar manner as Bogey and Bailly (2009). For this purpose, let us begin with the non-conservative form of eq. (B.14), using the chain rule and eq. (B.7) we can write:

$$\overline{\rho}\frac{\partial(\tilde{u}_i)}{\partial t} + \overline{\rho}\tilde{u}_j\frac{\partial(\tilde{u}_i)}{\partial x_j} = -\frac{\partial \overline{P}}{\partial x_i} + \frac{\partial}{\partial x_j}\left(\tilde{\tau}_{i,j} - \tau^t_{i,j}\right) \tag{B.25}$$

multiplying last equation by the Favre fluctuation u_i'' defined in B.24, we write:

$$\underbrace{\overline{\rho}u_i''\frac{\partial(\tilde{u}_i)}{\partial t}}_{\text{A}} + \underbrace{\overline{\rho}u_i''\tilde{u}_j\frac{\partial(\tilde{u}_i)}{\partial x_j}}_{\text{B}} = \underbrace{-u_i''\frac{\partial \overline{P}}{\partial x_i}}_{\text{C}} + \underbrace{u_i''\frac{\partial}{\partial x_j}\left(\tilde{\tau}_{i,j} - \tau^t_{i,j}\right)}_{\text{D}} \tag{B.26}$$

Recalling eq. (B.24) and using the chain rule we can expand the term A as:

$$\text{A} = \overline{\rho}u_i''\frac{\partial(\{\tilde{u}_i\} + u_i'')}{\partial t} = \overline{\rho}u_i''\frac{\partial\{\tilde{u}_i\}}{\partial t} + \overline{\rho}u_i''\frac{\partial u_i''}{\partial t} = \overline{\rho}u_i''\frac{\partial\{\tilde{u}_i\}}{\partial t} + \frac{1}{2}\frac{\partial \overline{\rho}u_i''u_i''}{\partial t} - \frac{u_i''^2}{2}\frac{\partial \overline{\rho}}{\partial t} \tag{B.27}$$

After averaging on time yields:

$$\langle \text{A} \rangle = \frac{1}{2}\frac{\partial \langle \overline{\rho}u_i''^2 \rangle}{\partial t} + \langle -\frac{u_i''^2}{2}\frac{\partial \overline{\rho}}{\partial t} \rangle \tag{B.28}$$

Expanding now term B on eq. (B.26) by using again eq. (B.24), we have

$$\mathrm{B} = \overline{\rho} u_i'' \tilde{u}_j \frac{\partial(\{\tilde{u}_i\} + u_i'')}{\partial x_j} = \underbrace{\overline{\rho} u_i'' \tilde{u}_j \frac{\partial\{\tilde{u}_i\}}{\partial x_j}}_{\mathrm{B.1}} + \underbrace{\overline{\rho} u_i'' \tilde{u}_j \frac{\partial u_i''}{\partial x_j}}_{\mathrm{B.2}} \tag{B.29}$$

and so,

$$\mathrm{B.1} = \overline{\rho} u_i''(\{\tilde{u}_j\} + u_j'') \frac{\partial\{\tilde{u}_i\}}{\partial x_j} = \overline{\rho} u_i'' \{\tilde{u}_j\} \frac{\partial\{u_i\}}{\partial x_j} + \overline{\rho} u_i'' u_j'' \frac{\partial\{\tilde{u}_i\}}{\partial x_j}, \tag{B.30}$$

$$\mathrm{B.2} = \overline{\rho}\tilde{u}_j \frac{\partial}{\partial x_j}\left(\frac{u_i''^2}{2}\right) = \frac{\partial}{\partial x_j}\left(\overline{\rho}\{\tilde{u}_j\}\frac{u_i''^2}{2}\right) + \frac{\partial}{\partial x_j}\left(\overline{\rho} u_j'' \frac{u_i''^2}{2}\right) - \frac{u_i''^2}{2}\frac{\partial}{\partial x_j}\left(\overline{\rho}\tilde{u}_j\right) \tag{B.31}$$

Now averaging on time the term B and knowing that $\langle \overline{\rho} u_i'' \rangle = 0$, yields:

$$\langle \mathrm{B} \rangle = \langle \overline{\rho} u_i'' u_j'' \rangle \frac{\partial\{\tilde{u}_i\}}{\partial x_j} + \frac{\partial}{\partial x_j}\left(\langle \overline{\rho}\frac{u_i''^2}{2}\rangle\{\tilde{u}_j\}\right) + \frac{\partial}{\partial x_j}\langle \overline{\rho} u_j'' \frac{u_i''^2}{2}\rangle - \langle \frac{u_i''^2}{2}\frac{\partial}{\partial x_j}\left(\overline{\rho}\tilde{u}_j\right)\rangle. \tag{B.32}$$

On doing $\langle \mathrm{A} \rangle + \langle \mathrm{B} \rangle$ we can identify the filtered mass conservation equation and simplify the sum as:

$$\langle \mathrm{A} \rangle + \langle \mathrm{B} \rangle = \frac{1}{2}\frac{\partial \langle \overline{\rho} u_i''^2 \rangle}{\partial t} + \langle \overline{\rho} u_i'' u_j'' \rangle \frac{\partial\{\tilde{u}_i\}}{\partial x_j} + \frac{\partial}{\partial x_j}\left(\langle \overline{\rho}\frac{u_i''^2}{2}\rangle\{\tilde{u}_j\}\right) + \frac{\partial}{\partial x_j}\langle \overline{\rho} u_j'' \frac{u_i''^2}{2}\rangle \tag{B.33}$$

Using the relation $\overline{P} = \langle \bar{P} \rangle + P'$, term C yields:

$$\langle \mathrm{C} \rangle = \langle u_i'' \rangle \frac{\partial \langle \bar{P} \rangle}{\partial x_i} + \langle u_i'' \frac{\partial P'}{\partial x_i} \rangle = \langle u_i'' \rangle \frac{\partial \langle \bar{P} \rangle}{\partial x_i} + \frac{\partial \langle P' u_i'' \rangle}{\partial x_i} - \langle P' \frac{\partial u_i''}{\partial x_i} \rangle \tag{B.34}$$

Adding and subtracting $\langle \bar{P} \rangle \frac{\partial \langle u_i'' \rangle}{\partial x_i}$ we can rearrenge the term C as:

$$\langle \mathrm{C} \rangle = \frac{\partial \langle P' u_i'' \rangle}{\partial x_i} + \langle \bar{P} \frac{\partial u_i''}{\partial x_i} \rangle + \frac{\partial \left(\langle \bar{P} \rangle \langle u_i'' \rangle\right)}{\partial x_i} \tag{B.35}$$

Finally term D is averaged as

$$\langle \mathrm{D} \rangle = \langle u_i'' \frac{\partial \tilde{\tau}_{i,j}}{\partial x_j} \rangle - \langle u_i'' \frac{\partial \tau_{i,j}^t}{\partial x_j} \rangle = \frac{\partial \langle u_i'' \tilde{\tau}_{i,j} \rangle}{\partial x_j} - \langle \tilde{\tau}_{i,j} \frac{\partial u_i''}{\partial x_j} \rangle - \langle u_i'' \frac{\partial \tau_{i,j}^t}{\partial x_j} \rangle \tag{B.36}$$

Then, the equation governing the turbulent kinetic energy of the resolved-scale fluctuations $\frac{1}{2}\langle\overline{\rho}u_i''^2\rangle$ can be expressed as in the work of Atoufi, Fathali, and Lessani (2015):

$$\frac{1}{2}\frac{\partial\langle\overline{\rho}u_i''^2\rangle}{\partial t} + \underbrace{\frac{\partial}{\partial x_j}\left(\frac{1}{2}\langle\overline{\rho}u_i''^2\rangle\{\tilde{u}_j\}\right)}_{\text{Mean convection}} = - \underbrace{\frac{\partial}{\partial x_j}\langle\overline{\rho}u_j''\frac{u_i''^2}{2}\rangle}_{\text{Turbulent difusion}} - \underbrace{\langle\overline{\rho}u_i''u_j''\rangle\frac{\partial\{\tilde{u}_i\}}{\partial x_j}}_{\text{Production}} \tag{B.37}$$

$$- \underbrace{\frac{\partial\left(\langle\bar{P}\rangle\langle u_i''\rangle\right)}{\partial x_i}}_{\text{Pressure diff.}} - \underbrace{\frac{\partial\langle P'u_i''\rangle}{\partial x_i}}_{\text{Fluctuating P diff.}} + \underbrace{\langle\bar{P}\frac{\partial u_i''}{\partial x_i}\rangle}_{\text{Pressure dilatation}} + \underbrace{\frac{\partial\langle u_i''\tilde{\tau}_{i,j}\rangle}{\partial x_j}}_{\text{Viscous transport}} \tag{B.38}$$

$$- \underbrace{\langle\tilde{\tau}_{i,j}\frac{\partial u_i''}{\partial x_j}\rangle}_{\text{Viscous dissipation}} - \underbrace{\langle u_i''\frac{\partial\tau_{i,j}^t}{\partial x_j}\rangle}_{\text{Sgs dissipation}} \tag{B.39}$$

We can define the following quantities for the energy budget:

The turbulent kinetic energy of the resolved-scale fluctuations, is obtained through a Favre average of the velocity fluctuations of the resolved scales: $k = \frac{1}{2}\{u_i''^2\} = \frac{1}{2}\langle\overline{\rho}u_i''^2\rangle/\overline{\rho}$.

The flux of turbulent kinetic energy can be defined by considering the following terms:

$$\nabla\cdot T' = \underbrace{\frac{\partial}{\partial x_j}\langle\overline{\rho}u_j''\frac{u_i''^2}{2}\rangle}_{\text{Turbulent difusion}} + \underbrace{\frac{\partial\langle P'u_j''\rangle}{\partial x_j}}_{\text{Fluctuating P diff.}} - \underbrace{\frac{\partial\langle u_i''\tilde{\tau}_{i,j}\rangle}{\partial x_j}}_{\text{Viscous transport}} + \underbrace{\frac{\partial\left(\langle\bar{P}\rangle\langle u_j''\rangle\right)}{\partial x_j}}_{\text{Pressure diff.}} \tag{B.40}$$

Turbulent kinetic energy dissipation transformed into internal energy can be expressed as

$$\epsilon = \underbrace{\langle\bar{P}\frac{\partial u_i''}{\partial x_i}\rangle}_{\text{Pressure dilatation}} - \underbrace{\langle\tilde{\tau}_{i,j}\frac{\partial u_i''}{\partial x_j}\rangle}_{\text{Viscous dissipation}} - \underbrace{\langle u_i''\frac{\partial\tau_{i,j}^t}{\partial x_j}\rangle}_{\text{Sgs dissipation}} \tag{B.41}$$

in which the pressure dilatation, also called pressure-fluctuation dilatation correlation, expressed the transformation of turbulent kinetic energy into internal energy due to compressible effects. The viscous dissipation represents the increase of internal energy due to the work of the fluctuating velocity gradients. And the sub-grid dissipation corresponds to the dissipation of the unresolved motions of the fluid.

Production , or also called "shear production", expressed the turbuent kinetic energy transformed into kinietic enegry of the mean flow, it is definde as:

$$\mathcal{P} = \langle \bar{\rho} u_i'' u_j'' \rangle \frac{\partial \{u_i\}}{\partial x_j} \tag{B.42}$$

Finally, the transport equation for the turbulent kinetic energy of the resolved scales can be expressed as:

$$\frac{\partial \left(\langle \bar{\rho} \rangle k \right)}{\partial t} + \frac{\partial \left(\langle \bar{\rho} \rangle \{\tilde{u}_i\} k \right)}{\partial x_i} + \nabla \cdot T' = \mathcal{P} - \epsilon \tag{B.43}$$

B.3 Computation of LES statistical quantities for variable density flows

Solving the set of equation (B.7 - B.16) provides unsteady and spatially-filtered quantities whereas normally we are interested on average values, to this end we use time average or Favre average operations. Unfortunately, when computing averages from filtered values, they are not straightforward to compute since sub-grid scales have an impact on statistical values.
Considering that filtering average quantities has a negligible effect, i.e the filter size Δ is small when compare to the gradient of average quantities:

$$\langle \bar{\rho} \rangle \approx \langle \rho \rangle, \quad \langle \bar{\rho} \tilde{f} \rangle = \langle \overline{\rho f} \rangle \approx \langle \rho f \rangle, \quad \langle \bar{\rho} \widetilde{f^2} \rangle = \langle \overline{\rho f^2} \rangle \approx \langle \rho f^2 \rangle, \tag{B.44}$$

B.3.1 Velocity variance

Poinsot and Veynante (2005) proposed the computation of the variance of the velocity component u_i from filtered values, as

$$\langle \rho \rangle \left(\{u_i u_j\} - \{u_i\}\{u_j\} \right) \approx \underbrace{\left(\langle \bar{\rho} \tilde{u}_i \tilde{u}_j \rangle - \frac{\langle \bar{\rho} \tilde{u}_i \rangle \langle \bar{\rho} \tilde{u}_j \rangle}{\langle \bar{\rho} \rangle} \right)}_{\text{Explicitly resolved by LES}} + \underbrace{\langle \bar{\rho} \left(\widetilde{u_i u_j} - \tilde{u}_i \tilde{u}_j \right) \rangle}_{\text{Sub-grid scale variance}}, \tag{B.45}$$

and using the model for the unresolved Reynolds stresses of eq. (B.12) we have:

$$\langle \rho \rangle \left(\{u_i u_j\} - \{u_i\}\{u_j\} \right) \approx \left(\langle \bar{\rho} \tilde{u}_i \tilde{u}_j \rangle - \frac{\langle \bar{\rho} \tilde{u}_i \rangle \langle \bar{\rho} \tilde{u}_j \rangle}{\langle \bar{\rho} \rangle} \right) + \langle \tau_{i,j}^t \rangle \tag{B.46}$$

then, temperature and velocity variances are discussed below.

B.3.2 Temperature variance

Regarding the computation of the temperature variance, following the work of Poinsot and Veynante (2005), we have:

$$\{T^2\} - \{T\}^2 \approx \underbrace{\frac{1}{\langle\rho\rangle}\left(\langle\bar{\rho}\left(\widetilde{T}\right)^2\rangle - \frac{\langle\bar{\rho}\widetilde{T}\rangle^2}{\langle\bar{\rho}\rangle}\right)}_{\text{Explicitly resolved by LES}} + \underbrace{\frac{1}{\langle\rho\rangle}\langle\bar{\rho}\left(\widetilde{T^2} - \left(\widetilde{T}\right)^2\right)\rangle}_{\text{Sub-grid scale variance}}, \tag{B.47}$$

which is, up to the moment not explicitly resolved. We can approximate the SGS temperature fluctuations as a function of the size filter Δ, the turbulent Prandtl number Pr_t and a characteric lenght for the gradient temperature δ by:

$$\frac{1}{\langle\rho\rangle}\langle\bar{\rho}\left(\widetilde{T^2} - \left(\widetilde{T}\right)^2\right)\rangle = \langle\widetilde{T}\rangle\frac{C_m}{Pr_t}\frac{\Delta}{\delta} \tag{B.48}$$

where C_m is a constant set to $C_m = \sqrt{2/3}\frac{A}{\pi K_0^{3/2}}$, being $A = 0.44$ and $K_0 = 1.4$. Then, the temperature variance is expressed as :

$$\{T^2\} - \{T\}^2 \approx \frac{1}{\langle\rho\rangle}\left(\langle\bar{\rho}\left(\widetilde{T}\right)^2\rangle - \frac{\langle\bar{\rho}\widetilde{T}\rangle^2}{\langle\bar{\rho}\rangle}\right) + \langle\widetilde{T}\rangle\frac{C_m}{Pr_t}\frac{\Delta}{\delta} \tag{B.49}$$

B.4 Pope Criterion

Large eddy simulations can have a strong dependency on the filter size Δ utilized to compute the solution. In order to measure the ratio of turbulent kinetic energy that we are actually resolving to the total kinetic energy, Pope (2004) proposed a simple methodology based on the measure $M(\mathbf{x}, t)$ of the turbulent resolution:

$$M(\mathbf{x}, t) = \frac{k_{sgs}(\mathbf{x}, t)}{k(\mathbf{x}, t) + k_{sgs}(\mathbf{x}, t)} \tag{B.50}$$

where $k(\mathbf{x}, t)$ is the turbulent kinetic energy which can be solved explicitly from filter variables:

$$k(\mathbf{x}, t) = \frac{1}{2}\left(\{\tilde{u}_i\tilde{u}_i\} - \{\tilde{u}_i\}\{\tilde{u}_i\}\right) = \frac{1}{2\langle\rho\rangle}\left(\langle\bar{\rho}\tilde{u}_i\tilde{u}_j\rangle - \frac{\langle\bar{\rho}\tilde{u}_i\rangle\langle\bar{\rho}\tilde{u}_j\rangle}{\langle\bar{\rho}\rangle}\right), \tag{B.51}$$

and $k_{sgs}(\mathbf{x}, t)$ stands for the turbulent kinetic energy of the sub-grid scales which can be expressed as

$$k_{sgs}(\mathbf{x}, t) = \frac{1}{2}\left(\{\widetilde{u_i u_i}\} - \{\tilde{u}_i\tilde{u}_i\}\right) = \frac{1}{2\langle\rho\rangle}\left(\langle\bar{\rho}\widetilde{u_i u_i}\rangle - \langle\bar{\rho}\tilde{u}_i\tilde{u}_i\rangle\right), \tag{B.52}$$

which is no explicitly resolved and thus we need to modeled it in order to compute its value. A known model used, for example, in the work of Coussement, Gicquel, and Degrez (2012), expresses the k_{sgs} as a function of the turbulent viscosity ν_t by:

$$k_{sgs}(\mathbf{x},t) = \frac{\langle \nu_t^2 \rangle}{(C_m \Delta)^2} \tag{B.53}$$

where C_m is a constant of the model set to $C_m = \sqrt{2/3}\frac{A}{\pi K_0^{3/2}}$, being $A = 0.44$ and $K_0 = 1.4$.

Having the measure of the turbulent resolution, one can control the level of resolution through the filter size $\Delta = \sqrt[3]{\Delta x \Delta y \Delta z}$, which corresponds to the mesh spacing. A value of $M(\mathbf{x},t)$ smaller than 0.2 is typically used as a reference of a well resolved LES, such a value ensures a resolution of 80% of the total turbulent kinetic energy.

Appendix C

Derivation of Boundary conditions for the Acoustic Speed Reduction method

In this Appendix the non-reflecting boundary conditions are derived for a simplified one-dimensional non-viscous form of the modified ASR system. The term non-reflecting refers to boundary conditions for which compression outgoing waves leave the domain without any kind of reflection. To derive such conditions, a characteristic analysis following the works of Hedstrom (1979) and Thompson (1987) is performed to the set of governing equations presented in the work of Wang and Trouvé (2004). These are the continuity equation, the momentum and energy transport equations, respectively:

$$\frac{\partial \rho}{\partial t} + \frac{\partial (\rho u)}{\partial x} = 0, \tag{C.1}$$

$$\frac{\partial u}{\partial t} + u\frac{\partial u}{\partial x} + \frac{1}{\rho}\frac{\partial p}{\partial x} = 0, \tag{C.2}$$

$$\frac{p}{\partial t} + u\frac{\partial p}{\partial x} + \frac{\gamma p}{\alpha^2}\frac{\partial u}{\partial x} = 0, \tag{C.3}$$

To develop a wave analysis of the ASR system, the governing equations are expressed in the form:

$$\frac{\mathcal{U}}{\partial t} + \mathcal{A}\frac{\partial \mathcal{U}}{\partial x} = 0, \tag{C.4}$$

where $\mathcal{U}$ is the vector of dependent variables defined by

$$\mathcal{U} = \begin{pmatrix} \rho \\ u \\ p \end{pmatrix}, \tag{C.5}$$

and $\mathcal{A}$ is a square matrix:

$$\mathcal{A} = \begin{pmatrix} u & \rho & 0 \\ 0 & u & 1/\rho \\ 0 & \gamma p/\alpha^2 & u \end{pmatrix} \tag{C.6}$$

Then, C.4 is expressed in the characteristic form as:

$$\mathcal{S}\frac{\partial \mathcal{U}}{\partial t} + \mathcal{D}\mathcal{S}\frac{\partial \mathcal{U}}{\partial x} = 0 \tag{C.7}$$

where $\mathcal{S}$ is a matrix whose rows are the left eigenvectors of $\mathcal{A}$, and $\mathcal{D}$ is the diagonal matrix defined by

$$\mathcal{D} = \mathcal{S}\mathcal{A}\mathcal{S}^{-1}. \tag{C.8}$$

To determine the matrix $\mathcal{S}$, the eigenvalues of the matrix $\mathcal{A}$ are first computed following the expression

$$det(\mathcal{A} - \lambda\mathcal{I}) = det\left[\begin{pmatrix} u & \rho & 0 \\ 0 & u & 1/\rho \\ 0 & \gamma p/\alpha^2 & u \end{pmatrix} - \begin{pmatrix} \lambda_1 & 0 & 0 \\ 0 & \lambda_2 & 0 \\ 0 & 0 & \lambda_3 \end{pmatrix}\right] = 0, \tag{C.9}$$

where $\mathcal{I}$ is the identity matrix. Then, from Eq. C.9 the eigenvalues are:

$$\lambda_1 = u - \frac{1}{\alpha}\sqrt{\gamma p/\rho}, \quad \lambda_2 = u, \quad \lambda_3 = u + \frac{1}{\alpha}\sqrt{\gamma p/\rho}, \tag{C.10}$$

Once the eigenvalues are defined, the three left eigenvectors (l_i) are determined by

$$l_i\mathcal{A} = \lambda_i l_i \text{ for } i = 1, 2, 3, \tag{C.11}$$

Then, the matrix $\mathcal{S}$ is formed by placing each left eigenvector in each row:

$$\mathcal{S} = \begin{pmatrix} 0 & \frac{\rho}{\alpha}\sqrt{\gamma p/\rho} & -1 \\ 1 & 0 & -\alpha^2\frac{\rho}{\gamma p} \\ 0 & \frac{\rho}{\alpha}\sqrt{\gamma p/\rho} & 1 \end{pmatrix} \tag{C.12}$$

Following Eq. C.8 the diagonal matrix $\mathcal{D}$ is defined by

$$\mathcal{D} = \begin{pmatrix} u - \frac{1}{\alpha}\sqrt{\gamma p/\rho} & 0 & 0 \\ 0 & u & 0 \\ 0 & 0 & u + \frac{1}{\alpha}\sqrt{\gamma p/\rho} \end{pmatrix} \tag{C.13}$$

Replacing Eqs. C.12 and C.13 in Eq. C.7 gives the characteristic governing equations wih the ASR modification for a one-dimensional non-viscous fluid

$$\frac{\partial p}{\partial t} - \frac{\rho}{\alpha}\sqrt{\frac{\gamma p}{\rho}}\frac{\partial u}{\partial t} + \left(u - \frac{1}{\alpha}\sqrt{\frac{\gamma p}{\rho}}\right)\left(\frac{\partial p}{\partial x} - \frac{\rho}{\alpha}\sqrt{\frac{\gamma p}{\rho}}\frac{\partial u}{\partial x}\right) = 0, \tag{C.14}$$

$$\frac{\partial p}{\partial t} - \frac{1}{\alpha^2}\frac{\gamma p}{\rho}\frac{\partial \rho}{\partial t} + u\left(\frac{\partial p}{\partial x} - \frac{1}{\alpha^2}\frac{\gamma p}{\rho}\frac{\partial \rho}{\partial x}\right) = 0, \tag{C.15}$$

$$\frac{\partial p}{\partial t} - \frac{\rho}{\alpha}\sqrt{\frac{\gamma p}{\rho}}\frac{\partial u}{\partial t} + \left(u + \frac{1}{\alpha}\sqrt{\frac{\gamma p}{\rho}}\right)\left(\frac{\partial p}{\partial x} + \frac{\rho}{\alpha}\sqrt{\frac{\gamma p}{\rho}}\frac{\partial u}{\partial x}\right) = 0. \tag{C.16}$$

Note that the sound velocty is $c = \sqrt{\gamma p/\rho}$. Likewise, an artificial sound velocity can be defined as $c' = c/\alpha$. The three eigenvalues λ_i defined in Eq. C.10 correspond to the velocities of the characteristic waves, and their amplitues $\mathcal{L}_i$ are described by

$$\mathcal{L}_1 = \lambda_1\left(\frac{\partial p}{\partial x} - \rho c'\frac{\partial u}{\partial x}\right) \tag{C.17}$$

$$\mathcal{L}_2 = \lambda_2\left(\frac{\partial p}{\partial x} - c'^2\frac{\partial \rho}{\partial x}\right) \tag{C.18}$$

$$\mathcal{L}_3 = \lambda_3\left(\frac{\partial p}{\partial x} + \rho c'\frac{\partial u}{\partial x}\right). \tag{C.19}$$

Finally, identifying the amplitue of the characterisc waves $\mathcal{L}_i$ in Eqs. C.14 to C.16 the time derivatives of the primitive variables are computed using the following expressions:

$$\frac{\partial p}{\partial t} = -\frac{1}{2}\left(\mathcal{L}_3 + \mathcal{L}_1\right), \tag{C.20}$$

$$\frac{\partial \rho}{\partial t} = \frac{1}{c'^2}\left(\mathcal{L}_2 - \frac{1}{2}(\mathcal{L}_3 + \mathcal{L}_1)\right). \tag{C.21}$$

$$\frac{\partial u}{\partial t} = -\frac{1}{2\rho c'}\left(\mathcal{L}_3 - \mathcal{L}_1\right), \tag{C.22}$$

All waves amplitudes $\mathcal{L}_i$ corresponding to outgoing waves are computed at the boundaries using interior nodes from Eqs. C.17 to C.19 while incoming wave amplitudes in a perfectly non-reflecting boundary are theoretically zero. However, when setting perfectly non-reflecting boundary conditions, the problem might be ill-posed. Therefore, by adjusting the amplitude of the incoming waves, partially non-reflecting boundaries are imposed following the implementation of Coussement, Gicquel, Caudal, Fiorina, and Degrez (2012).

Appendix D

Effects of variable air properties on transient natural convection for large temperature differences

Effects of variable air properties on transient natural convection for large temperature differences

J.M. Armengol[a], F.C. Bannwart[a], J. Xamán[b], R.G. Santos[a,*]

[a]*Faculty of Mechanical Engineering, University of Campinas (UNICAMP), CP 6066, CEP 13081-970, Campinas-SP, Brazil*
[b]*Centro Nacional de Investigación y Desarrollo Tecnológico (CENIDET-TNM-SEP) Prol. Av. Palmira S/N. Col. Palmira, Cuernavaca, Morelos, CP. 62490, Mexico*

Abstract

This paper aims to study the effects of air variable properties in the transient case of the classical differentially heated square cavity problem. A SIMPLE algorithm using a low Mach number approximation is applied for coupling the heat and momentum transport equations, which are discretized by the finite volume method. A fully implicit scheme is used for time discretization. The numerical code is validated with benchmark results obtaining a maximum deviation of 0.13% in the average Nusselt number for the non-Boussinesq approach. The temperature and velocity fields as well as the local Nusselt number are numerically studied for Rayleigh numbers ranging between 10^4 - 10^7. A temperature difference of 720K is considered. We have found that the effects of variable properties are especially relevant along the flow development period, amongst which the average Nusselt number, for instance, differs up to roughly 10% with respect to the constant properties case; in contrast, once in steady state regime, such a difference remains less important and is no longer oscillating, resulting around 2%. An investigation is therefore put forward covering additional effects under regard of the principle of energy conservation, such as the time evolution of the total energy and its components for both transient regime and steady state cases. Excepting for the kinetic energy, the internal, potential and total energies are consistently and significantly higher for the case of variable properties; a suitable discussion is provided.

Keywords: `unsteady natural convection, square cavity, variable properties, low Mach number approximation.`

---

1. Introduction

Natural convection consists in a heat transport mode in which the fluid motion is spontaneously produced by its density variation under gravitational field, which is generated by a temperature and/or concentration gradients. This subject has attracted attention from many researchers due to its extensive engineering applications, such as cooling electrical and electronic devices [1–3], or natural ventilation in buildings [4–6]. It has been widely treated either experimentally, analytically or numerically.

The numerical approaches to model natural convective phenomena have been studied for many different geometrical configurations, such as cylindrical [7–9], triangular [10–12] or hemispherical cavities [13, 14]. Nevertheless, the most broadly studied case has been the rectangular 2D cavity representing a rectangular parallelepiped section. In

---

[*] Corresponding author
Email address: `roger7@fem.unicamp.br` (R.G. Santos)

Preprint submitted to International Journal of Thermal Sciences *April 15, 2019*

Nomenclature

$\bar{N}u$	Average Nusselt number
$\bar{P}$	thermodynamic average pressure, Pa
$\tilde{p}$	dynamic pressure, Pa
A	aspect ratio
c_p	heat capacity at constant pressure, $J{\cdot}kg^{-1}{\cdot}K^{-1}$
c_v	heat capacity at constant volume, $J{\cdot}kg^{-1}{\cdot}K^{-1}$
e	total energy per volume unit, $J \cdot m^{-3}$
E_i	internal energy, $J \cdot m^{-1}$
E_k	kinetic energy, $J \cdot m^{-1}$
E_p	gravitational potential energy, $J \cdot m^{-1}$
E_{tot}	total energy, $J \cdot m^{-1}$
g	gravity, $g = 9.81\ m \cdot s^{-2}$
H	cavity height and width, m
i	internal energy per mass unit, $J \cdot kg^{-1}$
M	Mach number
Nu	Nusselt number
P	pressure, Pa
Pr	Prandtl number
Q	heat transfer rate, $W \cdot m^{-1}$
R	gas constant for air, 287 $J \cdot (kg \cdot K)^{-1}$
Ra	Rayleigh number
T	temperature, K
t	time, s
u	horizontal velocity, $m \cdot s^{-1}$
v	vertical velocity, $m \cdot s^{-1}$
$V\!\!\!{-}$	volume, m^3
x	horizontal coordinate, m
y	vertical coordinate, m

Greek symbols

α	thermal diffusivity, $m^2 \cdot s^{-1}$
$\bar{\rho}$	average density, $kg \cdot m^{-3}$
β	thermal expansion coefficient, K^{-1}
ϵ	non-dimenional temperature difference parameter, $\epsilon = (T_h - T_c)/(T_h + T_c)$
γ	ratio of specific heats, $\gamma = 1.4$
λ	thermal conductivity, $W \cdot m^{-1} \cdot K^{-1}$
μ	dynamic viscosity, $Pa \cdot s$
ρ	density, $kg \cdot m^{-3}$
υ	kinematic viscosity, $m^2 \cdot s^{-1}$

Superscripts

$*$	dimensionless variable

Subscripts

0	initial value
C	constant properties
c	cold wall
h	hot wall
ref	reference value
V	variable properties

1983, de Vahl Davis [15] published the first set of benchmark solutions for the case of steady state natural convection in a square cavity, wherein the two vertical walls are isothermal and the two horizontal walls are adiabatic. Proceeding with these benchmark solutions, many different numerical approaches have been validated through this problem. In 1990, Saitoh and Hirose [16] published another benchmark solution, in this case using the finite difference method. One year later, Hortmann *et al.* [17] computed this problem by employing the finite volume method and taking advantage of the multi-grid technique and second-order schemes for convection and diffusions fluxes. More recently, other methods such as Lattice Boltzman [18] or the integral transform method [19] have been used to resolve this same problem. A comprehensive review of natural convection in enclosures is found in Baïri *et. al* [20], which also embraces transient regime - however still restricted to incompressible flow.

Compared with the steady state, the transient natural convection has received much less attention in the literature, in spite of its relevance for a better understanding of this kind of heat transfer mechanism [21]. Among the most relevant works regarding the transient regime of natural convection in differentially heated enclosures, one can cite Patterson and Imberger [22], one of the first papers which studied the classical rectangular cavity. They performed a scale analysis to show that a number of initial flow types are possible, collapsing ultimately onto two basic types of steady flow. Proceeding with this study, Hyun and Lee [23] examined the effect of Prandtl number finding a distinct oscillatory behavior when the criterion $Ra > Pr^4 A^{-4}$ and $Pr \geq 1$ is strongly satisfied. Sai *et al.* [24] solved the square cavity problem using the finite element method for Rayleigh numbers between 10^3 and 10^6. Christon *et al.* [25] presented a benchmark solution for 8:1 differentially heated cavity. A recent review of transient natural convection flow in enclosures can be found in Hussein *et. al* [21].

Most of the works regarding natural convection admit the density variation solely as a source term in the momentum equation through the Boussinesq approximation, considering it constant for the remaining conservation equations. Nevertheless, there are many applications which can not be modeled through the Boussinesq approximation due to temperature gradients high enough to invalidate this assumption. In this sense, as an illustrative example wherein a more accurate modeling may be needed, there is the solar cavity receivers for solar thermal power plants [26]. Likewise, other examples are industrial furnaces or walls of nuclear reactors with air gaps inside for insulation, also subjected to high temperature gradients. Indeed, some efforts have been done to solve the compressible natural convection through a non-Boussinesq approach; for example, Quéré *et. al* [27] published a benchmark solution for the case of large temperatures differences, where density variation must be taken into account in all equations. In the literature, one can find several studies regarding the limit of application of the Boussinesq approximation in the steady state [28–30], where good results are found restricted to small temperature differences between hot and cold walls and to low Rayleigh numbers.

As another approach toward precise modeling, Sehyun *et al.* [31] considered the viscosity variation with temperature and found that the local Nusselt numbers for oil resulted 70-80% higher over those for a constant viscosity, and 40-50% higher in the case of water. Such results were in excellent agreement with corresponding experimental data [32]. Leal *et al.* [33] presented results for the transient version of the classical differentially heated square cavity problem considering both constant and variable fluid properties. They concluded that the effects of variable properties are significant, especially along the flow development period. More recently, Sun *et al.* [34] addressed a study on the non-Boussinesq effects, where they considered double-diffusive convection.

Despite the literature points out the importance of considering variable properties in the solution of the time dependent natural convection, according to our knowledge, there is a lack of studies quantifying such effects. Therefore, the motivation of this study is to quantify and analyze the effects of considering density, viscosity and thermal conductivity as variable thermophysical properties. The temperature and velocity fields and the Nusselt number are numerically studied for Rayleigh number between 10^4 and 10^7, since most engineering applications reside in this range. To explicit such effects on the heat transfer processes, an additional study is conducted concerning the internal, gravitational potential and kinetic energies.

2. Mathematical and physical model

For a Newtonian fluid, the two-dimensional conservation equations governing the natural convection for the transient case can be written as follows:

$$\frac{\partial \rho}{\partial t} + \frac{\partial(\rho u)}{\partial x} + \frac{\partial(\rho v)}{\partial y} = 0, \tag{1}$$

$$\frac{\partial(\rho u)}{\partial t} + \frac{\partial(\rho u\ u)}{\partial x} + \frac{\partial(\rho v\ u)}{\partial y} = -\frac{\partial P}{\partial x} + \frac{\partial}{\partial x}\left(\mu \frac{\partial u}{\partial x}\right) + \frac{\partial}{\partial y}\left(\mu \frac{\partial u}{\partial y}\right), \tag{2}$$

$$\frac{\partial(\rho v)}{\partial t} + \frac{\partial(\rho u\ v)}{\partial x} + \frac{\partial(\rho v\ v)}{\partial y} = -\frac{\partial P}{\partial y} + \frac{\partial}{\partial x}\left(\mu \frac{\partial v}{\partial x}\right) + \frac{\partial}{\partial y}\left(\mu \frac{\partial v}{\partial y}\right) + (\rho - \overline{\rho})\vec{g}, \tag{3}$$

$$\frac{\partial(c_p\ \rho\ T)}{\partial t} + \frac{\partial(c_p\ \rho\ u\ T)}{\partial x} + \frac{\partial(c_p\ \rho\ v\ T)}{\partial y} = \frac{\partial}{\partial x}\left(\lambda \frac{\partial T}{\partial x}\right) + \frac{\partial}{\partial y}\left(\lambda \frac{\partial T}{\partial y}\right), \tag{4}$$

where viscous dissipation is neglected in Eq. (4) since velocities and viscosity have moderated values (Brinkman number $<< 1$), and laminar regime is assumed - in accordance with [35] for the covered range of Rayleigh number.

For the Boussinesq approximation the density is assumed constant and the source of motion is modeled by a source term in the momentum equation on the vertical direction. That leads to an incompressible formulation, which neglects acoustic effects; moreover, the averaged static pressure remains constant in time. Such approximation is done by replacing the last term on Eq. (3) by an expression solely dependent on temperature:

$$(\rho - \overline{\rho})\vec{g} = \rho_0 \vec{g} \beta (T - T_0). \tag{5}$$

For the sake of generalization, the following variables are adimensionalized:

$$T^* = \frac{T - T_c}{T_h - T_c}, \quad x^* = \frac{x}{H}, \quad y^* = \frac{y}{H}, \quad u^* = \frac{uH}{\alpha_0}, \quad v^* = \frac{vH}{\alpha_0}, \quad \text{and} \quad t^* = t\frac{\alpha_0}{H^2}, \tag{6}$$

where the adimensionalized time t^* is chosen following the work of Leal *et al.* [33].

Prandt and Rayleigh numbers are defined as

$$Pr = \frac{c_p \mu_{ref}}{\lambda_{ref}} \quad \text{and} \quad Ra = Pr\frac{\rho_{ref}^2 g (T_h - T_c) H^3}{T_{ref} \mu_{ref}^2}, \tag{7}$$

where T_{ref} is a reference temperature defined as $T_{ref} = (T_h + T_c)/2$; and λ_{ref}, ρ_{ref} and μ_{ref} are, respectively, the thermal conductivity, density and dynamic viscosity evaluated at T_{ref}.

The local Nusselt number at the hot wall, $Nu(y)\Big|_{x=0}$, and the average Nusselt number, $\overline{Nu}\Big|_{x=0}$, are determined as follows:

$$Nu(y)\Big|_{x=0} = \frac{H}{\lambda_{ref}(T_h - T_c)} \lambda(T) \frac{\partial T}{\partial x}\Big|_{x=0} \quad \text{and} \quad \overline{Nu}\Big|_{x=0} = \frac{1}{H}\int_0^H Nu(y)\Big|_{x=0} dy. \tag{8}$$

2.1. Boundary and initial conditions

Motion on an air parcel initially static is induced by means of a density difference with respect to its neighbor parcels, which is caused by a temperature difference between the vertical walls of the square cavity, while its both horizontal walls are imposed adiabatic. Figure 1 describes the physical model of the cavity.

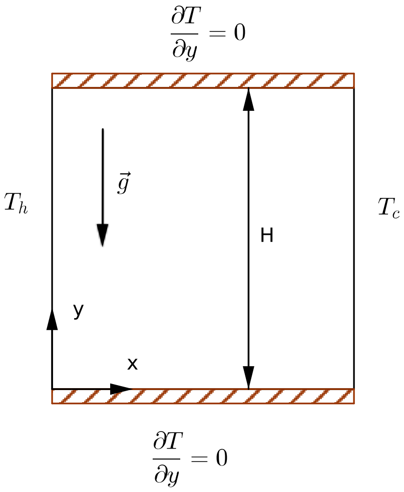

Figure 1: Sketch of the physical model.

A large temperature difference $\epsilon = 0.6$ is set, following typical values of previous studies [27], where $\epsilon = (T_h - T_c)/(T_h + T_c)$. Thus, for $T_{ref} = 600$K the maximum temperature difference results 720K. Also setting the Prandtl and Rayleigh numbers, the problem is completely defined with the following conditions:

Left boundary $(x = 0;\ 0 < y < H)$ Isothermal non-slip wall:

$$u = v = 0 \text{ and } T = T_h = T_{ref}(1 + \epsilon), \tag{9}$$

Right boundary $(x = H;\ 0 < y < H)$ Isothermal non-slip wall:

$$u = v = 0 \text{ and } T = T_c = T_{ref}(1 - \epsilon), \tag{10}$$

Bottom $(y = 0)$ **and top** $(y = H)$ **boundaries.** Adiabatic non-slip wall:

$$u = v = 0 \text{ and } \frac{\partial T}{\partial y} = 0, \tag{11}$$

Initial conditions $(t = 0)$**.** Stationary flow at spatially uniform temperature T_0 and pressure P_0, wherein fluid properties are computed at T_0:

$$u_0 = v_0 = 0,\ T_0 = T_{ref} = 600K,\ P_0 = 101325Pa,\ \rho_0 = \frac{P_0}{R\ T_0},\ \mu_0 = \mu(T_0) \text{ and } \lambda_0 = \lambda(T_0). \tag{12}$$

The consideration of the adiabatic boundary conditions aims to reproduce the effects of an ideal insulator, which result in a simple asymptotic thermal behavior - not reachable in realistic conditions. Despite such a simplicity, this cavity configuration ends up comprising all features that characterize the natural convection phenomenon; mainly, it permits to evaluate the impact of considering variable properties through a numerical solution.

2.2. Transport properties of air

The study of the effects of variable properties is performed for the transient natural convection in a square cavity filled with air ($Pr = 0.71$) with constant $c_p = 1004.5J/(kgK)$. Since air is here approximated as ideal gas, the viscosity and thermal conductivity are temperature dependent and therefore can be computed using the Sutherland's law:

$$\mu(T) = \mu' \left(\frac{T}{T'}\right)^{3/2} \frac{T' + S}{T + S} \quad \text{and} \quad \lambda(T) = \mu(T) \frac{\gamma R}{(\gamma - 1)Pr}, \tag{13}$$

where $T' = 273K$, $S = 110.5K$, $\gamma = 1.4$, $R = 287Jkg^{-1}K^{-1}$, $\mu' = 1.68 \cdot 10^{-5}m^{-1}s^{-1}kg$ and $Pr = 0.71$. Figure 2 shows how air dynamic viscosity and thermal conductivity tends to increase as temperature increases following Sutherland's law.

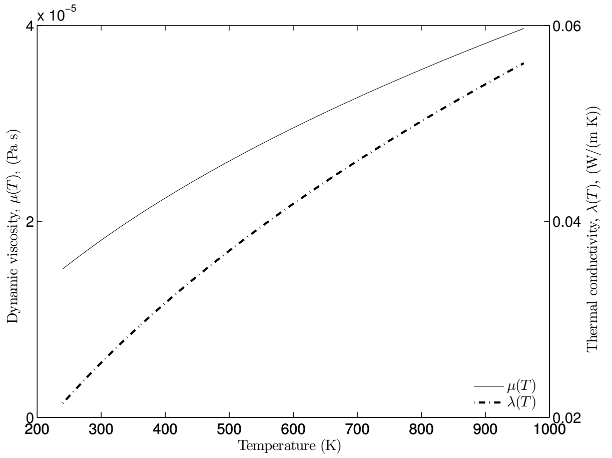

Figure 2: Dynamic viscosity and thermal conductivity dependences with temperature.

Either the Prandtl number or the specific heat are assumed constant since for the temperature range here considered they vary around 10% [36], while the viscosity and the thermal conductivity computed using Eq.13 vary much more significantly, over 160% for the same temperature range.

2.3. Non-Boussinesq approach

For large temperature differences the Boussineq approximation gives inaccurate results. A correlation proposed by Zhong [30] defines the following limit of validity:

$$\theta_0 = 0.0244 \; Ra^{0.243}, \tag{14}$$

where $\theta_0 = (T_h - T_c)/T_c$.

The non-Boussinesq approach entails the computation of a density field varying over time and space, leading to a compressible formulation. Since natural convection deals with low velocities, a low Mach number approximation was applied in this work. This approach entails a more efficient algorithm since there is no need to account for acoustic propagation and still captures the relevant physics. Firstly, the total pressure is decomposed into the thermodynamic pressure $\bar{P}(t)$ and the dynamic pressure $\tilde{p}$ by the expression

$$P(x, y, t) = \bar{P}(t) + \tilde{p}(x, y, t). \tag{15}$$

Asymptotic analysis [37] shows that $\bar{P}(t)/P_0 = O(1)$ and $\tilde{p}/P_0 = O(M^2)$, where P_0 is the initial pressure and M is the Mach number. Therefore, the local density is calculated from the ideal gas equation using the thermodynamic pressure and local temperature. This approximation is valid for low Mach numbers. The thermodynamic pressure is time-dependent, but it is constant in space, as described in [37]. Consequently, the density is decoupled from the dynamic pressure, so no acoustics are accounted.

In the case of impermeable walls, closed system, the amount of mass is constant over time; considering as well the fluid as ideal gas and integrating the equation of state over the entire space domain, the thermodynamic pressure $\bar{P}(t)$ can be defined as in [27]:

$$\bar{P}(t) = P_0 \frac{\int \frac{1}{T_0} dV\!\!\!/}{\int \frac{1}{T} dV\!\!\!/}. \tag{16}$$

Finally, the local density field can be computed from the ideal gas law as

$$\rho = \frac{\bar{P}(t)}{RT}. \tag{17}$$

The reader is referred to [38] for a comparison of low Mach number models for natural convection problems.

3. Methodology for the numerical solution

In order to solve the governing equations a Fortran code was implemented. The governing equations are discretized by the finite volume method using a fully implicit scheme for time discretization (Patankar [39] and Versteeg and Malalasekera [40]). A non-uniform staggered marker-and-cell (MAC) mesh [41] is used, where the velocity components are calculated at a staggered grid, and the scalar variables are calculated at the main grid (not staggered). Coupling between mass and momentum conservation equations is carried out using the SIMPLE algorithm (Patankar and Spalding [42]). An hybrid scheme approximates the convection terms, while a central difference scheme is used for the diffusive terms. When the residuals of the mass balance for every control volume, as well as the residual values for the rest of the governing equations, are sufficiently low, an overall convergence is achieved. Global residual values for each transport equation are computed using the quadratic mean and considered converged when values lower than 10^{-8} are obtained.

For the case of variable properties, the matrices containing the local values of ρ, λ and μ are computed in every iteration for each temperature field, as shown in Fig. 3. To interpolate the properties values in the control volume interfaces, a linear variation between the two neighbor nodes was assumed.

The set of algebraic equations, resulting from the discretization, are solved by an ADI iterative method. In addition, under-relaxation parameters have been used in order to minimize the number of iterations required to obtain converged solutions.

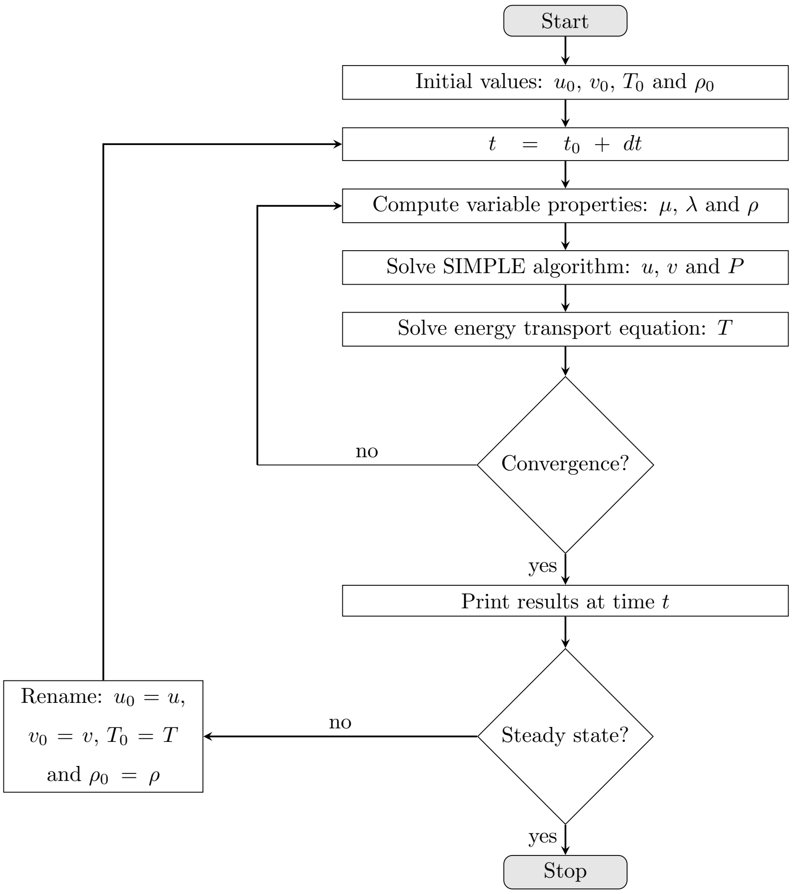

Figure 3: Flowchart of the algorithm for the case of variable properties.

The grid size and time step independence are achieved after numerous tests taking as reference the average Nusselt number in the hot wall for Rayleigh numbers between $10^3 - 10^7$. This numerical analysis reveals that higher Rayleigh numbers demand more refined meshes as well as smaller time steps. Based on the results for $Ra = 10^7$, a non-uniform mesh of 256 x 256 nodes and a non-dimensional time step of 10^{-4} are selected, for which a maximum deviation of 0.1 % is obtained for the average Nusselt number at the specific time $t^* = 0.05$.

3.1. Verification

In order to verify the numerical code used in the present work, some benchmark problems are reproduced and compared with the results of the present work. Firstly, the results for the steady state solution using constant properties and the Boussinesq approximation are compared with some classical solutions [15, 17]. Secondly, the compressible solutions with and without variable properties are compared with [27]. Finally, the transient natural convection is compared with the results published in [33].

Steady state with constant properties and Boussinesq approximation

A set of comparisons is performed under the Boussinesq approximation with constant properties for the classical square cavity problem with differentially heated vertical walls making use of Eq. (5). In Table 1, results for steady state regime for Rayleigh numbers between 10^3 and 10^6 are compared with the benchmark solutions [15, 17] for $Pr = 0.71$. The selected comparative results are: the maximum horizontal velocity, u^*_{max}, in the vertical mid-plane ($x^* = 0.5$); the maximum vertical velocity, v^*_{max}, in the horizontal mid-plane ($y^* = 0.5$); and the maximum, minimum and average Nusselt number in the hot wall, Nu_{max}, Nu_{min}, $\overline{Nu}$. The overall agreement is quite reasonable with a maximum deviation of 1.99% with respect to [15] and a 0.22% with respect to [17].

Table 1: Comparison of the present work with some steady state benchmark results for constant properties and Boussineq approximation.

Ra		u^*_{max}	v^*_{max}	Nu_{max}	Nu_{min}	$\overline{Nu}$
10^3	De Vahl Davis [15]	3.649	3.697	1.505	0.692	1.118
	Hortmann *et al.* [17]	-	-	-	-	-
	Present work	3.6450	3.6998	1.5100	0.6935	1.1207
10^4	De Vahl Davis [15]	16.178	19.617	3.528	0.586	2.243
	Hortmann *et al.* [17]	16.1802	19.6295	3.53087	-	2.24475
	Present work	16.1838	19.6296	3.5319	0.5851	2.2452
10^5	De Vahl Davis [15]	34.73	68.59	7.717	0.729	4.519
	Hortmann *et al.* [17]	34.7399	68.6396	7.72013	-	4.52164
	Present work	34.7410	68.6212	7.7242	0.7280	4.5225
10^6	De Vahl Davis [15]	64.63	219.36	17.925	0.989	8.800
	Hortmann *et al.* [17]	64.8367	220.461	17.536	-	8.82513
	Present work	64.8473	220.5518	17.5752	0.9794	8.8300

Steady state with a non-Boussinesq approach with and without variable properties

Quéré *et al.* [27] published a benchmark solution for the compressible case with and without variable properties. This reference solution is based on the results of five independent authors, whose methods and procedures are detailed in [43–47]. Three tests are available for the following conditions:

Test 1: $Ra = 10^6$, $\epsilon = 0.6$, $\mu = \mu_0$ and $\lambda = \lambda_0$,

Test 2: $Ra = 10^6$, $\epsilon = 0.6$, $\mu = \mu(T)$ and $\lambda = \lambda(T)$,

Test 3: $Ra = 10^7$, $\epsilon = 0.6$, $\mu = \mu(T)$ and $\lambda = \lambda(T)$,

where the initial conditions are $P_0 = 101325$ Pa and $T_0 = 600$ K. Viscosity and thermal conductivity are computed using Sutherland law defined in Eq. (13).

Table 2 presents a comparison of the average Nusselt in the hot wall ($\overline{Nu}_h$) and the non-dimensional thermodynamic pressure ($\bar{P}(t)/P_0$) obtained in this present work with the ones published in [27]. The percentage deviation when comparing with the reference values are shown between parentheses. The results obtained for the non-Boussinesq approximation are in good agreement with previous solutions since the maximum deviation obtained is 0.129%.

Table 2: Comparison of the present work with steady state benchmark results with a non-Boussinesq approach.

		$\bar{P}(t)/P_0$	$\overline{Nu}_h$
Test 1	Quéré *et al.* [27]	0.856338	8.85978
	Present work	0.8565 (0.019%)	8.8640 (0.048%)
Test 2	Quéré *et al.* [27]	0.924487	8.6866
	Present work	0.9249 (0.045%)	8.6938 (0.083%)
Test 3	Quéré *et al.* [27]	0.92263	16.2410
	Present work	0.92224 (0.042%)	16.2619 (0.129%)

Transient regime with constant properties and Boussinesq approximation

To conclude the verification of the code, results for the unsteady regime are compared with previous publications [33]. Again, the Boussinesq approximation and constant properties formulation are used. Figures 4 and 5 show non-dimensional temperature and dimensionless vertical velocity component distribution, respectively, in the cavity mid-plane ($y^* = 0.5$) for Rayleigh numbers between 10^3 and 10^6, $Pr = 0.71$ and $T_0 = T_c$. In addition, for the same Rayleigh range, the time evolution of the average Nusselt number is compared with the same authors in Fig. 6. Figures 4 to 6 show an excellent agreement, at least, at the graph scale. The expected increasing oscillations of the average Nusselt number as the Rayleigh number increases are also well reproduced. Results for $Ra = 10^6$ are presented yet not compared with previous work since no data could be found for the sake of comparison. A distinguished agreement is achieved between every average Nusselt number at the end of the transient period and the ones found in the steady state formulation.

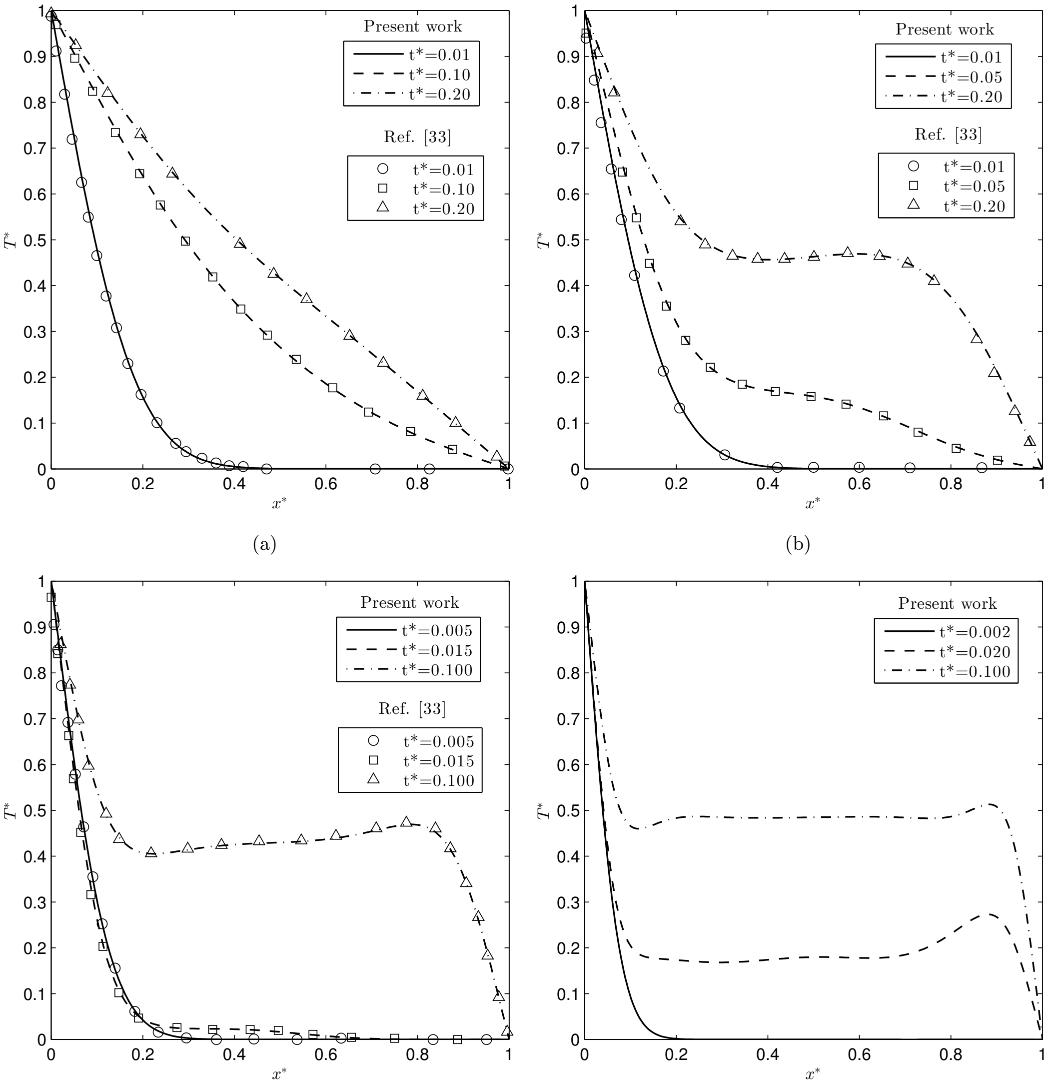

(a) (b)

(c) (d)

Figure 4: Comparison of dimensionless temperature in the horizontal mid-plane for (a) $Ra = 10^3$, (b) $Ra = 10^4$, (c) $Ra = 10^5$ and (d) $Ra = 10^6$.

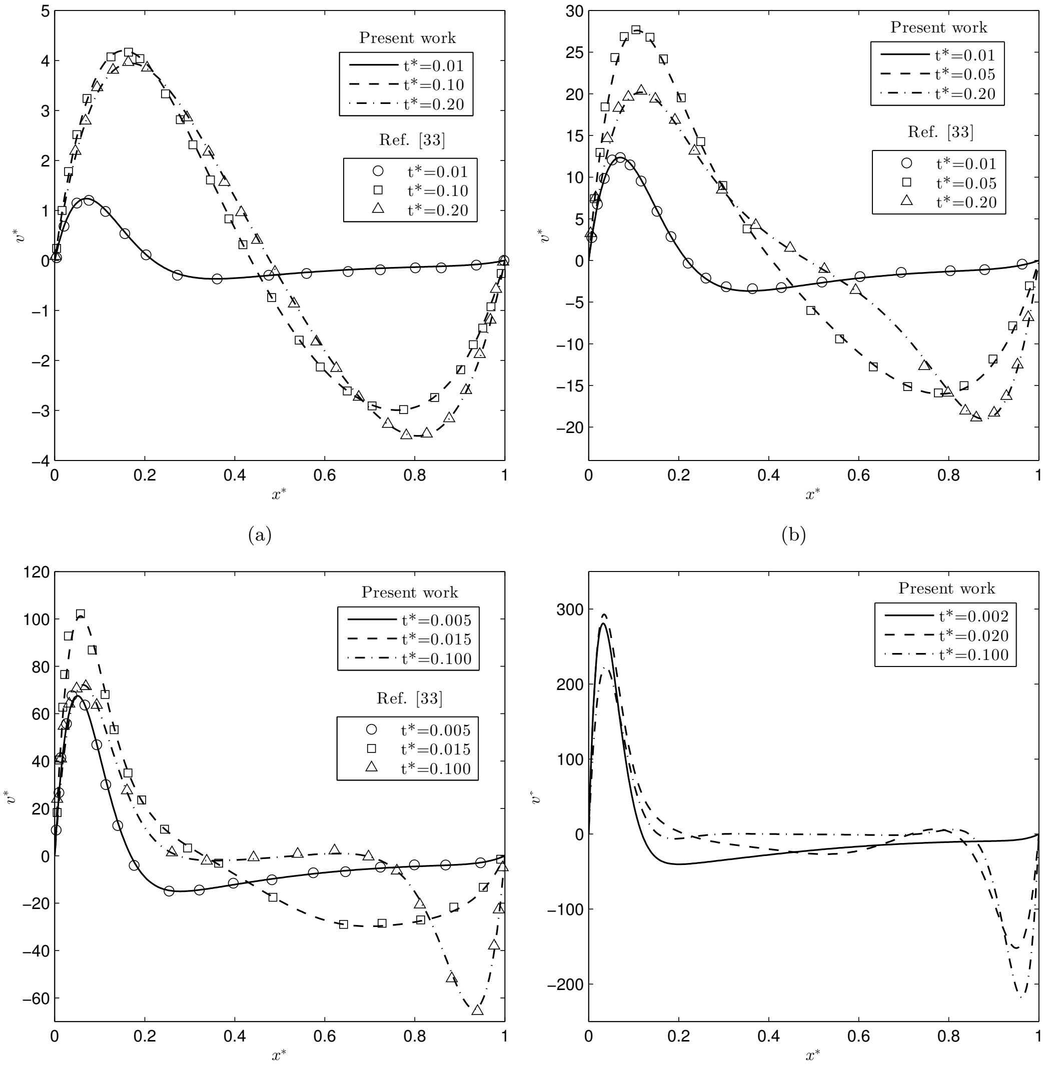

(a) (b)

(c) (d)

Figure 5: Comparison of dimensionless vertical velocity in the horizontal mid-plane for (a) $Ra = 10^3$, (b) $Ra = 10^4$, (c) $Ra = 10^5$ and (d) $Ra = 10^6$.

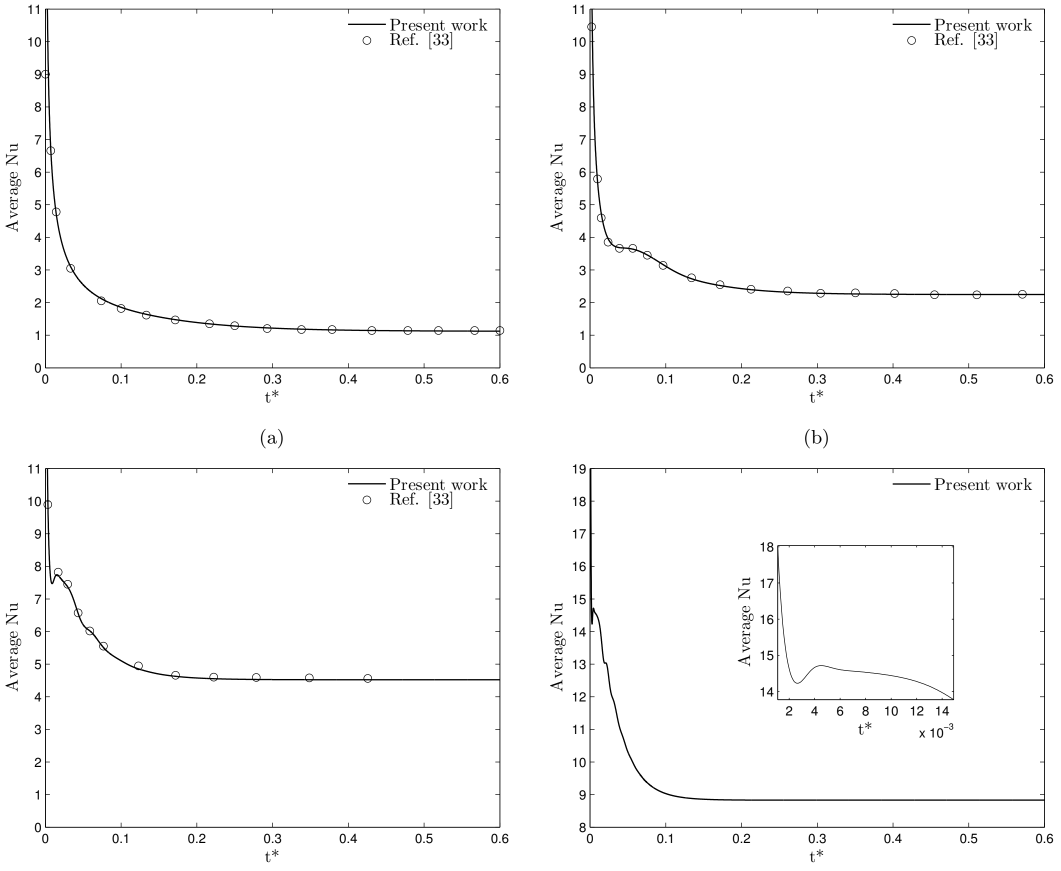

(a) (b) (c) (d)

Figure 6: Comparison of average Nusselt number in the hot wall over time for (a) $Ra = 10^3$, (b) $Ra = 10^4$, (c) $Ra = 10^5$ and (d) $Ra = 10^6$.

4. Results and discussion

4.1. Effects of variable viscosity and thermal conductivity using a non-Boussinesq approach

In order to study the effects of considering variable properties in the transient regime, numerical simulations are performed for the Rayleigh numbers 10^4, 10^5, 10^6, and 10^7. The solution for constant and variable properties are computed using a non-Boussinesq approach for a large temperature difference of $\epsilon = 0.6$ for each Rayleigh number. Boundary and initial conditions are detailed in Eqs. (9) to (12). In order to attain each Rayleigh number, the cavity dimension is adapted following Eq. (7). Table 3 in the following shows the resulting dimensions.

Table 3: Cavity dimensions for each Rayleigh number.

Ra	H
10^3	$2.63 \cdot 10^{-2}$ m
10^4	$5.66 \cdot 10^{-2}$ m
10^5	$1.22 \cdot 10^{-1}$ m
10^6	$2.63 \cdot 10^{-1}$ m
10^7	$5.66 \cdot 10^{-1}$ m

The time evolution of the average Nusselt number in the hot wall for constant properties ($\overline{Nu_C}$) and variable properties ($\overline{Nu_V}$) are shown in Fig. 7. It can be observed for all investigated Rayleigh numbers, that the Nusselt number for variable properties is larger than for constant properties in the very first instants of the transient regime. Nevertheless, such a behavior is inverted at a specific instant of time, which varies with the Rayleigh number, and is kept that way ever since. Also, the oscillation of the average Nusselts presents a slightly different behavior between the cases of constant and variable properties.

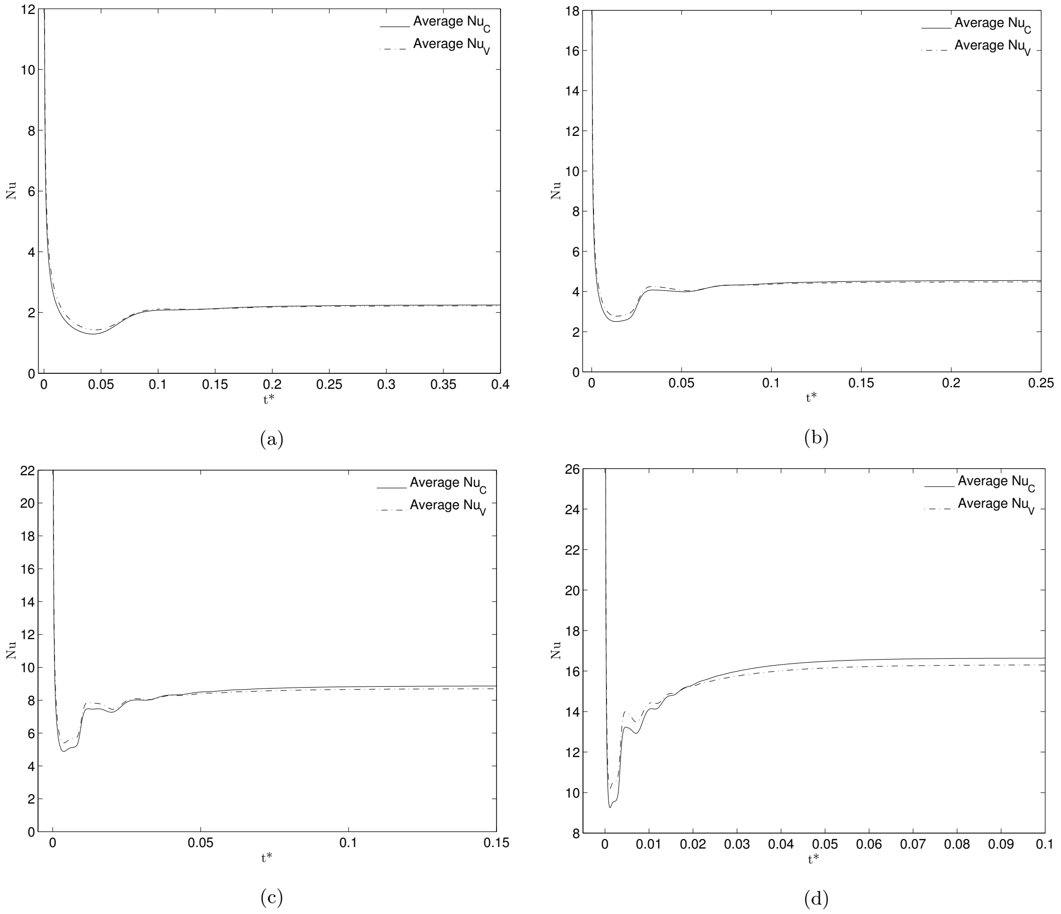

(a) (b)

(c) (d)

Figure 7: Transient behavior of average Nusselts for constant properties ($\overline{Nu_C}$) and variable properties ($\overline{Nu_V}$) for (a) $Ra = 10^4$, (b) $Ra = 10^5$, (c) $Ra = 10^6$ and (d) $Ra = 10^7$.

The lower value of the average Nusselt number reached during the transient period $\overline{Nu}_{min}$, its corresponding specific instant of time as well as the duration of the transient regime are shown in Table 4 for constant and variable properties. We consider that the system arrives at the steady state when two consecutive values of the average Nusselt number differs less than 10^{-3} %. Note that the local minimum of the average Nusselt numbers shows up earlier when increasing the Rayleigh number. Comparing the cases of constant and variable properites, it can be observed that values of Nu_{min} vary significantly, while $t^*(\overline{Nu}_{min})$ and $t^*_{steady\ state}$ are slightly different.

Table 4: Minimum Nusselt number reached during the transient period, its corresponding time, and required time to reach the steady state for Ra numbers between 10^4 and 10^7.

Ra		10^4	10^5	10^6	10^7
$\overline{Nu}_{min}$	Variable properties	1.4300	2.7758	5.3987	10.2134
	Constant properties	1.2906	2.5064	4.8838	9.2549
$t^*(\overline{Nu}_{min})$	Variable properties	0.0451	0.0140	0.0037	0.0012
	Constant properties	0.0428	0.0137	0.0037	0.0012
$t^*_{steady\ state}$	Variable properties	0.2776	0.1795	0.1195	0.0789
	Constant properties	0.2849	0.1846	0.1223	0.0782

To better compare the Nusselt number between both cases, their ratio $\frac{Nu_C}{Nu_V}$ is shown in Fig. 8 for their corresponding average ($\frac{\overline{Nu_C}}{\overline{Nu_V}}$), minimum ($\frac{Nu_{C,min}}{Nu_{V,min}}$) and maximum ($\frac{Nu_{C,max}}{Nu_{V,max}}$) values in the hot wall over time.

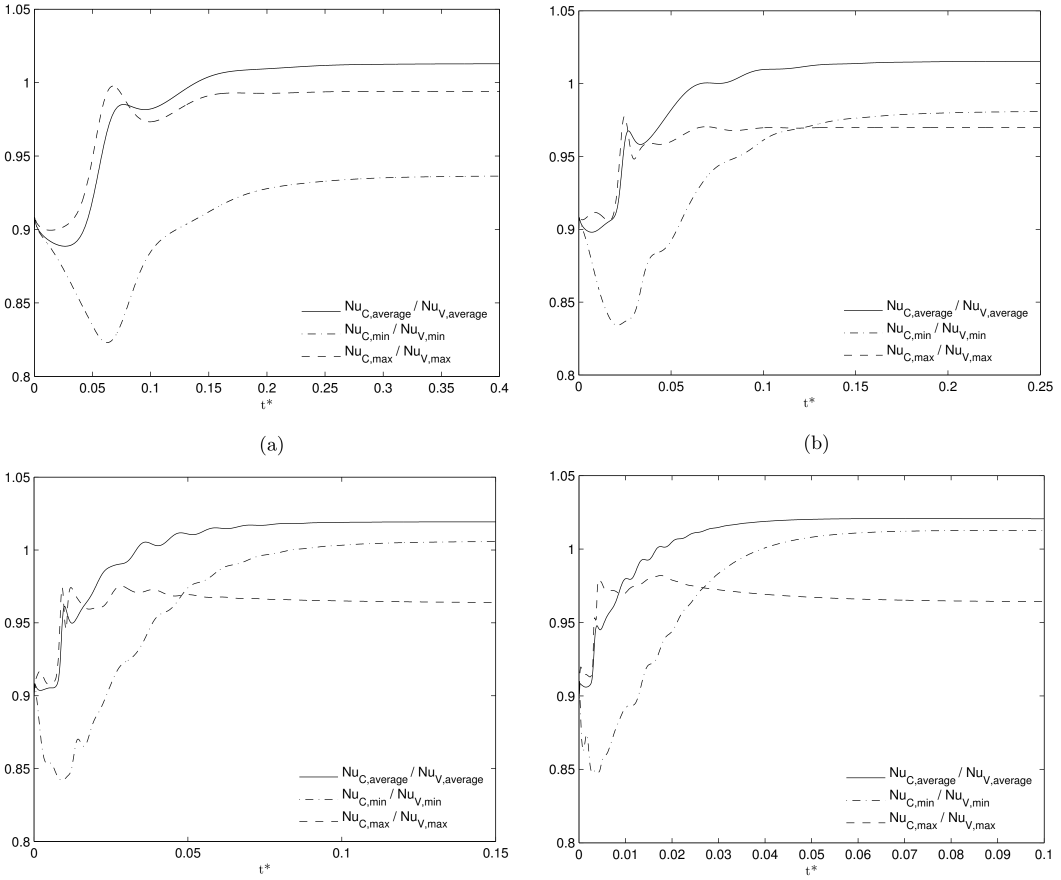

(a) (b)

(c) (d)

Figure 8: Ratio of $\frac{Nu_C}{Nu_V}$ for corresponding average, minimum and maximum values of the Nusselt number, along the transient regime, for (a) $Ra = 10^4$, (b) $Ra = 10^5$, (c) $Ra = 10^6$ and (d) $Ra = 10^7$.

Comparing the case of constant and variable properties, it can be seen that transient regime presents larger differences of Nusselt number than the steady state. Also, it should be noticed that as the Rayleigh increases the relative difference between average Nusselt numbers observed in the transient regime decreases slightly, while the relative difference in the steady state behaves in opposite way. Thus, it can be observed that the average Nusselt deviation in the transient regime is of the order of 10 %, while in the steady state it barely reaches the value of 2 %.

In Figs. 9 and 10 the differences between constant and variable properties are put in evidence for Rayleigh numbers between 10^4 and 10^7. Despite the qualitative differences observed in the isotherms and the isovalue lines of velocity between the two cases, flow patterns show no significant impact when variable properties are considered. Those figures also show that for all studied Rayleigh numbers the temperature gradient in the hot wall is higher for the constant properties case, while it is lower in the cold wall. To quantify the amount of energy crossing the vertical

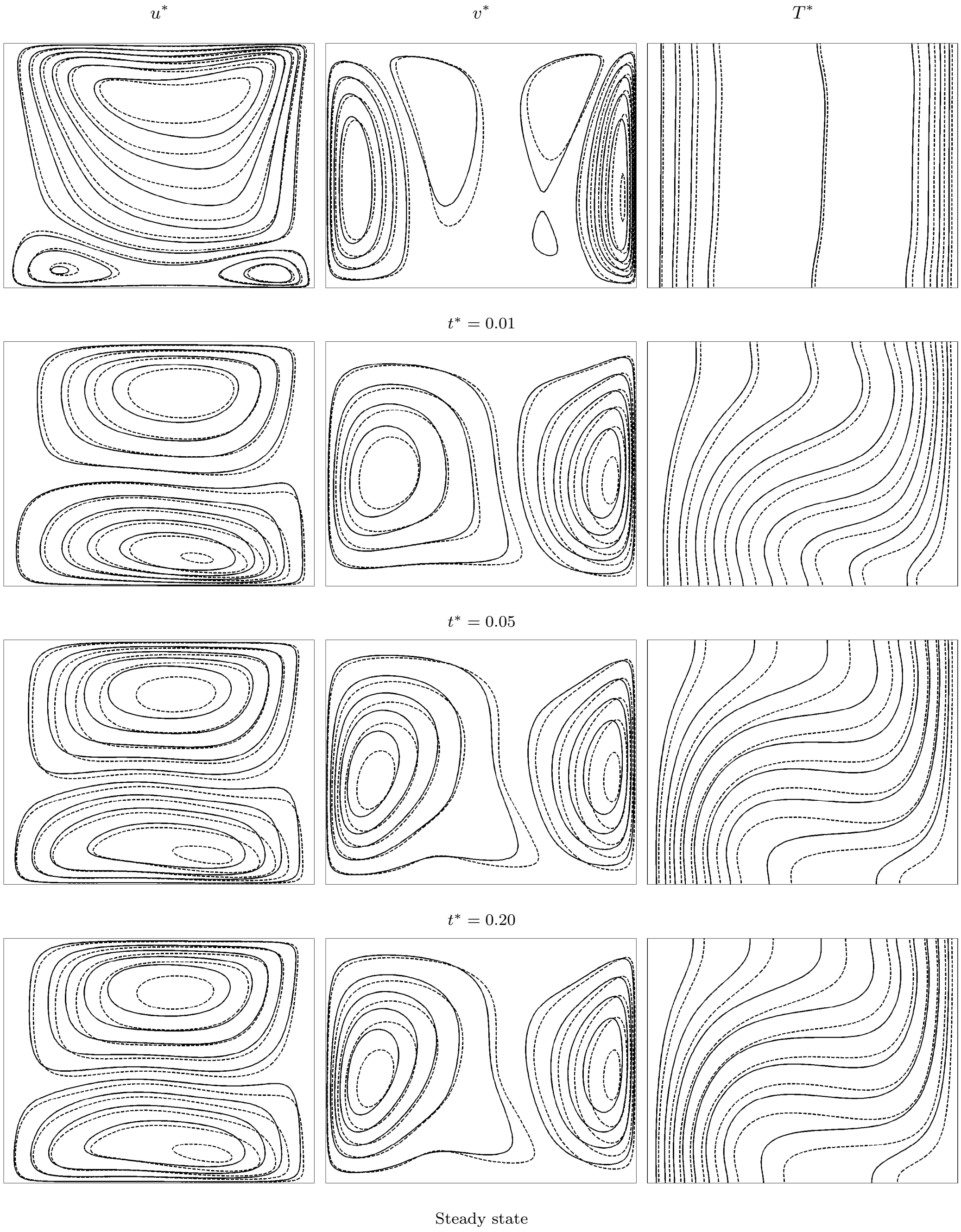

Figure 9: Isovalues of horizontal velocity, vertical velocity and temperature for $Ra = 10^4$ for constant properties (——) and variable properties (- - -).

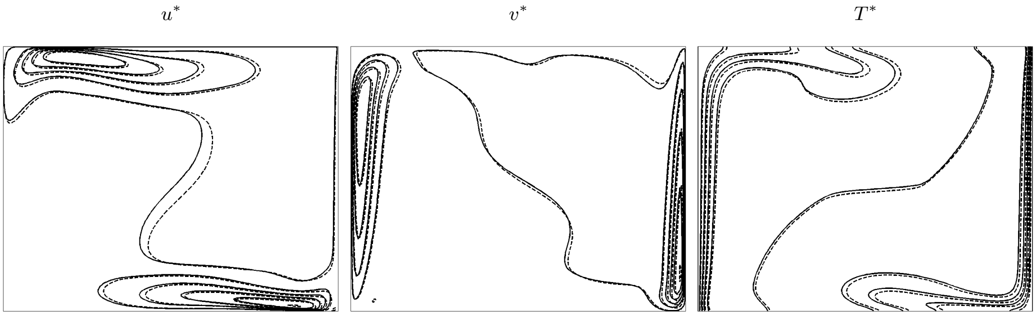

$t^* = 0.002$

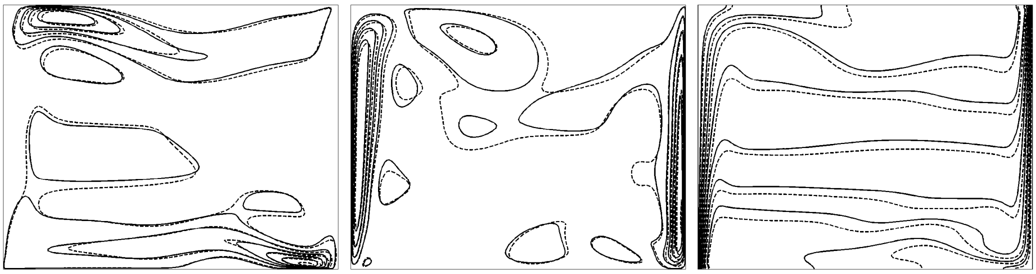

$t^* = 0.010$

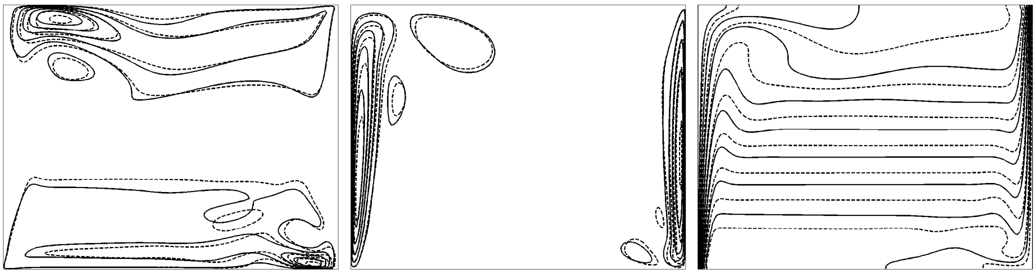

$t^* = 0.050$

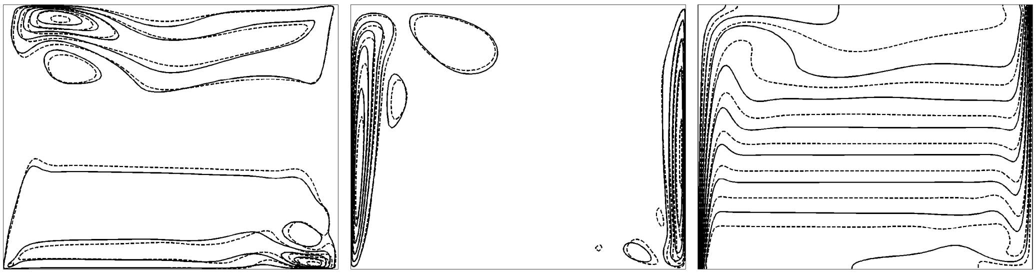

Steady state

Figure 10: Isovalues of horizontal velocity, vertical velocity and temperature for $Ra = 10^7$ for constant properties (——) and variable properties (- - -).

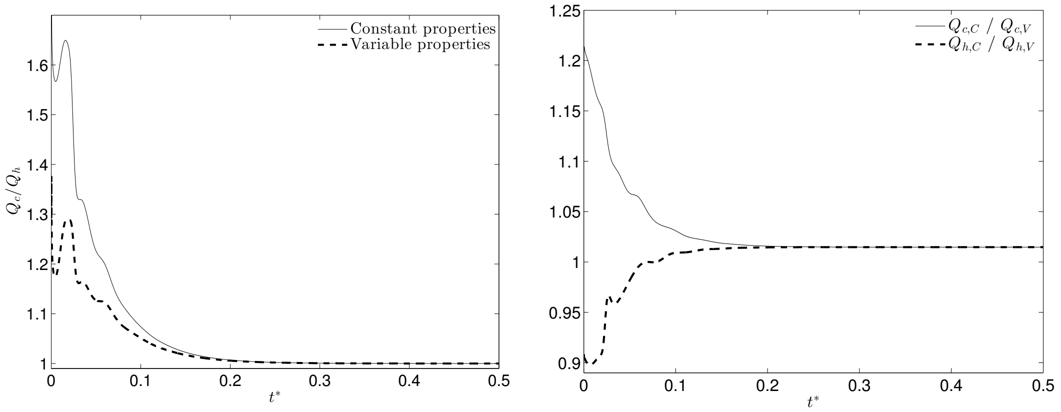

(a)

(b)

Figure 11: (a) Ratio of $\frac{Q_c}{Q_h}$ for constant and variable properties. (b) Ratio of heat fluxes $\frac{Q_C}{Q_V}$ at the hot and at the cold walls.

walls, the heat transfer rate is computed as

$$Q_h = \int_0^H -\lambda(t)\frac{\partial T}{\partial x}\bigg|_{x=0} dy \quad \text{and} \quad Q_c = \int_0^H -\lambda(t)\frac{\partial T}{\partial x}\bigg|_{x=H} dy. \tag{18}$$

Figure 11a shows that heat transfer rate is higher at the cold wall when compared with the hot wall for constant and variable properties. Note that the ratio $\frac{Q_c}{Q_h}$ is higher in the constant property case during the transient period and, as expected, tends to unity in the steady state. Figure 11b reveals that the heat transfer rate in the hot wall during the beginning of the transient regime is larger for the variable properties case. On the other hand, once in the steady state, the heat flux in this wall is larger for the constant properties case. This phenomenon depends on the transient evolution of the thermal conductivity as well as on the temperature in the surroundings of the hot wall.

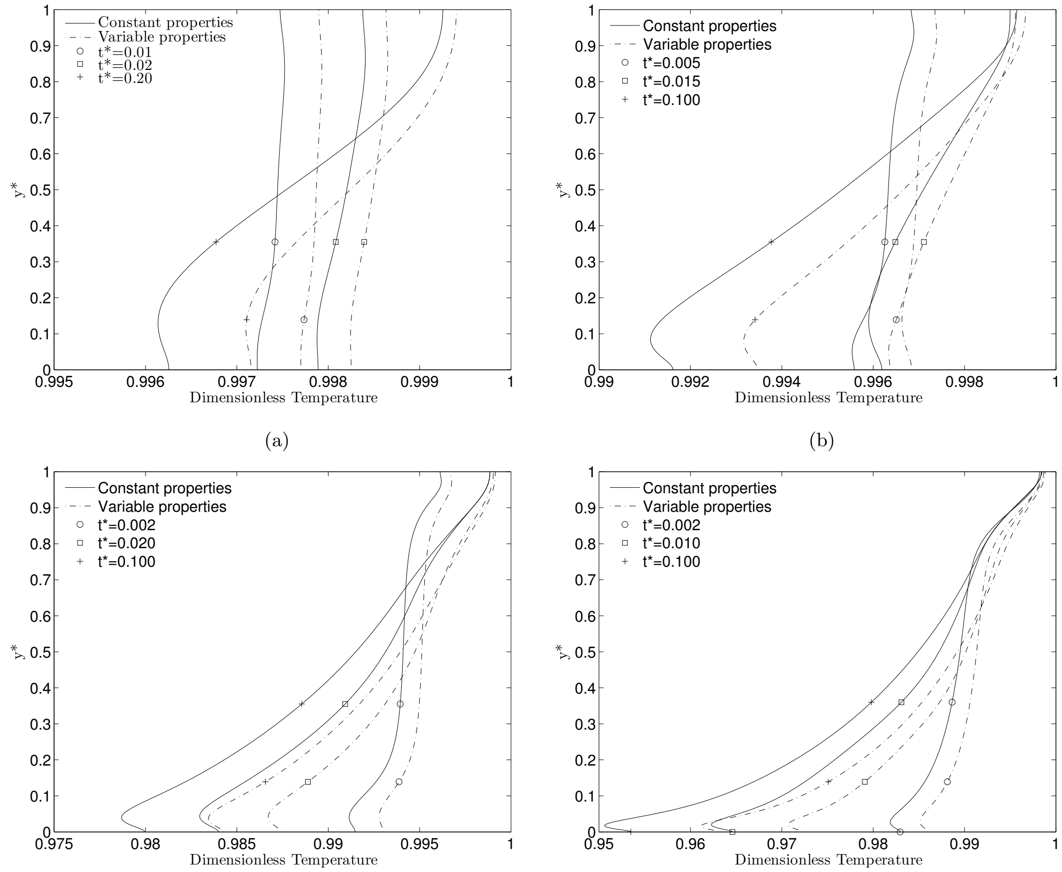

(a) (b) (c) (d)

Figure 12: Local dimensionless temperature distributions in the surroundings of the hot wall at different instants of times for constant and variable properties. (a) $Ra = 10^4$, (b) $Ra = 10^5$, (c) $Ra = 10^6$ and (d) $Ra = 10^7$.

Because the temperature near the hot wall is larger than T_{ref}, the thermal conductivity presents larger values for the variable properties case, in accordance with Fig. 2, where the increase is directly proportional. Nevertheless, the temperature in the surroundings of the hot wall is slightly lower for the constant properties case, as shown in Fig. 12, which implies a greater temperature gradient. The balance of the contributions of the thermal conductivity and the temperature gradient in the hot wall determines in which case Q_h presents larger values.

Figure 13 shows the local Nusselt number distribution along the hot wall at different instants of time. It can be seen that, in the first instants, the Nusselt number for variable properties is greater all along the hot wall. This fact must be due to larger values of $\lambda(T)$, since the temperature gradient is grater for the constant properties case, as shown in Fig. 12. Note that, as time passes, the Nusselt numbers for the constant properties case are larger due to the greater temperature gradient in the hot wall, since the thermal conductivity remains greater for the variable properties case.

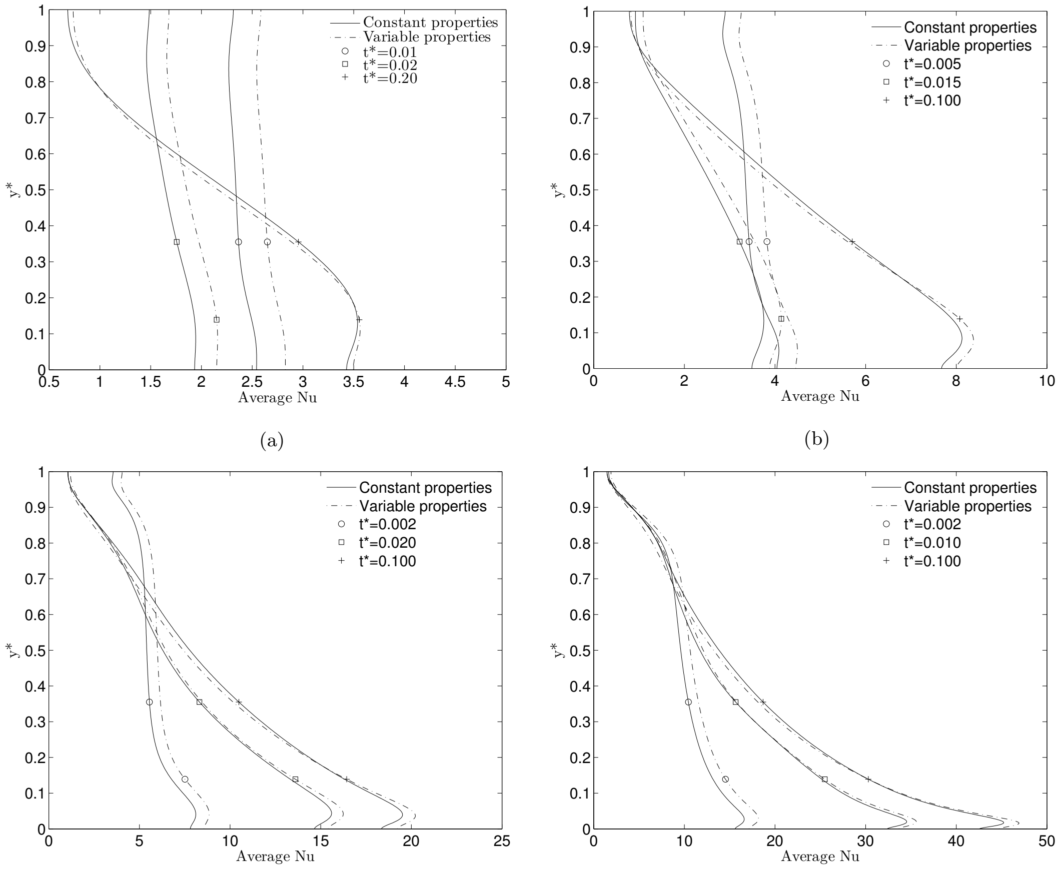

(a)

(b)

(c)

(d)

Figure 13: Local Nusselt number distributions along the hot wall at different times for constant and variable properties. (a) $Ra = 10^4$, (a) $Ra = 10^5$, (a) $Ra = 10^6$ and (a) $Ra = 10^7$.

Total energy per unit of volume e is defined as

$$e = \rho \left(\frac{1}{2}(u^2 + v^2) + i + g\ y \right), \tag{19}$$

where i is the specific internal energy per mass unit, $\frac{1}{2}(u^2 + v^2)$ stands for kinetic energy per mass unit and $g\ y$ for gravitational potential energy per mass unit.

Since air is considered as ideal gas, its internal energy depends on temperature only. Taking the reference temperature at 0K, the local value of i can be defined as

$$i(T) = c_v\ T, \tag{20}$$

where c_v is the specific heat at constant volume. Recalling the ideal gas approximation: $c_v = c_p - R$, with c_p being the specific heat at constant pressure and R the constant for air.

Integrating e over the space domain, one can obtain the total energy $E_{tot}(t)$ inside the cavity as a function of time,

$$E_{tot}(t) = \int_0^H \int_0^H e(x,y,t)\; dx\; dy. \tag{21}$$

Similarly, to put in evidence the importance of each term, one can obtain the internal energy $E_i(t)$, kinetic enrgy $E_k(t)$ and gravitational potential energy $E_p(t)$ inside the cavity.

Figure 14a shows the total energy adimensionalized with the initial total energy $E_{tot,0}$. In agreement with Fig. 11, the total energy decreases faster for the constant property case since the ratio $\frac{Q_c}{Q_h}$ is higher all along the transient regime. This is caused because of the thermal conductivity distribution for the variable properties case (higher values of $\lambda(t)$ near the hot wall and lower values near the cold wall) despite temperature gradient accounts against this behavior.

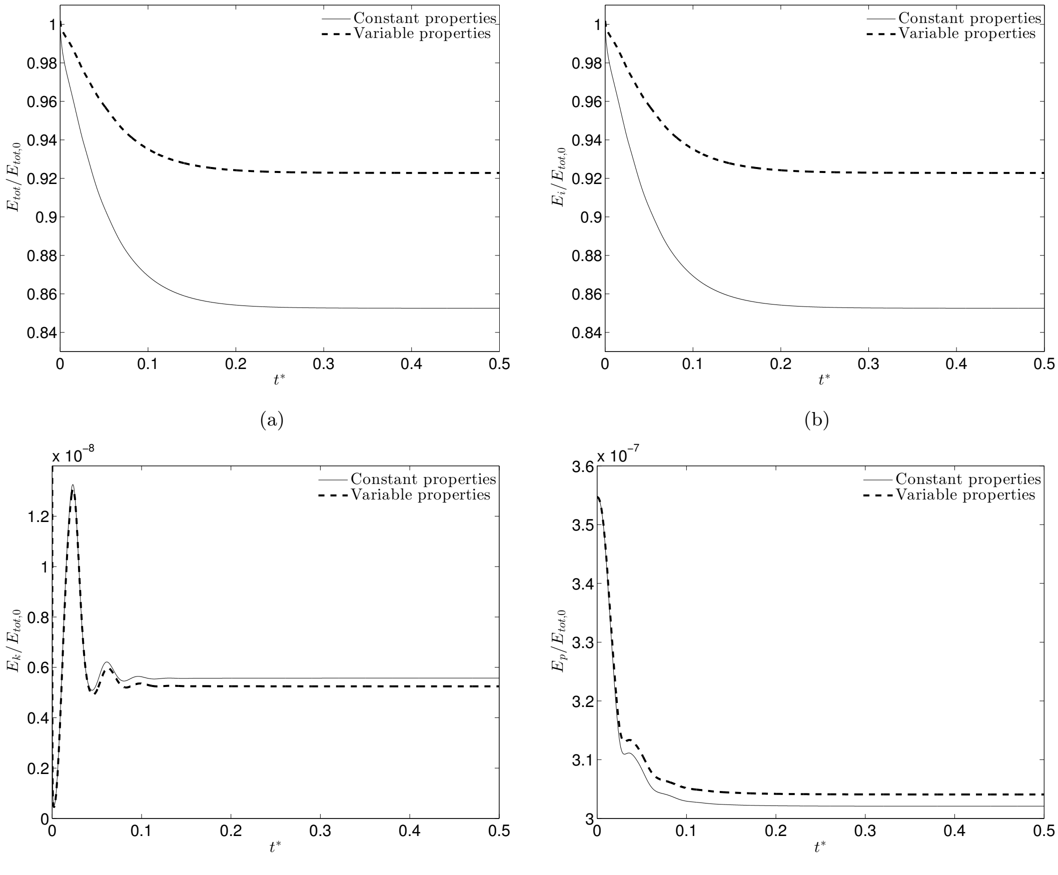

(a) (b)

(c) (d)

Figure 14: (a) Total energy E_{tot}, (b) internal energy E_i, (c) kinetic energy E_k and (d) gravitational potential energy E_p undimensioned by the initial total energy $E_{tot,0}$ along the transient regime for $Ra = 10^5$.

In Fig. 14c, as expected, kinetic energy E_k increases from the initial value with an oscillatory behavior, and gravitational potential energy E_p (Fig. 14d)decreases in accordance with the density distribution (low density values at the top of the cavity and higher values at the bottom). It can also be observed that kinetic energy and gravitational potential energy are nonessential for the determination of the total energy, even in the transient regime, since E_k is eight orders of magnitude lower than internal energy (Fig. 14b) while E_p is seven orders lower for $Ra = 10^5$.

4.2. Validity of the Boussinesq approximation for transient results in a differentially heated cavity

The limit of application of the Boussinesq approximation has been largely studied for the steady state [28–30, 48]. However, as far as we know, there are no previous works in which the validity of the Boussinesq approximation for the transient regime had been quantitatively studied in the differentially heated cavity problem. Besides, since variable properties are more influential for transient regime than for steady state, as demonstrated before, the validity of such an approximation is more compromised and can be a critical issue in terms of accuracy. Thus, in order to have an insight of the validity of this approximation, the differences with the non-Boussinesq approach are studied. Viscosity and thermal conductivity are considered constant since the interest is now focused on density.

Firstly, in Fig. (15b) the maximum difference in the local Nusselt number at the hot wall observed during the transient regime is plotted as a function of Rayleigh number and dimensionless temperature difference ϵ. The results show that the validity of the Boussinesq approximation is manly affected by the temperature differences between hot and cold walls, and this is specially true for Rayleigh numbers larger than $5 \cdot 10^5$. For the sake of comparison, Fig. (15a) shows this same difference once the steady state is reached. As expected, the validity of the Boussinesq approximation is more restrictive for the transient regime than for steady state.

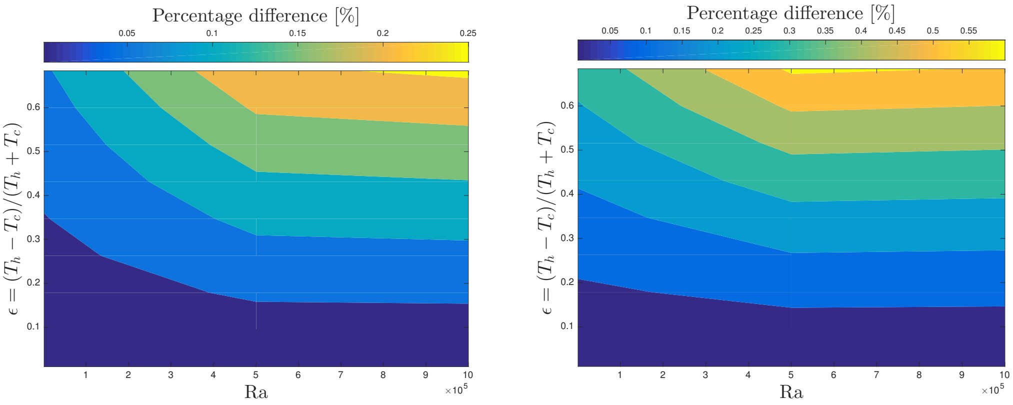

(a)

(b)

Figure 15: Maximum difference for the local Nusselt number at the hot wall as a function of Rayleigh number and dimensionless temperature difference. (a) Steady state. (b) Maximum peak value reached during transient regime.

Finally, Fig. 16a presents the maximum percentage difference of the local Nusselt number in the hot wall versus the adimensional temperature difference ϵ for a fixed Nusselt number of $5 \cdot 10^5$ for both transient regime and steady state cases. Figure 16a reveals an almost linear relation between ϵ and the peak value of the difference for the local Nusselt number. Moreover, looking at the transient behaviour of this difference for several values of ϵ, in Fig. 16b, one can observed that the peak is clearly reached in the transient regime.

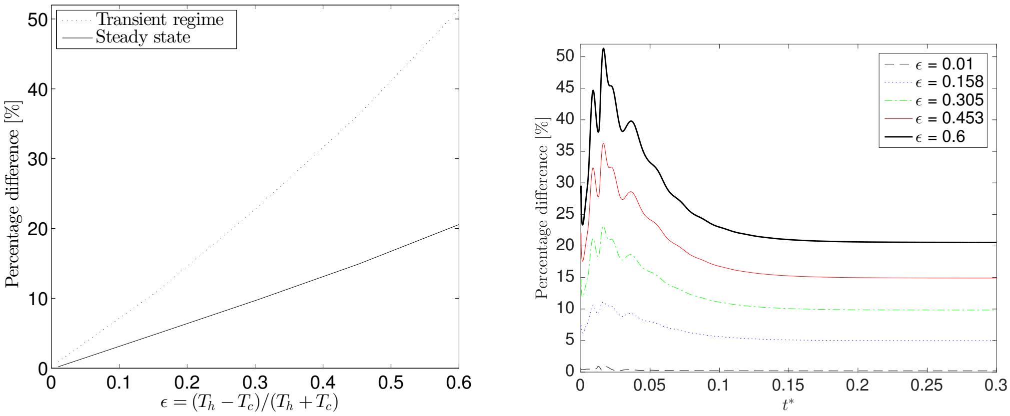

(a) (b)

Figure 16: Maximum difference on the local Nusselt number at the hot wall. (a) Maximum peak value versus ϵ. (b) Transient behavior for several temperature differences.

5. Conclusions

A successful numerical solution for the modeling of transient natural convection with a non-Boussinesq approximation for variable properties, large temperature differences and different Rayleigh numbers has been accomplished. The computational code has been validated against benchmark results for both steady state and transient regime, as well as the Boussinesq approximation and the non-Boussinesq approach with and without variable properties. The effects of considering variable viscosity and thermal conductivity in a non-Boussinesq formulation were studied for an unsteady problem. Additionally, a comparison between the Boussinesq and non-Boussinesq approaches for several temperature differences was presented.

We have shown that the effects of variable properties are especially relevant along the flow development period, amongst which the average Nusselt number, for instance, differs up to roughly 10% with respect to the constant properties case; in contrast, once in steady state regime, such a difference remains less important and is no longer oscillating, resulting around 2%. The average Nusselt number is greater for the variable properties case in the beginning of the transient natural convection, while it becomes smaller afterwards, once in the steady state regime.

Also, the temperature gradient aside of the hot wall is greater for the constant properties case. On the other hand, the thermal conductivity in the same region is larger when variable properties are considered. These two conditions determine the amount of heat flux delivered by the hot wall, which is considerably larger during the first instants of the transient period for the variable properties case. Indeed, this heat flux is larger for almost the whole transient period, in coherence with the Nusselt number behavior. Moreover, the validity of the Boussinesq approximation has been quantitatively brought to light: it resulted specially more restricted for the transient case, directly proportional to the temperature difference between hot and cold walls.

When comparing the total energy of the enclosure, the variable properties case prevails progressively along the whole transient period and remains so once in steady state. An explanation for that may come from the fact that when taking into account the conductivity variation with temperature, the heat fluxes vary in the direct nonlinear proportion - although inversely with the temperature gradient - leading to a resulting increase in the heat income and, at the same time, to a decrease in the heat outcome. Once again a coherence is found with the Nusselt number behavior, which enhances to conclude how important is the variable properties consideration for an accurate numerical modeling for the transient case.

The main application of this work is to support the choice of an specific formulation when modeling natural convection phenomena. To this end, the accuracy that each specific consideration entails has been evaluated and discussed.

Acknowledgments

The authors wish to thank CAPES and CNPq for the financial support.

References

[1] A. Baïri, Thermal design of tilted electronic assembly with active QFN16 package subjected to natural convection, International Communications in Heat and Mass Transfer 66 (2015) 240–245.

[2] H. Bhowmik, K. Tou, Experimental study of transient natural convection heat transfer from simulated electronic chips, Experimental Thermal and Fluid Science 29 (2005) 485–492.

[3] H. F. Öztop, P. Estellé, W. Yan, K. Al-Salem, J. Orfi, O. Mahian, A brief review of natural convection in enclosures under localized heating with and without nanofluids, International Communications in Heat and Mass Transfer 60 (2015) 37–44.

[4] J. O. Juárez, J. F. Hinojosa, J. P. Xamán, M. P. Tello, Numerical study of natural convection in an open cavity considering temperature-dependent fluid properties, International Journal of Thermal Sciences 50 (2011) 2184–2197.

[5] M. J. Suárez, C. Sanjuan, A. J. Gutiérrez, J. Pistono, E. Blanco, Energy evaluation of an horizontal open joint ventilated façade, Applied Thermal Engineering 37 (2012) 302–313.

[6] J. Xamán, J. Tun, G. Álvarez, Y. Chavez, F. Noh, Optimum ventilation based on the overall ventilation effectiveness for temperature distribution in ventilated cavities, International Journal of Thermal Sciences 48 (2009) 1574–1585.

[7] A. Baïri, Transient natural 2D convection in a cylindrical cavity with the upper face cooled by thermoelectric peltier effect following an exponential law, Applied Thermal Engineering 23 (2003) 431–447.

[8] D. Edwards, I. Catton, Prediction of heat transfer by natural convection in closed cylinders heated from below, International Journal of Heat and Mass Transfer 12 (1969) 23–30.

[9] D. Huang, S. Hsieh, Analysis of natural convection in a cylindrical enclosure, Numerical Heat Transfer, Part A: Applications 12 (1987) 121–135.

[10] T. Basak, S. Roy, C. Thirumalesha, Finite element analysis of natural convection in a triangular enclosure: effects of various thermal boundary conditions, Chemical Engineering Science 62 (2007) 2623–2640.

[11] V. A. Akinsete, T. Coleman, Heat transfer by steady laminar free convection in triangular enclosures, International Journal of Heat and Mass Transfer 25 (1982) 991–998.

[12] Y. E. Karyakin, Y. A. Sokovishin, O. Martynenko, Transient natural convection in triangular enclosures, International Journal of Heat and Mass Transfer 31 (1988) 1759–1766.

[13] Y. Shiina, K. Fujimura, T. Kunugi, N. Akino, Natural convection in a hemispherical enclosure heated from below, International Journal of Heat and Mass Transfer 37 (1994) 1605–1617.

[14] A. Baïri, J. G. de María, Numerical and experimental study of steady state free convection generated by constant heat flux in tilted hemispherical cavities, International Journal of Heat and Mass Transfer 66 (2013) 355–365.

[15] G. de Vahl Davis, I. Jones, Natural convection in a square cavity: a comparison exercise, International Journal for Numerical Methods in Fluids 3 (1983) 227–248.

[16] T. Saitoh, K. Hirose, High-accuracy bench mark solutions to natural convection in a square cavity, Computational Mechanics 4 (1989) 417–427.

[17] M. Hortmann, M. Perić, G. Scheuerer, Finite volume multigrid prediction of laminar natural convection: Benchmark solutions, International Journal for Numerical Methods in Fluids 11 (1990) 189–207.

[18] G. Huelsz, R. Rechtman, Heat transfer due to natural convection in an inclined square cavity using the lattice boltzmann equation method, International Journal of Thermal Sciences 65 (2013) 111–119.

[19] M. Leal, J. Pérez-Guerrero, R. Cotta, Natural convection inside two-dimensional cavities: the integral transform method, Communications in Numerical Methods in Engineering 15 (1999) 113–125.

[20] A. Baïri, E. Zarco-Pernia, J.-M. G. De María, A review on natural convection in enclosures for engineering applications. the particular case of the parallelogrammic diode cavity, Applied Thermal Engineering 63 (2014) 304–322.

[21] A. K. Hussein, M. M. AWAD, L. Kolsi, F. Fathinia, I. Adegun, A comprehensive review of transient natural convection flow in enclosures, Journal of Basic and Applied Scientific Research 4 (2014) 17–27.

[22] J. Patterson, J. Imberger, Unsteady natural convection in a rectangular cavity, Journal of Fluid Mechanics 100 (1980) 65–86.

[23] J. M. Hyun, J. W. Lee, Numerical solutions for transient natural convection in a square cavity with different sidewall temperatures, International Journal of Heat and Fluid Flow 10 (1989) 146–151.

[24] B. Krishna Satya Sai, K. Seetharamu, P. Aswatha Narayana, Solution of transient laminar natural convection in a square cavity by an explicit finite element scheme, Numerical Heat Transfer 25 (1994) 593–609.

[25] M. A. Christon, P. M. Gresho, S. B. Sutton, Computational predictability of time-dependent natural convection flows in enclosures (including a benchmark solution), International Journal for Numerical Methods in Fluids 40 (2002) 953–980.

[26] J. Samanes, J. García-Barberena, F. Zaversky, Modeling solar cavity receivers: a review and comparison of natural convection heat loss correlations, Energy Procedia 69 (2015) 543–552.

[27] P. Le Quéré, C. Weisman, H. Paillère, J. Vierendeels, E. Dick, R. Becker, M. Braack, J. Locke, Modelling of natural convection flows with large temperature differences: a benchmark problem for low mach number solvers. part 1. reference solutions, ESAIM: Mathematical Modelling and Numerical Analysis 39 (2005) 609–616.

[28] D. D. Gray, A. Giorgini, The validity of the boussinesq approximation for liquids and gases, International Journal of Heat and Mass Transfer 19 (1976) 545–551.

[29] L. Spradley, S. Churchill, Pressure-and buoyancy-driven thermal convection in a rectangular enclosure, Journal of Fluid Mechanics 70 (1975) 705–720.

[30] Z. Zhong, K. Yang, J. Lloyd, Variable property effects in laminar natural convection in a square enclosure, Journal of Heat Transfer 107 (1985) 133–138.

[31] S. Sehyun, Y. I. Cho, W. K. Gringrich, W. Shyy, Numerical study of laminar heat transfer with temperature dependent fluid viscosity in a 2:1 rectangular duct, International Journal of Heat and Mass Transfer 36 (1993) 4365–4373.

[32] C. Xie, J. Hartnett, Influence of variable viscosity of mineral oil on laminar heat transfer in a 2:1 rectangular duct, International Journal of Heat and Mass Transfer 35 (1992) 641–648.

[33] M. Leal, H. Machado, R. Cotta, Integral transform solutions of transient natural convection in enclosures with variable fluid properties, International Journal of Heat and Mass Transfer 43 (2000) 3977–3990.

[34] H. Sun, G. Lauriat, D. Sun, W. Tao, Transient double-diffusive convection in an enclosure with large density variations, International Journal of Heat and Mass Transfer 53 (2010) 615–625.

[35] L. Quéré, Accurate solutions to the square differentially heated cavity at high rayleigh number, Computers & Fluids 20 (1991) 2941.

[36] E. W. Lemmon, R. T. Jacobsen, S. G. Penoncello, D. G. Friend, Thermodynamic properties of air and mixtures of nitrogen, argon, and oxygen from 60 to 2000 k at pressures to 2000 mpa, Journal of physical and chemical reference data 29 (3) (2000) 331–385.

[37] S. Paolucci, Filtering of sound from the navier-stokes equations, Sandia National Laboratories Livermore.

[38] H. Paillere, C. Viozat, A. Kumbaro, I. Toumi, Comparison of low mach number models for natural convection problems, Heat and mass transfer 36 (2000) 567–573.

[39] S. Patankar, Numerical heat transfer and fluid flow, CRC Press, 1980.

[40] H. K. Versteeg, W. Malalasekera, An introduction to computational fluid dynamics: the finite volume method, Pearson Education, 2007.

[41] F. H. Harlow, J. E. Welch, Numerical calculation of time-dependent viscous incompressible flow of fluid with free surface, The Physics of Fluids 8 (1965) 2182.

[42] S. V. Patankar, D. B. Spalding, A calculation procedure for heat, mass and momentum transfer in three-dimensional parabolic flows, International journal of heat and mass transfer 15 (10) (1972) 1787–1806.

[43] R. Becker, M. Braack, R. Rannacher, Numerical simulation of laminar flames at low Mach number by adaptive finite elements, Taylor & Francis, 1999.

[44] F. U. Guide, Finite element analysis toolbox, British Energy, Gloucester, UK.

[45] R. Becker, M. Braack, Solution of a stationary benchmark problem for natural convection with large temperature difference, International journal of thermal sciences 41 (5) (2002) 428–439.

[46] J. Vierendeels, K. Riemslagh, E. Dick, A multigrid semi-implicit line-method for viscous incompressible and low-mach-number flows on high aspect ratio grids, Journal of Computational Physics 154 (2) (1999) 310–341.

[47] P. Le Quéré, R. Masson, P. Perrot, A chebyshev collocation algorithm for 2d non-boussinesq convection, Journal of computational physics 103 (2) (1992) 320–335.

[48] E. Graham, Numerical simulation of two-dimensional compressible convection, Journal of Fluid Mechanics 70 (1975) 689–703.

Appendix E

Numerical investigation of heat transfer by natural convection and radiation in a cavity with participating media

Numerical investigation of heat transfer by natural convection and radiation in a cavity with participating media

C.U. Mendoza, cristian.uriel@fem.unicamp.br[1]
C.T Salinas, csalina@fem.unicamp.br[1]
J.M. Armengol, jan.mateu.armengol@gmail.com[1]
R. Beicker, rbeicker@gmail.com[1]
R.G. Santos, roger7@fem.unicamp.br[1]

[1]UNICAMP

Abstract: *This paper deals with the numerical solution of combined heat transfer by radiation and natural convection in a square cavity under normal room conditions, filled with an absorbing-emitting and isotropic scattering medium. The finite volume method (FVM) has been adopted to solve the governing equations of natural convection. In turn, the discrete ordinates method (DOM) is applied to solve the radiative transfer equation (RTE), using a Tn6 angular quadrature. Natural convection and radiative transfer equations are solved simultaneously. The numerical model is validated by comparison with results taken from literature. In this work, Nusselt number and temperature and velocity fields are numerically studied for scattering albedos between* $0.0 - 1.0$ *ranging the Rayleigh number and the optical thickness. The results show that the effects of radiation are greater when the Rayleigh number increases. Similarly, it is shown that the influence of scattering albedo is stronger for cavities with higher Rayleigh numbers and optical thicknesses.*

Keywords: *Numerical Simulation, Natural Convection, Radiative Heat Transfer, Finite Volumes, Discrete Ordinates Method.*

1. NOMENCLATURE

c_p	Specific heat capacity, $J \cdot kg^{-1} \cdot K^{-1}$	t	Time, s
g	gravity, g = 9.81 ms^{-2}	T	Temperature, K
H	Cavity height and width, m	u	Horizontal velocity, $m \cdot s^{-1}$
I	Radiative intensity $W\ m^{-2}\ sr^{-1}$	v	Vertical velocity, $m \cdot s^{-1}$
m	Angular direction	V	Volume, m^3
M	Number of total angular directions	W	Quadrature weight of vector director
n	Director vector of area	x	Horizontal coordinate, m
Nu	Nusselt number	y	Vertical coordinate, m
$\bar{P}$	Thermodynamic average pressure, Pa	**Greek symbols**	
Pl	Plank number	α	Thermal diffusivity
Pr	Prandt number	$\bar{\beta}$	Thermal expansion coefficient, K^{-1}
q	Heat flux, $W\ m^{-2}$	β	Extinction coefficient, m^{-1}
r	Position vector , m	$\bar{\epsilon}$	Non-dimenional temperature difference
R	Gas constant for air, 287 $J \cdot (kg \cdot K)^{-1}$		parameter, $\bar{\epsilon} = (T_h - T_c)/(T_h + T_c)$
Ra	Rayleigh number	ε	Surface emissivity

κ	Absorption coefficient, m^{-1}
λ	Thermal conductivity, $W \cdot m^{-1} \cdot K^{-1}$
μ	Dynamic viscosity, $Pa \cdot s$
$\bar{\mu}$	x- projection of the director vector
Ω	Director vector
ρ	Density, $kg \cdot m^{-3}$
σ	Scattering coefficient, m^{-1}
$\bar{\sigma}$	Stephan-Boltzman constant
τ	Optical thickness
$\bar{v}$	Kinematic viscosity, $m^2 \cdot s^{-1}$
ω	Scattering albedo, $m^2 \cdot s^{-1}$
$\bar{\omega}$	Intensity interpolation scheme constant
Superscripts	
$*$	Dimensionless variable
m	m discrete direction
$'$	Incident direction
Subscripts	
b	Black body
c	Cold wall
Cv	Convectivet
E	East
h	Hot wall
N	North
o	Initial condition
P	Node
ref	Reference value
Rd	Radiative

2. INTRODUCTION

The phenomenon of natural convection is essential for the functioning of several engineering applications, such as double-glazed windows, solar collectors, cooling devices for electronic gears, HVAC (heating, ventilation and air-conditioning) systems, crystal growth in liquids, and fire spreading. Thus, many works about natural convection are performed. Among many academic studies, natural convection in rectangular cavities filled with air has proved to be an excellent vehicle in light of both numerical and empirical analyses (Ampofo and Karayiannis (2003); Tian and Karayiannis (2000); Salat *et al.* (2004); Betts and Bokhari (2000); Yin *et al.* (1978)).

A benchmark study of numerical solutions for natural convection in a two-dimensional closed square cavity filled with air was done by de Vahl Davis and Jones (1983). They worked on this physical problem by matching the second-order finite-differences method with the Richardson extrapolation scheme. In his work, Churchill (1983) suggested an experimental approach - formulations and graphics - to determine the Nusselt number (Nu) at distinct Rayleigh numbers and situations, according to some empirical and numerical results. Over the last few years, owing to the development of algorithms more efficient and computers with high processing rates, solutions of the 2-D and 3-D laminar equations have been solved for values of Ra in wide ranges, as we can see in the works of Upson *et al.* (1980) and Saitoh and Hirose (1989).

Many papers that combine radiation and natural convection in closed rectangular cavity with air can be found in the literature (Sharma *et al.* (2007); Velusamy *et al.* (2001); Akiyama and Chong (1997); Behnia *et al.* (1990)). For example, Akiyama and Chong (1997) studied the relationship between natural convection and radiation in a square cavity filled with air. Their results have shown that the surface radiation changes considerably the temperature distribution and the flow templates, particularly at uppermost Ra. So, the radiative heat transfer represent a high percentage of the overall heat flux. Furthermore, this part of heat flux improves with the increment of fluid emissivity.

However, works which analyze the phenomena of natural convection and radiation in cavity filled with air considering participating media are less common, given the high quantity of computational resources required to process it (Colomer *et al.* (2004); Fusegi and Farouk (1989); Fiveland (1988)). Tan and Howell (1991) studied combined radiation and natural convection in emitting, absorbing, and isotropically scattering square cavities. By means of the product integration method, the precise formulation for radiation was established and discretized (Tan (1989b)). The non-linear successive-over-relaxation iterating scheme for associated radiation and convection-conduction heat transfer problems was also applied (Tan (1989a)). In 2011, Lari *et al.* (2011) conducted a study on this specific topic considering the Boussinesq approximation, steady state, and absorbing-emitting medium with gray gases. The objective of her work was to investigate the effect of radiation on total heat transfer in a square under standard conditions combined with a low temperature difference. Recently, Moufekkir *et al.* (2012) used the numerical approach to solve the natural convection and volumetric radiation in an isotropic scattering medium within a heated square cavity problem using a different version of the thermal lattice Boltzmann method. In his paper, the finite difference method was combined with the multiple relaxation time lattice Boltzmann method to work out the mass conservation, the Navier-Stokes and the energy equations. In turn, the discrete ordinates method was applied to resolve the radiative transfer equation. Done it, he studied the influence of some important parameters over the heat transfer (for example, scattering albedo, Rayleigh number and Planck number).

The present work determines the overall averaged Nusselt number, as well as, the natural convection and the radiation averaged Nusselt numbers in the presence of a low temperature difference. The problem of the square enclosure, differentially heated side walls, insulated top and bottom sides, and filled with air - participating medium and grey gas - is solved for some scattering albedos ranging the Rayleigh number and the optical thickness. The Boussinesq approach is used even as in the previously cited works. The discrete ordinates method was also applied to deal with the radiative transfer equation. It was used the assumption of constant properties - thermal conductivity, thermal diffusivity, density, dynamic and cinematic viscosity. As far as we known, there is not any published work that shows how the radiation contribution varies for the total heat transfer when ranging the scaterring albedo, the Rayleigh number and the optical thickness in an incompressible formulation only using the finite volume method to calculate the mass conservation, the Navier-Stokes and the energy equations.

3. MATHEMATICAL AND PHYSICAL MODEL

The case of study of the present work is a square cavity filled with an absorbing, emitting, and isotropic scattering gray medium whose horizontal walls are considered adiabatic and the vertical walls have a fixed temperature. The motion of fluid initially static is induced by a temperature difference between the vertical walls, setting the right and left walls at T_c and T_h respectively, as shown in Fig. 1. All walls are considered black and diffusely reflective.

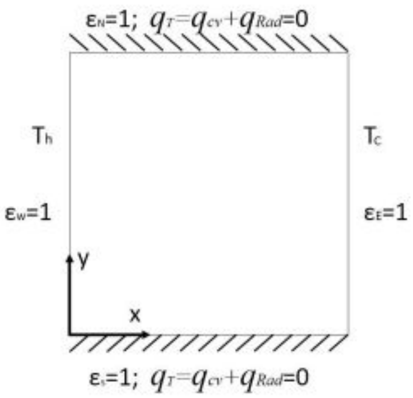

Figure 1: **Skecth of the physical model.**

The governing equations for two-dimensional flow, using the Boussinesq approximation, corresponding to mass conservation, transport of momentum in both directions and transport of energy are, respectively :

$$\frac{\partial \rho}{\partial t}+\frac{\partial(\rho u)}{\partial x}+\frac{\partial(\rho v)}{\partial y}=0, \tag{1}$$

$$\frac{\partial(\rho u)}{\partial t}+\frac{\partial(\rho u\cdot u)}{\partial x}+\frac{\partial(\rho v\cdot u)}{\partial y}=-\frac{\partial P}{\partial x}+\frac{\partial}{\partial x}\left(\mu\frac{\partial u}{\partial x}\right)+\frac{\partial}{\partial y}\left(\mu\frac{\partial u}{\partial y}\right), \tag{2}$$

$$\frac{\partial(\rho v)}{\partial t}+\frac{\partial(\rho u\cdot v)}{\partial x}+\frac{\partial(\rho v\cdot v)}{\partial y}=-\frac{\partial P}{\partial y}+\frac{\partial}{\partial x}\left(\mu\frac{\partial v}{\partial x}\right)+\frac{\partial}{\partial y}\left(\mu\frac{\partial v}{\partial y}\right)+\rho_0\vec{g}\bar{\beta}(T-T_0), \tag{3}$$

$$\frac{\partial(\rho T)}{\partial t}+\frac{\partial(\rho u\cdot T)}{\partial x}+\frac{\partial(\rho v\cdot T)}{\partial y}=\frac{\partial}{\partial x}\left(\frac{\lambda}{c_p}\frac{\partial T}{\partial x}\right)+\frac{\partial}{\partial y}\left(\frac{\lambda}{c_p}\frac{\partial T}{\partial y}\right)-\frac{1}{c_p}\nabla q_{Rd}. \tag{4}$$

The term $\frac{1}{c_p}\nabla q_{Rd}$ in Eq. (4) denotes the divergence of the radiative flux which can be calculated with the radiative intensity field by the expression:

$$\nabla q_{Rd} = \kappa \left(4\pi I_b(r) - \int_{4\pi} I(r,\Omega) d\Omega \right). \tag{5}$$

To obtain the intensity field to compute the Eq. (5) is necessary to solve the radiative transfer equation (RTE), which for an absorbing, emitting and isotropic scattering gray medium is determined by:

$$(\Omega\nabla)I(r,\Omega) = -\beta I(r,\Omega) + \kappa I_b(r) - \frac{\sigma}{4\pi}\int_{4\pi} I(r,\Omega')d\Omega'. \tag{6}$$

In order to generalize, the dimensionless parameters used are:

$$T^* = \frac{T - T_c}{T_h - T_c}, \quad x^* = \frac{x}{H}, \quad y^* = \frac{y}{H}, \quad u^* = \frac{uH}{\alpha_o}, \quad \text{and} \quad v^* = \frac{vH}{\alpha_o}. \tag{7}$$

The dimensionless temperature difference parameter, Plank, Prandt and Rayleigh numbers are defined as:

$$\bar{\epsilon} = \frac{T_h - T_c}{T_h + T_c}, \quad Pl = \frac{\lambda_{ref}}{4\sigma_B T_{ref}^3 H}, \quad Pr = \frac{c_p \mu_{ref}}{\lambda_{ref}}, \quad \text{and} \quad Ra = \frac{g\bar{\beta}(T_h - T_c)H^3}{\upsilon_{\bar{r}ef}\alpha_{ref}}. \tag{8}$$

where T_{ref} is a reference temperature defined as $T_{ref} = (T_h + T_c)/2$; and λ_{ref}, α_{ref}, ρ_{ref}, μ_{ref} and υ_{ref} are the thermal conductivity, thermal diffusivity, density, dynamic and cinematic viscosity evaluated at T_{ref}, respectively, which are considered spatially constants. For that, the dynamic viscosity and thermal conductivity are calculated using the expressions as follows called Sutherland's law:

$$\mu(T) = \mu' \left(\frac{T}{T'}\right)^{3/2} \frac{T' + C}{T + C} \tag{9}$$

$$\lambda(T) = \mu(T)\frac{\gamma R}{(1-\gamma)Pr} \tag{10}$$

At the present work, the used values are $\mu' = 1.68\text{x}10^{-5} Kg/ms$, $T' = 273K$, $C = 110{,}5\ Kg/msK^{1/2}$, $\gamma = 1.4$, $R = 287 J/KgK$ and $Pr = 0.71$.

The heat transfer through the cavity is characterized by the Nusselt number, which involves the convective and radiative heat transfer effects. The local convective and radiative Nusselt numbers at the hot wall are determined as follows:

$$Nu(y)_{Cv}\Bigg|_{x=0} = \frac{H}{(T_h - T_c)}\frac{\partial T}{\partial x}\Bigg|_{x=0} \quad \text{and} \quad Nu(y)_{Rd}\Bigg|_{x=0} = \frac{q_{Rd}\, H}{\lambda_{ref}(T_h - T_c)}. \tag{11}$$

The average Nusselt numbers for convective and radiative effects are expressed as:

$$\overline{Nu}_{Cv}\Bigg|_{x=0} = \frac{1}{H}\int_0^H Nu(y)_{Cv}\Bigg|_{x=0} dy. \quad \text{and} \quad \overline{Nu}_{Rd}\Bigg|_{x=0} = \frac{1}{H}\int_0^H Nu(y)_{Rd}\Bigg|_{x=0} dy. \tag{12}$$

The overall averaged Nusselt number is determinated by:

$$Nu(y)_T\Bigg|_{x=0} = Nu(y)_{Cv}\Bigg|_{x=0} + Nu(y)_{Rd}\Bigg|_{x=0} \quad \text{and} \quad \overline{Nu}_T\Bigg|_{x=0} = \overline{Nu}_{Cv}\Bigg|_{x=0} + \overline{Nu}_{Rd}\Bigg|_{x=0}. \tag{13}$$

3.1 Boundary and initial conditions

The boundary conditions for the situation described in the Fig. 1 can be modeled as:

Left boundary **(**$x = 0$**;** $0 < y < H$**)** Isothermal, non-slip, impermeable and diffusively reflective black wall:

$$u = v = 0, \quad T_h = T_{ref}(1 + \bar{\epsilon}) \text{ and } \varepsilon_h = 1.0. \tag{14}$$

Right boundary **(**$x = H$**;** $0 < y < H$**)** Isothermal, non-slip, impermeable and diffusively reflective black wall:

$$u = v = 0 \quad T_c = T_{ref}(1 - \bar{\epsilon}) \text{ and } \varepsilon_c = 1.0. \tag{15}$$

Bottom ($y = 0$) and Top ($y = H$) boundaries. Adiabatic, non-slip, impermeable and diffusively reflective black wall:

$$u = v = 0, \quad q_{Cv} + q_{Rd} = 0 \text{ and } \varepsilon_s = \varepsilon_n = 1.0. \tag{16}$$

Initial conditions ($t = 0$). Stationary flow at spatially uniform temperature T_0 and pressure P_0, wherein fluid properties are computed at T_0:

$$u_0 = v_0 = 0,\ T_0 = T_{ref},\ P_0 = 101325\ Pa,\ \rho_0 = \frac{P_0}{R\,T_0},\ \mu_0 = \mu(T_0) \text{ and } \lambda_0 = \lambda(T_0). \tag{17}$$

For opaque walls that emit and reflect diffusely, the boundary conditions for RTE (Eq. 6) are calculated by:

$$I(r_w, \Omega) = \varepsilon I_b(r_w) + \frac{(1-\varepsilon_w)}{\pi} \int_{\vec{n}\cdot\Omega'<0} I(r_w, \Omega')\, |\vec{n}\cdot\Omega'|\, d\Omega'. \tag{18}$$

4. METHODOLOGY FOR THE NUMERICAL SOLUTION

In order to solve the Naver-Stokes, mass conservation and energy equations (Eq.(1)-(4)), the finite volume method (FVM) is used for their discretization applying a false transient formulation and using a fully implicit scheme for time discretization (Patankar (1980), and Versteeg and Malalasekera (2007)). The diffusive term is approximated by using central difference scheme while the hybrid scheme is used for the convective term. Due to the equations of conservation of mass and momentum are strongly coupled, the algorithm SIMPLE is implemented with a non-uniform staggered marker-and-cell (MAC) mesh, where all scalar quantities are calculated on the main grid while the components of the velocity are associated to the staggered grid. The properties C_p, ρ, λ and μ are assumed spatially constants and are evaluated at the reference temperature.

To obtain the source term in Eq.4, corresponding to the radiative flux, the intensity field is solved by RTE, for which the angular discretization is done by the discrete ordinates method (DOM) as explains Fiveland (1984) using a Tn6 quadrature as calculated in Thurgood *et al.* (1995). The FVM is used to make the spatial discretization. Thus, the intensity of the point P in the m direction can be described as a function of the intensities at the faces of the control volume as:

$$\bar{\mu_m}(A_E I_E^m - A_W I_W^m) + \bar{\xi_m}(A_N I_N^m - A_S I_S^m) = -\beta I_p^m V_p + \kappa I_{b,p}^m V_p + \left(\frac{\sigma}{4\pi}\sum_{k=1}^{M} W_k I^k\right) V_p. \tag{19}$$

The number of variables in the Eq. (19) are reduced using the linear correlation:

$$I_p^m = \bar{\omega} I_E^m + (1-\bar{\omega}) I_W^m = \bar{\omega} I_S^m + (1-\bar{\omega}) I_N^m. \tag{20}$$

where $\bar{\omega}$ is a constant between $0.0 - 1.0$. Note that $\bar{\omega}$ = 1.0 and $\bar{\omega}$ = 0.5 denote step and diamond scheme respectively. From Eq. (20) and Eq. (19), it is obtained the numerical expression used in this work:

$$I_p^m = \frac{|\bar{\mu}|\triangle y I_w^m + |\bar{\xi}|\triangle x I_s^m + \bar{\omega}\kappa I_{b,p} V_p + \bar{\omega}\left(\frac{\sigma}{4\pi}\sum\limits_{k=1}^{M} W_k I^k\right) V_p}{|\mu|\triangle y + |\xi|\triangle x + \bar{\omega}\beta V_p}. \tag{21}$$

To determine the effect of the scattering on the flow, it is introduced the single scattering albedo defined as:

$$\omega = \frac{\sigma}{\sigma+\kappa} = \frac{\sigma}{\bar{\beta}}. \tag{22}$$

Note that for a non-scattering medium, ω=0.0, while ω=1.0 in a non-absorbing medium ($\kappa = 0.0$).

Similarly, the DOM is used in the boundary conditions for the RTE (Eq.18). The expression to calculate the source term in the energy equation (Eq.5) at node P which is associated to one control volume of the domain is given by the expressions used at the model of numerical implementation:

$$I_w^m = \varepsilon_w I_{b,w} + \frac{(1-\varepsilon_w)}{\pi}\sum_{k=1}^{M'} W_{k'} I_w^{k'} \left|\Omega_k'\right|. \tag{23}$$

$$\nabla q_{Rd} = \kappa \left(4\pi I_{b,p} - \sum_{k=1}^{M} W_k I_p^k\right). \tag{24}$$

The set of algebraic equations generated by the discretization of the governing equation of the flow is solved by an alternating direction implicit (ADI) iterative method. Additionally, under-relaxation parameters have been used to minimize the number of iterations required to reach the convergence criteria.

4.1 Grid sensivity and code verifications

The accuracy of the numerical results has been verified through numerous tests based on grid size covering Rayleigh numbers between $10^3 - 10^7$. The Table 1 summarizes the results for $Ra = 10^6$ and $\tau = 1.0$. The numerical analysis revealed that higher Rayleigh numbers demand refiner meshes. A non-uniform mesh of 161 x 161 nodes is selected, for which a maximum deviation of 0.1 % is obtained for the average Nusselt number.

Table 1: **Radiative and total averaged Nusselt number for $Ra = 10^6$, $Pr = 0.717$ and $\tau = 1.0$.**

		61x61	81x81	101x101	121x121	141x141	161x161	181x181	201x201
$\tau = 1.0$	Nu_{Rd}	9.577	9.563	9.557	9.554	9.553	9.528	9.525	9.522
	Nu_T	16.947	16.920	16.910	16.906	16.904	16.864	16.861	16.857

In order to verify the results obtained from the numerical model considering the radiative heat transfer effects, the Table 2 shows a comparison with values of average Nusselt number at hot wall obtained by Lari *et al.* (2011) for two different optical thicknesses and Rayleigh numbers with values of Pr=0.717, scattering albedo $\omega = 0.0$, $T_h = 310$ K, and $T_c = 290$ K. It shows a maximum deviation of 1.625%. The Figure 2 corroborates the results of the present work showing a good compatibility with the streamlines and the isotherms.

Table 2: **Comparison of the present work with the results of Lari *et al.***

		$Ra = 10^5$	$Ra = 10^6$
$\tau = 1.0$	Lari *et al.*	8.367	17.086
	Present work	8.231 (1.625 %)	16.864 (1.300 %)
$\tau = 5.0$	Lari *et al.*	6.811	14.514
	Present work	6.732 (1.160 %)	14.439 (0.517 %)

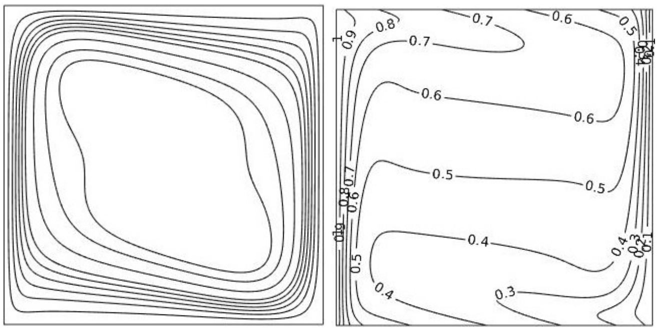

(a) (b)

Figure 2: $Ra = 10^6, Th = 310K, Tc = 290K, \tau = 1.0$ **(a) Streamlines. (b) Dimensionless Isotherms lines.**

Similarly, the Table 3 shows a comparison with results taken from Moufekkir *et al.* (2012) and Yucel *et al.* (1989) for a cavity with $Ra = 5x10^6$, $Pr = 0.71$, $Pl = 0.2$, scattering albedo $\omega = 0$ and two different optical thicknesses. The maximum deviation showed is 1.11%. It can be observed a good agreement of the results of this work with values from the literature.

Table 3: **Comparison of the present work with the results of Moufekkir *et al.* and Yucel *et al.***

		Nu_Rd	Nu_T
	Yucel *et al.*	31.550 (0.41 %)	39.210 (0.68 %)
$\tau = 1.0$	Moufekkir *et al.*	31.108 (1.00 %)	38.725 (0.57 %)
	Present work	31.421	38.945
	Yucel *et al.*	23.640 (1.11 %)	31.760 (0.43 %)
$\tau = 5.0$	Moufekkir *et al.*	23.801 (0.57 %)	31.778 (0.37 %)
	Present work	23.936	31.896

5. Results

For the purpose of keeping the flow in the laminar regime, all tests were made with a Rayleigh number between 10^4- $- 10^7$ as well as the difference of temperature between vertical walls was established at low enough value to guarantee that all considerations in the mathematical model are appropriated. To evaluate the effects of the scattering albedo on the velocity and temperature fields, tests with values between $0.0 - 1.0$ were made too. The Table 4 shows the average Nusselt number at the hot wall for distinct scattering albedos, two optical thicknesses and two Rayleigh numbers in a cavity filled with an absorbing, emitting, and isotropic scattering gray medium in which Pr=0.717 and the temperatures at the left and right walls are $T_h = 310$K and $T_c = 290$K respectively.

Table 4: **Radiative, convective and total average Nusselt number for different values of scattering albedo.**

		$Ra = 10^4$			$Ra = 10^7$		
		Nu_{Cv}	Nu_{Rd}	Nu_T	Nu_{Cv}	Nu_{Rd}	Nu_T
ω=0.0	τ=1.0	2.2055	1.7892	3.9947	13.1853	21.0650	34.2510
	τ=5.0	2.2248	0.8334	3.0582	13.7687	16.5181	30.2868
ω=0.5	τ=1.0	2.1722	1.8079	3.9800	13.3762	20.1321	33.5083
	τ=5.0	2.1310	0.8484	2.9794	13.2159	14.6531	27.8690
ω=0.7	τ=1.0	2.1617	1.8142	3.9759	13.5570	19.6613	33.2183
	τ=5.0	2.0956	0.8477	2.9433	13.1439	13.2263	26.3702
ω=1.0	τ=1.0	2.1533	1.8195	3.9728	14.1118	18.7775	32.8892
	τ=5.0	2.1089	0.7768	2.8857	14.2281	8.3179	22.5460
Pure convection		2.2409	0.0	2.2409	16.5924	0.0	16.5924

Table 4 shows that, for the studied cases, the influence of scattering albedo is stronger for a larger Rayleigh number and higher values of optical thickness. When scattering albedo increases, keeping constant the others parameters of the flow, the heat transfer decreases. It should be noted that these effects are more pronounced in the radiative heat transfer, while the convective effects suffer lower variations. For the case of pure convection, the variation of scattering albedo has not any effect on the flow, because this parameter is directly related to the conditions of the radiative heat transfer.

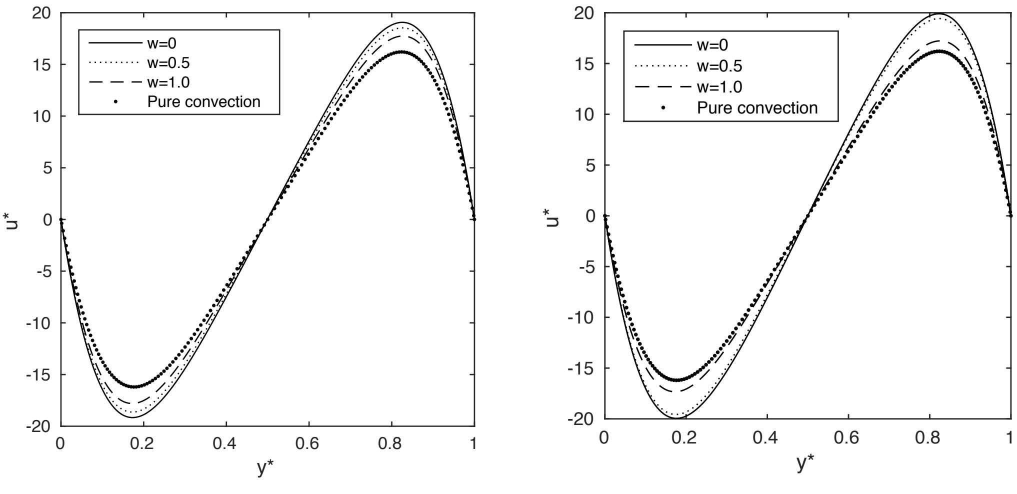

(a)

(b)

Figure 3: **Dimensionless horizontal velocity profile at the mid-plane for** $Ra = 10^4$. (a) $\tau = 1.0$ (b) $\tau = 5.0$

The Figures (3) and (4) show the dimensionless horizontal velocity profile at the mid-plane of the cavity for $Ra = 10^4$ and $Ra = 10^7$ respectively. They reveal that when the scattering albedo increases, the dimensionless horizontal velocity profile at the mid-plane declines. Can be observed that , these effect is stronger for a higher Rayleigh number and a lower optical thickness.

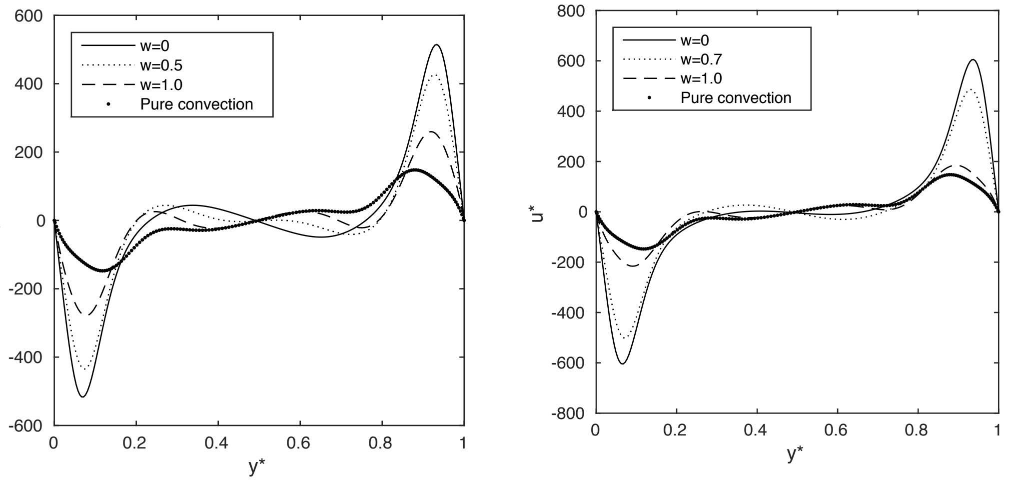

(a) (b)

Figure 4: **Dimensionless horizontal velocity profile at the mid-plane for** $Ra = 10^7$. (a) $\tau = 1.0$ (b) $\tau = 5.0$

6. CONCLUSIONS

The heat transfer by natural convection and radiation in a cavity under normal room conditions filled with an absorbing-emitting and isotropic scattering gray medium has been studied at present work. The equations of mass conservation, momentum and transport of energy have been solved by the FVM using the SIMPLE algorithm. The RTE has been discretized angularly by the DOM and spatially by the FVM to evaluate the source term in the equation of energy associated with the radiative heat transfer. The code of the present work has been verified by comparison with results of the bibliography. The heat transfer and the characteristic of the fluid were analyzed for a variation of scattering albedo in a range from 0.0 to 1.0 at different Rayleigh numbers and optical thicknesses. The next conclusions have been obtained from this study:

- For a more absorbing medium (a lower scattering albedo) flowing with the same characteristics, the heat transfer through the cavity is greater.
- The magnitudes of the velocity in a more scattering medium (a higher scattering albedo) are lower.
- The effects of scattering albedo are stronger for a flow with a higher Rayleigh number and a medium with lower optical thickness.

7. ACKNOWLEDGEMENTS

The authors wish to thanks CAPES and FAPESP for the financial support.

8. REFERENCES

Akiyama, M. and Chong, Q., 1997. “Numerical analysis of natural convection with surface radiation in a square enclosure”. *Numerical Heat Transfer, Part A Applications*, Vol. 32, No. 4, pp. 419–433.

Ampofo, F. and Karayiannis, T., 2003. “Experimental benchmark data for turbulent natural convection in an air filled square cavity”. *International Journal of Heat and Mass Transfer*, Vol. 46, No. 19, pp. 3551–3572.

Behnia, M., Reizes, J. and de Vahl Davis, G., 1990. “Combined radiation and natural convection in a rectangular cavity with a transparent wall and containing a non-participating fluid”. *International Journal for Numerical Methods in Fluids*, Vol. 10, No. 3, pp. 305–325.

Betts, P. and Bokhari, I., 2000. “Experiments on turbulent natural convection in an enclosed tall cavity”. *International Journal of Heat and Fluid Flow*, Vol. 21, No. 6, pp. 675–683.

Churchill, S., 1983. “Free convection in layers and enclosures”. *Heat exchanger design handbook*, Vol. 2, No. 8.

Colomer, G., Costa, M., Consul, R. and Oliva, A., 2004. “Three-dimensional numerical simulation of convection and radiation in a differentially heated cavity using the discrete ordinates method”. *International Journal of Heat and Mass Transfer*, Vol. 47, No. 2, pp. 257–269.

de Vahl Davis, G. and Jones, I., 1983. “Natural convection in a square cavity: a comparison exercise”. *International Journal for numerical methods in fluids*, Vol. 3, No. 3, pp. 227–248.

Fiveland, W., 1984. “Discrete-ordinates solution of the radiative transport equation for rectangular enclosures”. *Journal of Heat Transfer*, Vol. 106, pp. 699–706.

Fiveland, W., 1988. “Three-dimensional radiative heat-transfer solutions by the discrete-ordinates method”. *Journal of Thermophysics and Heat Transfer*, Vol. 2, No. 4, pp. 309–316.

Fusegi, T. and Farouk, B., 1989. “Laminar and turbulent natural convection-radiation interactions in a square enclosure filled with a nongray gas”. *Numerical Heat Transfer*, Vol. 15, No. 3, pp. 303–322.

Lari, K., Baneshi, S.A., Nassab, S.A.G., Komiya, A. and maruyama, S., 2011. “Combined heat transfer of radiation and natural convection in a square cavity containing participant gases”. *International journal of heat and mass transfer*, Vol. 54, pp. 5087–5099.

Moufekkir, F., MOussauoui, M.A., Mezrhad, A., Naji, H. and Lemonnier, D., 2012. “Numerical prediction of heat transfer by natural convection and radiation in an enclosure filled with an isotropic scattering medium”. *Journal of quantitative spectroscopy & radiative transfer*, Vol. 113, pp. 1689–1704.

Patankar, S., 1980. *Numerical heat transfer and fluid flow*. CRC Press.

Saitoh, T. and Hirose, K., 1989. “High-accuracy bench mark solutions to natural convection in a square cavity”. *Computational Mechanics*, Vol. 4, No. 6, pp. 417–427.

Salat, J., Xin, S., Joubert, P., Sergent, A., Penot, F. and Le Quere, P., 2004. “Experimental and numerical investigation of turbulent natural convection in a large air-filled cavity”. *International Journal of Heat and Fluid Flow*, Vol. 25, No. 5, pp. 824–832.

Sharma, A.K., Velusamy, K., Balaji, C. and Venkateshan, S., 2007. “Conjugate turbulent natural convection with surface radiation in air filled rectangular enclosures”. *International journal of heat and mass transfer*, Vol. 50, No. 3, pp. 625–639.

Tan, Z., 1989a. “Combined radiative and conductive heat transfer in two-dimensional emitting, absorbing and anisotropic scattering square media”. *International communications in heat and mass transfer*, Vol. 16, No. 3, pp. 391–401.

Tan, Z., 1989b. “Radiative heat transfer in multidimensional emitting, absorbing, and anisotropic scattering media—mathematical formulation and numerical method”. *Journal of heat transfer*, Vol. 111, No. 1, pp. 141–147.

Tan, Z. and Howell, J.R., 1991. “Combined radiation and natural convection in a two-dimensional participating square medium”. *International journal of heat and mass transfer*, Vol. 34, No. 3, pp. 785–793.

Thurgood, C.P., Pollard, A. and Becker, H.A., 1995. “The tn quadrature set for the discrete ordinates method.” *Journal of Heat Transfer*, Vol. 117, pp. 1068–1070.

Tian, Y. and Karayiannis, T., 2000. “Low turbulence natural convection in an air filled square cavity: part i: the thermal and fluid flow fields”. *International Journal of Heat and Mass Transfer*, Vol. 43, No. 6, pp. 849–866.

Upson, C., Gresho, P. and Lee, R., 1980. “Finite element simulations of thermally induced convection in an enclosed cavity”. Technical report, California Univ., Livermore (USA). Lawrence Livermore Lab.

Velusamy, K., Sundararajan, T. and Seetharamu, K., 2001. “Interaction effects between surface radiation and turbulent natural convection in square and rectangular enclosures”. *Journal of heat transfer*, Vol. 123, No. 6, pp. 1062–1070.

Versteeg, H.K. and Malalasekera, W., 2007. *An introduction to computational fluid dynamics: the finite volume method*. Pearson Education.

Wang, H., Xin, S. and Le Quéré, P., 2006. “Étude numérique du couplage de la convection naturelle avec le rayonnement de surfaces en cavité carrée remplie d’air”. *Comptes Rendus Mécanique*, Vol. 334, No. 1, pp. 48–57.

Yin, S., Wung, T. and Chen, K., 1978. “Natural convection in an air layer enclosed within rectangular cavities”. *International Journal of Heat and Mass Transfer*, Vol. 21, No. 3, pp. 307–315.

Yucel, A., Acharya, S. and Williams, M.L., 1989. “Natural convection and radiation in a square enclosure.” *Numer heat transfer*, Vol. A15, pp. 261–278.

9. RESPONSIBILITY NOTICE

The authors are the only responsible for the printed material included in this paper.

References

Abadi, S. N. R., A. Ahmadpour, S. Abadi, and J. P. Meyer (2017). Cfd-based shape optimization of steam turbine blade cascade in transonic two phase flows. *Applied Thermal Engineering 112*, 1575–1589. *(p. xviii)*

Abramovich, G. N. (1963). *The theory of turbulent jets.* M.I.T. Press. *(p. 74)*

Antonia, R., L. Browne, A. Chambers, and S. Rajagopalan (1983). Budget of the temperature variance in a turbulent plane jet. *International Journal of Heat and Mass Transfer 26*(1), 41–48. *(p. 85, 88, 153)*

Armengol, J., F. Bannwart, J. Xamán, and R. Santos (2017). Effects of variable air properties on transient natural convection for large temperature differences. *International Journal of Thermal Sciences 120*, 63–79. *(p.)*

Atoufi, A., M. Fathali, and B. Lessani (2015). Compressibility effects and turbulent kinetic energy exchange in temporal mixing layers. *Journal of Turbulence 16*(7), 676–703. *(p. 181, 183)*

Badinand, T. and T. Fransson (2001). Improvement of the finite volume method for coupled flow and radiation calculations by the use of two grids and rotational periodic interface. In *ICHMT DIGITAL LIBRARY ONLINE*. Begel House Inc. *(p. 48)*

Becker, R. and M. Braack (2002). Solution of a stationary benchmark problem for natural convection with large temperature difference. *International journal of thermal sciences 41*(5), 428–439. *(p. 33)*

Becker, R., M. Braack, and R. Rannacher (1999). *Numerical simulation of laminar flames at low Mach number by adaptive finite elements.* Taylor & Francis. *(p. 33)*

Berger, S., S. Richard, F. Duchaine, G. Staffelbach, and L. Gicquel (2016). On the sensitivity of a helicopter combustor wall temperature to convective and radiative thermal loads. *Applied Thermal Engineering 103*, 1450–1459. *(p. xx, 120, 121)*

Bogey, C. and C. Bailly (2009). Turbulence and energy budget in a self-preserving round jet: direct evaluation using large eddy simulation. *Journal of Fluid Mechanics 627*, 129–160. *(p. 74, 181)*

Bradbury, L. (1965). The structure of a self-preserving turbulent plane jet. *Journal of Fluid Mechanics 23*(01), 31–64. *(p. 74, 79, 80, 151)*

Browne, L., R. Antonia, S. Rajagopalan, and A. Chambers (1983). Interaction region of a two-dimensional turbulent plane jet in still air. In *Struc-*

ture of complex turbulent shear flow, pp. 411–419. Springer. *(p. 87, 88, 153)*

Burns, S. P. (1999). Turbulence radiation interaction modeling in hydrocarbon pool fire simulations. Technical report, Sandia National Labs., Albuquerque, NM (US); Sandia National Labs., Livermore, CA (US). *(p. 54)*

Castela, M., B. Fiorina, A. Coussement, O. Gicquel, N. Darabiha, and C. O. Laux (2016). Modelling the impact of non-equilibrium discharges on reactive mixtures for simulations of plasma-assisted ignition in turbulent flows. *Combustion and Flame 166*, 133–147. *(p. 83)*

Caudal, J. (2013). *Simulation numérique du reformage autothermique du méthane*. Ph. D. thesis, Ecole Centrale Paris. *(p. 6, 7)*

Chassaing, P., R. Antonia, F. Anselmet, L. Joly, and S. Sarkar (2013). *Variable density fluid turbulence*, Volume 69. Springer Science & Business Media. *(p. 81, 173, 181)*

Chen, C. J. and W. Rodi (1980). Vertical turbulent buoyant jets: a review of experimental data. *Nasa STI/Recon Technical Report A 80*, –. *(p. 85)*

Choi, Y.-H. and C. L. Merkle (1993). The application of preconditioning in viscous flows. *Journal of Computational Physics 105*(2), 207–223. *(p. 8)*

Coelho, P. (2004). Detailed numerical simulation of radiative transfer in a nonluminous turbulent jet diffusion flame. *Combustion and flame 136*(4), 481–492. *(p. xix, 120, 121)*

Coelho, P. J. (2007). Numerical simulation of the interaction between turbulence and radiation in reactive flows. *Progress in Energy and Combustion Science 33*(4), 311–383. *(p. xix, 98)*

Coelho, P. J. (2010). A general closure model for the time-averaged radiative transfer equation in turbulent flows. In *2010 14th International Heat Transfer Conference*, pp. 847–856. American Society of Mechanical Engineers. *(p. 53, 54)*

Coelho, P. J. (2012). Assessment of a presumed joint pdf for the simulation of turbulence–radiation interaction in turbulent reactive flows. *Applied Thermal Engineering 49*, 22–30. *(p. 53, 54)*

Coussement, A. (2012). *Direct numerical simulation and reduced chemical schemes for combustion of perfect and real gases*. Ph. D. thesis, PhD thesis, Ecole Centrale des Arts et Manufactures (ECP). *(p. 6, 7, 75)*

Coussement, A., O. Gicquel, J. Caudal, B. Fiorina, and G. Degrez (2012). Three-dimensional boundary conditions for numerical simulations of reactive compressible flows with complex thermochemistry. *Journal of computational physics 231*(17), 5571–5611. *(p. 10, 190)*

Coussement, A., O. Gicquel, and G. Degrez (2012). Large eddy simulation of a pulsed jet in cross-flow. *Journal of fluid mechanics 695*, 1–34. *(p. 186)*

da Silva, C. B., I. Malico, and P. J. Coelho (2009). Radiation statistics in homogeneous isotropic turbulence. *New Journal of Physics 11*(9), 093001. *(p. xix, 120, 121)*

Darmofal, D. L. and P. Schmid (1996). The importance of eigenvectors for local preconditioners of the euler equations. *Journal of Computational Physics 127*(2), 346–362. *(p. 8)*

Davies, A., J. Keffer, and W. Baines (1975). Spread of a heated plane turbulent jet. *The physics of fluids 18*(7), 770–775. *(p. 85, 88, 153)*

de Vahl Davis, G. and I. Jones (1983). Natural convection in a square cavity: a comparison exercise. *International Journal for Numerical Methods in Fluids 3*, 227–248. *(p. 30, 32, 33)*

Deo, R. C., J. Mi, and G. J. Nathan (2007). The influence of nozzle-exit geometric profile on statistical properties of a turbulent plane jet. *Experimental Thermal and Fluid Science 32*(2), 545–559. *(p. 61, 74)*

Deo, R. C., J. Mi, and G. J. Nathan (2008). The influence of reynolds number on a plane jet. *Physics of Fluids 20*(7), 075108. *(p. 74)*

Deshmukh, K., M. Modest, and D. Haworth (2008). Direct numerical simulation of turbulence–radiation interactions in a statistically one-dimensional nonpremixed system. *Journal of Quantitative spectroscopy and Radiative transfer 109*(14), 2391–2400. *(p. xx, 120, 121)*

Deshmukh, K. V. and D. C. Haworth (2009). Higher-order spherical harmonics to model radiation in direct numerical simulation of turbulent reacting flows. *Computational Thermal Sciences: An International Journal 1*(2), 1–24. *(p. xx)*

dos Santos, R. G., M. Lecanu, S. Ducruix, O. Gicquel, E. Iacona, and D. Veynante (2008). Coupled large eddy simulations of turbulent combustion and radiative heat transfer. *Combustion and Flame 152*(3), 387–400. *(p. xx)*

EC (2018). European comission long term strategy. `https://ec.europa.eu/clima/policies/strategies/2050_en`. Accessed: 16/02/2019. *(p. xv)*

Edwards, D. (1976). Molecular gas band radiation. In *Advances in heat transfer*, Volume 12, pp. 115–193. Elsevier. *(p. xx)*

EEA (2015). United nations framework convention on climate change. `https://europa.eu`. Accessed: 16/02/2019. *(p. xvi)*

EP (2018). European parlament. `http://www.europarl.europa.eu`. Accessed: 16/02/2019. *(p. xvi)*

Evans, K. F. (1998). The spherical harmonics discrete ordinate method for three-dimensional atmospheric radiative transfer. *Journal of the Atmospheric Sciences 55*(3), 429–446. *(p. 43)*

Faeth, G., J. Gore, and S.-M. Jeng (1987). Spectral and total radiation properties of turbulent carbon monoxide/air diffusion flames. *AIAA journal 25*(2), 339–345. *(p. xix)*

Fiveland, W. (1984). Discrete-ordinates solutions of the radiative transport equation for rectangular enclosures. *Journal of heat transfer 106*(4), 699–706. *(p. 43)*

Foysi, H., J. P. Mellado, and S. Sarkar (2010). Large-eddy simulation of variable-density round and plane jets. *International Journal of Heat and*

Fluid Flow 31(3), 307–314. *(p. 89, 114)*

Fraga, G., F. Centeno, A. Petry, and F. França (2017). Evaluation and optimization-based modification of a model for the mean radiative emission in a turbulent non-reactive flow. *International Journal of Heat and Mass Transfer 114*, 664–674. *(p. 144)*

Gaitonde, D. and M. Visbal (1999). Further development of a navier-stokes solution procedure based on higher-order formulas. In *37th Aerospace Sciences Meeting and Exhibit*, pp. 557. *(p. 6, 75, 83)*

Gamache, R. R., R. L. Hawkins, and L. S. Rothman (1990). Total internal partition sums in the temperature range 70–3000 k: atmospheric linear molecules. *Journal of molecular spectroscopy 142*(2), 205–219. *(p. 47)*

Garmann, D. and M. Visbal (2014). Dynamics of revolving wings for various aspect ratios. *Journal of Fluid Mechanics 748*, 932–956. *(p. 83)*

Garnier, E., N. Adams, and P. Sagaut (2009). *Large eddy simulation for compressible flows*. Springer Science & Business Media. *(p. 180)*

Ghosh, S. and R. Friedrich (2015). Effects of radiative heat transfer on the turbulence structure in inert and reacting mixing layers. *Physics of Fluids 27*(5), 055107. *(p. xx, 121, 135)*

Ghosh, S., R. Friedrich, M. Pfitzner, C. Stemmer, B. Cuenot, and M. El Hafi (2011). Effects of radiative heat transfer on the structure of turbulent supersonic channel flow. *Journal of Fluid Mechanics 677*, 417–444. *(p. xx, 120, 121)*

Goldschmidt, V. and M. Young (1975). Energy spectrum and turbulent scales in a plane air jet. *(p. 38, 78, 79, 148, 150)*

Goody, R. M. and Y. L. Yung (1995). *Atmospheric radiation: theoretical basis*. Oxford university press. *(p. 46)*

Gore, J., U. Ip, and Y. Sivathanu (1992). Coupled structure and radiation analysis of acetylene/air flames. *Journal of Heat Transfer 114*, 487–93. *(p. 53)*

Gruber, A., J. H. Chen, D. Valiev, and C. K. Law (2012). Direct numerical simulation of premixed flame boundary layer flashback in turbulent channel flow. *Journal of Fluid Mechanics 709*, 516–542. *(p. 83)*

Guide, F. U. (1997). Finite element analysis toolbox. *British Energy, Gloucester, UK*. *(p. 33)*

Gupta, A., D. Haworth, and M. Modest (2013). Turbulence-radiation interactions in large-eddy simulations of luminous and nonluminous nonpremixed flames. *Proceedings of the Combustion Institute 34*(1), 1281–1288. *(p. 120, 121)*

Gupta, A., M. F. Modest, and D. C. Haworth (2009). Large-eddy simulation of turbulence-radiation interactions in a turbulent planar channel flow. *Journal of Heat Transfer 131*(6), 061704. *(p. xx, 121, 144)*

Gutmark, E. and I. Wygnanski (1976). The planar turbulent jet. *Journal of Fluid Mechanics 73*(03), 465–495. *(p. 37, 38, 74, 78, 79, 148, 150)*

Harlow, F. H. and J. E. Welch (1965). Numerical calculation of time-dependent viscous incompressible flow of fluid with free surface. *The physics of fluids 8*(12), 2182–2189. *(p. 26)*

Hedstrom, G. (1979). Nonreflecting boundary conditions for nonlinear hyperbolic systems. *Journal of computational Physics 30*(2), 222–237. *(p. 187)*

Henkes, R. and C. Hoogendoorn (1995). Comparison exercise for computations of turbulent natural convection in enclosures. *Numerical Heat Transfer, Part B Fundamentals 28*(1), 59–78. *(p. 20)*

Heskestad, G. (1965). Hot-wire measurements in a plane turbulent jet. *Journal of Applied Mechanics 32*(4), 721–734. *(p. 74)*

Heyerichs, K. and A. Pollard (1996). Heat transfer in separated and impinging turbulent flows. *International Journal of Heat and Mass Transfer 39*(12), 2385–2400. *(p. 63)*

Hortmann, M., M. Perić, and G. Scheuerer (1990). Finite volume multigrid prediction of laminar natural convection: Bench-mark solutions. *International Journal for Numerical Methods in Fluids 11*, 189–207. *(p. 30, 32, 33)*

Howell, J. R. (1998). The monte carlo method in radiative heat transfer. *Journal of Heat Transfer 120*(3), 547–560. *(p. 43)*

Huang, P., G. Coleman, and P. Bradshaw (1995). Compressible turbulent channel flows: Dns results and modelling. *Journal of Fluid Mechanics 305*, 185–218. *(p. 81, 173)*

IEA (2017). Key world energy statistics 2017. *International Energy Agency*. *(p. xvi)*

IEA (2018). International energy agency. `https://www.iea.org`. Accessed: 16/02/2019. *(p. xv)*

Jang, H. J., S. Y. Kang, J. J. Lee, T. S. Kim, and S. J. Park (2015). Performance analysis of a multi-stage ultra-supercritical steam turbine using computational fluid dynamics. *Applied Thermal Engineering 87*, 352–361. *(p. xvii, 60, 66)*

Jenkins, P. and V. Goldschmidt (1973). Mean temperature and velocity in a plane turbulent jet. *Journal of Fluids Engineering 95*(4), 581–584. *(p. 38, 77, 78, 79, 85, 86, 88, 148, 150, 153)*

Joe, S. and F. Y. Kuo (2008). Constructing sobol sequences with better two-dimensional projections. *SIAM Journal on Scientific Computing 30*(5), 2635–2654. *(p. 44)*

Jones, W. and B. Launder (1972). The prediction of laminarization with a two-equation model of turbulence. *International journal of heat and mass transfer 15*(2), 301–314. *(p. 20)*

Jones, W. and M. Paul (2005). Combination of DOM with LES in a gas turbine combustor. *International journal of engineering science 43*(5-6), 379–397. *(p. 120, 121)*

Kabashnikov, V. (1985). Thermal radiation of turbulent flows in the case of large fluctuations of the absorption coefficient and the planck function. *Journal of engineering physics 49*(1), 778–784. *(p. 52)*

Kabashnikov, V. and G. Kmit (1979). Influence of turbulent fluctuations on thermal radiation. *Journal of Applied Spectroscopy 31*(2), 963–967. *(p. xx, 52)*

Kennedy, C. A. and M. H. Carpenter (1994). Several new numerical methods for compressible shear-layer simulations. *Applied Numerical Mathematics 14*(4), 397–433. *(p. 6, 75)*

Klein, M., A. Sadiki, and J. Janicka (2003). Investigation of the influence of the reynolds number on a plane jet using direct numerical simulation. *International Journal of Heat and Fluid Flow 24*(6), 785–794. *(p. 38, 61, 71, 74, 77, 78, 148)*

Kolmogorov, A. (1942). Equations of motion of an incompressible turbulent fluid. *Izv Akad Nauk SSSR Ser Phys 6*, 56–58. *(p. 21)*

Kolmogorov, A. N. (1941). The local structure of turbulence in incompressible viscous fluid for very large reynolds numbers. In *Dokl. Akad. Nauk SSSR*, Volume 30, pp. 299–303. *(p. 5)*

Koren, C. (2016). *Modélisation des transferts de chaleur couplés pour la simulation multi-physique des chambres de combustion.* Ph. D. thesis, Université Paris-Saclay. *(p. 44)*

Koren, C., R. Vicquelin, and O. Gicquel (2018). Multiphysics simulation combining large-eddy simulation, wall heat conduction and radiative energy transfer to predict wall temperature induced by a confined premixed swirling flame. *Flow, Turbulence and Combustion 101*(1), 77–102. *(p. xix, 120, 121)*

Kritzstein, F. and A. Soufiani (1993). Infrared gas radiation from a homogeneously turbulent medium. *International journal of heat and mass transfer 36*(7), 1749–1762. *(p. xix, 120, 121)*

Lari, K., M. Baneshi, S. G. Nassab, A. Komiya, and S. Maruyama (2011). Combined heat transfer of radiation and natural convection in a square cavity containing participating gases. *International Journal of Heat and Mass Transfer 54*(23-24), 5087–5099. *(p. 44)*

Launder, B. and B. Sharma (1974). Application of the energy-dissipation model of turbulence to the calculation of flow near a spinning disc. *Letters in heat and mass transfer 1*(2), 131–137. *(p. 20, 62, 147, 151)*

Launder, B. E., G. J. Reece, and W. Rodi (1975). Progress in the development of a reynolds-stress turbulence closure. *Journal of fluid mechanics 68*(3), 537–566. *(p. 19)*

Le Quéré, P., R. Masson, and P. Perrot (1992). A chebyshev collocation algorithm for 2d non-boussinesq convection. *Journal of computational physics 103*(2), 320–335. *(p. 33)*

Le Quéré, P., C. Weisman, H. Paillère, J. Vierendeels, E. Dick, R. Becker, M. Braack, and J. Locke (2005). Modelling of natural convection flows with large temperature differences: a benchmark problem for low mach number solvers. part 1. reference solutions. *ESAIM: Mathematical Modelling and Numerical Analysis 39*, 609–616. *(p. 30, 33)*

Le Ribault, C., S. Sarkar, and S. Stanley (1999). Large eddy simulation of a plane jet. *Physics of Fluids 11*(10), 3069–3083. *(p. 74, 79)*

Leal, M., H. Machado, and R. Cotta (2000). Integral transform solutions of transient natural convection in enclosures with variable fluid properties. *International Journal of Heat and Mass Transfer 43*, 3977–3990. *(p. 30, 32, 34)*

Lemieux, C. (2008). *Monte Carlo and Quasi-Monte Carlo Sampling.* Springer. *(p. 44)*

Lemieux, G. and P. Oosthuizen (1985). Experimental study of the behavior of plane turbulent jets at low reynolds numbers. *AIAA journal 23*(12), 1845–1846. *(p. 71)*

Lemmon, E., M. McLinden, and D. Friend (2005). Thermophysical properties of fluid systems. *NIST chemistry webbook, NIST standard reference database 69.* *(p. 62)*

Leonard, B. (1988). Simple high-accuracy resolution program for convective modelling of discontinuities. *International Journal for Numerical Methods in Fluids 8*(10), 1291–1318. *(p. 25)*

Li, G. and M. F. Modest (2002). Application of composition pdf methods in the investigation of turbulence–radiation interactions. *Journal of Quantitative Spectroscopy and Radiative Transfer 73*(2), 461–472. *(p. 53)*

Li, G. and M. F. Modest (2003). Importance of turbulence-radiation interactions in turbulent diffusion jet flames. *Journal of heat transfer 125*(5), 831–838. *(p. xix, 120, 121)*

Lien, F.-S. and M. Leschziner (1994). Upstream monotonic interpolation for scalar transport with application to complex turbulent flows. *International Journal for Numerical Methods in Fluids 19*(6), 527–548. *(p. 25)*

Liu, C. and Z. Liu (1993). High order finite difference and multigrid methods for spatially evolving instability in a planar channel. *Journal of Computational Physics 106*(1), 92–100. *(p. 8)*

Lodato, G., P. Domingo, and L. Vervisch (2008). Three-dimensional boundary conditions for direct and large-eddy simulation of compressible viscous flows. *Journal of Computational Physics 227*(10), 5105–5143. *(p. 13)*

Martin, M. P., U. Piomelli, and G. V. Candler (2000). Subgrid-scale models for compressible large-eddy simulations. *Theoretical and Computational Fluid Dynamics 13*(5), 361–376. *(p. 179, 180)*

Mazumder, S. and M. F. Modest (1999). Turbulence-radiation interactions in nonreactive flow of combustion gases. *Transactions-American Society of Mechanical Engineers Journal of Heat Transfer 121*, 726–728. *(p. 144)*

Mehta, R., D. Haworth, and M. Modest (2010). Composition pdf/photon monte carlo modeling of moderately sooting turbulent jet flames. *Combustion and Flame 157*(5), 982–994. *(p. 55)*

Mehta, R. and M. Modest (2006). Modeling absorption tri in optically thick eddies. In *Proceedings of Eurotherm seminar*, Volume 78. *(p. 54)*

Mehta, R. S., M. F. Modest, and D. C. Haworth (2010). Radiation characteristics and turbulence–radiation interactions in sooting turbulent jet flames. *Combustion Theory and Modelling 14*(1), 105–124. *(p. 55)*

Mendoza, C., C. Salinas, J. Armengol, R. Beicker, and R. Santos (2016). Numerical investigation of heat transfer by natural convection and radiation in a cavity with participating media. *Proceedings of ENCIT Conference Paper*(0626), 1–9. *(p.)*

Mignon, P. (1992). *Etude théorique du couplage convection turbulente rayonnement dans un écoulement de gaz dans un canal. Thermodégradation de la paroi.* Ph. D. thesis. *(p. 53)*

Modest, M. F. and D. C. Haworth (2016). *Radiative Heat Transfer in Turbulent Combustion Systems: Theory and Applications.* Springer. *(p. xix, 98)*

Moufekkir, F., M. Moussaoui, A. Mezrhab, H. Naji, and D. Lemonnier (2012). Numerical prediction of heat transfer by natural convection and radiation in an enclosure filled with an isotropic scattering medium. *Journal of Quantitative Spectroscopy and Radiative Transfer 113*(13), 1689–1704. *(p. 44)*

Moureau, V., P. Domingo, and L. Vervisch (2011). Design of a massively parallel cfd code for complex geometries. *Comptes Rendus Mécanique 339*(2-3), 141–148. *(p. xviii)*

Naot, D. and W. Rodi (1982). Calculation of secondary currents in channel flow. *Journal of the Hydraulics Division 108*(8), 948–968. *(p. 19)*

O'Rourke, P. and F. Bracco (1979). Two scaling transformations for the numerical computation of multidimensional unsteady laminar flames. *Journal of Computational Physics 33*(2), 185–203. *(p. 9)*

Palluotto, L., N. Dumont, P. Rodrigues, C. Koren, R. Vicquelin, and O. Gicquel (2017). Comparison of monte carlo methods efficiency to solve radiative energy transfer in high fidelity unsteady 3d simulations. In *ASME Turbo Expo 2017: Turbomachinery Technical Conference and Exposition.* American Society of Mechanical Engineers. *(p. 44)*

Passot, T. and A. Pouquet (1987). Numerical simulation of compressible homogeneous flows in the turbulent regime. *Journal of Fluid Mechanics 181*, 441–466. *(p. 7, 76)*

Patankar, S. (1980). *Numerical heat transfer and fluid flow.* CRC press. *(p. 23, 30)*

Patankar, S. V. and D. B. Spalding (1983). A calculation procedure for heat, mass and momentum transfer in three-dimensional parabolic flows. In *Numerical Prediction of Flow, Heat Transfer, Turbulence and Combustion*, pp. 54–73. Elsevier. *(p. 27)*

Peaceman, D. W. and H. H. Rachford, Jr (1955). The numerical solution of parabolic and elliptic differential equations. *Journal of the Society for industrial and Applied Mathematics 3*(1), 28–41. *(p. 30)*

Peng, S.-H. and L. Davidson (1999). Computation of turbulent buoyant flows in enclosures with low-reynolds-number k-ω models. *International Jour-*

nal of heat and fluid flow 20(2), 172–184. *(p. 20, 22)*

Pérez-Segarra, C., A. Oliva, M. Costa, and F. Escanes (1995). Numerical experiments in turbulent natural and mixed convection in internal flows. *International Journal of Numerical Methods for Heat & Fluid Flow 5*(1), 13–33. *(p. 20)*

Poinsot, T. and D. Veynante (2005). *Theoretical and numerical combustion.* RT Edwards, Inc. *(p. 179, 184, 185)*

Poinsot, T. J. and S. Lele (1992). Boundary conditions for direct simulations of compressible viscous flows. *Journal of computational physics 101*(1), 104–129. *(p. 9, 75)*

Poitou, D., J. Amaya, M. El Hafi, and B. Cuenot (2012). Analysis of the interaction between turbulent combustion and thermal radiation using unsteady coupled les/dom simulations. *Combustion and Flame 159*(4), 1605–1618. *(p. xx, 120, 121)*

Pope, S. B. (1985). Pdf methods for turbulent reactive flows. *Progress in Energy and Combustion Science 11*(2), 119–192. *(p. 54)*

Pope, S. B. (2001). Turbulent flows. *(p. 22, 74, 83, 158, 177)*

Pope, S. B. (2004). Ten questions concerning the large-eddy simulation of turbulent flows. *New journal of Physics 6*(1), 35. *(p. 185)*

Rajaratnam, N. (1976). *Turbulent jets.* Elsevier Scientific, New York. *(p. 61, 74, 78)*

Ramaprian, B. and M. Chandrasekhara (1985). LDA measurements in plane turbulent jets. *Journal of Fluids Engineering 107*(2), 264–271. *(p. 80, 151)*

Ramshaw, J., P. O'Rourke, and L. Stein (1985). Pressure gradient scaling method for fluid flow with nearly uniform pressure. *Journal of Computational Physics 58*(3), 361–376. *(p. 9)*

Raynal, L., J.-L. Harion, M. Favre-Marinet, and G. Binder (1996). The oscillatory instability of plane variable-density jets. *Physics of Fluids 8*(4), 993–1006. *(p. 85)*

Refahi, S. (2013). Development of a radiative transfer code and its coupling with a les code. *Theses, Ecole Centrale Paris*, 40. *(p. 44)*

Ren, T., M. F. Modest, and S. Roy (2018). Monte carlo simulation for radiative transfer in a high-pressure industrial gas turbine combustion chamber. *Journal of Engineering for Gas Turbines and Power 140*(5), 051503. *(p. xix, 120, 121)*

Richards, C. D. and W. M. Pitts (1993). Global density effects on the self-preservation behaviour of turbulent free jets. *Journal of Fluid Mechanics 254*, 417–435. *(p. 85, 90)*

Richardson, L. F. (1922). *Weather Prediction by Numerical Process.* Cambridge University Press. *(p. 5)*

Rivière, P. and A. Soufiani (2012). Updated band model parameters for h2o, co2, ch4 and co radiation at high temperature. *International Journal of Heat and Mass Transfer 55*(13-14), 3349–3358. *(p. 47, 92)*

Riviere, P., A. Soufiani, and J. Taine (1992). Correlated-k and fictitious gas methods for h2o near 2.7 μm. *Journal of Quantitative Spectroscopy and Radiative Transfer 48*(2), 187–203. *(p. 46)*

Rodi, W. (1993). *Turbulence models and their application in hydraulics.* CRC Press. *(p. 22)*

Rodrigues, P. (2018). *Modélisation multiphysique de flammes turbulentes suitées avec la prise en compte des transferts radiatifs et des transferts de chaleur pariétaux.* Ph. D. thesis, Paris Saclay. *(p. 44, 45, 46)*

Rodrigues, P., O. Gicquel, N. Darabiha, K. Geigle, and R. Vicquelin (2019). Assessment of external heat transfer modeling of a laboratory-scale combustor: Effects of pressure-housing environment and semi-transparent viewing windows. *Journal of Engineering for Gas Turbines and Power 141*(3), 031011. *(p. xix)*

Roe, P. L. (1985). Some contributions to the modelling of discontinuous flows. In *Large-scale computations in fluid mechanics*, pp. 163–193. *(p. 25)*

Roger, M., P. Coelho, and C. Da Silva (2011). Relevance of the subgrid-scales for large eddy simulations of turbulence–radiation interactions in a turbulent plane jet. *Journal of Quantitative Spectroscopy and Radiative Transfer 112*(7), 1250–1256. *(p. xix, 120, 121)*

Roger, M., P. J. Coelho, and C. B. da Silva (2010). The influence of the non-resolved scales of thermal radiation in large eddy simulation of turbulent flows: A fundamental study. *International Journal of Heat and Mass Transfer 53*(13-14), 2897–2907. *(p. xix, 120, 121)*

Roger, M., C. B. Da Silva, and P. J. Coelho (2009). Analysis of the turbulence–radiation interactions for large eddy simulations of turbulent flows. *International Journal of Heat and Mass Transfer 52*(9-10), 2243–2254. *(p. xix, 120, 121)*

Rothman, L. S., I. E. Gordon, R. J. Barber, H. Dothe, R. R. Gamache, A. Goldman, V. I. Perevalov, S. A. Tashkun, and J. Tennyson (2010, 10). HITEMP, the high-temperature molecular spectroscopic database. *Journal of Quantitative Spectroscopy and Radiative Transfer 111*(15), 2139–2150. *(p. 92)*

Sadeghi, H., P. Lavoie, and A. Pollard (2015). Equilibrium similarity solution of the turbulent transport equation along the centreline of a round jet. *Journal of Fluid Mechanics 772*, 740–755. *(p. 74)*

Sadeghi, H., M. Oberlack, and M. Gauding (2018). On new scaling laws in a temporally evolving turbulent plane jet using lie symmetry analysis and direct numerical simulation. *Journal of Fluid Mechanics 854*, 233–260. *(p. 74)*

Sakurai, A., R. Kanbayashi, and K. Matsubara (2017). Radiation effects on turbulent natural convection in optically thick participating fluids using direct numerical simulation. *Numerical Heat Transfer, Part A: Applications 72*(12), 904–920. *(p. xx)*

Salinas-Vázquez, M., W. Vicente, E. Barrios, E. Martínez, A. Palacio, and

A. Rodríguez (2013). A low-mach number method for the numerical simulation of complex flows. *Applied Mathematical Modelling 37*(22), 9132–9146. *(p. 9)*

Shan, H., L. Jiang, and C. Liu (2005). Direct numerical simulation of flow separation around a naca 0012 airfoil. *Computers & Fluids 34*(9), 1096–1114. *(p. 83)*

Silvestri, S., A. Patel, D. Roekaerts, and R. Pecnik (2018). Turbulence radiation interaction in channel flow with various optical depths. *Journal of Fluid Mechanics 834*, 359–384. *(p. xx)*

Snegirev, A. Y. (2004). Statistical modeling of thermal radiation transfer in buoyant turbulent diffusion flames. *Combustion and Flame 136*(1), 51–71. *(p. 53)*

Song, T. and R. Viskanta (1987). Interaction of radiation with turbulence-application to a combustion system. *Journal of thermophysics and heat transfer 1*(1), 56–62. *(p. xx)*

Soucasse, L., P. Rivière, and A. Soufiani (2016). Natural convection in a differentially heated cubical cavity under the effects of wall and molecular gas radiation at rayleigh numbers up to 3× 109. *International Journal of Heat and Fluid Flow 61*, 510–530. *(p. 120, 121)*

Soufiani, A., P. Mignon, and J. Taine (1990a). Radiation–turbulence interaction in channel flows of infrared active gases. In *Proceedings of the ninth international heat transfer conference*, Volume 6, pp. 403–408. *(p. 53)*

Soufiani, A., P. Mignon, and J. Taine (1990b). Radiation effects on turbulent heat transfer in channel flows of infrared active gases. In *Radiation heat transfer: Fundamentals and applications.* *(p. 53)*

Soufiani, A. and J. Taine (1997). High temperature gas radiative property parameters of statistical narrow-band model for H2O, CO2 and CO, and correlated-k model for H2O and CO2. *International journal of heat and mass transfer 40*(4), 987–991. *(p. 47, 92)*

Spalart, P. and S. Allmaras (1992). A one-equation turbulence model for aerodynamic flows. In *30th aerospace sciences meeting and exhibit*, pp. 439. *(p. 19)*

Stanley, S. and S. Sarkar (2000). Influence of nozzle conditions and discrete forcing on turbulent planar jets. *AIAA journal 38*(9), 1615–1623. *(p. 38, 78)*

Stanley, S., S. Sarkar, and J. Mellado (2002). A study of the flow-field evolution and mixing in a planar turbulent jet using direct numerical simulation. *Journal of Fluid Mechanics 450*, 377–407. *(p. 37, 38, 63, 65, 66, 71, 74, 76, 77, 78, 79, 80, 82, 83, 86, 87, 88, 90, 148, 150, 151, 153)*

Taine, J. and A. Soufiani (1999). Gas ir radiative properties: from spectroscopic data to approximate models. *Advances in heat transfer 33*, 295–414. *(p. 46)*

Tanuma, T. (2017). *Advances in Steam Turbines for Modern Power Plants.* Woodhead Publishing. *(p. xvii, 60, 66, 107)*

Terashima, O., Y. Sakai, and K. Nagata (2012). Simultaneous measurement of velocity and pressure in a plane jet. *Experiments in fluids 53*(4), 1149–1164. *(p. 82)*

Tessé, L., F. Dupoirieux, and J. Taine (2004). Monte carlo modeling of radiative transfer in a turbulent sooty flame. *International journal of heat and mass transfer 47*(3), 555–572. *(p. xx, 54, 61, 120, 121)*

Thiesset, F., R. Antonia, and L. Djenidi (2014). Consequences of self-preservation on the axis of a turbulent round jet. *Journal of Fluid Mechanics 748*. *(p. 74)*

Thomas, F. and H. Chu (1989). An experimental investigation of the transition of a planar jet: Subharmonic suppression and upstream feedback. *Physics of Fluids A: Fluid Dynamics (1989-1993) 1*(9), 1566–1587. *(p. 37, 38, 78, 79, 148, 150)*

Thomas, F. and K. Prakash (1991). An experimental investigation of the natural transition of an untuned planar jet. *Physics of Fluids A: Fluid Dynamics (1989-1993) 3*(1), 90–105. *(p. 80, 151)*

Thompson, K. W. (1987). Time dependent boundary conditions for hyperbolic systems. *Journal of computational physics 68*(1), 1–24. *(p. 187)*

Thring, M. and M. Newby (1953). Combustion length of enclosed turbulent jet flames. *Symposium (International) on Combustion*, 789–796. *(p. 85)*

Townsend, A. A. (1956). *The structure of turbulent shear flow.* Cambridge university press. *(p. 74)*

Turkel, E. (1987). Preconditioned methods for solving the incompressible and low speed compressible equations. *Journal of computational physics 72*(2), 277–298. *(p. 8)*

UNFCCC (2019). United nations framework convention on climate change. `https://unfccc.int`. Accessed: 16/02/2019. *(p. xv)*

Van Albada, G., B. Van Leer, and W. Roberts (1997). A comparative study of computational methods in cosmic gas dynamics. In *Upwind and High-Resolution Schemes*, pp. 95–103. Springer. *(p. 62, 148)*

van Albada, G., B. van Leer, and W. Roberts Jr (1982). A comparative study of computational methods in cosmic gas dynamics. *Astron. Astrophys 108*, 76–84. *(p. 25)*

Van Leer, B. (1977). Towards the ultimate conservative difference scheme iii. upstream-centered finite-difference schemes for ideal compressible flow. *Journal of Computational Physics 23*(3), 263–275. *(p. 25)*

Van Leer, B., W.-T. Lee, and P. L. Roe (1991). Characteristic time-stepping or local preconditioning of the euler equations. *(p. 8)*

Versteeg, H. K. and W. Malalasekera (2007). *An introduction to computational fluid dynamics: the finite volume method.* Pearson Education. *(p. 25)*

Vicquelin, R., Y. Zhang, O. Gicquel, and J. Taine (2014). Effects of radiation in turbulent channel flow: analysis of coupled direct numerical simulations. *Journal of Fluid Mechanics 753*, 360–401. *(p. xx, 120, 121,* *132, 133, 144, 158, 175)*

Vierendeels, J., K. Riemslagh, and E. Dick (1999). A multigrid semi-implicit line-method for viscous incompressible and low-mach-number flows on high aspect ratio grids. *Journal of Computational Physics 154*(2), 310–341. *(p. 33)*

Vreman, A. W. (1995). *Direct and large-eddy simulation of the compressible turbulent mixing layer*. University of Twente. *(p. 179, 180)*

Vreman, B., B. Geurts, and H. Kuerten (1995). A priori tests of large eddy simulation of the compressible plane mixing layer. *Journal of Engineering Mathematics 29*(4), 299–327. *(p. 179, 180)*

Wang, A. and M. F. Modest (2006). Photon monte carlo simulation for radiative transfer in gaseous media represented by discrete particle fields. *Journal of heat transfer 128*(10), 1041–1049. *(p. 55)*

Wang, A., M. F. Modest, D. C. Haworth, and L. Wang (2008). Monte carlo simulation of radiative heat transfer and turbulence interactions in methane/air jet flames. *Journal of Quantitative Spectroscopy and Radiative Transfer 109*(2), 269–279. *(p. 54)*

Wang, W., H. Zhang, P. Liu, Z. Li, W. Ni, H. Uechi, and T. Matsumura (2016). A finite element method approach to the temperature distribution in the inner casing of a steam turbine in a combined cycle power plant. *Applied Thermal Engineering 105*, 18–27. *(p. xviii)*

Wang, Y. and A. Trouvé (2004). Artificial acoustic stiffness reduction in fully compressible, direct numerical simulation of combustion. *Combustion Theory and Modelling 8*(3), 633–660. *(p. 9, 187)*

Wilcox, D. A. (1994). Simulation of transition with a two-equation turbulence model. *AIAA journal 32*(2), 247–255. *(p. 20, 22)*

Wilcox, D. C. et al. (1998). *Turbulence modeling for CFD*, Volume 2. DCW industries La Canada, CA. *(p. 20, 22, 158)*

Wróblewski, W., S. Dykas, and A. Gepert (2009). Steam condensing flow modeling in turbine channels. *International Journal of Multiphase Flow 35*(6), 498–506. *(p. xviii)*

Wu, Y., D. Haworth, M. Modest, and B. Cuenot (2005). Direct numerical simulation of turbulence/radiation interaction in premixed combustion systems. *Proceedings of the Combustion Institute 30*(1), 639–646. *(p. xix, xx, 120, 121)*

Wu, Y., M. F. Modest, and D. C. Haworth (2007). A high-order photon monte carlo method for radiative transfer in direct numerical simulation. *Journal of Computational Physics 223*(2), 898–922. *(p. xix, xx, 120, 121)*

Yoo, C. S., T. Lu, J. H. Chen, and C. K. Law (2011). Direct numerical simulations of ignition of a lean n-heptane/air mixture with temperature inhomogeneities at constant volume: Parametric study. *Combustion and Flame 158*(9), 1727–1741. *(p. 83)*

Yu, M.-H. and P. A. Monkewitz (1993). Oscillations in the near field of a heated two-dimensional jet. *Journal of fluid mechanics 255*, 323–347.

(p. 85)

Yücel, A., S. Acharya, and M. Williams (1989). Natural convection and radiation in a square enclosure. *Numerical Heat Transfer 15*(2), 261–278. *(p. 44)*

Zhang, J. (2011). *Radiation Monte Carlo approcah dedicated to the coupling with LES reactive simulation.* Ph. D. thesis, Ecole Centrale Paris. *(p. 44)*

Zhang, Y. (2013). *Coupled convective heat transfer and radiative energy transfer in turbulent boundary layers.* Ph. D. thesis, Ecole Centrale Paris. *(p. 44)*

Zhang, Y., O. Gicquel, and J. Taine (2012). Optimized emission-based reciprocity monte carlo method to speed up computation in complex systems. *International Journal of Heat and Mass Transfer 55*(25-26), 8172–8177. *(p. 46)*

Zhang, Y., R. Vicquelin, O. Gicquel, and J. Taine (2013). Physical study of radiation effects on the boundary layer structure in a turbulent channel flow. *International Journal of Heat and Mass Transfer 61*, 654–666. *(p. xx, 48, 120, 121, 144)*

université
PARIS-SACLAY

ÉCOLE DOCTORALE
Sciences mécaniques et énergétiques, matériaux et géosciences (SMEMAG)

Titre : Étude numérique des effets du couplage du rayonnement thermique aux jets turbulents libres de vapeur d'eau

Mots clés : Jet turbulent; Mise à l'échelle; Simulation numérique directe; Rayonnement; Monte-Carlo.

Résumé : Le rayonnement thermique joue un rôle important dans un large éventail d'applications de génie thermique comprenant des écoulements turbulents. La motivation principale de cette thèse est le besoin croissant de précision et fiabilité dans les simulations numériques appliqué à ce domaine.
Cette thèse s'intéresse tout particulièrement à la compréhension physique de l'impact du rayonnement thermique sur la dynamique des fluides et le transfert thermique, ainsi que de l'influence des fluctuations turbulentes sur le transfert radiatif dans les écoulements à couche de cisaillement. L'objectif de cette thèse est de fournir des données haute-fidélités de jets libres turbulents couplés au rayonnement thermique afin de développer et de valider des modèles turbulents d'écoulements à couche de cisaillement prenant en compte les interactions de couplage. À cette fin, les jets libres turbulents sont décrits par des simulations numériques directes (DNS) couplées à une méthode de Monte-Carlo réciproque pour résoudre l'équation de transfert radiatif. La dépendance spectrale des propriétés radiatives est prise en compte avec la méthode Correlated-k (ck).
Deux simulations directes de jets chauffés couplés au rayonnement thermique sont réalisées. D'une part, un jet chauffé avec un rayonnement modéré a été simulé et l'analyse de ses données DNS couplées a permis de dériver une nouvelle loi d'échelle pour la décroissance du profil de température. Cette mise à l'échelle rend compte des effets de la densité modifiée due à un rayonnement modéré. De plus, cela permet de distinguer si le rayonnement thermique modifie ou non la nature des mécanismes de transfert thermique dans la région développée du jet. D'autre part, un jet libre fortement chauffé a été calculé afin de quantifier les effets du rayonnement sur les champs de température et de vitesse moyens ainsi que sur les moments de second ordre.
Outre les données DNS couplées, un solver RANS pour les écoulements à densité variable couplé au rayonnement thermique a été développé au cours de cette thèse. L'objectif était de quantifier directement la précision des modèles turbulents existants et d'identifier les paramètres clés pour une modélisation plus poussée des interactions de couplage.

Title : Numerical Investigation of the Effects of Coupled Radiative Heat Transfer on Free Turbulent Jets of Water Vapor

Keywords : Turbulent jet; Scaling; Direct Numerical Simulation; Thermal radiation; Monte-Carlo.

Abstract :
Radiation plays an important role in a broad range of thermal engineering applications comprising turbulent flows. The growing need for accurate and reliable numerical simulations to support the design stages of such applications is the main motivation of this thesis. Of special interest in this work are the free-shear flows and the fundamental understanding of how radiation can modify their fluid dynamics and heat transport as well as how their turbulence fluctuations can alter radiative transfer. The goal of this thesis is to provide high-fidelity data of turbulent free jets coupled with thermal radiation in order to develop and validate free-shear turbulent models accounting for coupling interactions. To this end, turbulent free jets are described by direct numerical simulations (DNS) coupled to a reciprocal Monte-Carlo method to solve the radiative transfer equation. The spectral dependency of the radiative properties is accounted for with an accurate Correlated-k (ck) method.
Two direct simulations of heated jets coupled with thermal radiation are carried out. On the one hand, a heated jet with moderate radiation is simulated. The analysis of its high-fidelity coupled DNS data has allowed to derive a new scaling law for the decay of the temperature profile. This scaling accounts for the effects of modified density due to moderate radiation. Moreover, it allows for distinguishing whether thermal radiation modifies the nature of heat transfer mechanisms in the jet developed region or not. On the other hand, a strongly heated free jet is computed in order to quantify the effects of radiation on mean temperature and velocity fields as well as on second order moments.
Besides the coupled DNS data, a RANS solver for variable-density flows coupled with thermal radiation has been implemented during the course of this thesis. The goal is to directly quantify the accuracy of the existing turbulent models, and to identify key parameters for further modeling of coupling interactions.

Université Paris-Saclay
Espace Technologique / Immeuble Discovery
Route de l'Orme aux Merisiers RD 128 / 91190 Saint-Aubin, France